

MEMS Inertial Sensor to Measure the Gravity Gradient Torque in Orbit

THÈSE N° 5231 (2012)

PRÉSENTÉE LE 30 AVRIL 2012

À LA FACULTÉ DES SCIENCES ET TECHNIQUES DE L'INGÉNIEUR
LABORATOIRE DES MICROSYSTÈMES POUR LES TECHNOLOGIES SPATIALES
PROGRAMME DOCTORAL EN MICROSYSTÈMES ET MICROÉLECTRONIQUE

ÉCOLE POLYTECHNIQUE FÉDÉRALE DE LAUSANNE

POUR L'OBTENTION DU GRADE DE DOCTEUR ÈS SCIENCES

PAR

Kaustav GHOSE

acceptée sur proposition du jury:

Prof. P.-A. Farine, président du jury
Prof. H. Shea, directeur de thèse
Prof. B. Dutoit, rapporteur
Dr F. Filhol, rapporteur
Dr W. Noell, rapporteur



ÉCOLE POLYTECHNIQUE
FÉDÉRALE DE LAUSANNE

Suisse
2012

Abstract

Since the dawn of the Space Age, over six thousand satellites have been launched into Earth orbit. The function of determining the orientation of a satellite in orbit, so that it can point its antennas and instruments in the required direction is known as attitude determination. Depending on the nature of the mission, this important function is typically performed by means of optical instruments that determine the orientation of the satellite with respect to known bodies such as the Earth, the sun, and bright stars. Conventional Earth sensors use cameras and telescopes to locate the position of the Earth's horizon and hence to calculate the orientation of the satellite.

In the event that a satellite starts to tumble, existing Earth sensors that use optical sensing are severely limited in their ability to reacquire the attitude due to the limited field of view of the instruments. Also, due to this limited field of view, multiple Earth sensor units need to be placed on all faces of the satellite to ensure 4π steradian coverage. Because of the optical sensing principle of existing Earth sensors, constraints are imposed on the positioning of solar panels and antennas so that they do not block the field of view of optical sensors.

This thesis describes a novel inertial sensor that uses the Earth's gravity gradient as a reference for attitude determination on-board a satellite in low Earth orbit. Using the gravity gradient for attitude determination makes it possible to realise a single, compact Earth sensor instrument which can be positioned flexibly within the satellite. Due to its 4π steradian field of view, such an instrument can offer added capability as a backup sensor, or act as the main Earth sensor. By using Micro-Electro-Mechanical System (MEMS) technology for the inertial sensor, a target mass of 1 kg and target volume of 1 dm³ can be realised for the entire gravity gradient Earth sensor system.

The gravitational force decreases as the square of the distance from the center of the Earth. An elongated object in orbit around the Earth will have slightly different values of gravity acting over the different points in its volume. This gives rise to a small torque, the Gravity Gradient Torque (GGT), on the object. A compact micromachined inertial sensor was designed with an elongated proof mass and compliant spring to measure the GGT, so that the orientation of the proof mass with respect to the normal from the Earth's surface can be determined. Such a sensor on-board a satellite can act as an Earth sensor, and provide information about the satellite attitude with respect to the normal to the Earth's surface.

An inertial sensor to measure GGT, which with readout electronics fits within a 1 dm³ volume, has to measure a torque of magnitude 10^{-15} N.m. Currently, no inertial sensor is capable of such a fine measurement. In addition to the required performance in microgravity, the inertial sensor must be robust enough to be tested on Earth with no special handling, and must survive the vibration and shock of a launch, to be used in space. The readout scheme to measure the displacement due to GGT must also be simple and robust.

The designs of two generations of a novel inertial sensor to measure the GGT are presented in the thesis. To be able to measure the GGT with the required accuracy a sensor is designed that has a proof mass 5 cm long, suspended by springs which have widths less than ten microns. The sensor resonant frequency of the inertial sensor is on the order of 1 Hz. A new fabrication process is developed for the sensor, which incorporates hard stops to limit the motion of the proof mass along all the axes, thus making it robust enough for testing without any special precautions. The sensor survives low magnitude vibration tests. A digital electronic readout based on capacitive sensing of the displacement due to GGT, is developed based on commercially available ICs, and allows easy interfacing of the inertial sensor output to a PC or microcontroller. To test the sensor on Earth, a dedicated test setup is developed to replicate the nm-scale motion of the proof mass expected in orbit. The electronic readout is capable of measuring the sub-nm displacements due to GGT. The 2nd generation sensor design with capacitive displacement sensing is the first demonstration of an inertial sensor capable of measuring the GGT in low Earth orbit, and an important step towards realization of a 1 kg, 1 dm³ Earth sensor that uses the gravity gradient of the Earth for attitude determination.

Keywords: Earth sensor, attitude determination, MEMS, inertial sensor, gravity gradient torque, finite element modelling, microfabrication, fiber interferometer, capacitive displacement sensing

Résumé

Depuis l'aube de l'ère spatiale, plus de six mille satellites ont été lancés en orbite terrestre. La fonction visant à déterminer l'orientation d'un satellite en orbite pour qu'il puisse pointer ses antennes et ses instruments dans la direction requise est appelée la détermination d'attitude. Selon la nature de la mission, cette fonction cruciale est généralement remplie par des instruments optiques qui déterminent l'orientation du satellite par rapport à des corps connus tels que la Terre, le soleil, et des étoiles brillantes. Les capteurs de Terre classiques utilisent des caméras et des télescopes pour localiser la position de l'horizon terrestre, et calculent ainsi l'orientation du satellite.

Dans le cas où un satellite commence à perdre de l'altitude, les capteurs de Terre existants fonctionnant avec des capteurs optiques sont sévèrement limités dans leur capacité à acquérir de nouveau l'attitude, à cause du champ de vision limité des instruments. En outre, en raison de ce champ de vision limité, plusieurs unités de capteurs de Terre doivent être placées sur toutes les faces du satellite pour assurer une couverture de 4π stéradian. En raison du principe de détection optique des capteurs de Terre existants, des contraintes sont imposées sur le positionnement des panneaux solaires et des antennes afin qu'elles ne bloquent pas leur champ de vision.

Cette thèse décrit un nouveau capteur inertiel qui utilise le gradient de gravité de la Terre comme référence pour la détermination de l'attitude à bord d'un satellite en orbite terrestre basse. En utilisant le gradient de gravité pour la détermination de l'attitude, il est possible de réaliser un seul instrument capteur de Terre compact qui peut être positionné de manière flexible dans le satellite. En raison de son champ de vue de 4π stéradian, un tel instrument peut offrir une fonctionnalité supplémentaire comme capteur de secours, ou agir comme le capteur de Terre principal. En utilisant les technologies disponibles pour les *Micro-Electro-Mechanical Systems* (MEMS) pour fabriquer le capteur inertiel, le système complet du capteur du gradient de gravité terrestre peut être réalisé en remplissant des spécifications de 1 kg de masse et de 1 dm³ de volume-cible.

La force gravitationnelle diminue avec le carré de la distance au centre de la Terre. Un objet allongé en orbite autour de la Terre aura des valeurs légèrement différentes de pesanteur agissant sur les différents points de son volume. Cela donne lieu à un petit couple, le couple de gradient de gravité (GGT), sur l'objet. Un capteur inertiel compact micro-usiné a été conçu avec une masse d'épreuve allongée et un ressort très flexible pour mesurer le GGT, pour que l'orientation de la masse d'épreuve par rapport à la normale à la surface de la Terre puisse être déterminée. A bord d'un satellite, un tel capteur peut agir comme un capteur de Terre, et fournir des informations sur l'attitude du satellite par rapport à la normale à la surface de la Terre.

Un capteur d'inertie pour mesurer le GGT doit mesurer un couple de l'ordre de 10⁻¹⁵ Nm, en occupant un volume de 1 dm³ avec son électronique de lecture. Actuellement, aucun capteur inertiel n'est capable d'une telle finesse de mesure. En plus de la performance requise en microgravité, le capteur inertiel doit être suffisamment robuste pour être testé sur Terre sans manipulation particulière et

survivre aux vibrations et chocs d'un lancement afin de pouvoir être utilisé dans l'espace. Le principe de lecture pour mesurer le déplacement dû au GGT doit aussi être simple et robuste.

La conception de deux générations d'un nouveau capteur inertiel pour mesurer le GGT est présentée dans cette thèse. Pour être capable de mesurer le GGT avec la précision requise, le capteur est conçu avec une masse d'épreuve de 5 cm de long, suspendue par des ressorts qui ont des largeurs de moins de dix microns. La fréquence de résonance du capteur inertiel est de l'ordre de 1 Hz. Un nouveau procédé de fabrication est développé pour le capteur, qui comprend des butées pour limiter le mouvement de la masse d'épreuve selon tous les axes, ce qui rend assez robuste pour des tests, sans nécessiter aucune précaution particulière. Le capteur survit à des tests de vibrations de faible amplitude. Une acquisition électronique digitale par détection capacitive du déplacement dû au GGT a été développée sur la base de circuits disponibles dans le commerce, et permet un interfaçage aisément de la sortie du capteur inertiel à un PC ou un microcontrôleur. Pour tester le capteur sur la Terre, une configuration de test dédiée a été développée pour reproduire le mouvement nanométrique de la masse d'épreuve prévu en orbite. L'acquisition électronique est capable de mesurer les déplacements inférieurs au nanomètre dus au GGT. La conception de la 2ème génération de capteurs avec mesure de déplacement capacitive est la première démonstration d'un capteur inertiel permettant de mesurer le GGT dans l'orbite terrestre basse, et une étape importante vers la réalisation d'un système de capteur de Terre d'un 1 kg et 1 dm³, qui utilise le gradient de gravité de la Terre pour la détermination de l'attitude.

Mots-clés: capteur de Terre, détermination de l'attitude, MEMS, capteur inertiel, couple de gradient de gravité, modélisation par éléments finis, microfabrication, l'interférométrie à fibres optique, détection capacitive de déplacement.

Acknowledgements

The image of a graduate student toiling away alone in the basement laboratory getting results for their thesis is a popular one, but far removed from reality. Without the continuous support and help of friends and colleagues too many to count, this work would not have been possible.

My deepest thanks go to my advisor Professor Herbert Shea, who gave me the opportunity in the Microsystems for Space Technologies Laboratory, and followed it up with four years of consistent support and advice, and a lot of patience, especially with my constant struggle with getting documentation ready on time. It felt nice to be able to tell other PhD students that I could ask my advisor for a meeting whenever I faced problems. I am really grateful for his flexibility in allowing me the time I needed to resolve critical issues with my thesis work.

The critical task of micro fabrication was done with loads of help from the staff at COMLAB in Neuchatel. Many thanks go to Stephane Ischer, Pierre-Andre Clerc, Edith Millotte, Laurent Guillot, Eduardo Santoli, Remy Fournier and Sylviane Pochon. I would also like to thank George Andre Racine and his colleagues at the CMI in EPFL for their help. Thanks to colleagues in SMLAB and LMTS, Renato Krpoun, Phillippe Dubois, Muhammed Niklaus, Yves Petremand, and Samuel Rosset, who gave me time and the benefit of their expertise in training me to use the cleanroom equipment.

A very special thank you to Ben O'Brien and Caglar Ataman for their extremely useful and illuminating insights into the structure and presentation of my thesis. The comments and feedback went a long way towards putting together an effective dissertation and presentation. Thanks to my labmates, Joao Gomes, Samin Akbari, Luc Maffli, Vinu Venkatraman and Subha Chakraborty for the coffee breaks, questions and useful comments. I also greatly appreciate the help from Myriam Poliero and Martine Harmel during the years at LMTS.

I am indebted to the European Space Agency, the Swiss Space Office and EPFL STI seed fund, for the financial support of this project. I would like to thank Phil Airey and Torsten Vogel of ESA for their guidance during the early phases of the project. My thanks also to Terry Lockey, Elisabetta Rugi Grond and Reto Muff for their feedback regarding the system aspects of the sensor. It was a good learning experience to work with RUAG space towards developing complete instrumentation for the Earth Sensor.

I am grateful to my jury members, Dr. Fabien Filhol, Professor Bertrand Dutoit, Dr. Wilfried Noell, and the jury president Professor Pierre-Andre Farine, for their comments and feedback for an improved thesis.

A big thanks to the REXUS team, for all their work towards making the sensors ready to go ballistic! Herve Meyer, Benoit Chamot, Jean-Francois Labreque-Piedboeuf, Ioana Josan-Drinceanu, Yann Voumard, Deborah Mueller, Jean-Noel Pittet, it was great fun with a lot of ups and downs, and at the end, I am grateful to all of you for your dedication and efforts. Last but not the least, a huge thank you to good cop Simon Dandavino, for taking on the huge responsibility to ensure that the GGES experiment

was delivered to ESA. I would also like to express my gratitude to Muriel Richard, for a great learning experience, and the energy and insight she brings into everything.

Finally, I would like to thank my family for their love and support in this long journey. I dedicate this thesis to my father, for his unwavering faith, and for always being there for me.

List of Abbreviations and Common Notations

AD	Analog Devices
ADCS	Attitude Determination and Control System
COTS	Commercial off the Shelf
DRIE	Deep Reactive Ion Etching
ES	Earth Sensor
ESA	European Space Agency
GG	Gravity Gradient
GGES	Gravity Gradient Earth Sensor
GGT	Gravity Gradient Torque
I	Moment of Inertia
IC	Integrated Circuit
MEMS	Micro-Electro-Mechanical System
PCB	Printed Circuit Board
REXUS	Rocket Experiments for University Students, a sounding rocket program jointly run by ESA and the Swedish Space Corporation
SOI	Silicon-On-Insulator. A type of silicon wafer consisting of two wafers of silicon bonded together by a thin layer of silicon oxide
Ψ	Used to denote the angle to the nadir, which is the vector pointing normally towards the Earth's surface

Table of Contents

Chapter 1- Introduction	13
1.1. The Earth's Gravity Gradient	16
1.2. Earth sensor.....	18
1.3. MEMS Inertial Sensors	19
1.4. Thesis Objectives	22
1.5. Thesis Structure	24
Chapter 2 - Attitude Determination using the Gravity Gradient Torque	25
2.1. Gravity Gradient Torque.....	25
2.2. Earth Sensor Instrument Utilizing GGT	27
2.2.1. 180 Degree Periodicity of GGT Inertial Sensor.....	28
2.3. Factors Affecting Sensitivity and Robustness of MEMS Inertial Sensor.....	31
2.4. Length and Breadth of Proof Mass	34
2.5. Signal to Thermal Noise Ratio.....	35
2.5.1. SNR Dependence on Orbit Height.....	38
2.6. Conclusion	39
Chapter 3 - Design of 1 st Generation Earth Sensor.....	41
3.1. Proof mass design	41
3.2. Spring design.....	43
3.3. Proof mass balancing	44
3.4. Effect of the spacecraft gravity.....	45
3.5. Effect of the Moon's gravity	45
3.6. Effect of Temperature on spring constant	46
3.7. Readout Design and Selection	46
3.7.1. Capacitive Displacement Readout.....	46
3.7.2. Optical Displacement Readout.....	48
3.8. Conclusion	50
Chapter 4 - Fabrication of 1 st Generation Earth Sensor	51
4.1. Test Devices	51
4.1.1. Improvements from Test Device.....	53

4.2. Fabrication Steps.....	55
4.2.1. ES chip with proof mass.....	55
4.2.2. Pyrex chip fabrication steps.....	57
4.2.3. Earth Sensor final assembly.....	58
4.2.4. Stopper Design.....	59
4.3. Conclusion	61
4.3.1. Large variation in HF etch rate.....	63
Chapter 5 - Testing of 1st Generation Device.....	65
5.1. Testing Goals.....	65
5.2. Test Setup.....	65
5.2.1. Alignment of ES chip.....	67
5.3. Test Results.....	69
5.3.1. Discussion of Test Results.....	71
5.3.2. Sources of Noise	71
5.3.3. Electrostatic Actuation of Proof mass	72
5.4. Conclusion	73
Chapter 6 - Design of 2nd Generation Earth Sensor	75
6.1. Improvements from 1 st generation.....	76
6.1.1. Proof Mass Alignment for test	76
6.1.2. Design for operation on tumbling satellite.....	77
6.1.3. Capacitive displacement measurement	81
6.2. Design Details of Generation 2	83
6.2.1. Spring design.....	83
6.2.1.1. Compensation for non-vertical spring sidewalls.....	85
6.2.2. Proof mass design	88
6.2.3. Electrostatic Actuation of Proof Mass.....	89
6.2.4. Displacement measurement design.....	90
6.3. Quality Factor Estimation in Air.....	94
6.4. Conclusion	97
Chapter 7 - Fabrication of 2nd Generation Earth Sensor	101
7.1. Test Chip.....	101

7.1.2	Lessons Learned.....	103
7.2.	Fabrication Steps.....	1204
7.2.1	Fabrication of chip with proof mass.....	1204
7.2.2	Fabrication of hard stops.....	1207
7.2.3	Earth Sensor Assembly	1208
7.3.	Issue with HF release.....	1210
7.3.1	Solution to uniformity issues	110
7.3.2	Solution to Aluminum Damage.....	120
7.4.	ES Chip Mounting.....	123
7.4.1	Solution for Low Stress Mounting.....	123
7.5.	Differential Wafer Bow	123
7.5.1	Design Modification for Differential Bow.....	123
7.5.	Conclusion	123
	Chapter 8 - Testing of 2nd Generation Earth Sensor.....	119
8.1.	Test Goals	120
8.2.	Orientation of ES chips for test.....	120
8.3.	Estimation of Fundamental Resonant Frequency.....	121
8.4.	Characterization of Gap of Capacitance Sense Electrodes.....	123
8.5.	Noise of Capacitance to Digital Convertor	127
8.4.1.	AD7745 noise at output.....	128
8.4.2.	AD7747 noise at output.....	129
8.6.	Electrostatic Actuation of ES chip proof mass	130
8.7.	Readout Sensitivity (Change in Capacitance vs displacement)	132
8.7.1.	Issue with Electrostatic Actuation.....	134
8.8.	Test for spring stiffness	135
8.9.	Comparison with expected change of capacitance due to GGT	1357
8.10.	Step response of Earth sensor	139
8.10.1.	Step response measured by capacitance measurements	139
8.10.2.	Step response measured by Laser Doppler Vibrometer.....	140
8.10.3.	Q-factor improvement in 1 mbar for piston mode	142
8.10.4.	Predicted improvement for Q in vacuum in piston mode	142

8.11.	Vibration Testing of Earth Sensor chip	143
8.11.1.	Vibration tests based on REXUS Qualification Tests	144
8.11.2.	Design Modification for Spring	145
8.11.	Conclusion	146
	Chapter 9 - Conclusion.....	149
9.1.	1 st Generation MEMS Earth sensor	149
9.2.	2 nd Generation MEMS Earth sensor	150
9.3.	Summary	152
9.4.	Future Work.....	153
	Appendix A - Gravity Gradient Earth Sensor Experiment on REXUS 11	155
	Bibliography.....	159

Chapter 1

Introduction

From the very first space missions, a critical part of any satellite mission is the ability to know its orientation in space, with respect to a reference frame. Typically, any space mission today, such as a communication satellite, satellites that perform Earth observation functions such as monitoring the weather, and satellites that perform scientific measurements, have a number of instruments on board, such as antennas, telescopes, cameras, radars, etc. that can fulfill the mission requirements only when pointed in a specific direction. For instance, a communication satellite in geostationary orbit should be able to point an antenna towards a specific part of the Earth's surface so that the TV channel being transmitted through that antenna is available to the desired audience on Earth. The Hubble Space Telescope needs to point its primary mirror with great precision to be able to image distant astronomical objects. Many satellites need to periodically receive commands from their ground control station on Earth for their proper operation. For this, they need to point their receiving antenna towards the Earth. To be able to do that, the satellite must first know its current orientation, then the onboard computers utilize various methods to change the orientation to the desired position. Measuring the orientation of the satellite with respect to a known reference is called attitude determination, and in the last decades, many sensors have been developed to perform this function (Table 1-1).

To completely determine the attitude for a satellite in orbit, three angles are needed to fix its orientation completely in space, with respect to a known reference frame. But with respect to a known vector, two angles are sufficient to know the direction in which its instruments / antennas are pointing / should be pointed. Figure 1-1 left shows the body centered reference frame for a satellite in a circular orbit around the Earth [1]. One axis of the reference frame is the local vertical direction to the surface of the Earth, called the nadir. A second axis is defined by the normal to the orbit. The right of Figure 1-1 shows the satellite, and its on-board antenna pointing in a new direction. For the satellite to know this new position with respect to the body centered reference frame, and be able to point its antenna in a known direction, the attitude determination instrument on board the satellite must be able to measure the two angles Ψ and ξ . In Figure 1-1 the dashed line is the vector along which the antenna points. Z' is the projection of this vector on the XZ plane. Ψ is the angle between Z' and the nadir. ξ is the angle between the XZ plane and the direction in which the antenna is pointing. In this case, Ψ and ξ are measured with the nadir as the reference vector. ξ is also referred to as the roll angle, and Ψ as the pitch angle.

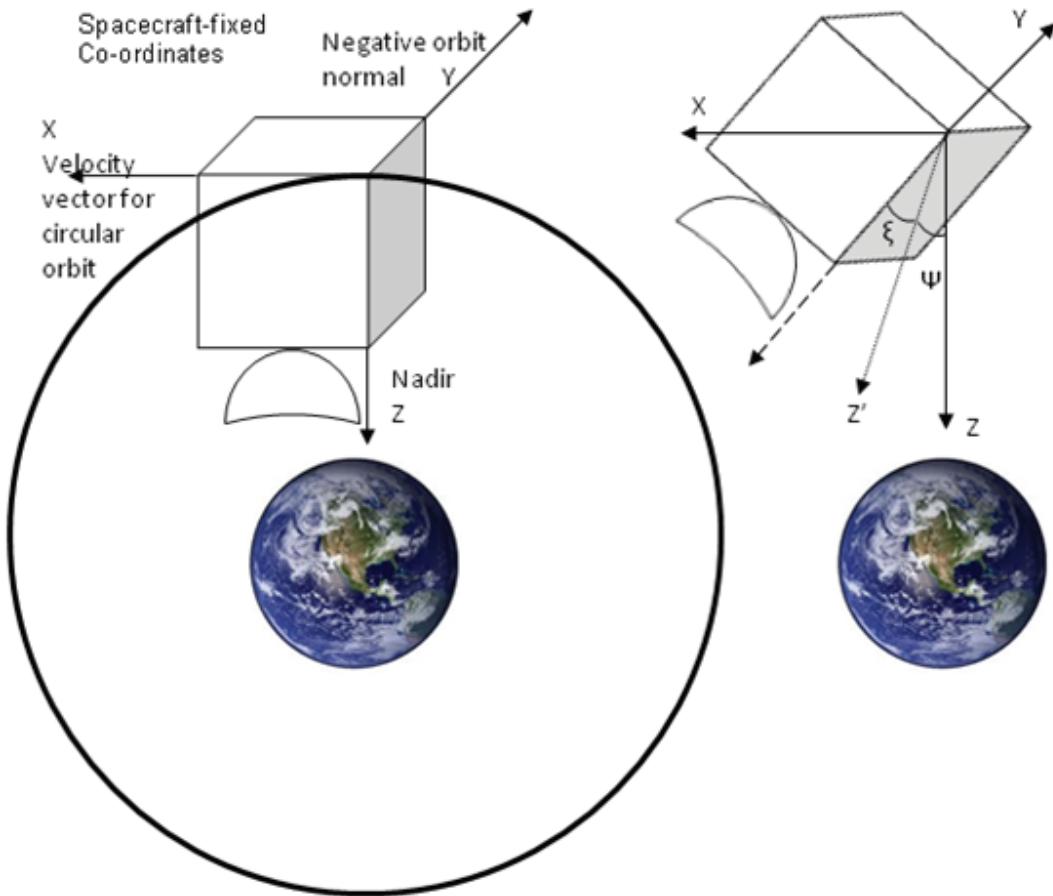


Figure 1-1 left: Satellite with antenna pointing to nadir with reference to spacecraft fixed co-ordinates right:
Angles Ψ and ξ define the direction of the antenna with respect to the reference frame

Table 1-1 lists the most commonly used sensors for attitude determination, with some typical values for accuracy. Star sensors are the most accurate attitude determination sensors available, but the field of view is typically limited, and the sensor can only acquire the attitude if any spin of the satellite is below a maximum rate [1]. Therefore satellites that employ star sensors typically first perform a coarse attitude acquisition initially using the other types of sensors listed in the table. Once the satellite attitude is known to within a few degrees, a fine attitude acquisition is performed using the star sensor. Even after the star sensor starts operation, the coarse sensor can continue to serve as a backup.

If the mission requirements do not require the accuracy of a star sensor, then the attitude determination is performed completely by the less accurate sensors. Sometimes the nature of the mission influences the choice of sensor. For instance, for an Earth observation mission, the use of an Earth sensor is a natural fit, since it provides the attitude information with respect to the normal to the Earth's surface. Even if fine attitude determination is not needed, all spacecraft typically will have more than one way to determine the attitude, for the purposes of backup and recovery. For instance, if the

Chapter 1: Introduction

primary attitude determination is done using sun sensors, then no signal is received during an eclipse, when the satellite is in the Earth's shadow. In such a condition, attitude determination may still be performed using an Earth sensor.

Sensor	Reference for attitude measurement	Accuracy [°]	Mass range [kg]	Limitations
Star Sensor	Positions of known bright stars	0.0003 – 0.01	2 – 5	Limited field of view, requires coarse acquisition sensor, multiple sensors for coverage
Sun Sensor	Position of sun	0.005 - 3	0.1 – 2	Limited field of view (wider than star sensor), multiple sensors for coverage, no signal during eclipse
Earth Sensor	The Earth's horizon (IR imaging of the transition between the horizon and space)	0.1 - 1	1 – 4	Limited field of view ((wider than star sensor), multiple sensors for coverage, other bodies such as sun/moon can cause saturation
Magnetometer	Earth magnetic field	0.5 - 3	0.3 – 1.2	Variations in Earth's magnetic field requires spacecraft position to be known at all times, needs to be located carefully on satellite to avoid interference from onboard systems

Table 1-1 Common sensors used for attitude determination on satellites [1]

Building redundancy into a satellite design is an important goal for any mission, so that in the event of serious errors on board the satellite, some attitude determination sensor or another can continue to provide data to the onboard computers/satellite operator, for mission recovery. For instance, in case of some failure in the launch vehicle, anomalous separation from the booster may result, and the satellite may be tumbling about one or more axis in a wrong orbit. The satellite might still be able to continue the mission using its onboard propellant, though with reduced mission lifetime. To be able to do this, it must first orient itself such that it can receive commands from ground operations / provide data to the ground station so that operators can take corrective action. In such a scenario, none of the sensors listed in Table 1-1 may be able to acquire the attitude. The sun, earth and star sensors, with limited field of view may not be able to acquire the attitude due to satellite tumble, and the magnetometer data will not be useful if the satellite position is not known. New attitude determination methods, that add capability by using alternative physical sources for reference are desirable, to enable satellite operation and recovery in a wider range of conditions. A more recent development is the use of Global Satellite Navigation Systems (GNSS) for attitude determination. Multiple antennas on board the satellite receive signals from GNSS satellites and the information is used to compute the orientation of the satellite. Nevertheless this system also relies on the continuous availability of the GNSS signal. The only existing GNSS networks (GPS, GLONASS) today are maintained by defense organizations. GNSS services could be denied to non-military users in the event of conflict. An attitude determination sensor in a backup role must be available at all times.

Another goal of satellite design is to be able to perform the functions required for a mission while keeping the mass of the satellite to a minimum. For star, sun and earth sensors, the limited field of view means that multiple units need to be present on the satellite, to provide complete 4π steradian coverage. Similarly, for GNSS based attitude determination, the antennas need to be present on multiple faces, since the satellite body can block signals to an individual antenna sometimes.

This thesis presents work done towards developing an attitude determination sensor, which utilizes the gravity gradient of the Earth, for low earth orbit satellites which are three-axis stabilized. Since it relies on a different physical phenomenon from the sensors previously discussed, it has the potential to offer additional capability for functions such as coarse attitude determination, initial attitude acquisition after separation from launch vehicle, and as a backup sensor. Since the reference for this sensor is the normal to the Earth's surface, it can be classified as an Earth sensor. Another goal for this sensor is to enable power and mass savings as compared to existing Earth sensors.

1.1.The Earth's Gravity Gradient

The equation for the force \vec{F} acting on a 1 kg mass due to the Earth's gravity, at a point on or above the surface of the Earth is given by

$$\vec{F} = \frac{GM}{R^2} \vec{r} \quad [m/s^2] \quad 1-1$$

where G is the universal constant of gravitation, M the mass of the Earth, and R the distance from the center of the Earth to the point at which F is calculated. \vec{r} is the unit vector along the radial direction from the Earth's surface. If we follow this vector, and travel along it away from the Earth's surface, due to the inverse square relationship with R, gravity reduces as the height from the surface of the earth increases. Therefore, any object in orbit has a slightly different force of gravity over its volume, depending upon the distances of the individual points from the Earth's surface. This is known as the gravity gradient, and the direction of the gradient is always towards the Earth's surface (Figure 1-2). Therefore, to determine the angles Ψ and ξ using the gravity gradient, the nadir is a natural reference vector.

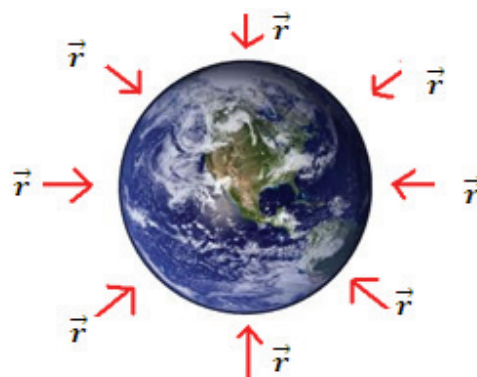


Figure 1-2 Direction of the Earth's gravity gradient

Chapter 1: Introduction

An elongated object in a gravity field, such as that of the Earth, will tend to align its longitudinal axis in the direction of the field, due to the gravity gradient along its length. This phenomenon has been used to passively stabilize the attitude of large satellites such as GEOSAT [15], used for radar altimetry, and experimental purposes such as deploying a tether in space. (NASA TSS-1R mission) [16]. Satellites have been designed with an elongated shape, or deploy a boom such that when the longitudinal axis is not aligned to the gravity gradient, there is a torque on the satellite that tends to align it in the direction of the gravity gradient (Figure 1-3). This is known as the Gravity Gradient Torque (GGT). The magnitude of the torque depends on the misalignment of the longitudinal axis of the satellite with the gravity gradient. As the satellite is gradually aligned with the gravity gradient due to the effects of this torque its magnitude drops to zero once the satellite is aligned.

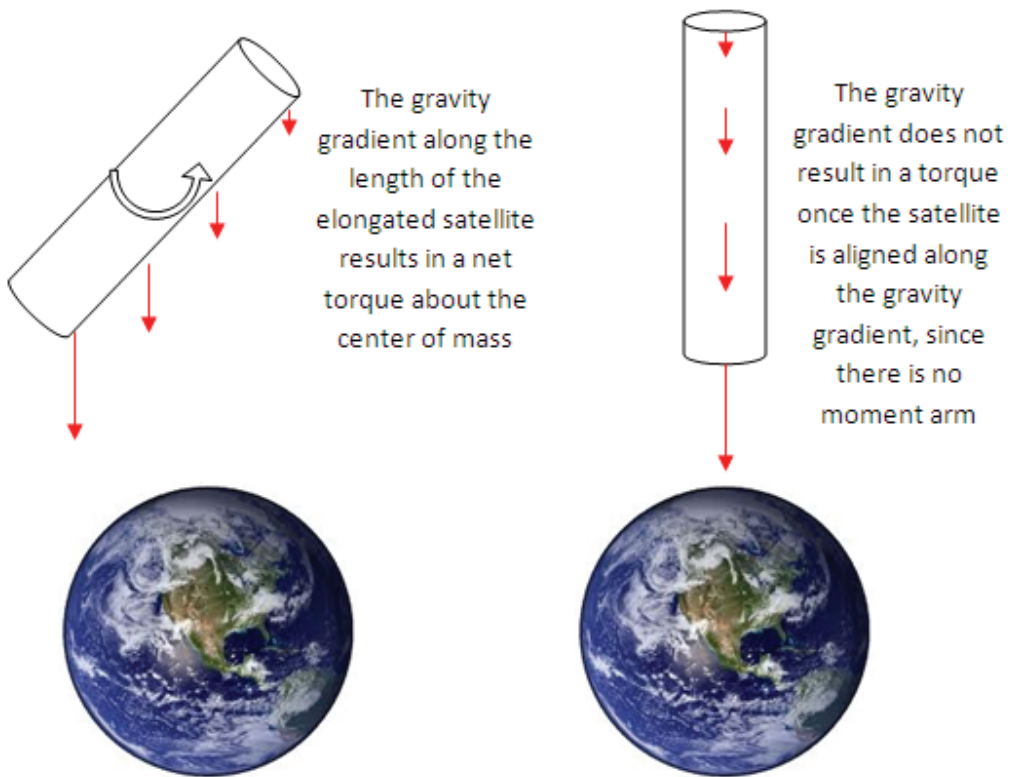


Figure 1-3 Left: An elongated satellite in the gravity field of the Earth has a torque about its center of mass due to the gravity gradient; Right: Once the satellite is aligned along the gravity gradient, this torque is zero.

The Gravity Gradient Torque (GGT) has never been used to sense the direction of the gravity gradient. The GGT depends on the volume, mass and alignment of a body with respect to the gravity gradient. This indicates that an inertial sensor, with a proof mass having the appropriate shape, can be designed to measure the GGT. The GGT will depend on the alignment of this proof mass with respect to the gravity gradient. Chapter 2 describes the concept of such an inertial sensor, and its use for attitude determination as an Earth sensor.

1.2.Earth sensor

Earth sensors based on imaging the infrared radiation from the Earth have been in use since 1957 [2], at the very dawn of the space age. Lunde (1963) describes attempts to improve the reliability of IR Earth sensors. Since then, numerous improvements have resulted in longer lifetimes, greater reliability, and improved accuracy, but the principle of sensing has fundamentally remained the same, with recently developed Earth sensors [3], [4] using more sophisticated IR imaging techniques to record the Earth horizon – space transition.

To understand the possible advantages of a gravity gradient based Earth sensor, the features of commonly used Earth sensors, manufactured by European companies, are listed in Table 1-2. The sensors are intended for operation in various orbit types, classified by the height of the orbit from the Earth's surface. Low Earth Orbit (LEO) is commonly defined as orbits between 160-2000 km. The Geostationary Orbit (GEO) is defined as the orbit at which the period of the orbit matches the period of rotation of the Earth. For Earth, this orbit height is 35,786 km. Medium Earth Orbit (MEO) is defined as all orbits above 2000 km and below GEO.

Sensor Name	IRES [3]	NES [4] (under development)	STD15 [5]	STD16 [6]
Manufacturer	Selex Galileo	Selex Galileo	Sodern	Sodern
Operational Domain	Medium Earth Orbit (MEO), Geostationary Orbit (GEO)	Low Earth Orbit (LEO), Medium Earth Orbit (MEO), Geostationary Orbit (GEO)	Geostationary Orbit (GEO)	Low Earth Orbit (LEO)
Field of view (FOV): Acquisition	+/-13° roll (GEO), +/22° pitch (GEO)	+/-90° roll (LEO), +/90° pitch (LEO)	+/-14.5° roll (GEO), +/15.6° pitch (GEO)	+/-33° roll (LEO), +/17° pitch (LEO)
Field of view (FOV): Pointing	+/-2.5° roll (GEO), +/5.5° pitch (GEO)	+/-90° roll (LEO), +/90° pitch (LEO)	+/-2.9° roll (LEO), +/12° pitch (LEO)	+/-33° roll (LEO), +/17° pitch (LEO)
Accuracy[°]	0.03° (GEO)	1° (LEO)	0.035° (GEO)	0.06° (LEO)
Mass[kg]	2.5	0.45	3.4	3.5
Dimensions and Volume	170 x 164 x 156 mm ³ 4.35 dm ³	target 140 x 125 x 95 mm ³ target 1.66 dm ³	206 x 206 x 168 mm ³ 7.13 dm ³	386 x 208 x 175 mm ³ 14.05 dm ³
Update rate	10 Hz	not available	1.25 hz	1 Hz

Table 1-2 List of Earth sensors in use and development today

Based on the characteristics listed in Table 1-2, the possible advantages and disadvantages of an Earth sensor based on measuring the gravity gradient torque are discussed below:

Advantages		
	IR Imaging based Earth Sensor	Gravity Gradient Earth Sensor
Greater Field of View (FOV) for Acquisition and Pointing	From Table 1-2, the under development NES has the best FOV, which is still limited to +/- 90°. So a single unit cannot always acquire the attitude if it cannot see the Earth's horizon.	FOV is +/- 180° roll, +/- 180° The gravity gradient can be sensed irrespective of satellite orientation using a single unit.
Fewer constraints on satellite design	Imposes constraints on satellite design: Since the FOV of the sensor must remain free, restrictions with respect to the positioning of antennas and solar panels.	The instrument can be situated flexibly within the satellite, since the gravity gradient is present over the entire volume of the satellite.
Disadvantages		
Operational Domain	LEO, MEO, GEO	Only LEO, since the gravity gradient decreases as the distance from the Earth's surface increases, at higher orbits, the GGT becomes smaller and difficult to measure.

Table 1-3 Comparison of existing Earth sensors to Earth sensing using the gravity gradient

Due to the +/-180 FOV, the gravity gradient sensor can be always available, and can serve a backup sensor. After separation from the booster, when the attitude of a satellite is not known, it can immediately start sensing the GGT, and perform initial attitude acquisition.

The NES sensor under development by Selex Galileo has a target mass of 0.45 kg and target volume of 1.66 dm³. Due to its +/-90 FOV, a minimum of two units would be needed for complete coverage, resulting in a total mass of 0.9 kg and volume of 3.3 dm³. For a new Earth sensor instrument, that aims for improvements in mass and volume, these numbers serve a guide for mass and volume targets. **For the Gravity Gradient Earth Sensor, we aim at an upper limit for the mass of 1 kg, and 1 dm³ for the volume. To meet these targets for a compact, low mass system, the inertial sensor to measure the GGT is made using Micro-Electro-Mechanical System (MEMS) technologies.**

1.3.MEMS Inertial Sensors

MEMS technology seeks to use and extend the microfabrication techniques, which were originally established during the development of silicon integrated circuits, to design and build solutions for various sensor and actuator applications. The reduction in size, power and cost enabled by micro-scale fabrication has made it possible to develop numerous applications for MEMS sensors. Inertial sensors are among the better established applications for MEMS. Micromachined accelerometers were first demonstrated by researchers at Stanford in 1979 and since then have been developed for a wide variety of applications [7]. Accelerometers and gyros costing a few dollars each are produced in the millions by various manufacturers such as Analog Devices and ST Microelectronics for use in consumer electronics and the automotive industry [44, 45]. For more specific applications such as vibration monitoring, companies such as Colibrys [49] and MMF [50] produce high performance accelerometers that can provide micro-g resolution.

Chapter 1: Introduction

To sense gravity on Earth MEMS inertial sensors such as accelerometers are commonly used, in applications such as protecting the hard disk of a laptop, by lifting the read/write head away from the hard disk surface in case the laptop is dropped. In orbit, since the satellite is in freefall around the Earth, the acceleration due to gravity will not be sensed by any accelerometer on-board the satellite.

The difference in the magnitude of gravity between two points depends on their vertical separation, and their mean distance from the Earth's surface (Figure 1-4). Table 1-4 shows this difference in magnitude for two point masses in an LEO orbit of 700 km.

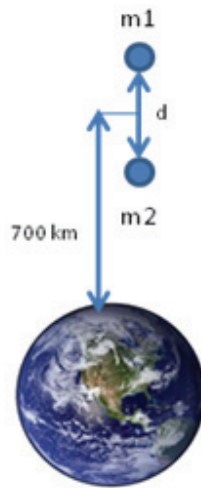


Figure 1-4 Two point masses vertically separated by distance d at an orbit of 700 km

Vertical distance d between masses [m]	Difference in magnitude of gravity for two 1 kg point masses m_1, m_2 [m/s^2]	Difference in magnitude of gravity for two 0.1 g point masses m_1, m_2 [m/s^2]
50	1×10^{-4}	1×10^{-8}
5	1×10^{-5}	1×10^{-9}
0.5	1×10^{-6}	1×10^{-10}
0.05	1×10^{-7}	1×10^{-11}

Table 1-4 Difference in magnitude of gravity for point masses of 1 kg, and 0.1 g for different vertical separations at an orbit of 700 km (Figure 1-4)

As discussed in previously, the target volume for an instrument that determines the attitude of a satellite using the gravity gradient is 1 dm^3 , in order to offer mass and volume savings. Accelerometers to sense the gravity gradient inside such an instrument will need to have a separation on the order of cm. Even with relatively large silicon proof masses for these accelerometers, the individual masses will be less than a gram.

Table 1-4 shows that for two 0.1g masses separated vertically by 5 cm the difference in the magnitude of gravity is $1 \times 10^{-11} \text{ m/s}^2$. No commercially available accelerometers are able to measure this low difference in acceleration. The best reported resolution in literature for micromachined accelerometers, on the order of $1 \times 10^{-10} \text{ m/s}^2/\text{Hz}^{1/2}$, has been for devices utilizing electron tunneling [8], or optical

Chapter 1: Introduction

gratings [9], [10] to detect the displacement of the proof mass due to the external acceleration. For an inertial sensor that has to be sent into orbit, there will be considerable vibration and shock during launch. The electron tunneling tip, or the grating fingers of such displacement sensing mechanisms will not survive such an environment.

Highly customized accelerometers, that have sensitivities of more than $1 \times 10^{-11} \text{ m/s}^2$, have been designed for gradiometry, for missions such as GOCE [11]. These accelerometers work in pairs to measure the difference in accelerations due to the separation between them. The mass of these instruments are in the range of tens of kilograms, and the power consumption is tens of watts, which is two orders above the magnitude desired for the mass and volume for an ES instrument that senses the gravity gradient. Atom interferometers offer the best sensitivity for measuring accelerations, and there are proposals to use atom interferometers as gradiometers [13]. The mass estimates for these instruments range in the hundreds of kilograms [14]. There is some work towards the design of a MEMS gradiometer by Flokstra et al. [13], but no fabricated device has been reported. To achieve the required sensitivity, the authors postulate an operational temperature of 77K. Keeping a sensor at this temperature for all the years of operation for a satellite will require some form of cryogenic cooling, and increase the mass and power requirements by one to two orders of magnitude.

The GGT results from the difference in gravity on different parts of a object in orbit. If the object is considered to be made up of a number of point masses, measuring the GGT is equivalent to directly measuring the difference in gravity between these point masses. Therefore, sensing the GGT directly is a better alternative to attempting to sense a difference of $1 \times 10^{-11} \text{ m/s}^2$ in the acceleration sensed by two MEMS accelerometers. Fabrication of two sensitive accelerometers matched well enough to obtain the accuracy necessary, is highly risky, compared to fabricating a single inertial sensor to measure the GGT. The devices reported in [8-10] employ sophisticated readout mechanisms which are not robust enough to withstand vibration during launch. The readout required for a differential accelerometer system will need to be even more sensitive, and is likely to be even more complex. Measuring the displacement of a single inertial sensor due to GGT can be done using simpler and robust sensing schemes (Chapters 3 and 6).

Another consideration for an attitude determination sensor is being able to function on a satellite that is tumbling, i.e. spinning around one or more axes. Such a situation can occur immediately after launch, when the satellite separates from the booster, and an attitude determination instrument must be able to provide data to the satellite at this stage, so that the satellite can orient itself to start operations. On a tumbling satellite, a pair of accelerometers designed to sense $1 \times 10^{-11} \text{ m/s}^2$ of acceleration will encounter centripetal forces of the magnitude of $1 \times 10^{-3} \text{ m/s}^2$ depending on the position of the accelerometer and the rate of spin. Detecting such a small signal in such a large offset is not feasible, and such a large force relative to the sensitivity of the accelerometer can saturate the device. So accelerometers are not suitable for the purpose of backup or initial attitude determination. The accelerometers on GOCE, can only work when the satellite attitude is highly stable and well known.

Therefore, instead of directly trying to measure the difference in gravity, a better approach is to measure the torque due to the gravity gradient on a body in orbit. Instead of a two accelerometer

approach, a novel inertial sensor can be designed, that can be used to measure the angles Ψ and ξ by means of measuring the gravity gradient torque.

1.4.Thesis Objectives

An inertial sensor to measure the Gravity Gradient Torque in low Earth orbit has not been proposed before. The advantages of an Earth sensor using such an inertial sensor have been summarized in Section 1.2. A MEMS based approach is followed to meet the mass (1 kg) and volume (1 dm³) goals for this sensor. This thesis describes the development of a MEMS inertial sensor to measure the GGT, its design, fabrication and test.

The initial funding for this project was provided by ESA under a fifteen month contract 21053/07/NL/CB as part of an ESA initiative for new low cost coarse Earth sensor concepts. Guidance from ESA at the start of the contract indicated that for a coarse Earth sensor an accuracy of +/- 2° in measuring the pitch and roll angle is acceptable, and an update rate of 1 Hz is sufficient. These are taken as the design goals for the inertial sensor. In Chapter 2, it will be shown that the GGT on the proof mass of an inertial sensor designed to fit within the target 1 dm³ volume is on the order of 10⁻¹⁵ N.m to 10⁻¹⁴ N.m.

A sensor that is sensitive enough so that the GGT can be measured also needs to be robust so that no special handling is required on Earth, and designed so that it can be tested on Earth. Ultimately, it must survive the vibrations of a launcher, to someday be usable in space. The design and fabrication process developed for the inertial sensor, has to balance the opposing demands of more sensitivity and greater robustness. The readout design is kept simple and robust as possible, again with the viewpoint that it should be someday usable in space.

A dedicated test setup was developed to reproduce the effect of GGT in microgravity, in 1g. Testing is geared towards determining how well the fabricated MEMS Earth sensor (ES) chips meet the design goals listed above.

The final phase of this project was funded by the Swiss Space Office in a collaborative project with RUAG Space, to design a complete attitude determination instrument around the MEMS sensor. The activity by RUAG involved the selection of space qualified components for the electronics, interfaces with a satellite bus, and mass and power budgets based on the experience RUAG has with satellite hardware, and defining a possible roadmap for development of the Gravity Gradient Earth Sensor.

Two generations of the MEMS ES to measure the GGT are realized. The design of the 1st generation of the sensor is done keeping in mind the fifteen month timeframe of the ESA contract that required a proof of concept MEMS ES to be developed. The 2nd generation incorporates additional design features, such as ensuring that the ES can function on a satellite that is tumbling.

Two generations of Earth sensor chips can be seen in Figure 1-5 and Figure 1-6. The chips were robust enough for routine handing in the lab, and survive low magnitude vibrations. The readout mechanisms

Chapter 1: Introduction

for both generations function, and a novel fabrication process is developed that can be applied to other MEMS inertial sensors having cm-scale proof masses.

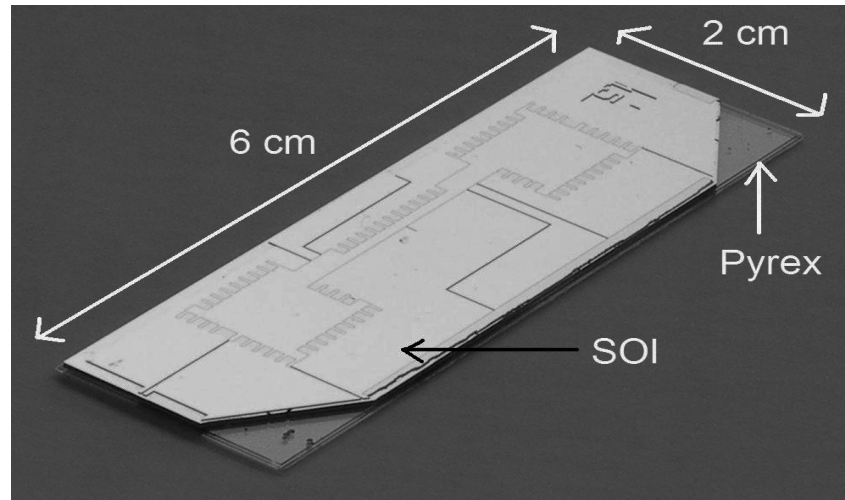


Figure 1-5 1st Generation MEMS Earth sensor chip; it utilizes an optical interferometer based displacement sensing; the outline of the 1 cm wide, 4 cm long and 600 micron thick proof mass is visible

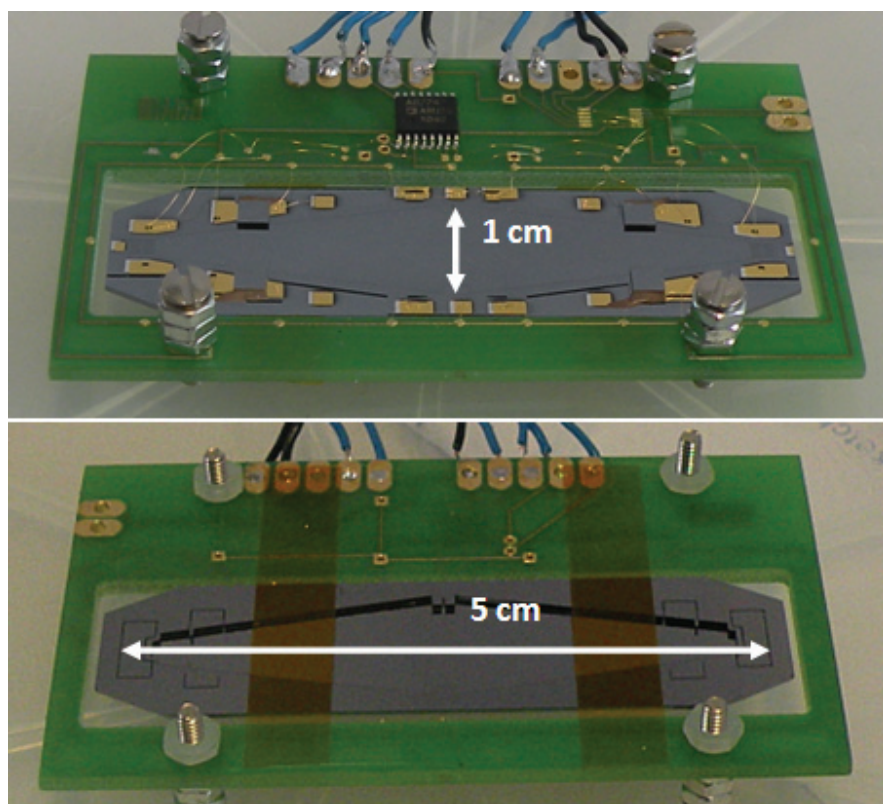


Figure 1-6 2nd Generation MEMS Earth sensor chip; it utilizes capacitive displacement sensing; Top: Front view of chip showing the 1 cm wide, 5 cm long, 130 micron thick proof mass; Bottom: Back view of chip mounted on PCB with the capacitance sense electronics

Chapter 1: Introduction

Mass	Volume	Power	Accuracy
1 kg	1 dm ³	< 5W	+/- 2°

Table 1-5 Summary of target specifications of Earth Sensor using the gravity gradient

1.5.Thesis Structure

- Chapter 1 has given an overview of Earth Sensors, and the possible advantages of an Earth Sensor that senses the gravity gradient.
- Chapter 2 discusses the design considerations and constraints of implementing such a sensor using MEMS. In low Earth orbit, the performance of the sensor can depend on the temperature, orbit height, etc. A discussion of these factors is provided along with estimates of the accuracy of the sensor.
- Chapter 3 discusses the detailed design of the sensor and readout for the 1st generation Earth sensor.
- Chapter 4 describes the fabrication process for the 1st generation sensor.
- Chapter 5 describes the test setup and tests performed on the 1st Generation sensor.

At the conclusion of the contract with ESA a better understanding was gained for some of the operational requirements of such a sensor, such as being able to function on a satellite that is tumbling. Though the 1st generation has a optical readout, an electronic readout is clearly more desirable from the point of view of having a compact instrument for space.

- Chapter 6 describes the design for a 2nd generation Earth sensor that has capacitive displacement readout.
- Chapter 7 describes the fabrication process of the 2nd generation sensor, and some work done towards a possible hermetic package.
- Chapter 8 describes the test setup and tests done on the 2nd generation sensor.
- Chapter 9 presents the conclusions from the thesis, and gives recommendations for future work.

A test in microgravity is planned for the 2nd generation sensor on a sounding rocket flight in February 2012, as a test for survivability of the chip during an actual rocket launch, and to obtain data about the possible performance in microgravity. A description of the electronic and mechanical system that is built around the chip for this test is described in the Appendix.

Chapter 2

Attitude Determination using the Gravity Gradient Torque

In the introduction to the thesis, current Earth sensors and their limitations were discussed. To obtain new capabilities for a coarse Earth sensor that uses the Earth's gravity gradient as a reference, while targeting low mass and volume requirements, an inertial sensor to measure the GGT is suitable. This chapter discusses the details for such an inertial sensor design.

2.1.Gravity Gradient Torque

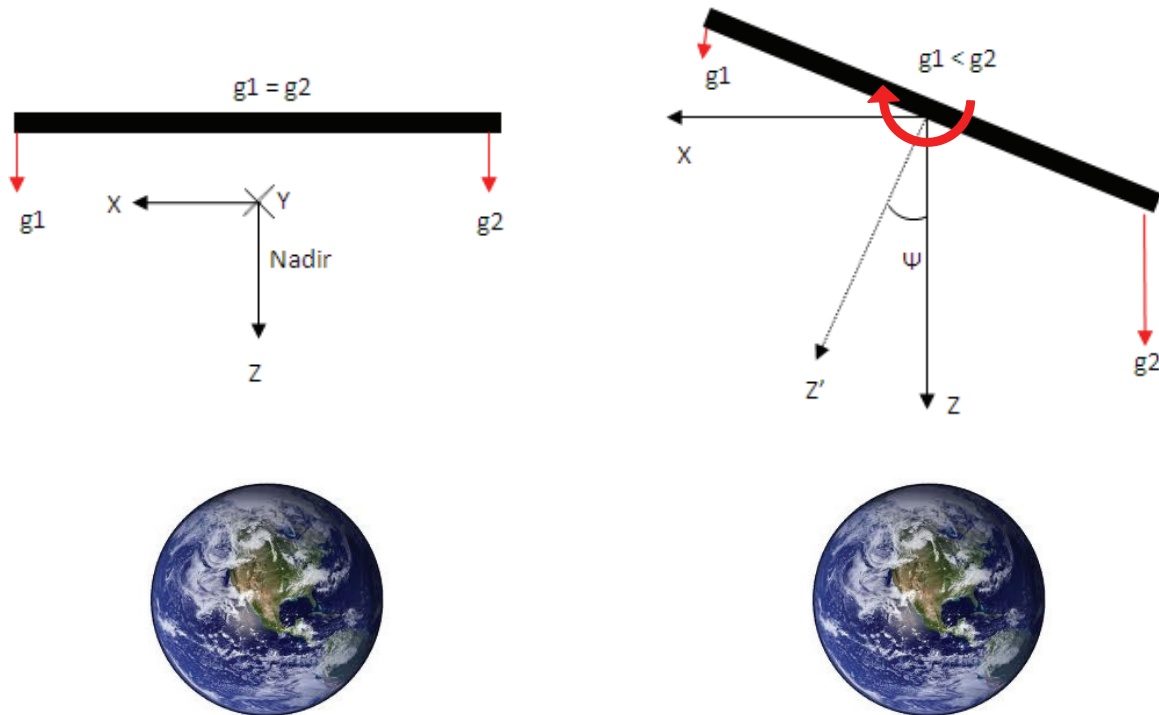


Figure 2-1 GGT on a body in orbit; the magnitude of GGT depends on the angle between the Z axis of the object and the nadir

The equation for GGT on a body in orbit around the Earth is given by [1]

$$GGT = \frac{3\mu \cdot |I_y - I_x| \cdot \sin(2\psi)}{2R^3} \quad 2-1$$

μ is the gravity constant of the Earth, I_y and I_x the moments of inertia around axes of the body as shown in Figure 2-1, ψ is the angle between the Z axis of the body and the nadir, and R is the radius of the orbit. In Equation 2-1, μ is a constant and R is fixed for the operational circular orbit of a satellite. By measuring the GGT on the body the angle ψ can be calculated. The GGT depends on the moments of

Chapter 2: Attitude Determination using the Gravity Gradient

inertia I_y and I_x . For a fixed mass of the body, maximizing the moment of inertia is desirable, to have a larger measurable GGT. While keeping the mass constant, if the shape of a body is made more elongated, its $|I_y - I_x|$ will increase.

Figure 2-1 shows how GGT depends on the angle ψ for an elongated body. The left of Figure 2-1 shows the body with its Z axis aligned with the nadir. The gravity all along the length of the body is the same, so there is no gravity gradient since the angle ψ is zero. As seen on the right of Figure 2-1 when ψ increases, the gravity gradient along the length of the body increases, due to the differing distances of points along the length from the surface of the Earth. So the GGT around the center of mass of the body changes with increasing ψ (Figure 2-2).

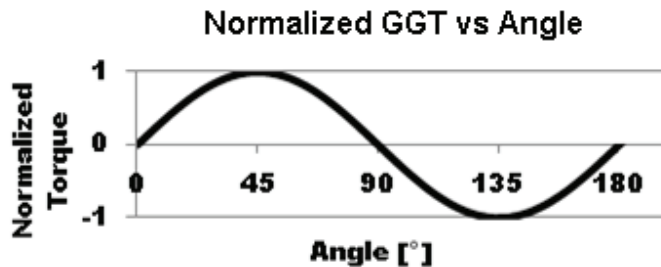


Figure 2-2 Periodicity of GGT with respect to angle Ψ . GGT is periodic in 180° (Equation 2-1)

Consider a body such as the one shown in Figure 2-1 as a proof mass on a satellite, anchored to the satellite body by means of a compliant spring (Figure 2-3 left). When the satellite is pointing towards the nadir, there is no GGT on the proof mass. If the satellite rotates through an angle Ψ , GGT will cause the body to try and align its longitudinal axis along the nadir. This will cause the spring to bend and provide a restoring torque with increasing rotation of the proof mass. The proof mass reaches a point of equilibrium where the GGT and the restoring torque of the spring are equal. This is given by

$$GGT = -k\theta \quad 2-2$$

where k is the designed spring constant, and θ the angle though which the proof mass is rotated due to GGT *relative* to the satellite body. This rotation results in a displacement d at the extremities of the proof mass, which is related to θ by the geometry of the proof mass. By measuring d , GGT can be determined, and therefore the angle Ψ that the satellite has rotated through, can be calculated.

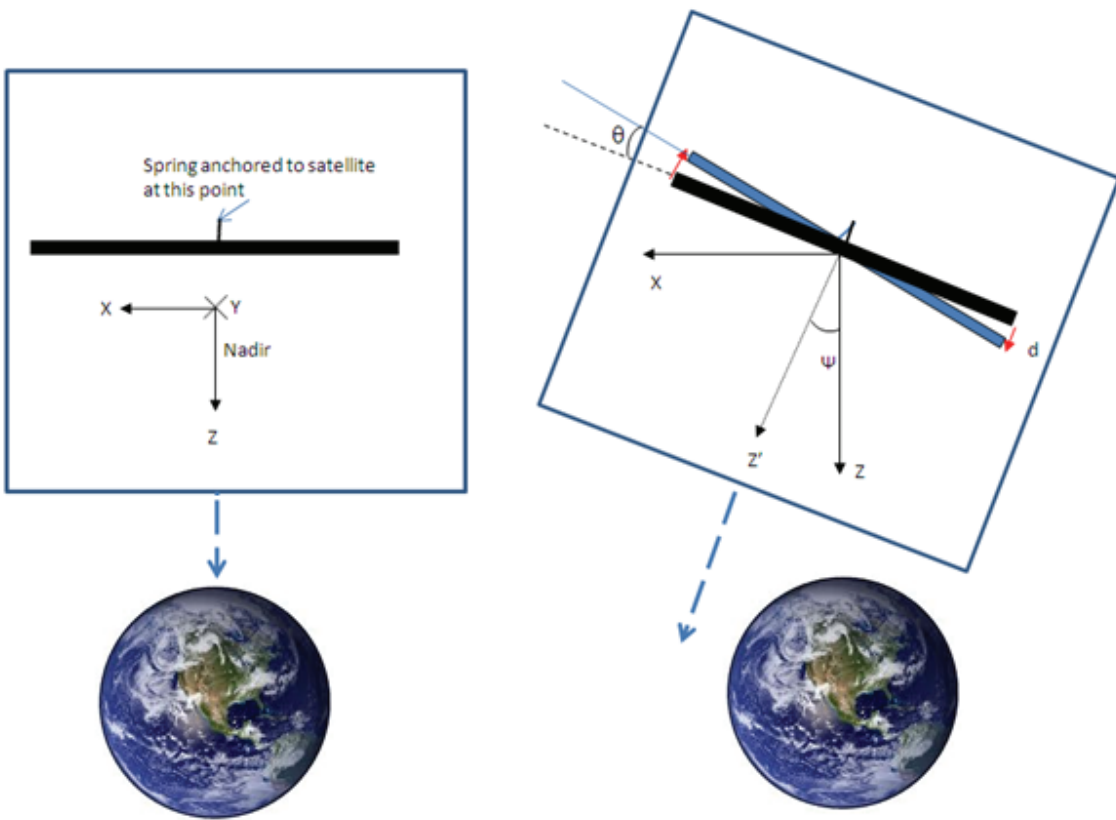


Figure 2-3 Rotation of proof mass and bending of spring due to GGT

The spring and proof mass thus comprise an inertial sensor that can be used to determine the satellite attitude by measuring the GGT.

2.2.Earth Sensor Instrument utilizing GGT

The inertial sensor described in the previous section can be used to measure just the angle Ψ in the orientation shown in Figure 2-3. For complete attitude determination more of such sensors are needed. As seen in Equation 2-1, the GGT depends on $\sin 2\Psi$. Due to the $\sin 2\Psi$ factor the GGT is periodic in 180 degrees (Figure 2-2). Due to the sinusoidal nature of GGT, the value of GGT for an angle of 30 degrees is the same as the value for 60 degrees (Figure 2-4 left). To unambiguously determine the angle Ψ , in the range of 0-180°, two sensors are required, with the second sensor mounted such that its response to GGT has a phase difference of 45 degrees relative to the first. Figure 2-4 (right) shows the response of the two sensors. The black line shows the response of the sensor oriented as shown in Figure 2-3, the red line shows the response of a sensor with a phase difference of 45 degrees (Figure 2-5).

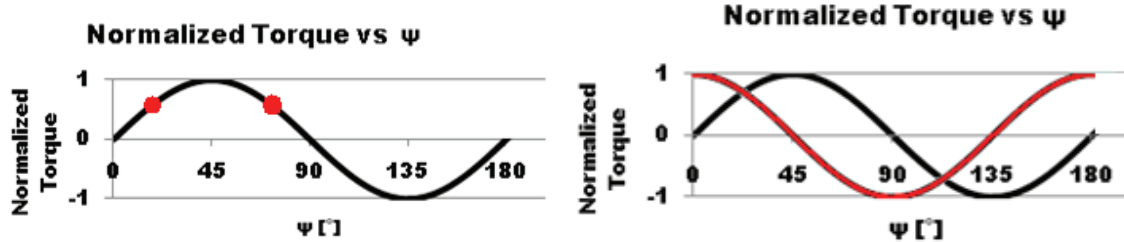


Figure 2-4 Left: GGT measured by a single inertial sensor; Right: Use of a second sensor, offset by a phase of 45° to determine the GGT unambiguously within $0-180^\circ$

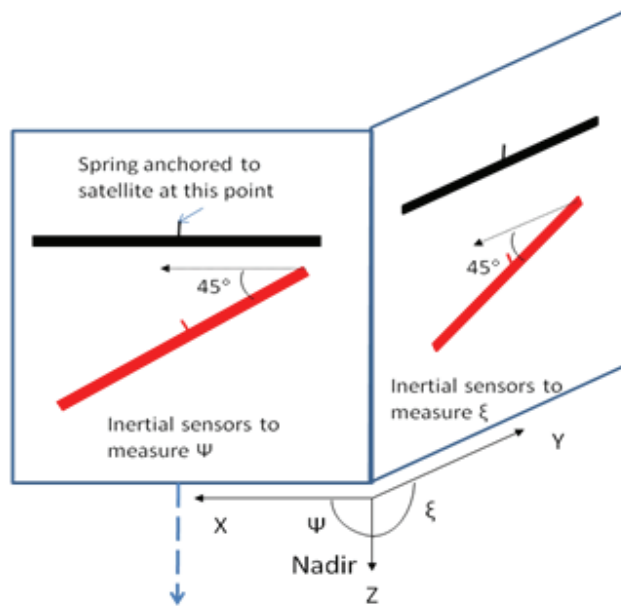


Figure 2-5 Four inertial sensors used to measure the pitch (ψ) and roll (ξ) angles of a satellite with respect to the nadir

Figure 2-5 shows two sets of inertial sensors mounted in planes orthogonal to each other. One set, in the XZ plane, is used to measure the ψ angle. The other set of inertial sensors is in the YZ plane, and the proof mass of these sensors is displaced due to GGT when the ξ angle of the satellite changes. Using these four sensors the direction in which the satellite is pointing can be determined. There is no change in the GGT for any of the sensors for a rotation of the satellite around the Z axis, so the yaw angle cannot be determined using GGT.

2.2.1. 180 degree Periodicity of GGT Inertial Sensor

As seen in Figure 2-6, the inertial sensor to measure the GGT has a periodicity of 180 degrees. An Earth sensor instrument needs to report the angle in a range of 0-360°. But the responses of the two sensors in the XZ plane that measure the ψ angle are identical when i.e. ψ is 30° or 210° (Figure 2-6). If the ES instrument already knows the attitude of the satellite, it can use that as a starting point to keep track of

Chapter 2: Attitude Determination using the Gravity Gradient

whether the current Ψ is in the $0\text{-}180^\circ$ range, or the $180\text{-}360^\circ$ range, by keeping track of the zero crossings of the inertial sensors.

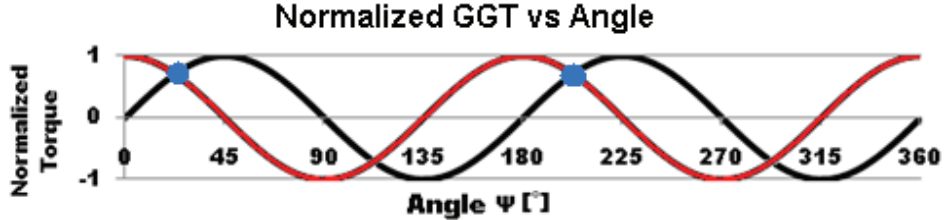


Figure 2-6 Periodicity of GGT in $0\text{-}360^\circ$. The GGT measured by two sensors offset by 45° is the same at two points in the $0\text{-}360^\circ$ range

In case of a scenario such as initial attitude acquisition after launch, some method is needed to determine a unique satellite attitude, and decide if the measurement made by the GGT inertial sensors falls in the $0\text{-}180^\circ$ range, or the $180\text{-}360^\circ$ range. A coarse measurement of the gravity gradient can be done using two accelerometers mounted in the same plane, to decide if the satellite is pointing at an angle of 0 or 180 degrees (Figure 2-7).

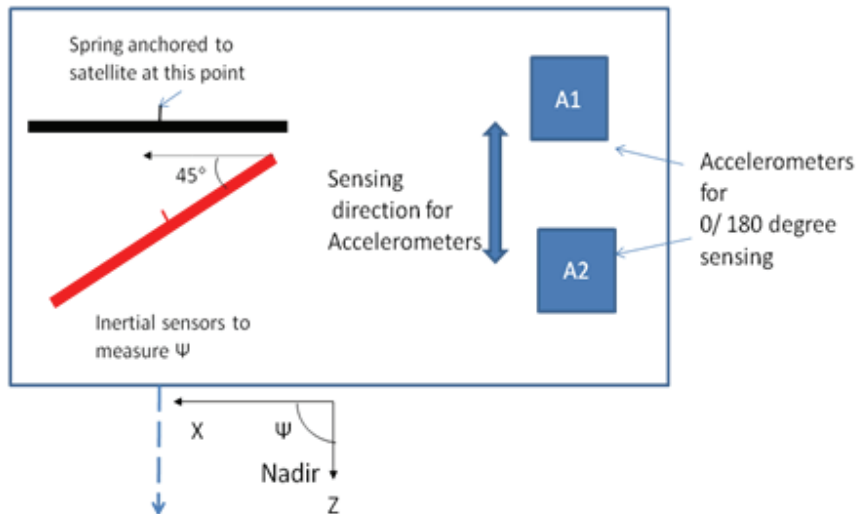
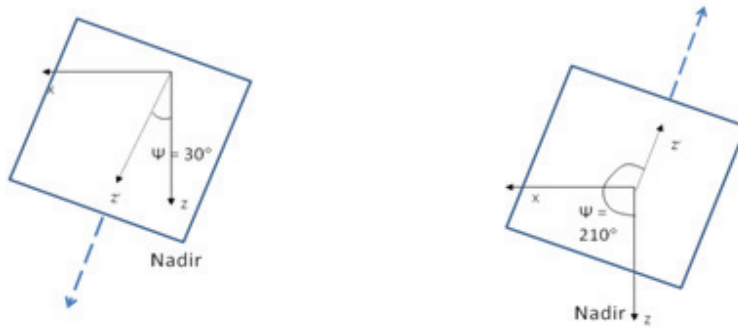


Figure 2-7 Coarse $0\text{/}180^\circ$ sensing using accelerometers

Two examples are presented of attitude acquisition performed by an ES instrument that uses inertial sensors to measure the GGT, for a 3 axis stabilized satellite whose initial attitude is unknown. The attitude could be in the $0\text{-}180^\circ$ range, or the $180\text{-}360^\circ$ range. For both cases, a solution is presented in which accelerometers are used for coarse attitude sensing. The ES instrument first determines the attitude using the inertial sensors for GGT only. If this attitude is wrong by 180° , a correction is made using the coarse attitude sensing performed by the accelerometers.



2-8 Left: Example of satellite orientation at 30°; Right: Example of satellite orientation at 210°

Example for satellite that is at 30 degrees from desired orientation of pointing towards the nadir

- The GGT inertial sensor provides information to the satellite about its current attitude, that the current angle is 30° to the nadir in the XZ plane.
- The satellite fires its thrusters to align its Z axis to the nadir. During this operation the accelerometers report a centripetal force much higher than the expected difference due to the gravity gradient, and their output can be ignored.
- After the satellite is aligned to the nadir and has stopped spinning, the accelerometers measure the difference in gravity at their respective locations, and the ES instruments records that the current attitude is 0° to the nadir.
- This attitude is then used as a reference, and by keeping track of zero crossings the sensor can determine if future GGT measurements fall in the 0-180° range, or the 180-360° range.

Example for satellite that is at 210 degrees from desired orientation of pointing towards the nadir

- The GGT inertial sensor initially provides incorrect information to the satellite about its attitude, and specifies that the current angle is 30° to the nadir in the XZ plane.
- The satellite fires its thrusters to align its Z axis to the nadir. During this operation the accelerometers report a centripetal force much higher than the expected difference due to the gravity gradient, and their output can be ignored.
- At the end of this operation the satellite is aligned at 180° from the nadir, but the ES instrument initially records the attitude as 0°.
- The accelerometers measure the difference in gravity at their respective locations, and the ES instrument updates the attitude to 180° degrees and provides the information to the satellite. This attitude is then used as a reference, and by keeping track of zero crossings the sensor can determine if future GGT measurement fall in the 0-180° range, or the 180-360° range.
- The satellite again fires its thrusters to orient itself to the nadir.

A hybrid approach for the 0/180° sensing can also be used, where other sensing instruments such as a commercially available magnetometer can determine if the ES instrument is pointing at 0 or 180°.

Chapter 2: Attitude Determination using the Gravity Gradient

The accelerometers can also be used to determine the local linear velocity of the ES instrument due to satellite spin. In Chapter 6, more details of the GGT inertial sensor operation on a tumbling satellite are discussed, and a possible role of these secondary accelerometers in compensating for errors introduced by satellite spin in the GGT measurement, is described.

A more complete discussion of an attitude determination instrument using the GGT is outside the scope of this thesis. This thesis focuses on the novel inertial sensor to measure the GGT, and the design, fabrication and characterization of a MEMS Earth Sensor chip for this purpose. A MEMS based approach is used for the inertial sensor in order to obtain a compact instrument.

2.3.Factors affecting sensitivity and robustness of MEMS inertial sensor

From Equations 2-1 and 2-2, to obtain a high displacement due to GGT for the MEMS ES chip, a high moment of inertia $|I_y - I_x|$ and a low spring constant k are desirable.

A higher $|I_y - I_x|$ will result in higher GGT for the same angle Ψ . For an elongated object, $I_y \gg I_x$ so $|I_y - I_x| \approx I_y$ which can be simply denoted as the moment of inertia I of the proof mass. A lower k will result in more displacement of the proof mass for the same GGT. To measure the GGT, the displacement of the proof mass is measured. Measuring a larger displacement for the same GGT is easier and offers a higher signal to noise ratio. A sensor design that results in greater displacement for the same GGT can be said to be more sensitive. For better sensitivity in microgravity, increasing I and lowering k increases the displacement for the same GGT, and therefore results in a more sensitive ES design.

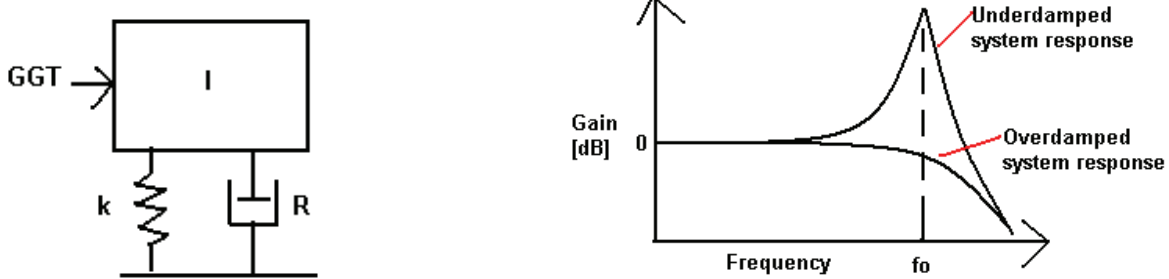


Figure 2-9 Left: A schematic of a second order system formed by the proof mass with moment of inertia I , spring with spring constant k , subject to a damping factor; Right: Frequency response of such a system is dependent on the resonant frequency f_0 and whether the system is over- or underdamped

The spring and proof mass system will be subject to some sources of damping. Figure 2-9 shows the schematic of such a system, where the sources of damping are lumped together into a single element with a damping factor R . Such a system can be represented by a second order differential equation [17]. The measure of sensitivity for such a system can be denoted by the fundamental mechanical resonant frequency of the sensor, which is given by the following equation

$$f_o = \frac{1}{2\pi} \sqrt{\frac{k}{I}} \quad 2-3$$

Chapter 2: Attitude Determination using the Gravity Gradient

The value of f_o depends on the moment of inertia and the spring stiffness. An ES design with lower f_o indicates a higher moment of inertia and a lower spring constant. Therefore a lower f_o indicates that the proof mass will have a greater displacement for the same GGT, and the design is more sensitive for GGT. To measure the GGT with more accuracy, f_o should be reduced. As seen in the right of Figure 2-9, the response of such a system depends on the resonant frequency f_o . The MEMS ES will be able to track changes in GGT only if they occur at a rate below the resonant frequency of the second order system.

When designing the MEMS ES chip for maximum sensitivity, the following constraints apply:

- The sensitivity cannot be arbitrarily increased by lowering the resonant frequency. The resonant frequency must be at a minimum, which is above the desired update rate of the ES instrument, which in this case is 1 Hz.
- The moment of inertia I depends on the length, breadth and depth of the proof mass with respect to the XZ plane, as shown in Figure 2-3.
 - Four of these proof masses (Figure 2-5) should fit into the target volume of 1 l (10 cm x 10 cm x 10 cm), which limits the maximum length of ES chips to well below 10 cm, since some of the volume will be needed for the electronics, and mechanical structures needed for a complete ES instrument.
 - The MEMS ES sensors are fabricated from silicon wafers using available production facilities at CSEM and EPFL. The maximum diameter of the wafers that can be processed is 100 mm. The four ES chips required for an instrument should be obtained from the same 100 mm diameter wafer, so their characteristics are well matched. This limits the proof mass dimensions as well.
 - The depth of the proof mass and the spring is determined by a vertical cut into the plane of the silicon wafer. This is done by a fabrication step known as Deep Reactive Ion Etching (DRIE) which is critical to the fabrication of the ES chip. As the depth of the cut using DRIE increases, the process becomes more challenging and risky. Limitations imposed on the depth by the DRIE process are discussed further in the thesis.
- It is not sufficient to design the ES chip for performance in microgravity. It is fabricated on Earth and has to be tested in a 1 g environment. Routine handling of the chip in a laboratory environment will impose at least a few g of shock on the sensor. To reduce the probability of the proof mass breaking off, the maximum possible displacement of the proof is limited along all axes by introducing hard stops around the periphery of the proof mass.
 - Limiting the displacement limits the peak stress on the spring to well below the critical stress of silicon when the proof mass is at the maximum displacement.
 - A lower displacement means that the proof mass has less room to move in response to an external acceleration. When the proof mass hits the hard stops, the kinetic energy accrued by the mass is lower in response to an external acceleration, if the distance it travels is less.
 - The distance between the proof mass and in-plane the hard stops in the XZ plane is governed by the width of the vertical cut made during the DRIE process.

Chapter 2: Attitude Determination using the Gravity Gradient

From the above points, for a fixed length and breadth of the proof mass, the design of the DRIE process step is important to obtaining a proof mass with a high moment of inertia (greater depth of the DRIE cut), but more robust and less prone to breakage (smaller width of the cut). This is discussed in more detail below.

Typically the risk of the DRIE step depends on the aspect ratio of the cut i.e. the ratio of the width of the etch opening, to the depth of the etch. Figure 2-10 and Table 2-1 compare two ES proof mass and spring designs with differing thicknesses of the silicon layer from which they would be fabricated. The thickness of design 2 is scaled up from that of design 1 by a factor s , keeping all other dimensions the same.

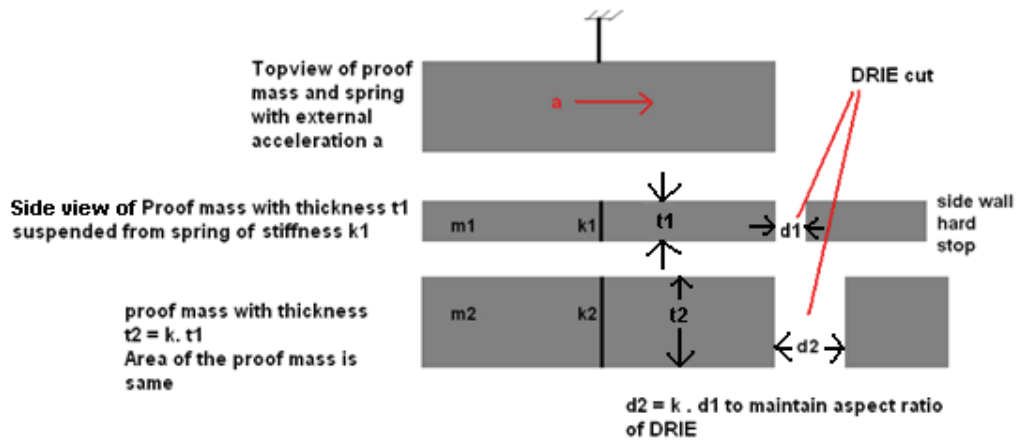


Figure 2-10 A proof mass suspended from a single spring. Two sensor designs that differ only in the thickness of the proof mass are compared. Properties of mass m_2 are scaled from mass m_1 by factor s

	Mass 1 properties	Mass 2 properties (scaled by factor S from Mass 1)
Thickness	t_1	$s \cdot t_1$
Mass	m_1	$s \cdot m_1$
DRIE etch gap	d_1	$s \cdot d_1$
Maximum Kinetic energy that can be gained by proof mass due to acceleration a as shown in Figure 2-10	$m_1 \cdot d_1 \cdot a$	$s \cdot m_1 \cdot s \cdot d_1 \cdot a$
Spring constant for acceleration a	k_1	$s \cdot k_1$
resonant frequency	$\sqrt{k_1 / m_1}$	$\sqrt{k_1 / s \cdot m_1}$
Ratio of kinetic energy gained to spring stiffness	$m_1 \cdot d_1 \cdot a / k_1$	$S \cdot (m_1 \cdot d_1 \cdot a / k_1)$

Table 2-1 Comparison of two proof masses of same area but different thickness (Figure 2-10) to understand the effect of increasing the thickness with respect to robustness

The DRIE aspect ratio is kept the same for both. In Figure 2-10, the aspect ratio for mass m_1 is $d_1:t_1$, and for mass m_2 it is $d_2:t_2$. Table 2-1 lists the properties of mass 1 and mass 2. The properties of mass 2 are scaled by the factor s .

Chapter 2: Attitude Determination using the Gravity Gradient

from mass 1, therefore $d_1:t_1 = d_2:t_2$. At the end of the table, it can be seen that with increasing thickness of the proof mass, the kinetic energy gained by the proof mass, when it hits the hard stop, increases by the factor s , as compared to the increase in the spring stiffness. This means that the proof mass with more thickness is less robust if the DRIE aspect ratio is kept the same. Under the high accelerations experienced for shock, the thinner proof mass has less kinetic energy relative to its spring stiffness when it hits the hard stop and a greater chance of surviving the impact as compared to the thicker proof mass.

To increase the moment of inertia of the proof mass by increasing its thickness, while maintaining the robustness of the sensor, there must a corresponding increase in the DRIE aspect ratio. DRIE becomes more challenging both with increasing aspect ratio, and increasing depth. With an increased aspect ratio, the etch time increases exponentially. Larger etch times require thicker etch masks during the DRIE over the parts of the wafer that are not cut. The possible mask thickness is limited by the properties of the materials available that are used to form the mask, so this ultimately limits the aspect ratio that can be reliably attempted during DRIE, which then limits the thickness of the proof mass. The maximum DRIE aspect ratio achievable is 1:20, which is extremely difficult. Etches with an aspect ratio of 1:10 are challenging, and typically some process iterations are needed to get the process parameters correct.

Since this thesis involves the complete development of the MEMS Earth sensor, the design and fabrication process is new. To reduce the fabrication risk it was advisable not to attempt a challenging DRIE aspect ratio. In discussions with the clean room technician responsible for DRIE, and considering the known reliable process options for forming an etch mask thick enough, a DRIE depth of 100 microns was initially chosen for fabrication with an aspect ratio of 1:3.

In practice, as the DRIE depth increases, the angle of the sidewall deviates more from the vertical. This has implications for the spring design as well, which are discussed in Chapter 6.

2.4.Length and Breadth of proof mass

A minimum of four MEMS chips are required for one unit that can be used on a satellite. To have matched characteristics, they should ideally be fabricated together on a single wafer. The fabrication work for this thesis was done using an available 100 mm wafer diameter process. As a starting point for a design, using the maximum possible area on a 100 mm diameter wafer, and keeping the length of each chip as long as possible, four chips of area $70.7 \times 17.67 \text{ mm}^2$ are possible. Within the area of a chip, leaving 5 mm along the boundary for mechanical support, and to accommodate a readout scheme, the proof mass that can be accommodated is $60.7 \text{ mm} \times 7.67 \text{ mm}$ (Figure 2-11). The orders of these dimensions are also in keeping with the target instrument volume of 1 dm^3 . Making chips larger than a few cm long is not desirable, since four such chips are required to fit into a 1 dm^3 volume. As discussed previously a thickness of 100 microns is chosen for the proof mass.

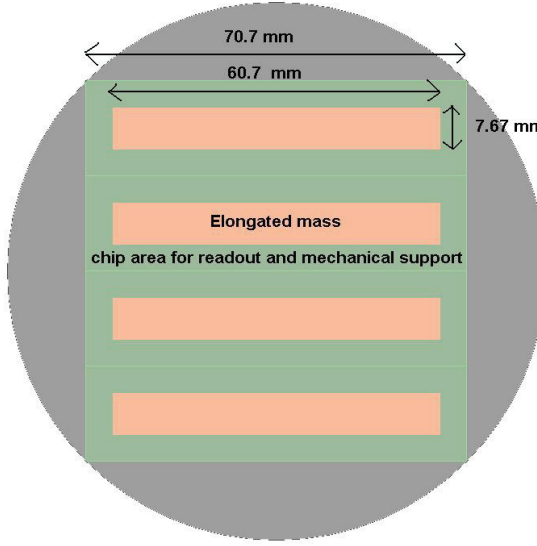


Figure 2-11 A first approximation to obtain the dimensions for four MEMS chips on a single 100 mm wafer

2.5.Signal to Thermal Noise Ratio

A mass of dimensions as shown in Figure 2-11, with 100 micron thickness has a moment of inertia of 3.4×10^{-8} N.m². The gravity gradient torque on a proof mass with this moment of inertia at an orbital attitude of 700 km ranges from 4.1×10^{-15} N.m, for a ψ of 2 degrees, to 6×10^{-14} N.m for a ψ of 45 degrees. To establish if the sensor is physically capable of measuring these low values of GGT, the Brownian noise (thermal noise) equivalent torque is calculated for the MEMS sensor, for a range of fundamental natural frequencies. The sensor cannot have arbitrarily low spring stiffness since a minimum update rate; hence fundamental natural frequency, of 1 Hz is required.

For a second order system, the expression for the thermal noise equivalent angular acceleration (TNEAA) is given by the expression [17]

$$TNEAA = \sqrt{\frac{4 K_B T 2\pi f_o}{QI}} \quad 2-4$$

where K_B is the Boltzmann constant, T the temperature in Kelvin, f_o the fundamental natural frequency, Q the quality factor and I the moment of inertia. Multiplying this by the moment of inertia I , we get the thermal noise equivalent torque (TNET).

$$TNET = \sqrt{\frac{4 K_B T 2\pi f_o I}{Q}} \quad 2-5$$

From this the signal to noise ratio due to thermal noise can be calculated as

Chapter 2: Attitude Determination using the Gravity Gradient

$$SNR_{thermal} = \frac{GGT}{\sqrt{\frac{4K_B T 2\pi f_o I}{Q}}} \quad 2-6$$

where GGT is the gravity gradient torque to be measured. In the above equation, for a given orbit height and angle Ψ of the satellite, the GGT is fixed. The moment of inertia I is fixed for the proof mass with the dimensions specified in Figure 2-11 (3.4×10^{-8} N.m 2). With a fixed moment of inertia the resonant frequency f_o will depend on the design of the spring, and the Q factor will depend on the various sources of damping in a second order system. Typically the largest source of damping for a MEMS device is the movement of the proof mass in air. With decreasing pressure, this damping is reduced and the quality factor increases until other sources of damping, such as mechanical losses in the spring, become dominant. The operational environment for the MEMS ES is hard vacuum. So the quality factor in space should increase from the quality factor in air till it saturates. Mechanical losses are typically orders of magnitude lower than that due to squeeze film damping of the proof mass in air, so it can be expected that the quality factor will be high in vacuum. The graphs in Figure 2-12 below indicate the quality factor necessary for different values of f_o for which the thermal noise is equal to the GGT to be measured. The graph is plotted for two temperatures of 50 C and -50 C, since these are the typical limits within which temperature is maintained onboard a satellite.

From Equation 2-6, Figure 2-12 shows that to be able to sense GGT and from it determine the Earth vector to an accuracy of 2 degrees the sensor should have a Q factor in the order of hundreds in vacuum. There are no reliable solutions to lower the mechanical losses of the ES proof mass and spring. It is difficult to control the point at which the quality factor will saturate in vacuum. So it is advisable to keep the resonant frequency of the sensor lower, keeping in mind the minimum required readout rate, so the minimum required quality factor in vacuum is also lower.

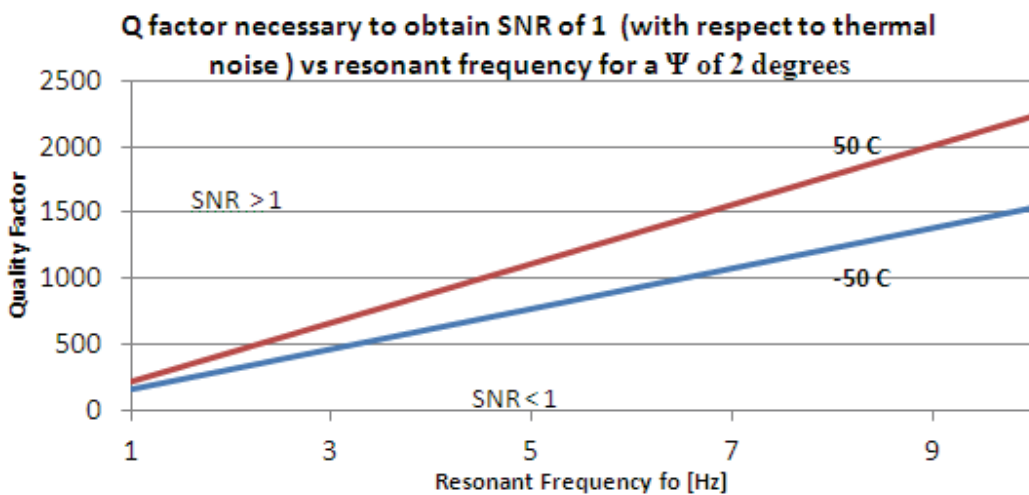


Figure 2-12 Required quality factor for measuring the GGT for a proof mass ($I = 3.4 \times 10^{-8}$ N.m 2) in orbit of 700 km tilted 2 degrees with respect to the nadir for different resonant frequencies. The area above each line represents indicates values of Q and f_o for which $SNR > 1$

Chapter 2: Attitude Determination using the Gravity Gradient

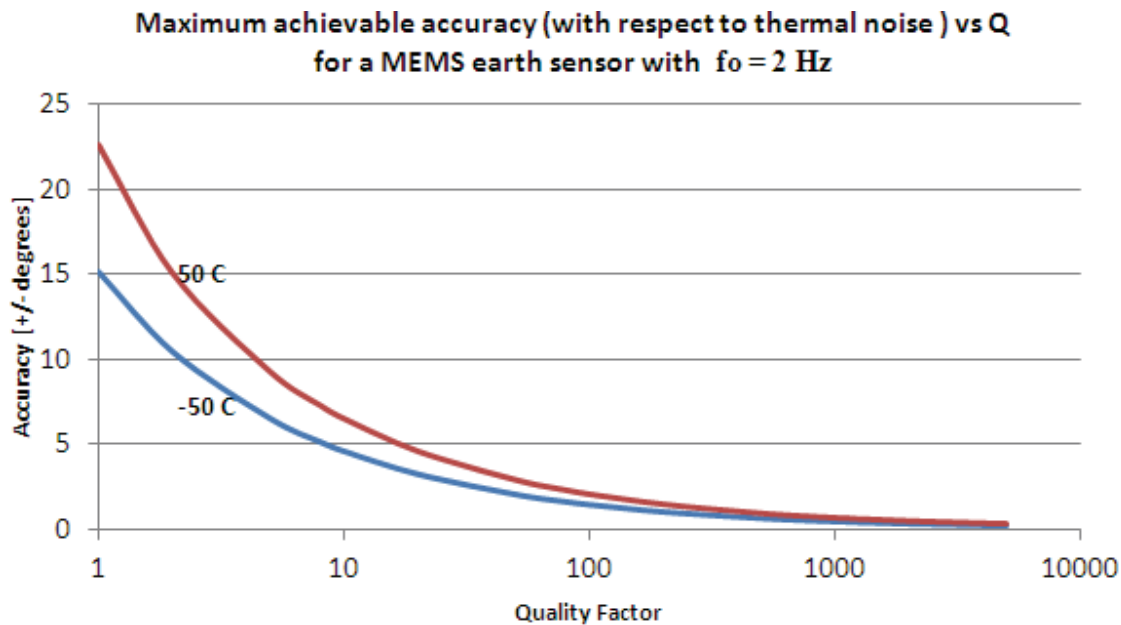


Figure 2-13 The accuracy for a sensor at an orbit of 700 km with resonant frequency of 2 Hz and proof mass moment of inertia $3.4 \times 10^{-8} \text{ N.m}^2$ for different Q factors, plotted for 50 C and -50 C

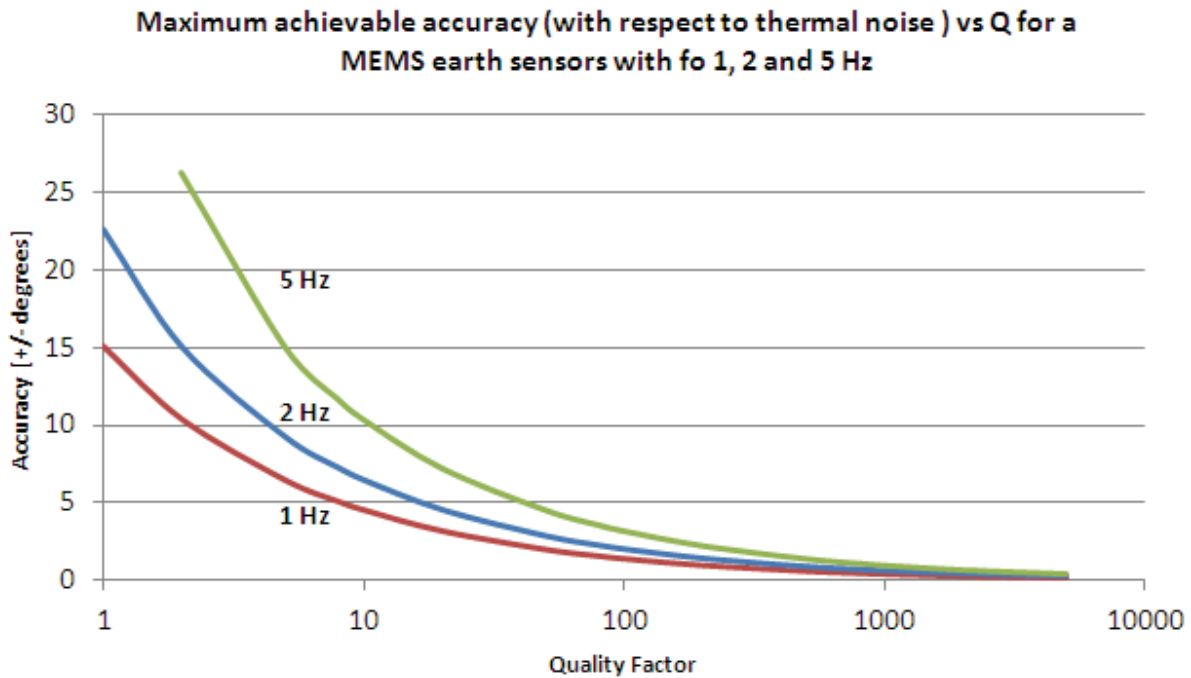


Figure 2-14 Achievable accuracy for sensors with different f_0 , at an orbital altitude of 700 km with respect to quality factor, all having a proof mass with a moment of inertia $3.4 \times 10^{-8} \text{ N.m}^2$, at a temperature of 300K

Figure 2-14 shows that, for the same quality factor, better accuracy is possible for a sensor with lower resonant frequency. To achieve an accuracy of 2° in measuring Ψ , for an ES chip with a lower resonant frequencies, the required Q factor is lower, so higher mechanical losses can be tolerated (Equation 2-6).

Chapter 2: Attitude Determination using the Gravity Gradient

Also, any readout scheme will have its own noise in measuring the displacement due to GGT. For lower f_o , the sensitivity of the ES will be more, and the displacement of the proof mass is more for the same GGT. So the readout scheme will also have a larger signal to measurement noise ratio.

2.5.1. SNR Dependence on Orbit Height

From Equation 2-1, the GGT for the same angle Ψ and proof mass with moment of inertia I inversely depends on the cube of the satellite orbit radius. For ES chips with resonant frequencies of 1, 2 and 5 Hz, a Q of 500, at a temperature of 50°C, the minimum accuracy of the ES is plotted for increasing orbit heights. From Figure 2-15, it can be observed that the accuracy gets worse as the orbit height increases. The SNR becomes worse since the GGT decreases. Therefore the MEMS based ES can be used only in low Earth orbit.

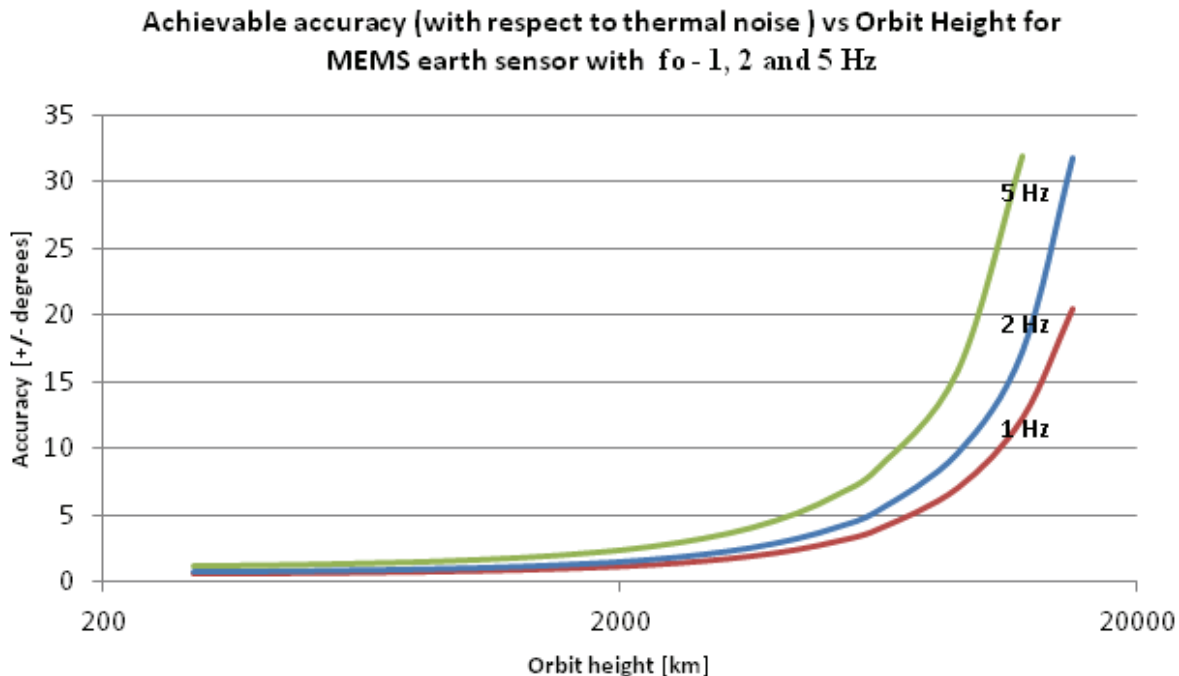


Figure 2-15 Achievable accuracy for sensors with different f_o for different orbital altitudes. The Q factor is assumed to be 500 for all the sensors, all have a proof mass with a moment of inertia $3.4 \times 10^{-8} \text{ N.m}^2$, at a temperature of 323K

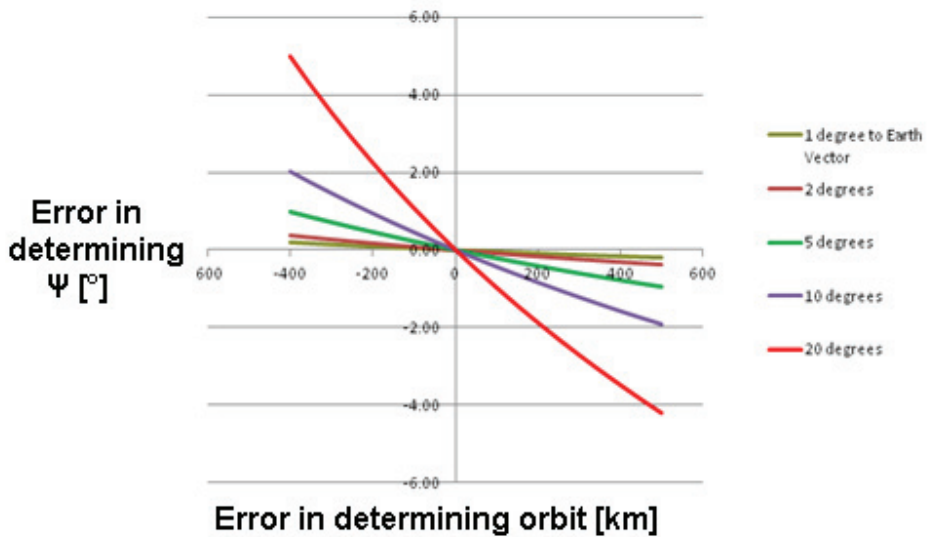


Figure 2-16 The different curves show the resulting error in determining the Earth Vector due to error in knowing the orbit height, for different angles to the Earth vector (ref. orbit 700 km from which relative error is calculated)

In Equation 2-1 it can be seen that GGT depends on the orbit height. The ES measures a displacement proportional to the GGT. To calculate the angles to the Earth vector, it is necessary to know the orbit height, and this is an input to the ES. If a wrong orbit height is specified then the wrong angle will be computed. Since this is an external input to the ES there is no way to compensate for this error in the ES itself. Figure 2-16 shows the error in calculating the angle Ψ . It depends on the actual attitude of the satellite, and the error in determining the orbit height of the satellite, and is independent of the accuracy of the MEMS ES.

2.6. Conclusion

Starting from the requirements of an attitude sensing instrument for a satellite, the design for a novel inertial sensor that measures the GGT is established. Accelerometers, in the configuration used in gradiometers, are not suitable to measure the GGT for attitude determination. The sensor consists of an elongated proof mass suspended from a compliant spring. Four such inertial sensors are required for an attitude determination instrument.

Since a MEMS based approach is followed to achieve the mass and volume goals for the instrument, a preliminary estimate is made of the size of the proof mass of the inertial sensor, based on the available production processes and process constraints constrains, desired volume of instrument, and the necessity to have four ES chips per wafer. A proof mass having dimensions of 6.07 cm x 0.7 cm x 100 microns is feasible.

The noise due to Brownian motion is a fundamental limitation in the accuracy of the sensor. With a MEMS ES having a proof mass of the above dimensions, to be able to measure the pitch and roll angles

Chapter 2: Attitude Determination using the Gravity Gradient

of a satellite in low earth orbit to an accuracy of 2° , the fundamental resonant frequency of the sensor should be of the order of a few Hz, and the quality factor in vacuum should be in the order of a few hundreds. The noise due to any electronics used to measure the displacement of the proof mass should be less than the thermal noise limit.

Length of proof mass	~ 6 cm
Breadth of proof mass	~ 1 cm
Thickness of proof mass	100 microns
Resonant frequency (determines spring dimensions)	> 1 Hz
Required Q factor in vacuum to achieve thermal noise floor low enough to measure Ψ with an accuracy of $+/- 2^\circ$	~ 500

Table 2-2 Summary of orders of magnitude for the various parameters for ES inertial sensor design, based on production constraints, target mass and volume for ES instrument, update rate

Chapter 3

Design of 1st Generation Earth Sensor

In the previous chapter the need for an ES chip design is discussed that has a proof mass many centimeters long, is suspended from a spring that is compliant enough so that the overall resonant frequency is on the order of Hz, and is as low as possible keeping in mind the required update rate from the sensor, then a lower quality factor would be needed to achieve a thermal noise to signal ratio of 1 in vacuum. This chapter discusses the design of the 1st generation earth sensor based on these guidelines, and presents a design based on available fabrication processes, and the necessity to have a design that is testable on Earth.

The start of the Earth sensor development was funded by ESA, and required a proof of concept to be developed in fifteen months. The conceptually straightforward design of an elongated proof mass suspended from a single compliant spring is chosen.

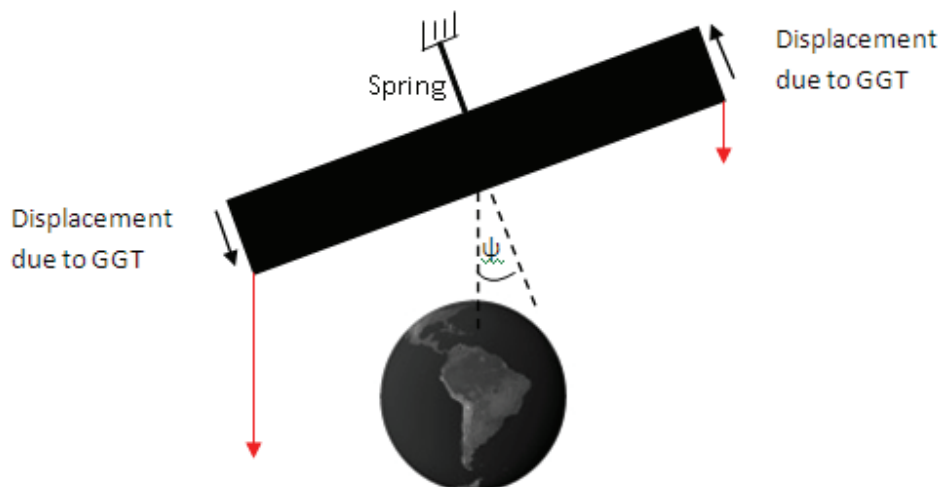


Figure 3-1 Elongated proof mass suspended from single spring

3.1. Proof mass design

In the previous chapter it was discussed that a high moment of inertia proof mass is desirable, but at the same time the thickness should be limited due to the limits of the DRIE process. The chip dimensions described were based on having only four chips per wafer. For a sensor in this stage of development a higher number of chips per wafer is desirable to have testable chips at the conclusion of the fabrication process, since the yield will be very low. Increasing the number of chips on a wafer will reduce the area available per chip, and therefore the moment of inertia of the proof mass.

Chapter 3: Design of 1st Generation Earth Sensor

Another important limitation on the dimensions of the proof mass is testability on Earth. This sensor is designed to operate in microgravity, and the low resonant frequency is required for sufficient signal to noise ratio. In 1 g on Earth, the sensor has to be robust enough to withstand routine handling and be testable. To increase the robustness of the proof mass its maximum possible displacement due to acceleration should be limited. This limits the peak stress on the spring, so the sensor should survive large accelerations. This implies that the DRIE etch should have a larger aspect ratio, so that for a given thickness of the proof mass, the peak displacement it can have is less.

Using a Silicon on Insulator (SOI) wafer, that is comprised of two layers of silicon bonded together by oxide, it is possible to increase the moment of inertia of the proof mass, while reducing the area it occupies. Typically the thinner silicon layer is referred to as the device layer, and the thicker silicon layer is referred to as the handle layer. The two silicon layers are etched individually, and a different aspect ratio can be designed for each layer, depending on the thickness of each layer. So the device layer can be used for the spring and etched with a higher aspect ratio to prevent excessive motion of the proof mass, while the handle layer, etched with a lower aspect ratio, can be used to increase the thickness of the proof mass.

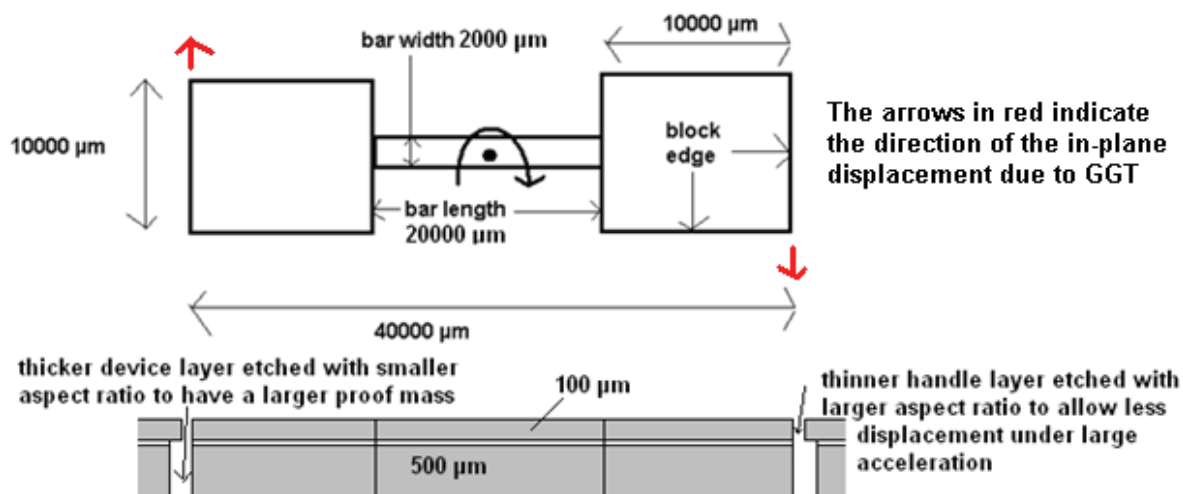


Figure 3-2 Dimensions of barbell shaped proof mass, for a SOI wafer of device layer thickness 100 microns, handle layer thickness 500 microns

A barbell shaped proof mass is designed with outline dimensions of 1 cm x 4 cm and total thickness of 600 microns, as shown in Figure 3-2. The smaller outline dimensions allow for six chips from a single wafer, and the moment of inertia of the barbell shaped proof mass is 6.8×10^{-8} N.m². The barbell shape is chosen so that the moment of inertia remains high while the weight of the proof mass is reduced, so that it is more robust for handling in 1 g.

3.2.Spring design

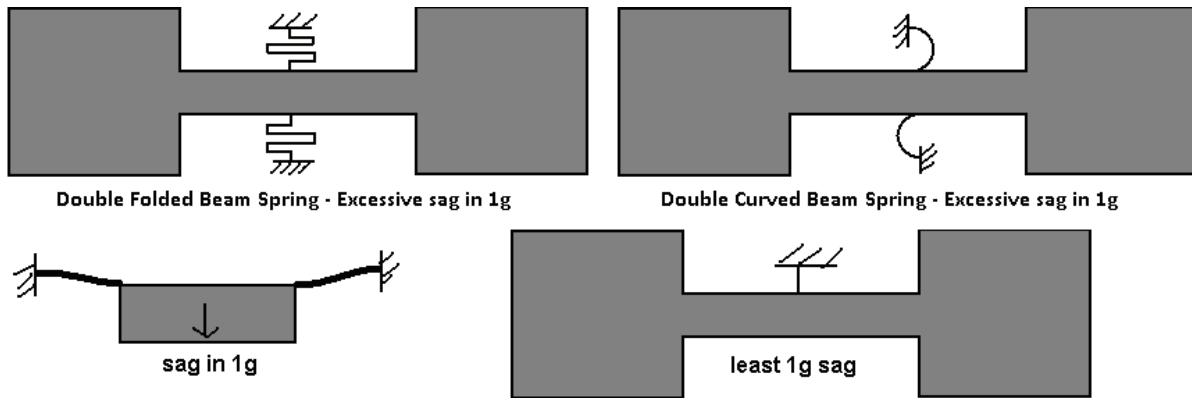


Figure 3-3 Different spring designs evaluated for 1st generation Earth sensor. ANSYS is used to model the displacement of the proof mass in 1g. The single cantilever design is chosen due to low sag in 1g.

Spring designs that suspend the proof mass using two springs were evaluated (Figure 3-3), and a single cantilever is chosen finally. The design target is a f_o of 1-2 Hz, and the springs are scaled accordingly, with a depth (with respect to Figure 3-3, looking into the plane of the figure) of 100 microns, since the spring is etched from the device layer of the SOI wafer.

Due to the weight of the 1 cm x 4 cm proof mass, there is a force on the spring that causes a downward displacement of the mass, called the sag of the spring-proof mass due to gravity. Since the device has to be testable on Earth, the sag of the spring in 1 g has to be low such that the proof mass remains within a few microns of plane the surrounding chip frame. The spring dimensions are chosen to provide high compliance to in-plane torque, but very high stiffness to gravity perpendicular to the chip plane. If it sags too much then the displacement readout will not function. Table 3-1 shows the sag of the different designs considered in Figure 3-3, due to the proof mass design as shown in the previous section. All the springs were sized such that f_o is ~ 1.4 Hz. The simple cantilever has the lowest sag of all three, hence it is chosen over the others since a ES chip with a proof mass suspended from a simple cantilever is testable on Earth.

Double Folded Long Cantilever	92 microns
Double Curved Springs	500 microns
Simple Cantilever	1 micron

Table 3-1 Comparison of the sag of different springs from Figure 3-3 in 1 g

The spring constant of the cantilever for the displacement due to GGT is given by [22]

$$k = \frac{E h w^3}{12 l} \quad 3-1$$

Chapter 3: Design of 1st Generation Earth Sensor

Where E is the Young's modulus of Silicon (180 GPa [39]), w is the width of the suspension, h is the height and l is its length. k is strongly dependent on w, the width of the spring.

This displacement relative to the satellite body is given by

$$\theta = GGT/k \quad 3-2$$

where GGT is the gravity gradient torque on the proof mass, k is the spring constant and θ the angle through which the mass rotates due to the torque. At the ends of the pendulum mass the displacement due to the rotation can be measured to determine θ and therefore the gravity gradient torque.

The fundamental resonant frequency is given by

$$f_o = \sqrt{k/I} / 2\pi = \sqrt{6.9e-14 / 5.06e-6} / 2\pi = 1.4 \text{ Hz} \quad 3-3$$

3.3.Proof mass balancing

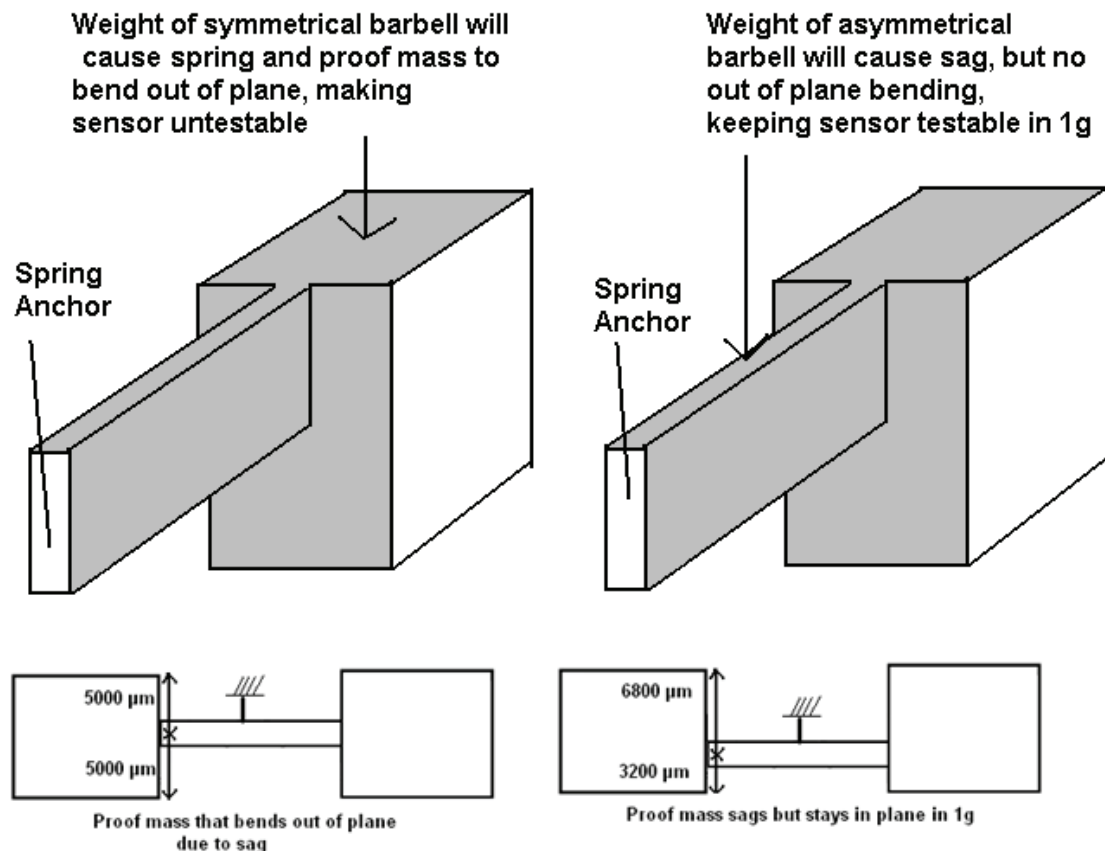


Figure 3-4 Proof mass is made asymmetric such that the barbell stays in plane with the chip frame.

To ensure that the sensor is testable in 1 g, the barbell proof mass is made asymmetric as shown in Figure 3-4. Due to the single spring suspension the proof mass on the left of the figure would bend out of plane in 1g. To prevent that, the blocks at the end are placed asymmetrically with respect to the central bar, so that in 1 g, the proof mass stays in plane, as shown by the ANSYS simulation in Figure 3-5. The center of mass of the proof mass is brought as close to the center of mass of the spring as possible rounded to 1 micron.

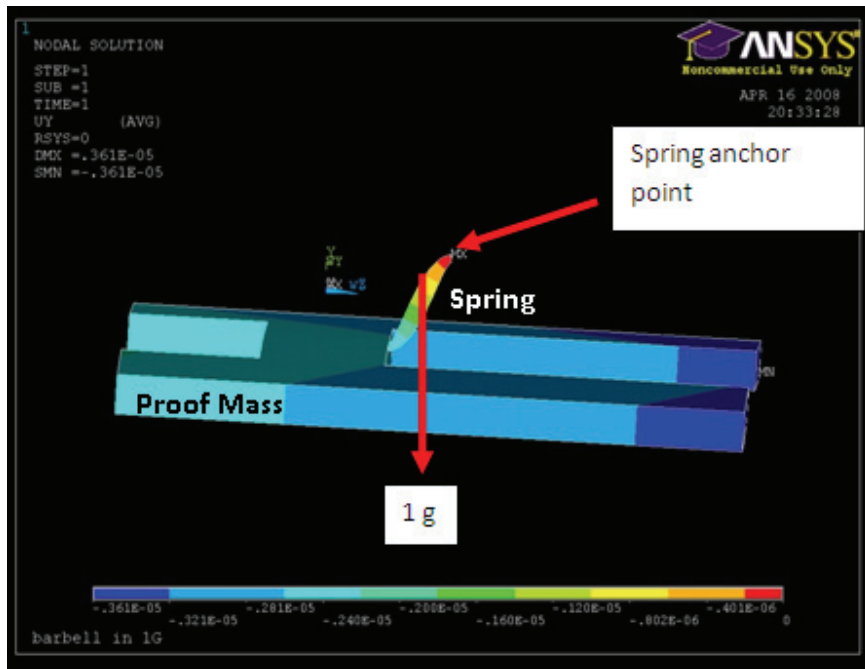


Figure 3-5 FEM simulation of chosen design showing a side view of the proof mass with $1 \times 4 \text{ cm}^2$ outline dimensions suspended by the $15 \times 100 \times 1000 \mu\text{m}^3$ spring in one gravity. The legend shows displacement in meters (max. sag of $3.6 \mu\text{m}$). The spring displacement is greatly exaggerated by ANSYS for clarity.

3.4. Effect of the spacecraft gravity

Due to the symmetrical nature of the barbell, the effect of spacecraft gravity on the pendulum is negligible. To obtain the magnitude of displacement, we assume that the sensor is located at a distance of 1 m from the center of mass of a spacecraft whose mass is approximated by a spherical fuel tank of 2000 kg. Using ANSYS, the displacement is seen to be on the order of 10^{-13} m , while the displacement from GGT is of order 10^{-9} m .

3.5. Effect of the Moon's gravity

Taking the moon's mass to be $7.35 \times 10^{22} \text{ kg}$ and the orbit to be at a distance of 380,000 km, the gravity due to the moon is calculated and by using ANSYS (Figure 3-6) we see that the worst case displacement due to the moon is on the order of picometers, 100 times smaller than the displacement due to GGT.

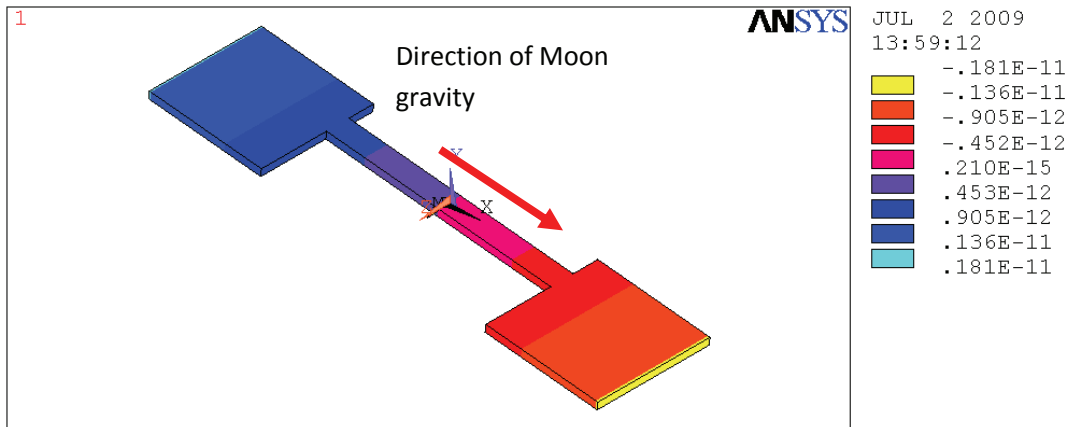


Figure 3-6 FEM Simulation of the Moon's gravity on the Earth sensor. The legend shows the displacement in meters.

3.6. Effect of Temperature on spring constant

The spring constant or k of the barbell suspension is calculated by equation 2-3. From that one can see there is a linear dependence on the Young's modulus E . The Young's modulus has a slight dependence on temperature and reduces with increasing temperature. The change is $-9.4 \times 10^{-5} \text{ K}^{-1} \text{ Pa}^{-1}$ [5]. For a temperature range of -20 to 60° C the E changes by a factor of 0.009. The spring constant is linearly dependent on E and reduces by the same factor. Therefore the displacement also changes by the same factor.

3.7. Readout Design and Selection

To measure the displacement of the proof mass, two approaches were compared. One was to measure the displacement by sensing a change in capacitance, and the other was to implement an optical fiber based interferometer. The methods were each evaluated on ease of fabrication, ease of integration, sensitivity and suitability in a space environment.

3.7.1. Capacitive Displacement Readout

Comb drives are typically used in a configuration where the opposing fingers move parallel to each other. In this case, with a displacement on the order of tens of nanometers, the change in capacitance due to changing area between the fingers is in the order of aF. The other configuration is one in which the fingers move perpendicular to each other (used in accelerometers from Analog Devices –Figure 3-7) which gives a capacitance change in the order of fF.

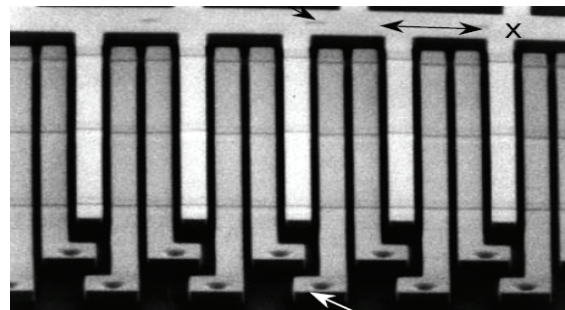


Figure 3-7 Capacitive displacement sensor from Analog Devices, showing the fingers on the moving mass (lighter gray) and the two sets of fixed comb fingers (darker gray). [44]

Figure 3-8 shows the pendulum mass with comb fingers for differential capacitance sensing, and the direction in which the fingers would move. For small displacements, higher order effects can be ignored and the output voltage is proportional to the difference in C1 and C2. Though this method can be sensitive to radiation due to dielectric charging, with careful design this can be mitigated.

However, to obtain the required sensitivity with this method, the gaps between the fingers have to be 5 microns or less. This again requires a DRIE process with a high aspect ratio of 1:20, which adds to the fabrication complexity and risk. Keeping in mind the fifteen month timeframe required by ESA, a lower risk, high sensitivity readout is required.

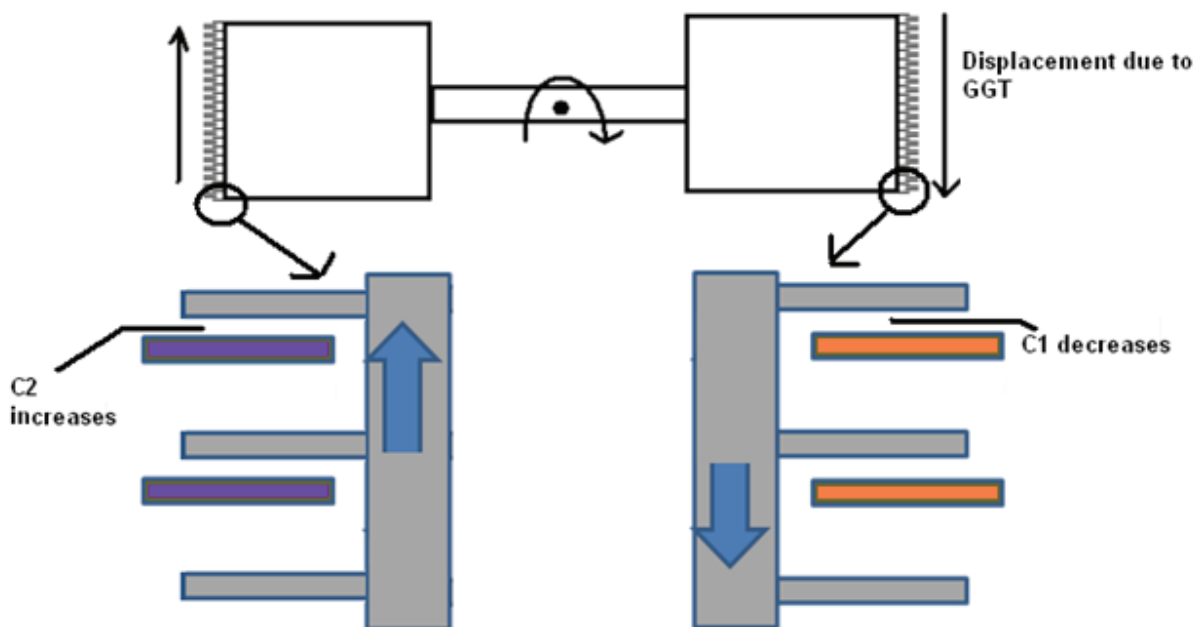


Figure 3-8 Earth sensor mass with comb fingers for capacitive sensing

3.7.2. Optical Displacement Readout

The displacement obtained from such a pendulum is in the range of 0-1 nm. Fiber optic based interferometers have been reported that are sensitive to sub-angstrom motion [40-43]. To detect the displacement of the Earth sensor proof, a fiber based interferometer is suitable. The tip of the fiber is placed at a fixed distance from the pendulum mass. The first interferometer beam is due to the 4% reflection where the light exits the fiber, and the second beam is the light that is reflected back into the fiber from the pendulum mass (Figure 3-9). The two beams are combined and the optical intensity is read using a photodiode. When the distance between the fiber tip and the pendulum changes, the interference conditions change, and the resulting change in beam intensity is recorded at the measuring photodiode (Figure 3-10). Two such interferometers are used to record the displacement at opposite ends of the barbell (Figure 3-11), thus facilitating a differential readout scheme.

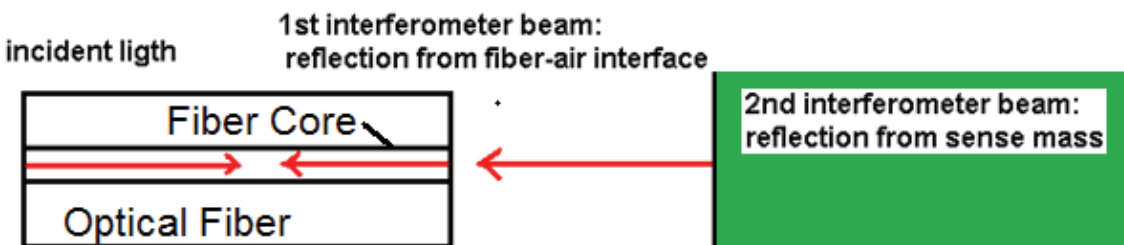


Figure 3-9 Interference between light reflected from mass, and light reflected from fiber tip

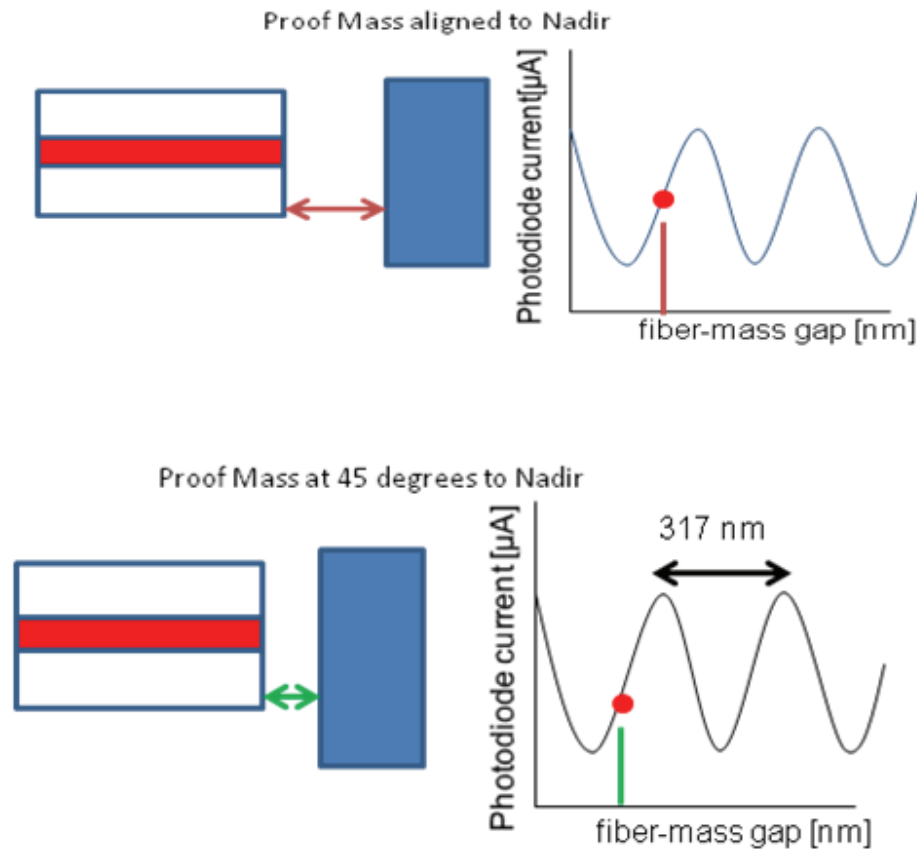


Figure 3-10 Example of interferogram showing how the photocurrent changes as fiber tip – proof mass distance changes due to GGT. The interferogram has a period of half the laser wavelength used (635 nm), and nm changes in distance are reflected in the photocurrent.

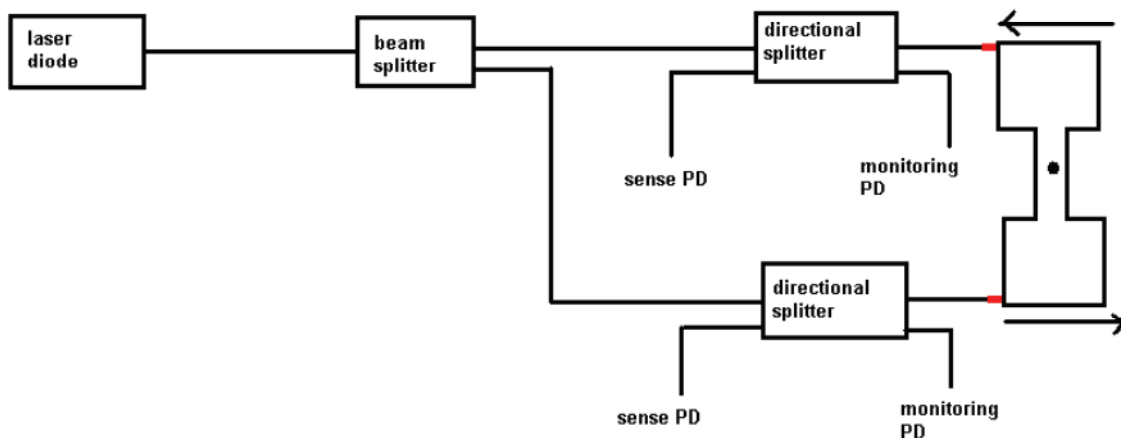


Figure 3-11 Interferometer schematic for differential measurement of proof mass displacement due to GGT

This method could be susceptible to radiation, since the laser used will have to be shielded and thermally stabilized, so in this respect the capacitive method is probably more robust. But for the

Chapter 3: Design of 1st Generation Earth Sensor

purposes of the prototype, it is much easier and less risky to fabricate the optical readout, and the fibers can be integrated easily in our silicon-based fabrication process. Also, the known sensitivity of interferometry methods is quite high.

3.8.Conclusion

The design of the 1st generation earth sensor is a barbell shaped proof mass of outline dimensions 1 cm x 4 cm, suspended from a cantilever of dimensions 15 microns x 1000 microns x 100 microns. The moment of inertia of the proof mass is 6.9×10^{-8} N.m² and the spring constant is 5×10^6 , which gives a fundamental natural frequency of 1.4 Hz. These values are chosen with the following criteria in mind: thermal signal to noise ratio, maximizing number of chips per wafer, and reducing fabrication risk. The displacement readout is done using an optical fiber interferometer. The readout scheme is also chosen such that the fabrication risk is low, and it is easily integrated into the chip.

Proof Mass Properties	
Proof Mass Total Length	4 cm
Proof Mass Bar Length	2 cm
Proof Mass Bar Breadth	0.2 cm
Proof Mass Breadth at extremities	1 cm
Proof Mass Thickness	600 μ m
Proof Mass Maximum Moment of Inertia	6.9×10^{-8} N.m ²
Proof Mass Weight	0.33 g
Spring Properties	
Spring Length	1000 μ m
Spring Width	15 μ m
Spring Depth	100 μ m
Sensor resonant frequency	1.36 Hz
Hard Stops	
Lateral Clearance	30 μ m
Vertical clearance	<4 μ m
Optical Displacement Sensing	
Fiber tip distance from Proof Mass	35 μ m
Laser Wavelength	635 nm

Table 3-2 Summary of design for 1st Generation ES chip

Chapter 4

Fabrication of 1st Generation Earth Sensor

This chapter describes the fabrication work carried out for the 1st generation MEMS ES. A new fabrication process is designed for the sensor. This was the first fabrication run carried out for this project with all process steps performed for the first time. Typically, the yield from a new fabrication process is quite low, on the order of a few percent, and in the case of this sensor, the risk is greater due to the scale of the proof mass (1 cm x 4 cm) being two orders of magnitude above typical MEMS devices, and the critical spring dimension (width) being 15 micron. Only six chips can result from each 100 mm wafer.

4.1. Test Devices

To reduce the risk of the fabrication process and increase the probable yield, the first step was to fabricate some test chips. These devices have a simpler design, and a lower risk fabrication process. The objective was to improve the ES design and fabrication process by first making test devices. The objectives were:

- Gain some experience in the design and execution of critical process steps required for the Earth Sensor, such as etch mask preparation for DRIE, and HF vapor release.
- The spring width is a critical dimension. The stiffness of the spring depends on the cube of the spring width. During any microfabrication process, the individual steps introduce some divergence from the CAD design due to over / under etching in various steps, starting right from the mask manufacture. A compensation factor is necessary in the CAD drawing that will result in the fabricated spring being close in value to the designed value. This factor can be obtained from the fabrication of the test chips.
- Obtain some chips to test the displacement sensing method using optical fibers, to check if the fiber-proof mass spacing is proper to obtain similar intensity between the light reflected from the fiber tip back into the fiber, and the light reflected from the proof mass.
- For a given fiber – proof mass spacing, to check if sufficient light is reflected from the proof mass. Since the proof mass wall from where light will be reflected back to the fiber is etched by DRIE, it has a roughness on the scale of 10 nm.

A simple design is chosen for the test chips, of a proof mass that is supported by eight springs, and moves in plane (Figure 4-1), such that the distance between the proof mass, and the fixed tip of an optical fiber, can be varied. The 100 mm SOI wafer for the test chip is the same as the chip to be used for the Earth Sensor, with a device layer thickness of 100 microns, and handle layer thickness of 500 microns, and the buried oxide layer of 1 micron. The size of the proof mass is 10 mm x 0.5 mm, and the overall size of the test chip is 2 cm x 2 cm, for all test chips. The spring length (1 mm) and depth (100 microns) are the same as that for the Earth Sensor spring for all the test chips. The spring width is varied

Chapter 4: Fabrication of 1st Generation Earth Sensor

among the test chips. A different spring width is chosen for all the springs on a particular chip. Chips were designed with spring widths of 5, 10, 15 and 20 microns. Post-fabrication the different spring widths were measured to calculate the change in spring width from the design to the fabricated spring. Springs of different widths were fabricated to see if the change in width from the design to fabrication had any dependency on the width itself. Each chip has four grooves to hold an optical fiber in place (Figure 4-2 left). Each groove terminates at a different gap from the proof mass. Different optical fibers in these grooves have their tips positioned at different distances from the proof mass. Depending on this distance, different amounts of light get reflected back into the fiber; greater the distance, less the light that is reflected back into the fiber.

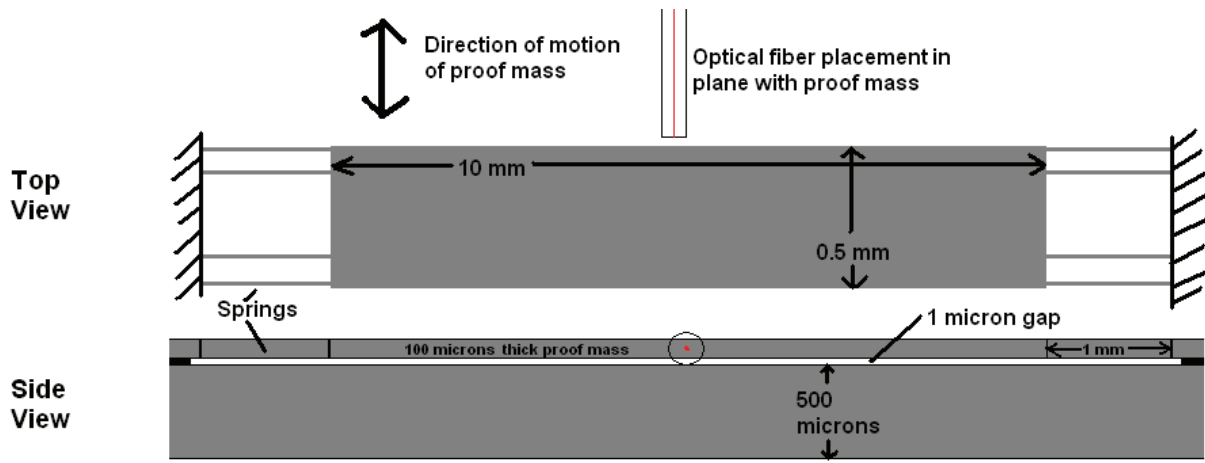


Figure 4-1 Test chip for 1st generation Earth Sensor. The proof mass is suspended from eight spring and moves orthogonally to the optical fiber placed in plane.

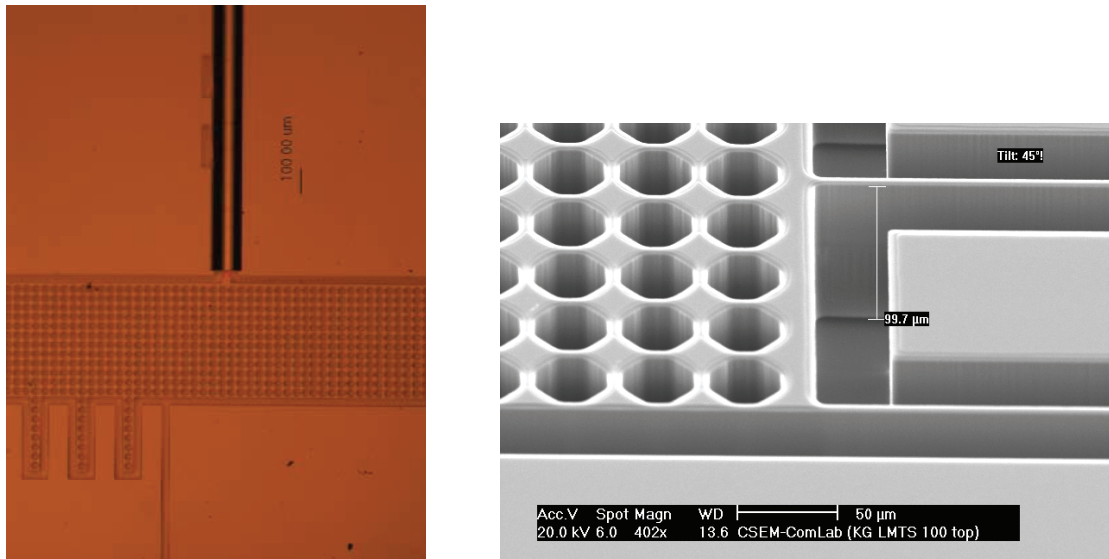
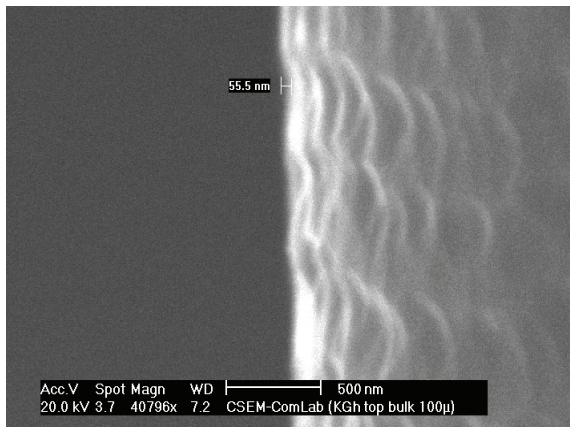


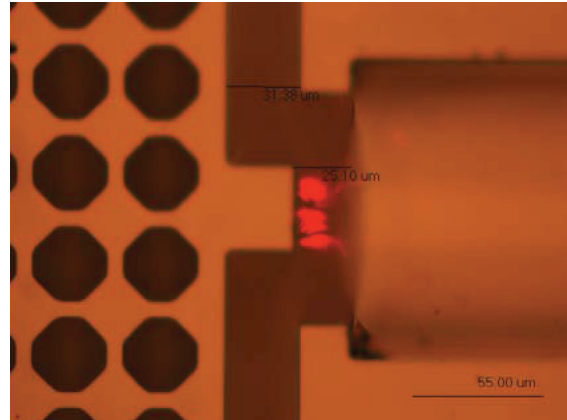
Figure 4-2 Left: Optical micrograph of proof mass with optical fibre integrated; Right: SEM photograph of proof mass with springs. The hexagonal holes in the proof mass are to allow HF vapour to enter and etch the oxide beneath the proof mass, so that the proof mass is released from the underlying Si layer

Chapter 4: Fabrication of 1st Generation Earth Sensor

The moving mass of the test chip was actuated by tilting the chip from -90 to +90 degrees (Figure 4-3 c) which changed the distance between the mass and the fiber tip. The resulting change in photocurrent was plotted to obtain an interferogram (Figure 4-3 d). Since the dimensions of the springs and the mass were known, the displacement due to changing gravity on the proof mass was calculated and plotted as the x-axis in the interferogram.

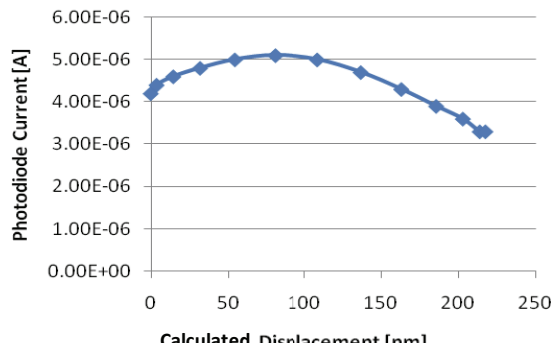


a) SEM picture of proof mass sidewall from which the light is reflected, showing nm scale roughness

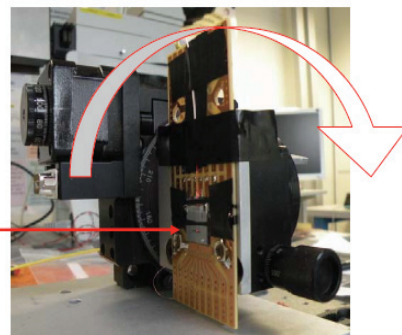


b) Optical micrograph of optical fiber tip aligned to proof mass, due to the nm scale roughness, light scattered from the proof mass is visible

Interferogram



d) Plot of current at the measuring photodiode recorded while the proof mass is moved by gravity as described in section c)



c) To displace the proof mass of the test chip, it is placed on a rotary stage that moves such that, at the start, the proof mass is pulled away from the fiber tip by 1g, and 180 degrees of rotation later, is pulled towards the fiber tip by 1g

Figure 4-3 a,b) Fabrication details, c) test setup and d) interferogram measured from test chip

4.1.1. Improvements from Test Device

Fabrication

The test chips were successfully fabricated, and a number of refinements for the process to make the Earth sensor were determined:

- The difference in the CAD drawing width for the spring and the width of fabricated spring is determined. Starting with a 15 microns wide spring in the CAD design of the test chip, the final width of the spring on the fabricated test chip was 12.5 microns. For the ES, a reduction in spring

Chapter 4: Fabrication of 1st Generation Earth Sensor

width from 15 to 12.5 microns would result in a spring 40% less stiff. The CAD design takes this factor into account for the spring.

- After the device and handle layers are etched by DRIE, the parts of the wafer are held together by the oxide layer, as seen in Figure 4-4. The oxide width has to be sufficient to provide enough strength to hold the wafer together, and in this case, the scale of the ES chip is in cm. The size of the ES proof mass (1 cm x 4 cm) is comparable to the size of the test chip (2 cm x 2 cm). For the test chip, the oxide width to hold the test chip to the wafer was insufficient, since some test chips broke off prematurely from the wafer. For the ES chips, the oxide width was made larger, so the ES proof mass and chip don't break off after DRIE.

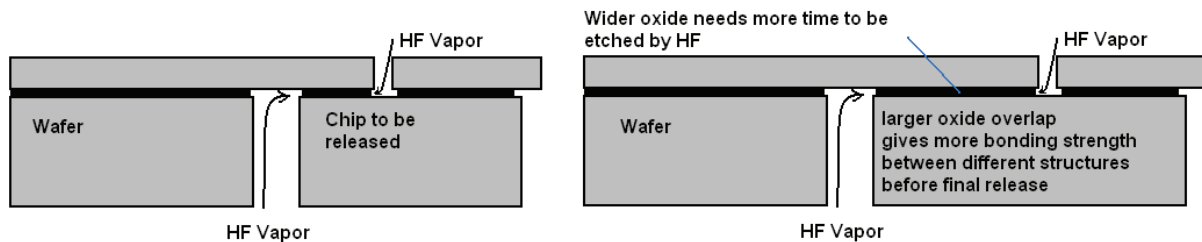


Figure 4-4 Diagram to show how the release time of a structure on an SOI wafer is controlled by the size of the overlap between the part to be released, and the wafer.

- The HF release process is critical to the ES fabrication. The ES has a two step release process, first the chip is released from the wafer, and then the proof mass is released. The total release time for the proof mass has to be longer than that of the chip. This is controlled by increasing the thickness of the oxide holding the proof mass to the chip (Figure 4-4). Even if the oxide is made wider, variations in the HF vapor etch rate can cause the proof mass to be released earlier. The variation in etch rate during HF release of the test chip is noted to estimate how much wider the oxide should be for the ES proof mass, and a margin of +100% variation in the HF etch rate is allowed for.
- Small clamps are etched into the side of the grooves to hold the optical fibers in place. The clamps designed to hold the optical fiber in place on the test chip were insufficiently stiff, and based on this, the stiffness of the clamps of the ES chip were increased, so that optical fibers could be successfully integrated into the test chip

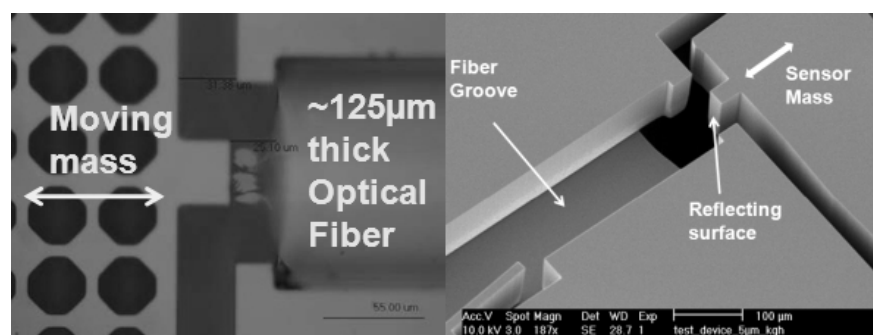


Figure 4-5 Optical Fiber Integration: The left image shows the fiber integrated into the test chips, laser light is seen reflecting from the mass back into the fiber, the right image shows the fiber mounting geometry in detail on the Earth sensor.

Optical Displacement sensing

Using an integrated optical fiber, sufficient light is reflected from the sidewall of the proof mass for an interferogram to be obtained (Figure 4-2 d). The fringe visibility (contrast between highest and lowest current of interferogram recorded on the photodiode) recorded on the test chip is lower than fringe visibility recorded from a wafer with a polished Silicon surface. This is due to the surface of DRIE etched silicon not being as smooth as polished Silicon and reflecting less light back into the fiber. SEM pictures of the sidewall from which light reflects back into the fiber show a roughness of around of 50 nm (Figure 4-2 a). To reduce this roughness, a post DRIE oxidation step is implemented in the ES chip fabrication. A thermal oxidation of 500 nm is done, and later the oxide is removed using HF vapor (Figure 4-6).

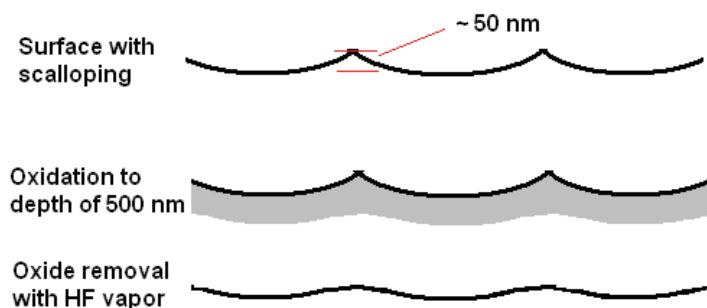


Figure 4-6 Steps to reduce sidewall roughness [48]

4.2.Fabrication Steps

The relatively large mass suspended by a very soft spring is susceptible to breakage of the spring at loads of just a few gravities. The motion of the mass must therefore be restricted to just a few microns, to limit the peak stress on the spring, so the sensor can tolerate routine handling. This restriction must be done as part of the fabrication process, prior to the mass being released. The major challenge solved was developing a new process flow that limits the motion of the 1×4 cm² long proof mass to 30 microns on all 3 axes, to make the device robust enough for testing on Earth. At the maximum allowed displacement, the peak stress on the spring is less than 25% of the yield strength of Silicon.

4.2.1. ES chip with proof mass

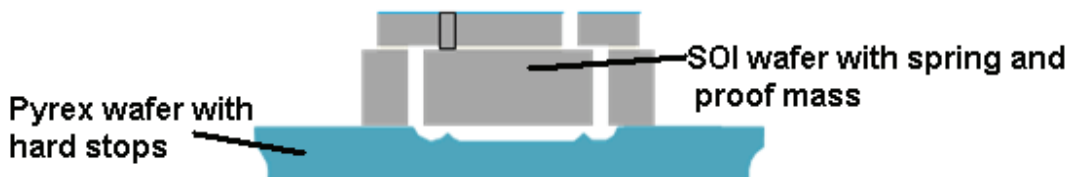


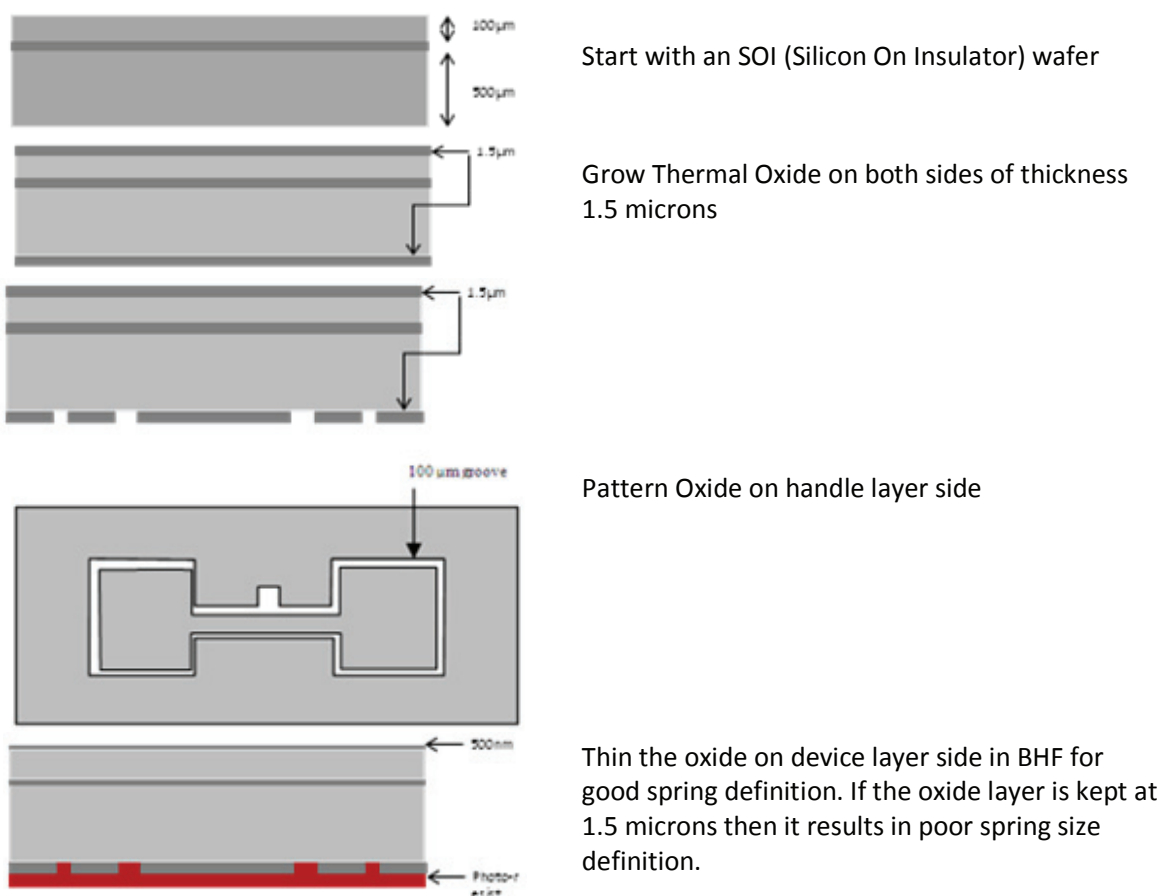
Figure 4-7 The ES chip fabrication process consists of 1) SOI chip with spring and proof mass 2) Pyrex chip with hard stops 3) assembly of the two chips before final release of the proof mass

Chapter 4: Fabrication of 1st Generation Earth Sensor

The fabrication process consists of three main parts. The first is the patterning and etching of the SOI wafer. The SOI wafer is comprised of two silicon layers (100 microns – called the device layer, 500 microns – called the handle layer) joined together by 1 micron of oxide between the layers. The first step is to grow a thermal oxide on both sides. Then a photolithography step is performed on the handle layer side and the grown thermal oxide is etched away. Then a DRIE step is performed to shape the Earth sensor mass.

Then the thermal oxide on the device layer side is thinned. Then a photolithography step is performed, followed by a second DRIE step to define the spring, grooves for the optical fibers, etc. The spring, fiber grooves, etc are etched in the device layer only. The Earth sensor mass is composed from both the handle and device layers of the SOI wafer. The stoppers to limit in-plane motion, and out of plane upwards motion, are etched into the device layer in this step.

After the DRIE etch is complete, the Earth sensor chip is freed from its wafer by placing it in HF vapor. But the Earth sensor mass is still attached to the chip by means of the oxide between handle and device layers.



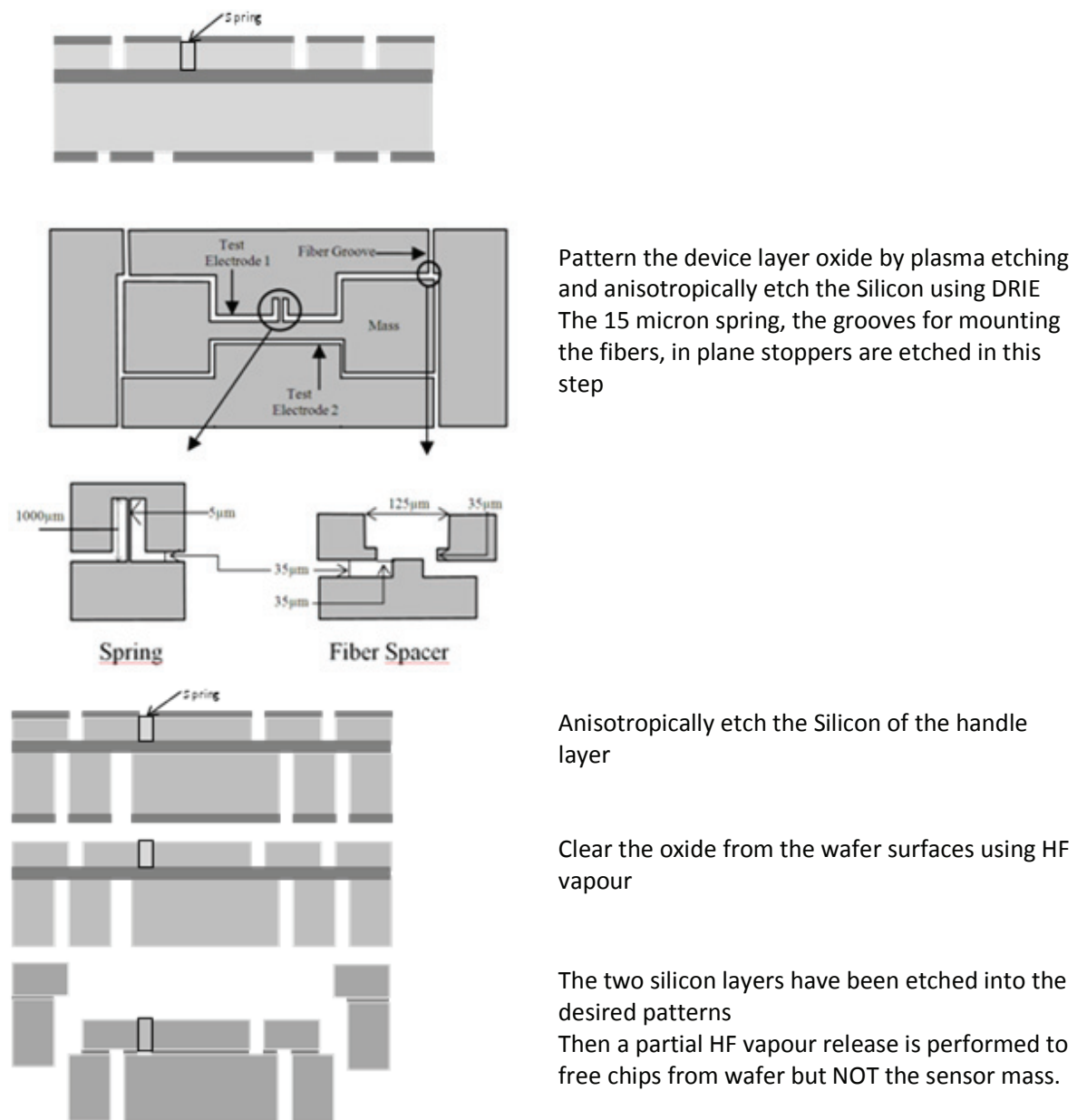


Figure 4-8 Etch of the SOI wafer and release

4.2.2. Pyrex chip fabrication steps

A Pyrex chip, bonded to the bottom of the SOI wafer, is used to limit out of plane downward motion of the Earth sensor mass. The first step is to deposit polysilicon on both sides of a 500 micron thick Pyrex wafer. A photolithography step is performed for the bottom side and a long etch is done in 20% liquid HF to define the edges of the chip. This is followed by a second photolithography step on the top side followed by a shorter etch in 20% HF to define the bumps and clearance to the underside of the Earth sensor mass. The polysilicon acts as an etch mask for the etching in 20% HF. Finally, after the etch is completed the polysilicon is removed.

Chapter 4: Fabrication of 1st Generation Earth Sensor

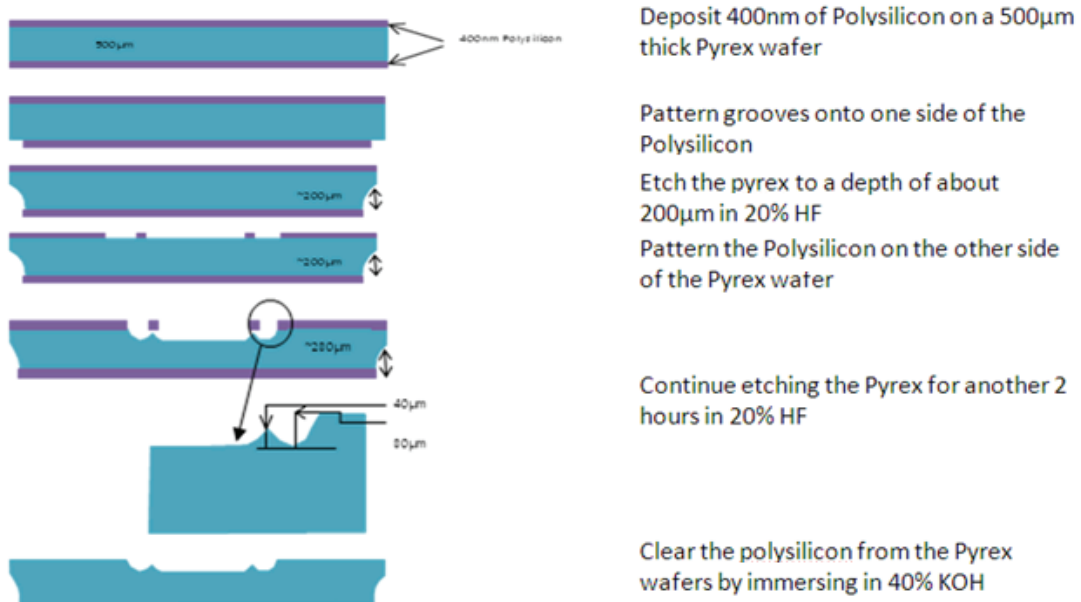


Figure 4-9 Fabrication of the Pyrex chip

4.2.3. Earth Sensor final assembly

Once the Earth sensor SOI and Pyrex chips are fabricated, they are bonded together using epoxy. This is done prior to the release of the Earth sensor mass, so that its motion is fully constrained before it is allowed to move freely. The final step is putting the bonded chip into HF vapor to etch away the remaining oxide holding the Earth sensor mass to the chip.

The complete fabrication process, from making the masks to a completed, released Earth sensor chip took nine months. There are twenty four individual steps. Some steps, such as the photolithography, and DRIE, were easily done. Other steps, such as the fabrication of the Pyrex chip, and especially the final HF release, took some time and numerous iterations to debug and develop.

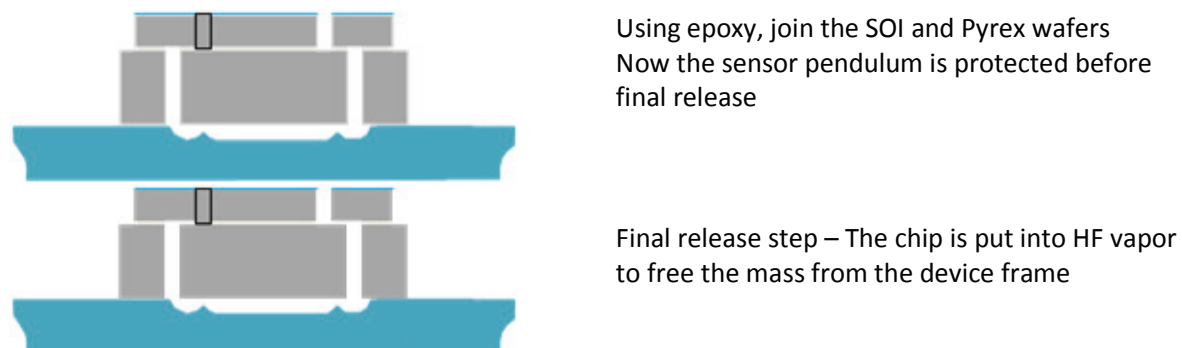


Figure 4-10 Bonding the Pyrex chip to the Earth sensor and final release

4.2.4. Stopper Design

The launch environment for a spacecraft typically has a large amount of vibration depending on the launcher used [60]. There are shocks due to events such as firing of pyros during stage separation, and engine start. At high shock, the displacement due the shock results in bending stress on the spring, especially at the spring anchors [61]. Devices with higher resonant frequencies can tolerate greater bending stresses before the spring fractures [61]. For the MEMS ES the resonant frequencies are limited to a few Hz as described in Chapter 2. If the bending stress exceeds the maximum stress that can be tolerated by the spring, the device will fail. The bending stress on the ES spring can be limited by limiting the displacement of the proof mass. A common method to limit the maximum displacement of the proof mass by incorporating hard stops into the device design, to constrain the motion of the proof mass along multiple axes. Another approach to limit the effects of vibration is to have high damping. The MEMS ES requires a Q-factor in the hundreds to achieve the required signal to noise ratio, so the damping in vacuum should be quite low.

Strategies have included incorporating additional encapsulation wafers to constrain out of plane motion [62], or additional processing steps to define out of plane stops [65], and using in-plane structures to limit the lateral motion of the proof mass [63]. The in-plane structures do not require additional process steps to be implemented. For some applications, the nature of the design can serve to limit the out of plane displacement of the device, such as a teeter-totter structure that uses the substrate to limit its out of plane motion [64]. The impact of the proof mass on the hard stops can result in debris and secondary shocks, which can also damage the device to the point it is unusable even if the spring is intact. Methods for mitigating the effects of shock and vibration that can reduce debris generation, include non-linear stops that reduce the jerk on impact [67], coating the hard stops with soft materials [61], and flexible stops [68]. For vibration isolation, methods have been proposed that implement a platform which is a low pass mechanical filter to damp out higher frequency vibrations [66].

For the MEMS ES, the displacement has to be limited along all axes to a few microns. This is done by combining one of more methods described in [62-65] to keep the fabrication complexity manageable, and increase the yield per wafer, by minimizing the total die size of the MEMS. More advanced methods [61, 66-68], that either requires increased fabrication complexity, or additional on-chip areas to implement, are not used in the design of the MEMS ES. For the purposes of a MEMS chip that can be easily handled in the lab and tested on Earth, and to prevent stiction, rudimentary hard stops, which limit the motion of the proof mass are sufficient. The bulk fabrication process of the MEMS ES puts the hard stops in place prior to the release of the proof mass, so that the mass is fully encapsulated prior to the oxide being etched away.

The proof mass suspended by the compliant spring is prevented from moving more than 30 microns on all axes to prevent it from breaking off. The motion in plane is constrained by etching stoppers around the proof mass.

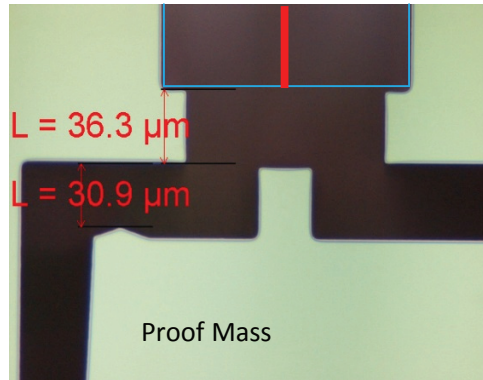


Figure 4-11 Optical micrograph of fibre mounting area of chip; In-plane stoppers that restrict proof mass motion to 30 microns, and in this image, prevent it from hitting the fibre tip. A drawing of the eventual position fibre tip is inserted into the image for reference

The motion upwards out of plane is constrained by having the device layer of the chip overhang the handle layer of the proof mass. The clearance between the chip device layer and the proof mass handle layer depends on the oxide thickness (1 micron) and the sag of the proof mass due to gravity. The sag is 1.5 micron for the proof mass suspended from a 15 micron wide spring. So the total clearance is 2.5 micron (1 micron + 1.5 micron) for the proof mass.

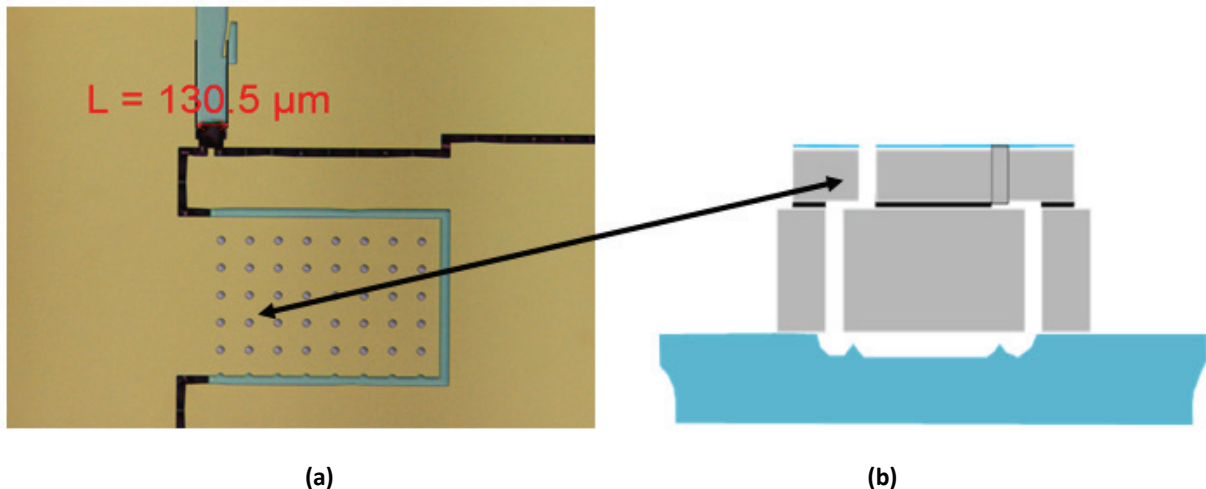


Figure 4-12 a) Top view of the device layer overhang to prevent out of plane motion; b) Side view of the chip showing overhang and the clearance to the proof mass

Downwards motion out of plane is prevented by bonding a Pyrex chip with spikes to the bottom of the chip. The height of the spikes determines the clearance to the proof mass. By controlling the etch time of the Pyrex, the height of the spikes can be controlled. A 30 micron clearance is maintained between the Pyrex spikes and the proof mass.

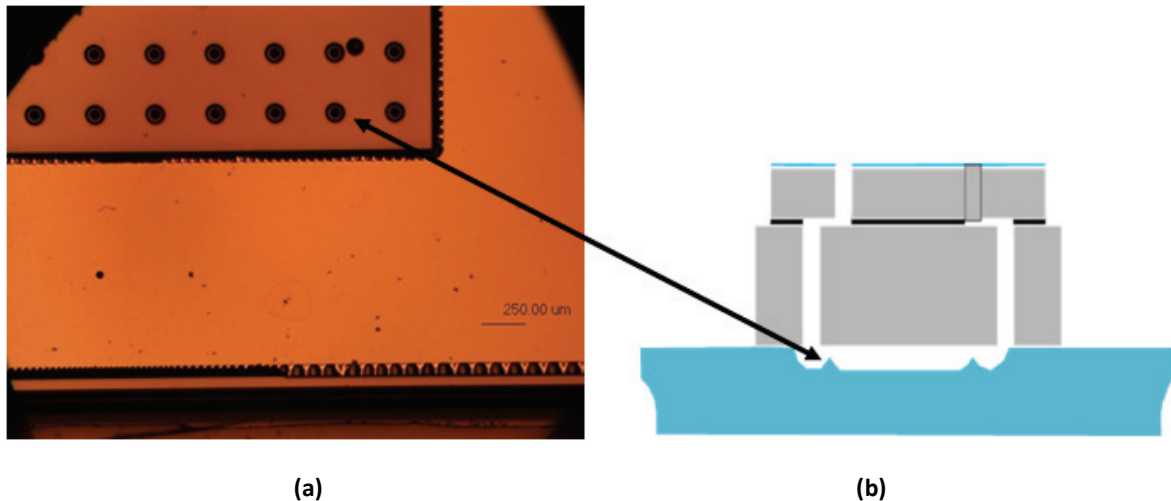


Figure 4-13 a) Top view of the pyrex chip showing a row of spikes; b) Side view of the chip showing the spikes and their clearance to the proof mass

4.3. Conclusion

At the end of the fabrication process, chips that could be used for testing were obtained (Figure 4-14). The yield was quite poor, with only two usable chips out of a potential eighteen. The greatest numbers of chips were lost during the final release step, due to problems with HF vapour release.

The HF vapour release process is further discussed in Section 7.3, and a method to control the etch rate variation is described.

Chapter 4: Fabrication of 1st Generation Earth Sensor

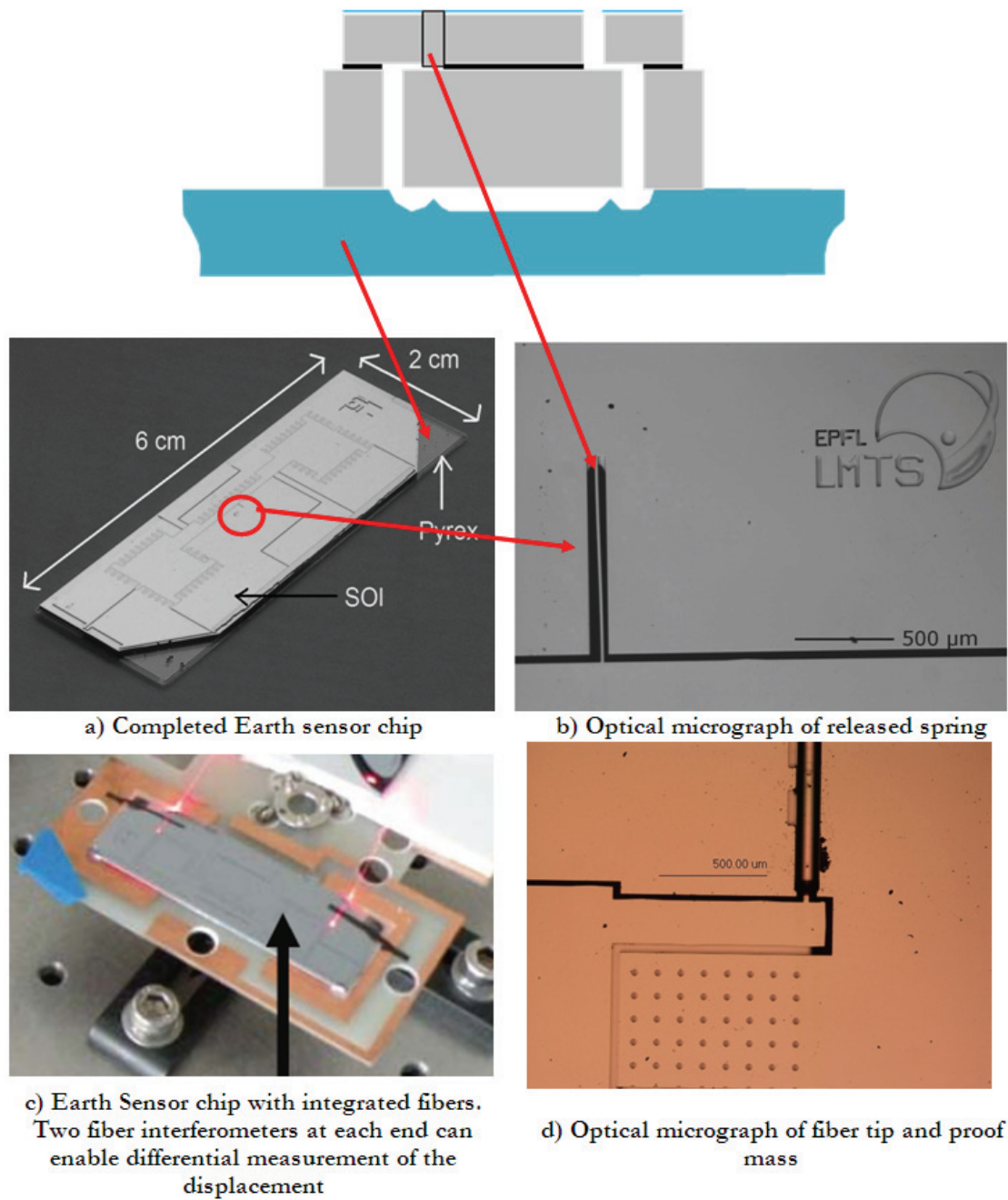


Figure 4-14 Different views of the completed ES chip showing the optical fibres integrated into the chip

4.3.1. Large variation in HF etch rate

Figure 4-15 shows a diagram of the setup used for HF vapor etch of the oxide that holds different structures of the ES chip together. The wafer is mechanically clamped around its edge to a chuck that has heating wires built in. The other surface of the wafer is open to HF vapor. The etch rate due to HF is exponentially dependent on the temperature of the oxide it is etching [ref. Idonus]. The temperature of the wafer is adjusted for the desired etch rate.

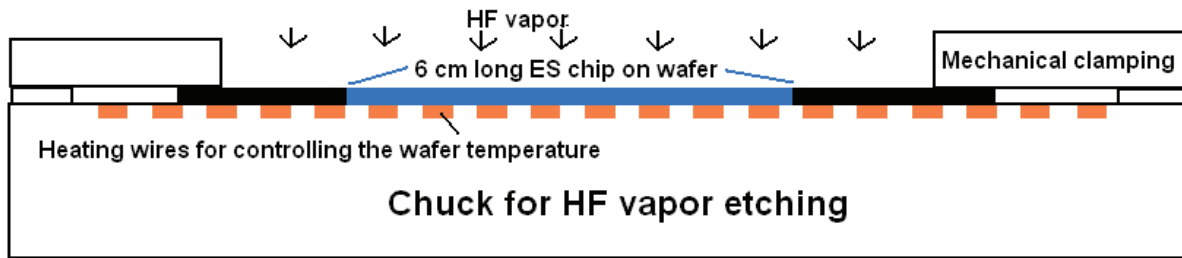


Figure 4-15 Setup for HF vapour etching

Previously, it was discussed that the proof mass of the ES chip should have a longer etching time for the oxide holding it to the ES frame, as compared to the etching time of the oxide holding the whole ES chip to the wafer. So the chip would be released, then the bottom pyrex hard stops would be bonded, and then the proof mass would be released. A 100% variation was allowed for in the etch rate, while deciding how much oxide should be etched to release the proof mass.

In practice, a variation of up to 300% was observed for the HF vapour release, between different sections of the same ES chip. This frequently resulted in the oxide holding the proof mass getting completely etched at the same time that the oxide holding the chip got etched. Without, the Pyrex chip underneath, and little or no oxide holding the proof mass, it often broke away.

This is probably due to non uniform heating of the ES chip. Unlike other MEMS devices, whose dimensions rarely exceed 1 cm, the whole ES chip is 6 cm long. The clamping of the wafer onto the chuck does not ensure uniform contact over the length of the chip. Variations of 2-3° C in temperature can result in the observed variation in etch rates.

To obtain chips that could be tested, the chips were released from the wafer without waiting for the complete oxide to be etched, by applying mechanical shear force. This was done so that the proof mass could have more oxide holding it to the ES chip frame. Then the Pyrex chip with the hard stops was attached to the chip using epoxy, and the HF vapour release was resumed. The downside of this approach was that the Pyrex chip was exposed to the HF vapour for much longer than initially anticipated.

Pyrex is composed of ~ 80% silicon dioxide and is also etched by HF, and the etching of Pyrex was expected during the release procedure in HF, but for a shorter time. Based on photos (Figure 4-16), it appears that some of the etching products from the Pyrex, such as the metal-fluoride salts and water, condensed onto the exposed silicon surfaces, causing stiction between them.

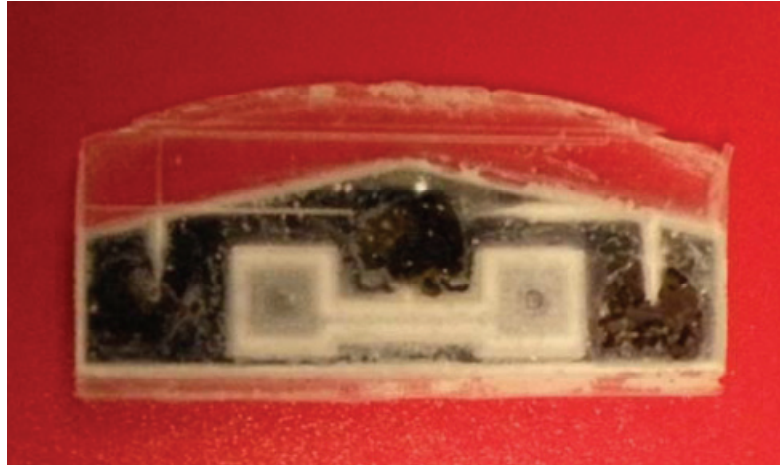


Figure 4-16 Backside picture after final HF vapour release step. The Pyrex is affected and there is contamination of the silicon part

Despite the stiction problem, we were able to fully fabricate and release the masses of two chips. Two chips were released by periodically interrupting the HF vapor release every 10-15 minutes and putting the chip into oxygen plasma, in an attempt to remove the water that accumulates on the silicon surfaces.

To increase the yield, in future fabrication runs, the following steps are needed:

- All hard stops need to be integrated onto the ES chip much earlier in the release process, ideally before the chip is released from the wafer.
- Pyrex was chosen due to the possibility of anodic bonding with Silicon. It is clearly not suitable, and any material chosen for the hard stops needs to be highly resistant to HF vapor etching. Silicon itself is a good alternative for all the hard stops.

These improvements are implemented in the fabrication process for the 2nd generation sensor, which is described in Chapter 7.

Chapter 5

Testing of 1st Generation Device

The Earth Sensor is designed to measure nm-scale displacements in microgravity. Though it is not possible to create microgravity conditions in the laboratory, the aim is to create a test setup that is capable of producing nm-scale motion of the proof mass in 1 g, in the direction that the Earth Sensor proof mass is expected to move due to GGT.

5.1. Testing Goals

- The proof mass of the sensor is 4 cm x 1 cm, and by design, is surrounded on all sides by hard stops. It has a clearance of approximately 2.5 microns before it touches a hard stop. It is necessary to develop a method to align the chip within 0.04° of tilt with respect to the XY plane (Figure 5-1) so the proof mass is suspended from the spring, and not touching any hard stops.
- Once the chip is aligned, establish a method to produce a displacement in the order of nm for the proof mass. The nm scale displacement of the proof mass is necessary in the direction that the displacement sensing method can detect. Due to the method used to measure the displacement, even if the total displacement of the proof mass is greater than nm, only the motion in the direction of the optical fiber tip will be registered.
- Verify whether the displacement sensing method of the Earth sensor, using the integrated fiber interferometer can be used to detect this motion.
- Measure the dynamic response of the sensor in air, and in vacuum. (Contingent on success of preceding goals).

5.2. Test Setup

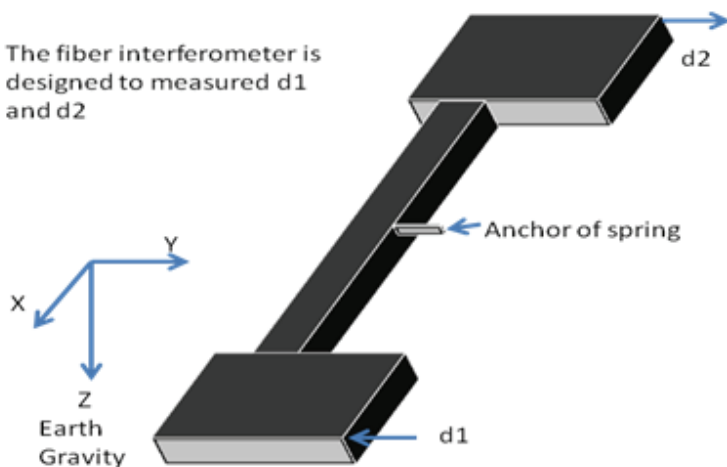


Figure 5-1 ES proof mass orientation for test; proof mass should be in XY plane, the Z axis is normal to the surface of the Earth

Chapter 5: Testing of 1st Generation Device

Figure 5-1 shows the desired alignment of the ES chip for test. Ideally, the sensor proof mass is flat in a plane orthogonal to the direction of the Earth's gravity. In this position, it should be hanging only from the spring, and not touch any of the hard stops.

Once the ES proof mass is aligned in this position, an actuator with multiple piezos is used to produce the nm scale displacement that is needed to test the displacement sensing. As shown in Figure 5-2 the ES chip is mounted on the piezo actuator. A 0-30 V ramp voltage with a period of 100s is applied to the piezos only on one side of the actuator which causes a see-saw tilt of 0-0.014° of the proof mass in the XZ plane. This motion also produces nm-scale motion of the sensor in the direction of Y axis, which changes the distance between the proof mass and the fiber tip. The resulting change in the photocurrent is recorded.

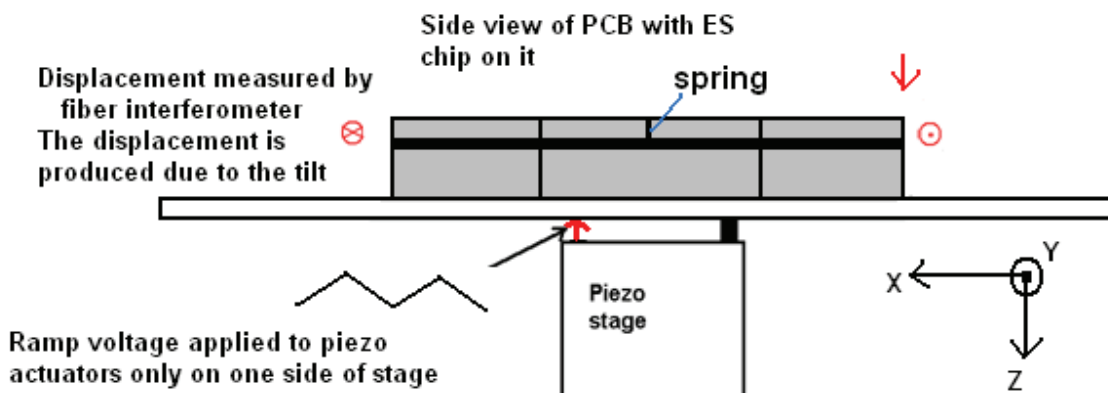


Figure 5-2 Ramp voltage applied to piezo actuator that produces a motion of the proof mass along the Y axis

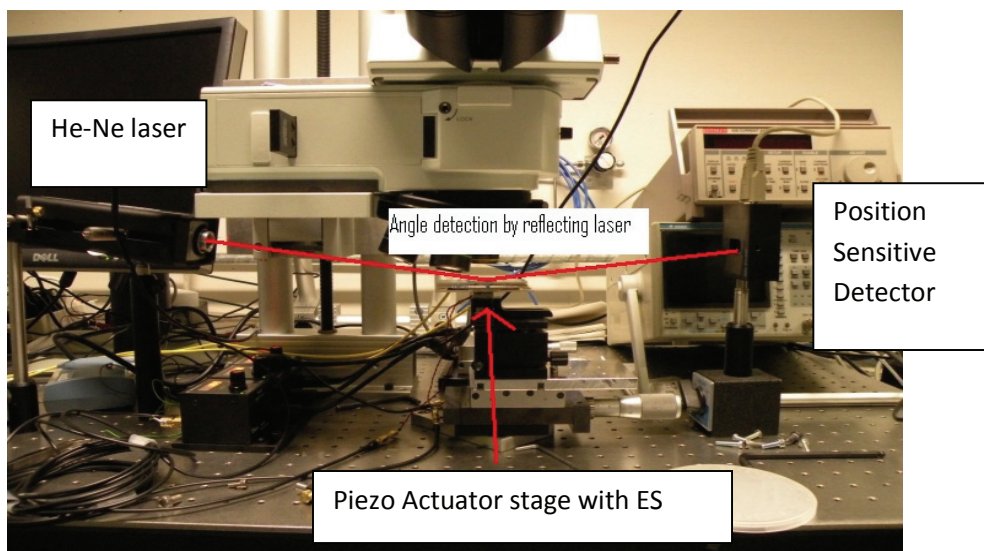


Figure 5-3 Monitoring the tilt angle of the piezo, which can be used to determine displacement of the proof mass; the path of the laser is indicated using a red line

To estimate the motion of the proof mass due to the motion imparted by the piezo stage, we use a separate He-Ne laser that reflects off the polished silicon surface of the Earth sensor chip and onto a Position Sensitive Detector (PSD) as seen in Figure 5-3. When the chip tilts, the position of the reflected laser spot on the PSD shifts. By recording the movement of the reflected laser on the PSD, and measuring the distance between the ES chip and the PSD, we can determine the angle through which the ES chip is tilted due to the 0-30 V ramp voltage. Then by simulating the displacement of the proof mass due to this tilt, using ANSYS, the magnitude of the displacement can be estimated.

The change in the angle of the ES chip is measured to be 0.014°. The ANSYS simulation predicts that the mass moves by about 21 nm relative to the fiber tip (Figure 5-4).

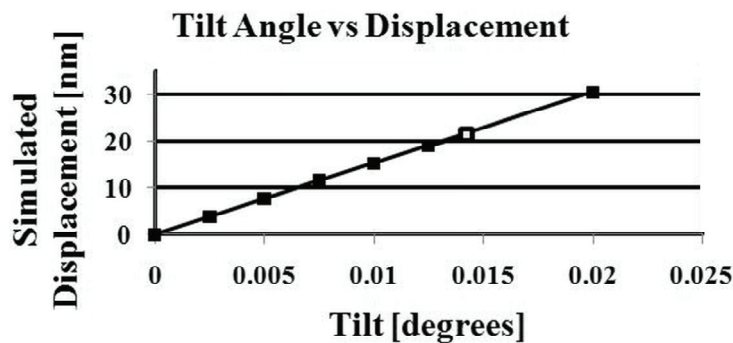


Figure 5-4 FEM simulation of the displacement of the sensor mass due to tilting by the piezo platform

5.2.1. Alignment of ES chip

To be able to test the ES in the manner described above, achieve this, the plane of the proof mass has to be adjusted carefully. If the alignment has too large an error from the position described in Figure 5-1, the proof mass will touch a hard stop, as shown in Figure 5-5. The maximum allowed error in alignment is 0.04°. This value is obtained using ANSYS modeling of the ES chip.

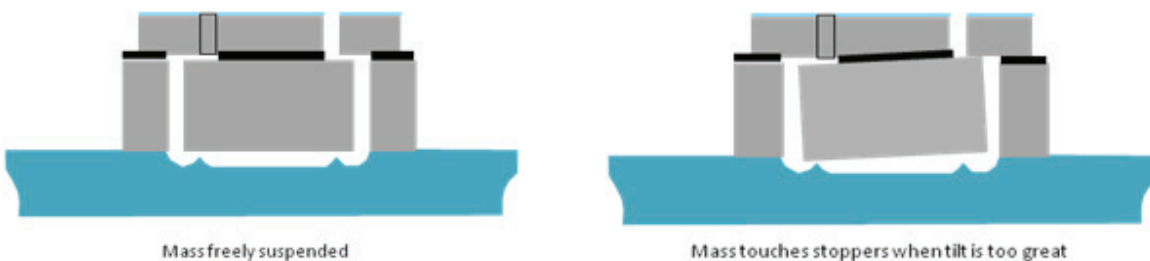


Figure 5-5 Effect of excessive tilt on the Earth sensor mass; the mass touches the stoppers

Chapter 5: Testing of 1st Generation Device

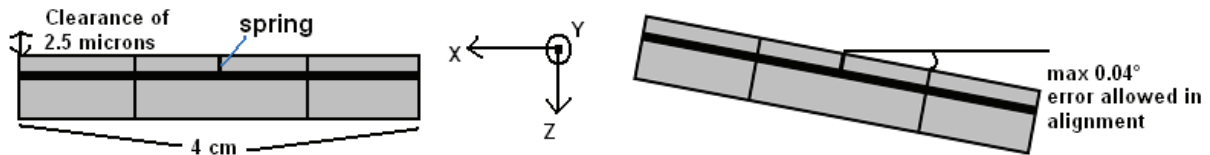


Figure 5-6 Diagram of allowed error in alignment of ES chip

Due to the $1 \times 4 \text{ cm}^2$ mass and the soft spring, very small tilts, of order a few tens of millidegrees, can cause the mass to bend a few μm out of plane, and touch one of the constraining elements. Figure 5-6 shows the maximum error in alignment before the proof mass touches one of the hard stops

To align the chip, the assembly of the chip with the piezo actuator, is placed on a stepper motor (Figure 5-7). The stepper motor is capable of 0.00125 degree steps, which is well within the $\pm 0.04^\circ$ alignment required for the ES chip.

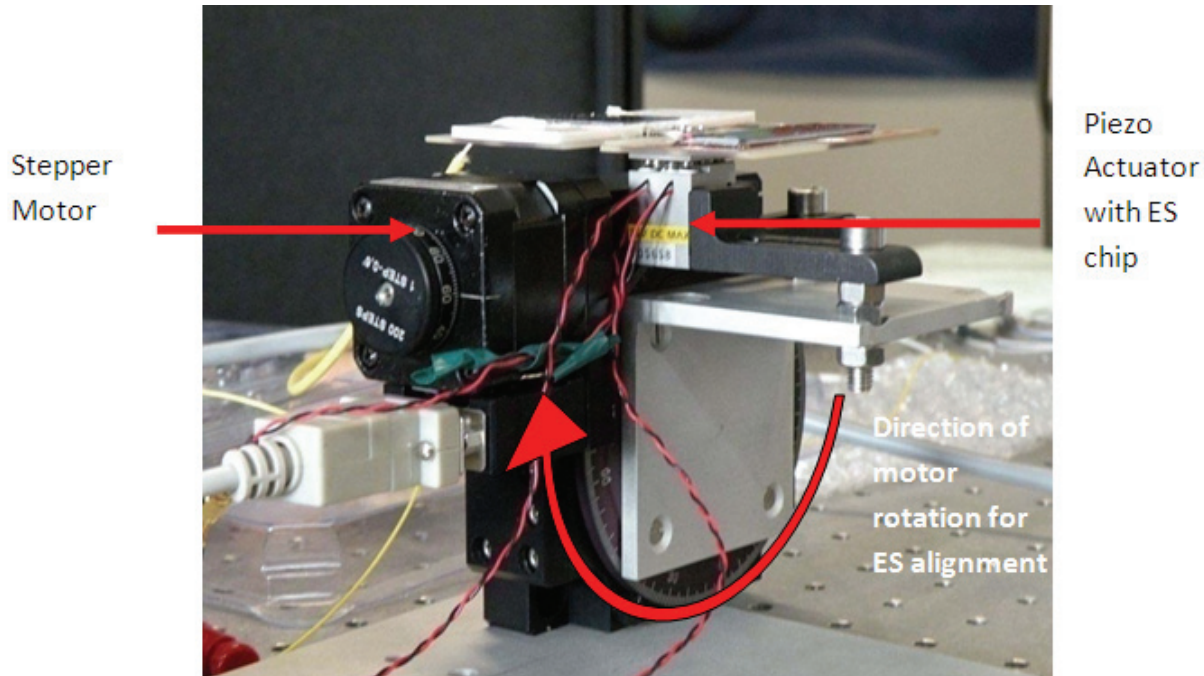


Figure 5-7 Test setup: Piezo tilt stage with Earth sensor chip mounted on stepper motor stage

The absolute angle of the ES chip with respect to the normal to the Earth's surface cannot be determined with millidegree accuracy. The ES chip is mounted on a PCB, which is screwed down onto the piezo actuator which is in turn bolted onto the stepper motor. The stepper motor position at which the proof mass is expected to be freely suspended is not known. The following procedure is used to align the chip:

Chapter 5: Testing of 1st Generation Device

1. Adjust the initial position of the stepper motor manually as close as possible to the desired alignment of the ES chip
2. From this position rotate the ES chip by -0.5 ° using the stepper motor.
3. Apply a ramp voltage to the piezo actuator starting from 0 V, and ramp up to 30 V, and then back down to 0 V. The photocurrent from the measuring and reference photodiodes of the interferometer is recorded while the voltage is ramped up and back down.
4. From the photocurrent measurements, determine if the proof mass was moving while the voltage was ramped up and down.
5. If the proof mass is not moving freely, then using the stepper motor, rotate the ES chip by +0.00125°.
6. Repeat steps 3, 4 and 5 until an interferogram is obtained that shows the proof mass is freely moving

To control the stepper motor, supply the voltages needed for the piezo actuator, and record the photocurrent, a PC with Labview is used. A diagram of the complete setup is seen in Figure 5-8.

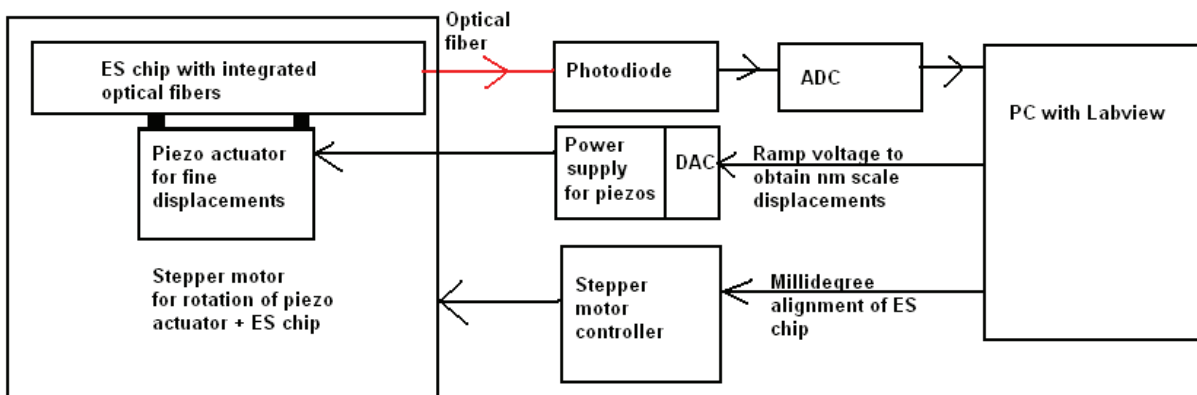


Figure 5-8 Complete setup for alignment and test of ES chip with fiber interferometer

5.3. Test Results

A large number of photocurrent readings were obtained while the ES proof mass was moved from 0 to 21 nm and back for various positions of the stepper motor. Due to the limited range in which the ES proof mass does not touch any hard stop, very few sets of photocurrent measurements showed a freely moving proof mass. The criteria to decide whether the proof mass is moving freely during a particular measurement, is whether the measurement during the 0-30 V ramp, roughly matches the measurement during the 30-0 V ramp. The piezo actuator is operated in open loop mode, so some allowance is made for possible piezo hysteresis and non-linearity. Figure 5-9 shows an measurement obtained by applying ramp voltage to the piezo actuator and moving the proof mass by 20 nm.

In the graph, the current measurement initially decreases, then increases, for a monotonic change in the displacement of the proof mass from 0 to 21 nm. This data is selected since it shows that the change in

Chapter 5: Testing of 1st Generation Device

photocurrent represents an interferogram. The same is observed in reverse when the displacement is decreased back to 0. A laser with a wavelength of 635 nm is used for the interferometer, so the period of a resulting interferogram is 317.5 nm. Since the displacement of the proof mass is only 20 nm, only a section of a complete interferogram period is seen. The noise in the measured photocurrent corresponds to being able to measure the displacement with an accuracy of approximately 1 nm.

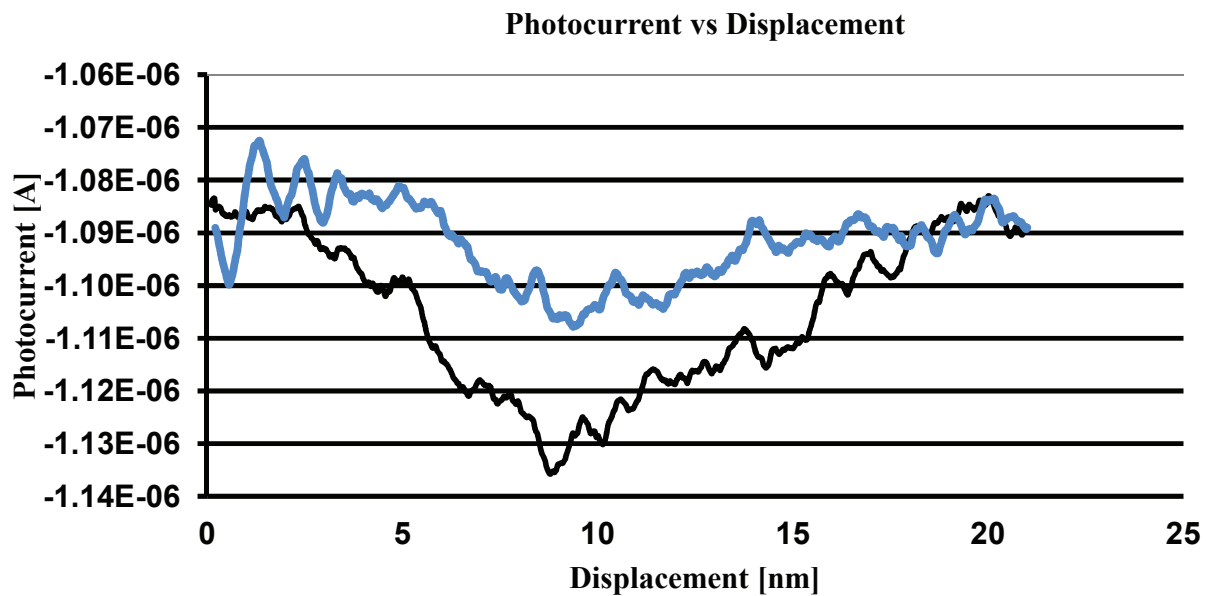


Figure 5-9 Photocurrent at measuring photodiode of the fiber interferometer of Earth sensor, as the voltage supplied to the piezo actuator is increased (in black), resulting in 20 nm of displacement between the proof mass and fiber tip. Then the voltage is decreased, and the photocurrent records the change in the displacement back to the starting position (in blue)

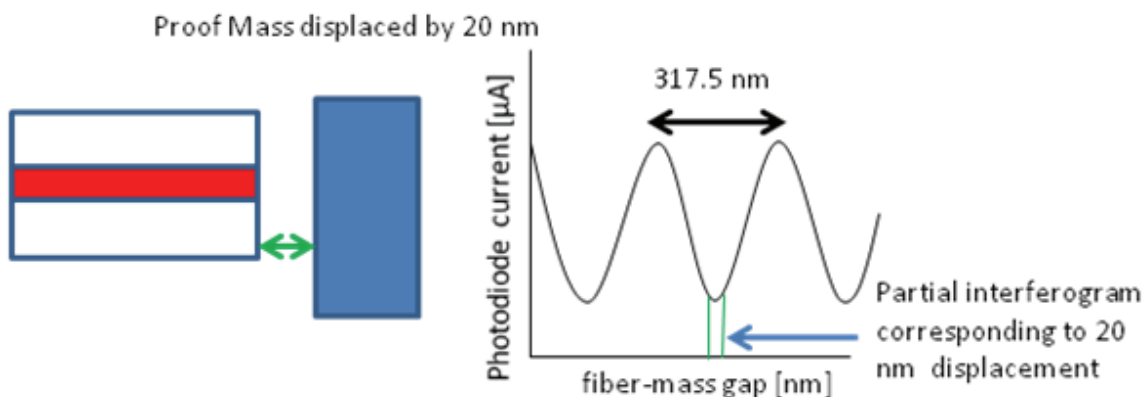


Figure 5-10 Part of the interferogram measured in Figure 5-9

5.3.1. Discussion of Test Results

For the 1st Generation ES, it was possible to test the displacement sensing. However, the results presented were very difficult to reproduce, since the alignment of the ES chip was extremely challenging. Typically at the start of the alignment process, the proof mass is touching one or more hard stops. The amount of force required to ensure that the proof mass comes unstuck typically resulted in the proof mass moving a large amount and touching the hard stops on the other side of the sensor. So obtaining a freely moving proof mass was a trial and error process. Sometimes the small shock due to the stepper motor movement was sufficient to dislodge the proof mass such that it did not impact the hard stops on the other side, and in this case testing the displacement sensing could proceed. Further testing, such as measuring the dynamic response of the sensor was not possible, since the proof mass touches the hard stops if a step input is applied via the piezo actuator.

The noise in the displacement measurement corresponds to approximately +/- 0.5 nm. This, in conjunction with differential measurement, will give an accuracy of roughly +/- 22.5 ° in measuring the angle of the proof mass makes with the nadir. This is an order of magnitude worse than the accuracy needed to measure the angle to the nadir with an accuracy of +/- 2 °.

5.3.2. Sources of Noise

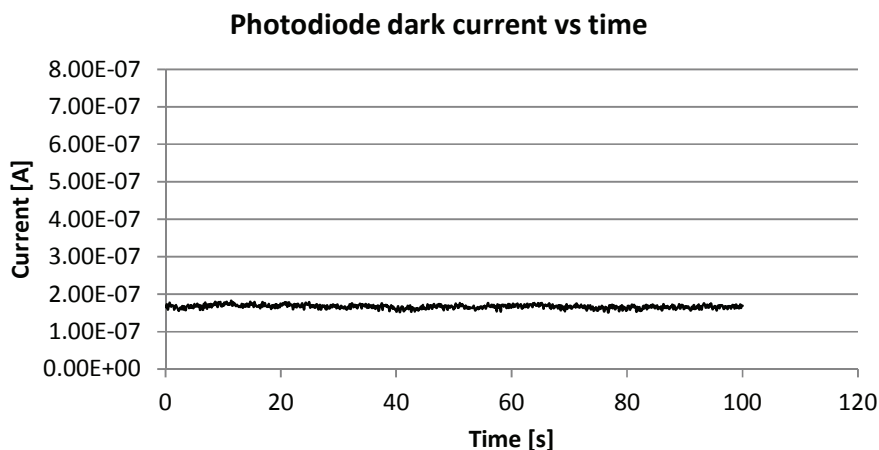


Figure 5-11 Dark current of sensing photodiode diode measured over time

As seen in Figure 5-11, the photodiode used to measure the interferogram photocurrent has a peak to peak noise of the order 1×10^{-8} A in the dark current, well below the change in photocurrent that will result from a displacement due to GGT arising from a +/- 2 ° angle with the nadir. Other sources of noise are discussed which can result in the observed noise level.

Ambient vibrations

The experiment is mounted on an optical bench. The bench can filter out ambient vibrations with a 3 dB frequency of around 5 Hz. The designed fundamental frequency of the ES is 1.4 Hz. So it is possible that

low frequency ambient vibrations, such as a person walking in an adjacent corridor, can be coupled into the proof mass of the sensor.

The interferometer is constructed from individual optical components such as fibers, beam splitters and photodiodes. These are connected together by mechanical connectors. Any vibration transmitted into the connectors can result in noise in the observed photocurrent.

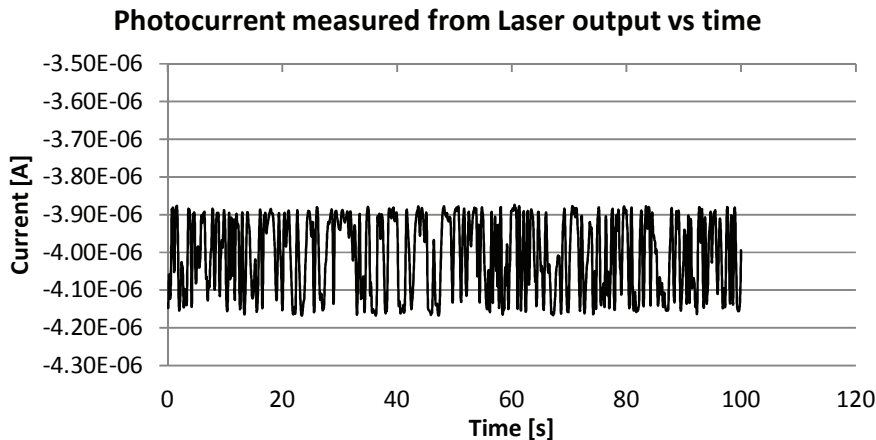


Figure 5-12 Photo current directly measured from the laser over time. The p-p noise of 2.5×10^{-7} A can be due to ambient vibrations affecting the mechanical connectors between individual interferometer components.

Figure 5-12 shows the direct output from the laser measured over time. The p-p noise of 2.5×10^{-7} A can be due to ambient vibrations transmitted to the connectors. Tightening the connectors helps reduce, but does not eliminate this noise.

Proof mass sidewall roughness

As shown in Chapter 4, the proof mass sidewall has a roughness on the order of many nanometers. For the see-saw motion used to displace the proof mass, some lateral motion can be expected as well. A lateral movement can result in a change in the local topology of the surface from which the light is reflected back into the fiber. This change will result in the light reaching the fiber travelling for a different distance, and the resulting phase change will show up as a noise in the observed photocurrent.

5.3.3. Electrostatic Actuation of Proof mass

A planned method to displace the proof mass relative to the fiber tip was by using electrostatic force.. Figure 5-13 shows the locations of electrodes on the fabricated ES chip, and the way a DC voltage could be applied to obtain a displacement of the proof mass. The sidewall of the proof mass and the sidewall of the electrode serve as the two plates of a parallel plate actuator for electrostatic force. Many attempts were made to apply a voltage to these electrodes to obtain a displacement of the proof mass. Instead of the expected displacement of the order of microns, no displacement was observed, even for voltages up to 100 V.

Chapter 5: Testing of 1st Generation Device

The electrical connections to these electrodes from the PCB were made using wire bonds to the silicon surface of the ES chip. It is possible that the connections formed Schottky contacts on the silicon surface, due to which no actuation was possible. In future fabrication runs, an aluminum deposition step, followed by an anneal will be implemented to ensure ohmic contacts to the on-chip electrodes.

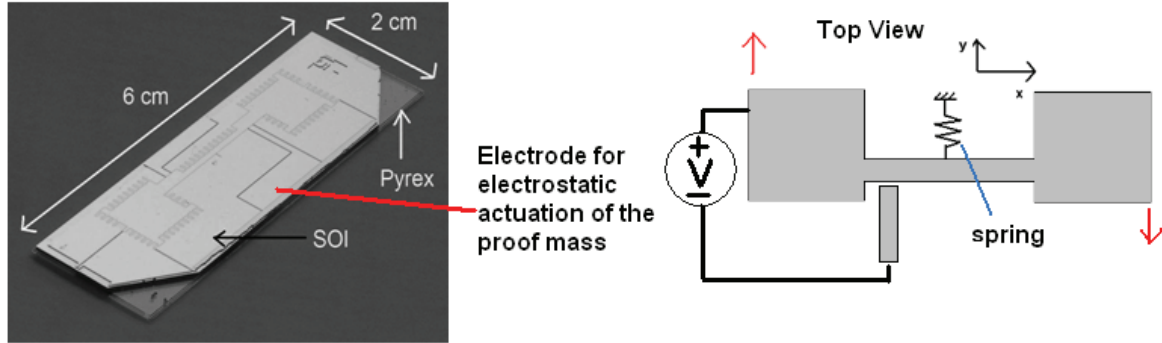


Figure 5-13 Left: Location of electrodes for electrostatic actuation of proof mass on ES chip; Right: DC voltage is applied between the proof mass and the on-chip electrodes

5.4.Conclusion

- A proof of concept ES, which is based on measuring the GGT, was designed, fabricated and tested within the 15 month frame of the ESA contract.
- A method using a piezo actuator to test the displacement sensing of the ES chip, by reproducing the nm scale displacements expected in micro-gravity in a 1g environment was implemented.
- The tests that could be performed on the sensor were quite basic, due to a very challenging requirement for the test setup. The test results were not readily reproducible due to the difficulty in placing the proof mass such that it was freely suspended.
- Through trial and error it was possible to have the proof mass freely suspended and measure the photocurrent due to displacement of the proof mass. There is considerable noise in the measurements, and the accuracy of this sensor is roughly +/- 22.5 °.

In the next chapter, the design of the improved 2nd generation sensor is presented, that learns from, and resolves the issues encountered in the test and displacement sensing of the 1st generation sensor.

Chapter 6

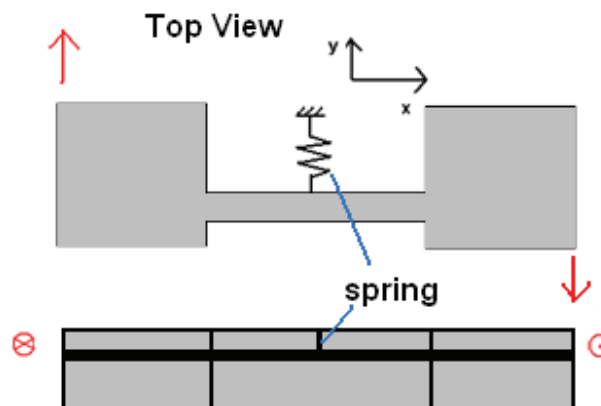
Design of 2nd Generation Earth Sensor

This chapter describes the design of the 2nd generation Earth Sensor. The design takes into account the problems encountered during test of the 1st generation sensor, and the spring design is modified to enable easier alignment for test.

At the conclusion of the work for the 1st generation sensor, ESA indicated that an electronic readout is much more desirable than an optical one, since a more compact instrument is possible, if no laser and optical fibers are required. Also, electronics can work within a wider temperature range, (with a measurable drift that can be compensated), unlike a laser, which has to be kept within a relatively narrow temperature band for operation. The 2nd generation sensor is designed to sense displacement by measuring a change in capacitance.

Figure 6-1 shows the change from Generation 1 to Generation 2, and the details behind the changed design is discussed in the following sections of the chapter. The sensor design is significantly modified. Instead of a proof mass suspended by a single spring, whose displacement is sensed in-plane, the proof mass of the new design is suspended from two springs, and the displacement is sensed *out-of-plane* by differential capacitive sensing

Schematic of 1st Generation Earth Sensor : Single spring with proof mass comprised of two layers



Schematic of 2nd Generation Earth Sensor:
Double springs with proof mass and springs in single layer

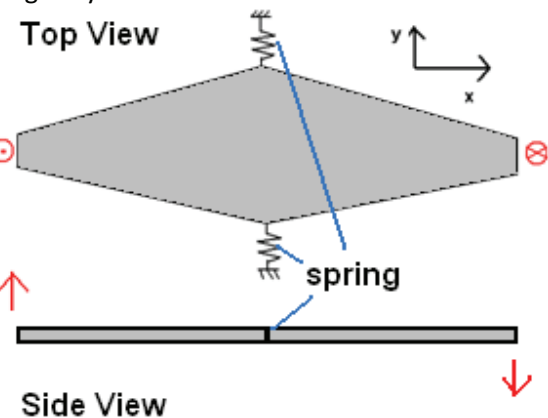


Figure 6-1 Comparison of 1st and 2nd generation ES designs. The arrows indicate the direction of displacement due to GGT, and measurement of the displacement.

The sensor should be able to operate on a satellite that is tumbling. An ES chip on a tumbling satellite will have a centripetal force on the proof mass of the sensor. This centripetal force can be orders of

magnitude larger than the GGT. The design of the proof mass and springs to minimize the error due to centripetal force is discussed. Section 6.2.1.1 shows that using an additional fabrication step, the error due to satellite spin can be reduced to within the same order of magnitude as the displacement due to GGT, and this error can then be compensated for.

Capacitive displacement sensing for accelerometers is typically done by designing a custom electronic circuit. For the Earth Sensor, in the time frame of this thesis, there were no resources to develop a custom circuit for displacement sensing. Some commercially available capacitance sensing components were compared, and the capacitive displacement electrodes of the sensor were designed for the chip best suited for the measurement.

6.1.Improvements from 1st generation

6.1.1. Proof Mass Alignment for test

To test the sensor on Earth, the chip has to be aligned such that the proof mass is not touching any of the hard stops, and is freely suspended. The attempts to do this were difficult and not repeatable for the 1st generation Earth sensor.

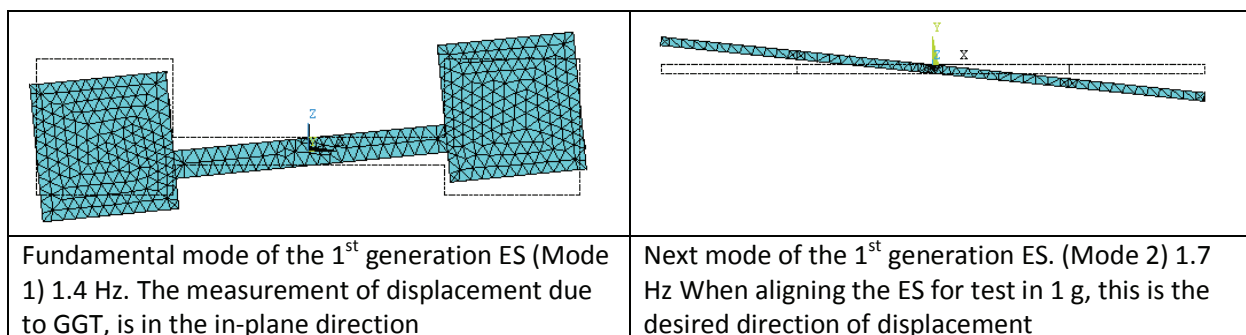


Figure 6-2 The in-plane GGT sensing mode (left) and out-of-plane mode (right) of the 1st Generation ES as seen in ANSYS

Figure 6-2 (left) shows the in-plane displacement of the fundamental resonant mode of the 1st generation sensor. Figure 6-2 (right) shows the out-of-plane displacement of the next resonant mode of the sensor. Due to the single spring design, the bending modes of the spring for these two cases have almost the same spring softness. While aligning the proof mass for test, the setup described in Chapter 5, with the stepper motor and piezo, is intended to change the displacement of the sensor in the out-of-plane direction only. Due to the spring stiffness being very similar for both in-plane and out-of-plane displacement, even a small off-axis error in the tilt applied for out-of-plane displacement, will result in an in-plane displacement.

This made the proof mass rotate around two axes, while movement around only one axis was preferable for the testing of the sensor. This made it very difficult to ensure that the proof mass was leveled and freely suspended for testing on Earth, since the freedom of movement around two axes reduced the range of allowed tilt of the proof mass before it touched one of the stoppers.

The spring stiffness in the fundamental mode of the ES has to be kept low to have a greater displacement to measure while measuring GGT. At the same time, to make the sensor easier to test, and avoid the alignment problem encountered in the 1st generation sensor, the spring stiffness for other modes of displacement should be increased..

The two spring design of the 2nd Generation sensor accomplishes that. The fundamental mode of the sensor is an out of plane tilt (Figure 6-3 left), and the higher mode is an in-plane rotation (Figure 6-3 right). The spring stiffness for out-of-plane displacement due to GGT is kept low, but now the spring stiffness for in-plane displacement is about a hundred times greater than the spring stiffness for out-of-plane displacement. This makes the proof mass alignment for test more tolerant to off-axis errors, so instead of carefully having to adjust the tilt of the chip on two axes, a one axis alignment is enough to ensure that the proof mass is not touching any hard stops.

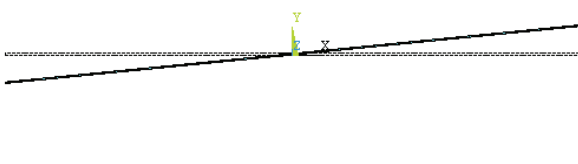
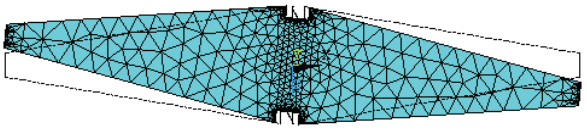
	
Fundamental natural mode of the 2 nd generation ES – 1.5 Hz. The measurement of displacement due to GGT, is in the out –of-plane direction.	Next natural mode of the 2 nd generation ES – 17 Hz. Due to its increased stiffness, when aligning the ES for test in 1 g, any motion in this direction is reduced

Figure 6-3 The out-of-plane mode (left) and out-of-plane mode (right) of the 1st Generation ES as seen in ANSYS

Another method to ease the alignment of the sensor for test is to increase the clearance to the hard stops is using a SOI wafer with a thicker buried oxide layer. In the 1st generation sensor, one of the limits on the maximum clearance of the proof mass to the hard stops was imposed by the oxide thickness of 1micron. For the 2nd generation sensor SOI wafers with a buried oxide layer of 5 microns are used. Increasing the oxide thickness beyond 5 microns is not possible due to the limits of the process used to manufacture SOI wafers, and constraints imposed by the fabrication process of the ES chip itself.

6.1.2. Design for operation on tumbling satellite

When satellite is tumbling, it is critical that its attitude be known, so that the correct thrust can be applied to bring it into the desired attitude. The ES must function under such circumstances, but being an inertial sensor, the centripetal force will have an effect on the ES, and it can be many orders of magnitude larger than the GGT. FEM using ANSYS is used to understand the effects of centripetal force on the ES, and examine the design choices necessary so the sensor can continue to measure GGT even when it is experiencing a centripetal force. Trying to minimize the error due to spin results in changes to the proof mass design for the 2nd generation ES. To understand these changes, first the effects of satellite spin on the 1st generation ES are discussed.

The centripetal force depends on the rate of spin, as well as the distance from the spin axis. To set conditions for the FEM analysis of satellite spin on the proof mass, we assume that the sensor is on a

Chapter 6: Design of 2nd Generation Earth Sensor

satellite spinning at a rate of 0.02 radians/s ($\sim 1.15^\circ/\text{s}$), and located at a distance of 1 m from the spin axis.

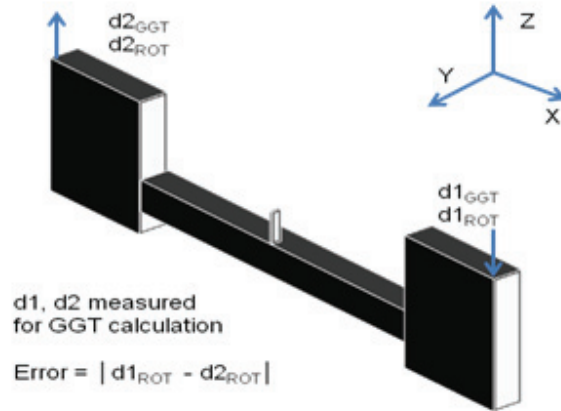


Figure 6-4 Schematic of Earth Sensor showing the displacements that are measured to calculate the GGT ($d_{1\text{GGT}}, d_{2\text{GGT}}$) and the displacements due to centripetal force that can cause an error ($d_{1\text{ROT}}, d_{2\text{ROT}}$)

Figure 6-4 shows the displacements of the ES proof mass due to GGT, and due to centripetal force. $d_{1\text{ROT}}$ and $d_{2\text{ROT}}$ depend on the orientation of the proof mass with respect to the axis of rotation. For instance, for the orientation shown in Figure 6-5, $d_{1\text{ROT}}$ and $d_{2\text{ROT}}$ will be roughly equal, and the error is negligible.

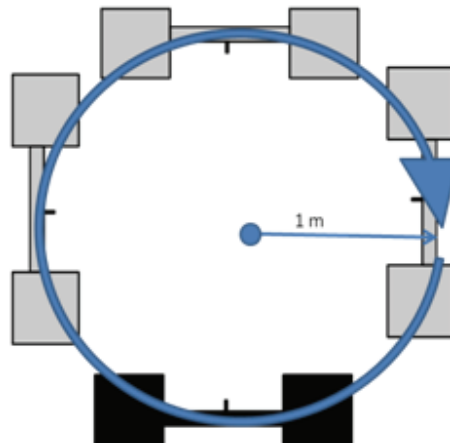


Figure 6-5 Position of ES chip relative to rotation axis that leads to no net error from centripetal force due to satellite rotation (0.02 radians/s)

The worst case orientation is shown in Figure 6-6. Since the centripetal force is orthogonal to the length of the spring, it can result in a net torque on the ES proof mass and spring, so $|d_{1\text{ROT}} - d_{2\text{ROT}}|$ needs to be estimated. The results of FEM simulation of the condition shown in Figure 6-6 can be seen in Figure 6-7.

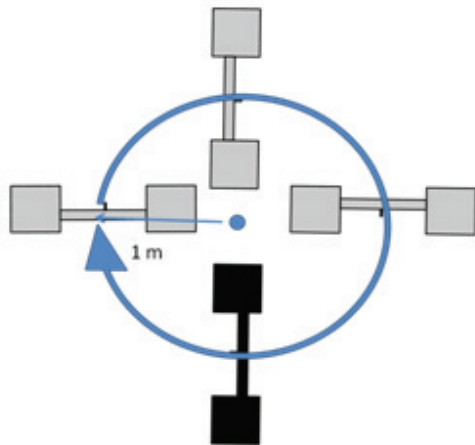


Figure 6-6 Position of ES chip relative to rotation axis that results in maximum error from centripetal force due to satellite rocket rotation (0.02 radians/s)

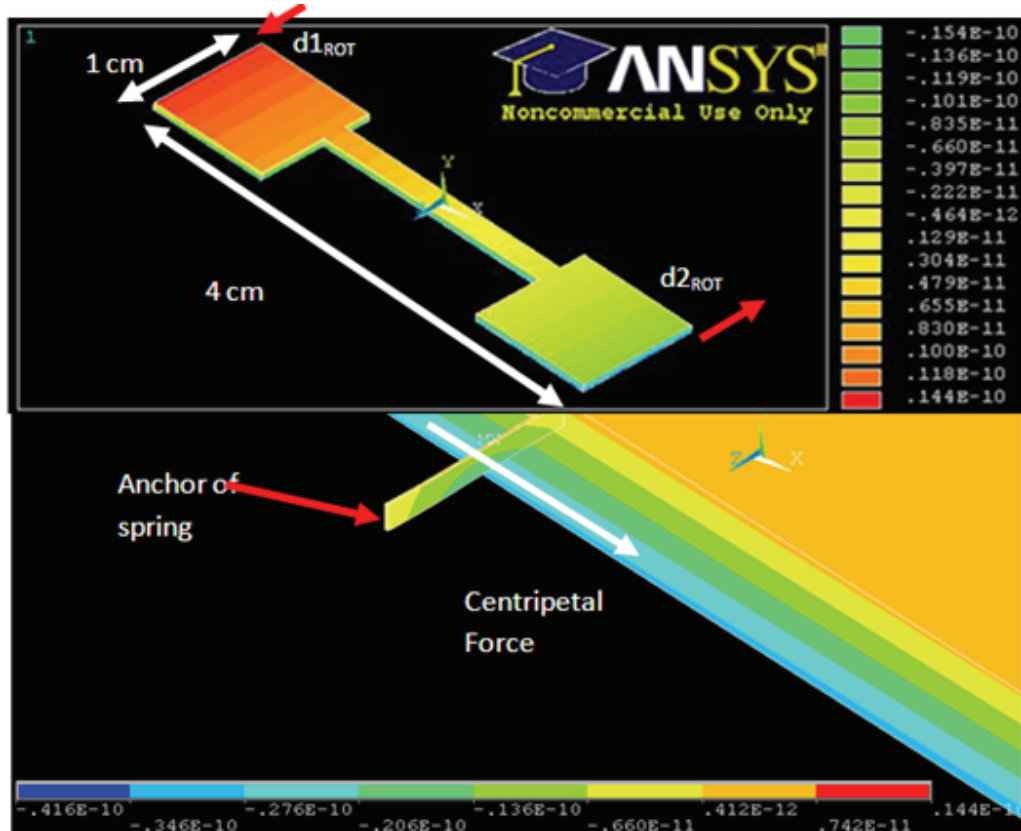


Figure 6-7 ANSYS model of displacement of ES proof mass, due to centripetal force from satellite spin as seen in Figure 6-6. The upper part shows the whole ES proof mass. The lower part shows a close-up of the spring. The displacement (in meters) is in the direction of d_1 and d_2 as seen in Figure 6-4

The total displacement of the proof mass due to the centripetal force is in nm, but most of it occurs along the X direction as defined in Figure 6-7. The displacement sensing is insensitive to motion in this

direction, and only senses the displacement at the extremities of the proof mass along the Z axis (d1 and d2).

As seen from Figure 6-7 the displacement of the proof mass in the directions of d1 and d2, due to centripetal force, is in the order of ten pm. To measure the GGT for an accuracy of 2° in the attitude determination, $|d_{1_{GGT}} - d_{2_{GGT}}|$ is roughly 200 pm.

This low error due to centripetal force is due to the shape of the proof mass. In Chapter 3, the proof mass is shaped so the center of mass of the proof mass and that of the spring coincide in the XZ plane (ref. Figure 6-7). Due to this any external force on the proof mass results in a net displacement, and not a torque. The dimensions of the proof mass in the ANSYS model in Figure 6-7 are rounded to a micron, so even the small displacements seen in the ANSYS result are due to a sub-micron mismatch in the simulated center of mass of the spring, from the simulated center of mass of the proof mass. But the model serves to confirm that if the two centers of mass coincide, then the error due to satellite spin can be ideally zero.

The FEM simulation in Figure 6-7 is for an ideal proof mass and spring. It does not take into account the effect of fabrication tolerances. As described in Chapter 4, the proof mass was fabricated out of the device and handle layers of a SOI wafer. During the fabrication process, first the device layer is patterned and etched. Then the handle layer is patterned using the device layer as a reference. The alignment process used can have a tolerance of up to a few microns. Further FEM simulations showed that this tolerance can result in errors on the order of few nm being introduced due to centripetal forces. A misalignment between the device and handle layers will result in the center of mass of the proof mass shifting with respect to the center of mass of the spring. To model the error due to centripetal force, as a result of this shift in the center of mass, simulations are performed by changing the relative position of the spring and the proof mass, as shown in Figure 6-8, to simulate the effect of a fabrication tolerance. For each relative shift in the centers of mass, a simulation is performed using the condition shown in Figure 6-6. Figure 6-9 shows the resulting error displacement of up to 3 nm for misalignments ranging from +5 to -5 microns.

Simulation of mismatch in center of mass of spring and center of mass of proof mass due to misalignment during fabrication



Figure 6-8 Schematic of ANSYS model used to determine error arising from fabrication misalignment. The simulated misalignment is a few microns; here it is shown exaggerated for clarity.

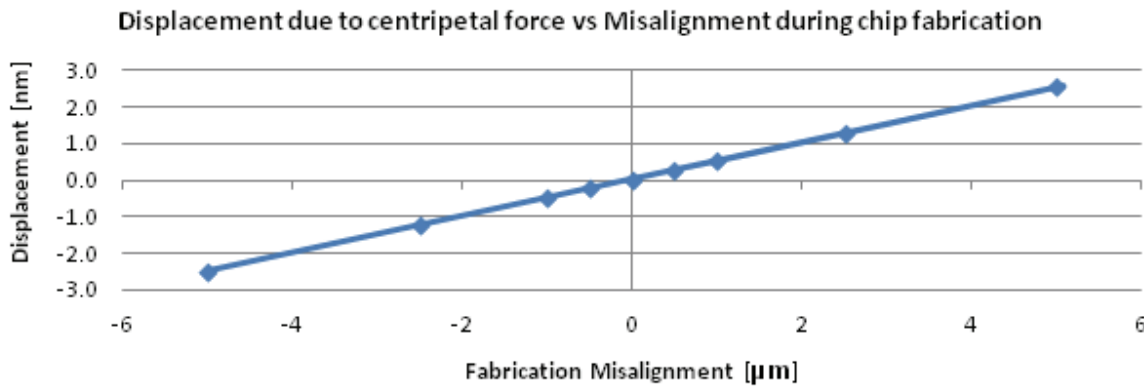


Figure 6-9 Displacement due to centripetal force due to conditions as indicated in Figure 6-6. The displacement is plotted for different proof mass - spring misalignments as shown in Figure 6-8.

To remove these sources of error, the proof mass and springs of the 2nd generation ES need to be patterned and etched in a single step, from one layer of silicon, thus removing alignment tolerances as a source of error due to satellite tumble. Therefore, for the 2nd generation sensor, as shown in Figure 6-1 (right), both proof mass and springs are etched from the device layer of a SOI wafer. Then, for the ideal design, the proof mass and springs (both springs taken together) have a common center of mass in all three axes, and the error introduced due to centripetal force remains negligible.

The fabrication process results in other non-ideal properties which result in a divergence between the center of mass of the springs and proof mass. These are further discussed in the more detailed design of the spring. ANSYS modeling is used to show how an additional fabrication step can be used to bring the spring center of mass back closer to the proof mass center of mass.

6.1.3. Capacitive displacement measurement

Optical displacement sensing was used to measure the displacement of the proof mass for the 1st Generation ES. The laser required for such a system in space will be prone to radiation induced damage. A laser requires radiation shielding and thermally stabilization for proper operation. This adds mass and increases the power required by the ES instrument. An electronic displacement sensing method has the advantages of not requiring thermal stabilization and being more compact, in keeping with the goals of a 1 dm³ instrument. The MEMS ES is designed to measure torque by detecting the displacement of the proof mass. This principle is similar to that of accelerometers which measure acceleration by detecting the displacement of a proof mass. Capacitive displacement sensing is widely used in accelerometers [44-47] and gyroscopes [51-54] to determine acceleration or rotation in one or more axes. Accelerometers sense a change in capacitance between the proof mass and a fixed electrode [44-50]. Another method is to sense the change in the resistance of piezoresistive elements on the proof mass due to deformation of the proof mass [70, 71]. The capacitive detection method is preferred when higher resolution is

required. For the MEMS ES, to measure the sub-nm displacements, capacitive displacement detection is necessary.

Commercial accelerometers are manufactured using customized fabrication process to integrate the MEMS with CMOS circuitry for capacitive displacement detection and in some cases, closed loop operation using force feedback [44-45]. The capacitance is formed using two sets of comb fingers, typically for in plane displacement sensing [46], or a parallel plate capacitance, typically for out of plane displacement sensing [47]. For the 2nd generation MEMS ES, due to the out of plane displacement of the proof mass, a parallel plate capacitance is used. Since the integrated fabrication methods used for commercial accelerometers are proprietary, results reported in literature typically use a hybrid approach where the MEMS and a separate ASIC CMOS die are bonded adjacent to each other on a common substrate and connected with wire bonds. This allows optimization of the detection circuit and resolution of <10 aF have been reported [69]. For this thesis, there was no access to a customized ASIC, thus we use COTS ICs for capacitance measurement with the best reported resolution of the order of 100 aF [20, 21] to measure the capacitance. Similar to the hybrid approach, these ICs are placed close to the MEMS, and connected with gold wirebonds. Future development of a customized ASIC could allow lower noise in the capacitance displacement sensing.

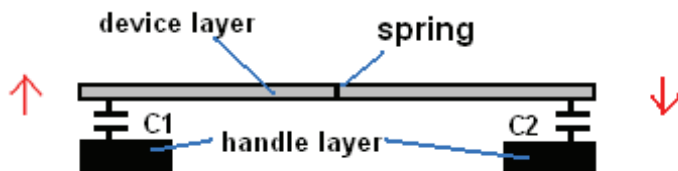


Figure 6-10 Out of plane displacement sensing using two capacitances at either end of the proof mass

As discussed in section 6.1.1 the two spring design of the 2nd generation sensor results in out of plane displacements due to GGT. The ES chip is made from an SOI wafer, and the proof mass and springs are made from the device layer. The handle layer can be used to define the electrodes to capacitively sense out of plane displacements. The oxide between the handle layer and device layer is etched away, and a sensing capacitance is formed between the proof mass in the device layer as one terminal of the capacitance, and the handle layer forming the second terminal of the capacitance. To enable a differential capacitance measurement a capacitance is defined at both ends of the proof mass, as shown in Figure 6-10. When the proof mass tilts out of plane due to GGT, the gap between the proof mass and the handle layer electrode decreases at one end and increases at the other. C1 increases and C2 decreases, or vice versa. The change in capacitance $dC = C1 - C2$, after suitable calibration, can be used to determine the GGT.

This method also has the advantage, that the capacitance sense gap is nominally defined by the thickness of the oxide between the device and handle layers. The oxide thickness is typically a few microns. To obtain a larger change in capacitance for the same displacement a smaller gap is desirable. The capacitance sensing is discussed in greater detail in further sections of this chapter.

6.2.Design Details of Generation 2

Based on the improvements desired from the 1st Generation ES, the 2nd Generation sensor has differential capacitive displacement sensing, and an elongated proof mass pivoted from two springs. The proof mass and springs are of the same thickness, since they are fabricated from the device layer of a SOI wafer. Further design details of the sensor are provided below.

6.2.1. Spring design

In Chapter 3, a suitable spring design for the 1st generation ES was a cantilever with a rectangular cross section. For the two springs of the 2nd generation ES, a similar design is discussed, since the springs need to be sensitive to GGT, while the chip should be testable in 1 g.

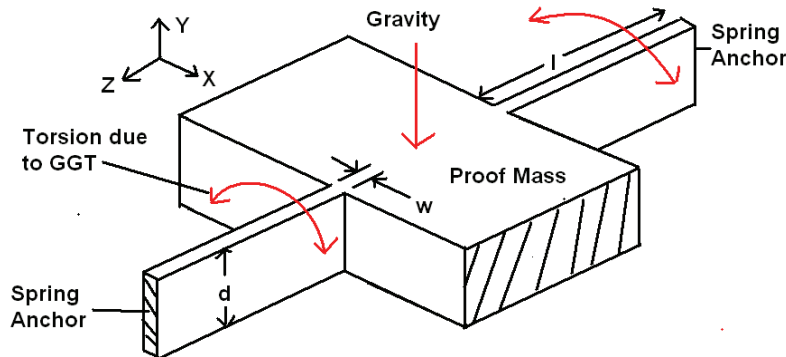


Figure 6-11 Diagram of springs of 2nd Generation ES. The displacement of the proof mass due to GGT produces torsion on the spring. In 1g, gravity results in the proof mass sagging in the -Y direction

The length l, width w, and depth d (Figure 6-11) are chosen based on the following considerations, listed in order of priority

- Fabrication risk – Ensuring that the chips can be fabricated is most important, and the risk of individual fabrication steps is reduced as much as possible.
- Testability of the ES chip – It should be straightforward to align the proof mass so that it is freely moving, and the sensor should survive routine handling in the laboratory. The sensor is aligned as shown in Figure 6-11, and due to gravity the proof mass and springs sag downwards. If this sag is too much, then the sensor will become untestable, since the proof mass will touch the capacitive measurement electrodes beneath it (Figure 6-10).
- Sensitivity of the ES – to increase the sensitivity the spring constant should be as low as possible. The lower limit is imposed by the requirement of having a fundamental resonant frequency > 1 Hz. As the 1 Hz resonant frequency is approached, the spring constant is reduced. As the spring constant reduces, typically the testability of the chip (more difficult to align due to increased sag, chip less robust), and fabrication risk increases (DRIE becomes more difficult, yield of HF vapor release process decreases)

Chapter 6: Design of 2nd Generation Earth Sensor

Figure 6-11 shows how torsion due to GGT and displacement due to gravity act on the springs. The springs should have a low torsional spring constant for high sensitivity to GGT, but a high spring constant in the direction of gravity, so that the sag is less and the chip can be tested.

The spring constant k_t for torsion, taking both springs together is proportional to [22]

$$k_t \propto \frac{2dw^3}{l} \quad 6-1$$

The spring constant k_g for gravity, taking both springs together is proportional to [22]

$$k_g \propto \frac{2wd^3}{l^3} \quad 6-2$$

From the above equations, the ratio k_g/k_t is given by

$$\frac{k_g}{k_t} = \frac{d^2}{l^2w^2} \quad 6-3$$

As seen in the above equation, to keep the chip testable yet sensitive, the ratio d/w should be as high as possible for a given length l of the spring. Hence the rectangular cross section is required for the springs of the 2nd generation sensor as well. In practice the d/w ratio is limited by the need to reduce the risk of the DRIE process step in which the spring is etched from the device layer.

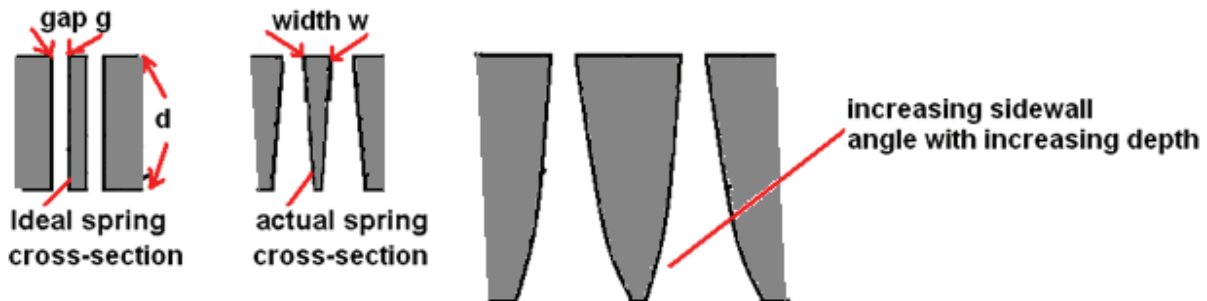


Figure 6-12 The DRIE process results in non-vertical sidewalls.

As seen in Figure 6-12, the spring needs to have a minimum width since the walls of the spring slope inward. As the depth d is increased, the angle of the sidewalls also increases, so the width w at the top also has to be increased, so the net benefit on increasing the depth is less. The effect of non-vertical sidewalls on the ES performance is discussed in the next section.

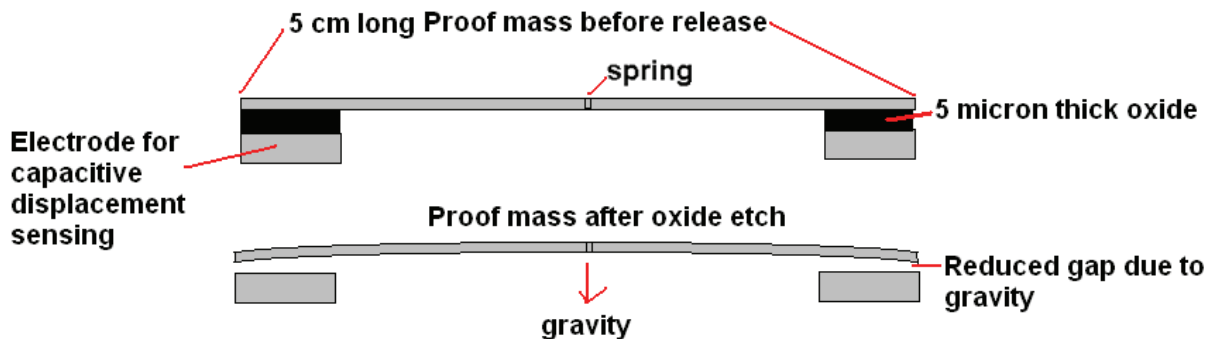


Figure 6-13 Limiting the sag of the proof mass in 1g is also important in selecting the thickness of the silicon layer from which the spring and proof mass are fabricated

Scaling the spring to be stiff due to gravity is not the only consideration in selecting depth d . The 5 cm long proof mass also sags at its extremities due to gravity, as shown in Figure 6-13. The depth of the spring is also the depth of the proof mass. The sag of the proof mass in 1 g depends on the depth as well. If the sag is excessive, then the proof mass will touch the sense electrodes below. Using ANSYS, simulations are performed for the two spring design with the chosen proof mass shape (discussed section 6.2.2) to fix a minimum required depth d such that the sag predicted by ANSYS at the extremities is around 2.5 microns, which leaves a 100% margin in case of a discrepancy between the ANSYS predictions and the measured sag of the fabricated sensor. This depth is 130 microns. Although an increased depth would result in less sag due to gravity and more clearance, the DRIE process for a thicker silicon layer becomes more risky.

The depth being fixed at 130 microns, the length of the spring also has to be limited. From Equation 6-2, the spring stiffness for gravity k_g decreases proportional to the cube of the length. Based on the analytical equations to calculate the sag due to the spring length, the length is set at 1 mm. Then the width of the spring is calculated at 8 microns to obtain k_t , such that the sensor fundamental resonant frequency is 1.5 Hz.

6.2.1.1 Compensation for non-vertical spring sidewalls

The effect of satellite spin on the 2nd generation sensor is discussed. Section 6.1.2 shows that the error due to the displacement of the sensor, introduced due to satellite spin, can be negligible if the center of mass of the springs and the proof mass coincide. In this condition, the centripetal force produces lateral in-plane motion only. The capacitive displacement sensing is designed to measure out-of-place displacement. To achieve this condition, the proof mass and springs of the 2nd generation sensor are made from a single layer of silicon.

Due to the non-vertical sidewalls due to DRIE, the center of mass of the springs and the proof mass will not coincide. The spring will have a trapezoidal cross section. Figure 6-16 shows a cross sectional view of the spring and proof mass, with the different centers of mass indicated. Figure 6-14 shows the orientation of the sensor with respect to the axis of spin that results in the maximum error due to

centripetal force. The right half of Figure 6-15 shows the centripetal force through the center of mass of the proof mass, due to the conditions in Figure 6-14. In this orientation, the centripetal force will produce the maximum torque on the spring which results in an out of plane displacement that causes an error in the GGT measurement.

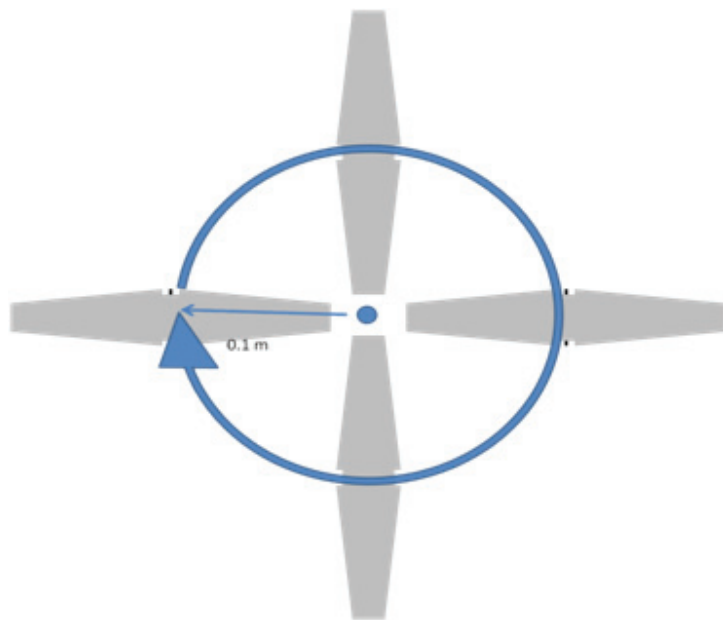


Figure 6-14 Worst case error due to centripetal force due to satellite rotation (0.02 radians/s) on ES.

Though the angle of the sidewall can be reduced by choosing better process parameters during DRIE, a non-vertical sidewall cannot be avoided. Figure 6-16 shows the additional process step to reduce the error due to centripetal force. An ANSYS model of the sensor is used to know the co-ordinates of the centers of mass of the spring and proof mass. From that, it can be determined, for the 8 micron wide spring, an etch of 22.5 microns from the top, brings back the center of mass of the springs closer to the center of mass of the proof mass. To validate this approach, the conditions in Figure 6-14 are applied to the ANSYS model of the ES. From the results enumerated in Figure 6-16, it can be seen that for the ES with ideal spring, the error due to spin is negligible, but increases significantly for the spring with non-vertical sidewalls. For the purposes of the simulation a sidewall slope of 1:100 is assumed. This is close to actual observed values on fabricated sensors. For the spring etched by 22.5 microns, the error is significantly reduced, and is in the same order of magnitude as the displacements due to GGT. This error can be calibrated and compensated for by using secondary sensors within the ES instrument. A secondary sensor that measures the linear velocity due to the spin in the vicinity of the ES chip can provide the information required to compensate for this error. The secondary accelerometers described in Chapter 2, which are a part of the ES instrument, can be used for this purpose.

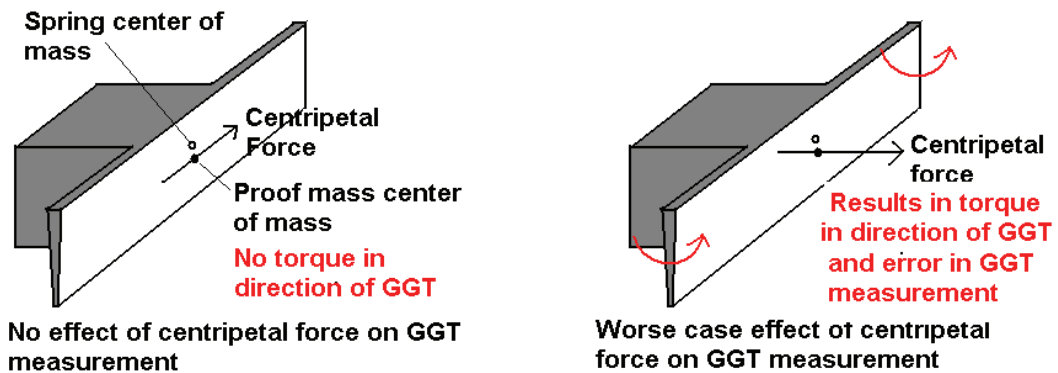


Figure 6-15 Cross sectional view of proof mass and spring between the two spring anchors; left: when centripetal force acts along length of the spring, there is no torque that causes an error in the GGT measurement; right: when centripetal force acts perpendicular to the spring, the torque causes an error

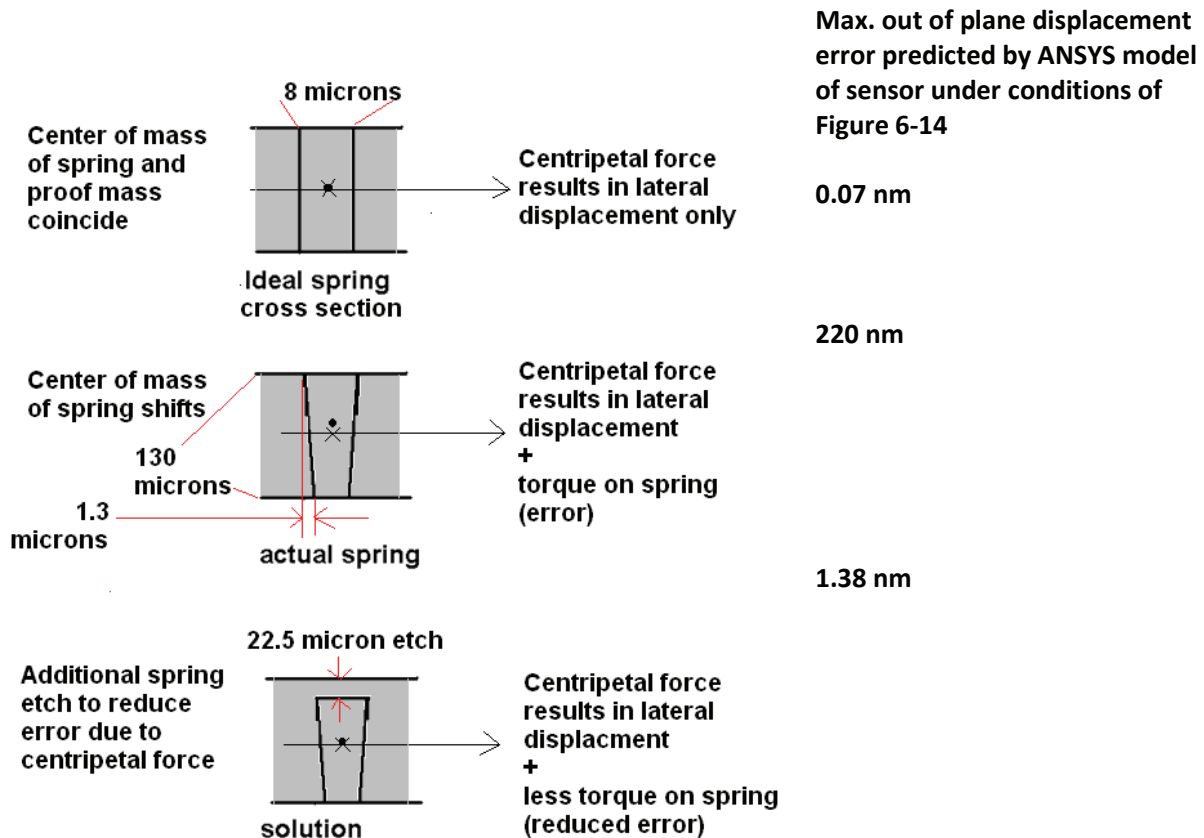


Figure 6-16 Additional spring etch process step to reduce the error due to the satellite spin. The etch of the spring brings the center of mass of the springs and the proof mass closer

When the sidewalls are non vertical, the spring cross section is trapezoidal, and the spring stiffness k_t changes from that of a spring with a rectangular cross section. For the final design of the ES chip the

ANSYS model uses springs with non-vertical sidewalls, and analytical equations for a spring with a trapezoidal cross section are used. For an ES chip intended for use as part of an instrument, a test SOI wafer is necessary to determine the sidewall angle for the spring. Based on the measurements of the springs on the test wafer, the depth of the spring etch for error compensation of the production ES chips can be estimated. The equations to calculate the spring constant of a spring with a trapezoidal cross section are:



$$K_{GGR} = \frac{G}{12L} d(w + b)(w^2 + b^2) - V_L w^4 - V_s b^4 \quad 6-4$$

where $V_L = 0.10504 - 0.10s + 0.0848s^2 - 0.06746s^3 + 0.0515s^4$

and $V_S = 0.10504 + 0.10s + 0.0848s^2 + 0.06746s^3 + 0.0515s^4$

$$s = \frac{w-b}{d}$$

G is the modulus of rigidity of silicon, L the length, d depth, w the top width and b the base width of the spring [22].

6.2.2. Proof mass design

The shape of the proof mass is changed from a barbell to an elongated shape that tapers off towards the extremities. The barbell shape was chosen to maximize the moment of inertia of the proof mass, but the proof mass of the 1st generation sensor is comprised of two layers of silicon, giving it a total thickness of 600 microns, which made it stiff with respect to gravity.

However, the 2nd generation proof mass is fabricated from a single layer of silicon to avoid alignment tolerances, and its thickness is 130 microns only. The thickness is again constrained by the need to limit fabrication risk due to DRIE. In the 1st generation sensor the DRIE aspect ratio was 1:3 for the device layer. For the 2nd generation sensor, the aspect ratio is increased to 1:13, in consultation with the clean room staff. The maximum lateral displacement of the proof mass is limited to 10 microns, to obtain a more robust sensor. If the barbell shape is used for the 2nd generation proof mass then it sags excessively in 1 g (Figure 6-17 left) and it cannot be tested since it will touch the hard stops. Hence a shape is chosen so that the sag in 1 g is minimized to keep the ES testable on Earth (Figure 6-17 right). The reduction in the moment of inertia is partially compensated for by increasing the length to 5 cm. The length is limited to 5 cm to minimize the sag, and also to obtain more chips from a 100 mm wafer. With this proof mass design, the number of chips possible per wafer is seven.

The proof mass is 1 cm wide at its center, and tapers to 2 mm at its extremity. The total length is 5 cm. Due to the proof mass being 130 microns thick, the moment of inertia is reduced by a factor of four as compared to the 1st generation sensor. By also scaling down the spring stiffness, the resonant frequency remains at 1.5 Hz. However, from equation 2-6 for the thermal signal to noise ratio, the 2nd generation ES requires a Q-factor four times higher in vacuum to achieve the same thermal noise floor.

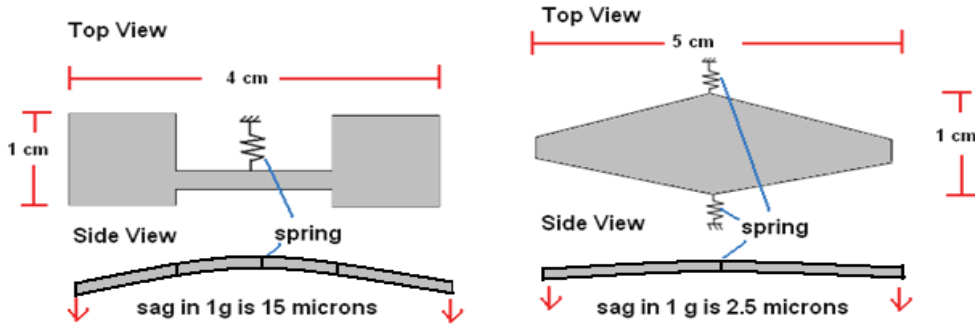


Figure 6-17 Left: Generation 1 proof mass shape with 130 micron thickness; Right: Change of shape for 2nd generation ES to minimize sag in 1g

The spring design section described the design of an ES chip with a resonant frequency of 1.5 Hz. Considering the issues seen in alignment for the 1st generation sensor, two stiffer versions of the ES chip is designed, one with a resonant frequency of 10 Hz, which is roughly 50 times stiffer than the 1.5 Hz ES, and a chip with a resonant frequency of 20 Hz, which is roughly 175 times stiffer. For the 10 and 20 Hz ES, except spring width, all other spring and proof mass dimensions are kept identical. Increasing the spring width increases the resonant frequency of the ES. In the case that alignment of the 2nd generation ES proves hard, this stiffer version of the ES should be easier to align, so that testing of the displacement sensing can be done. Table 6-1 lists the design parameters for the 1.5 Hz, 10 Hz and 20 Hz ES chips.

	1.5 Hz ES chip	10 Hz ES chip	20 Hz ES chip
Spring Depth (Trapezoidal cross section)	108.5 microns	108.5 microns	108.5 microns
Width	8 microns	18 microns	37 microns
Length	1 mm	1 mm	1 mm
Proof mass outline	5 cm x 1 cm	5 cm x 1 cm	5 cm x 1 cm
Proof mass depth	130 microns	130 microns	130 microns
Resonant frequency	1.5 Hz	9.9 Hz	20.5 Hz

Table 6-1 summary of Design values for stiff and soft ES springs

6.2.3. Electrostatic Actuation of Proof Mass

Apart from the capacitance sense electrodes, additional electrodes are added underneath the proof mass as shown in Figure 6-18. When a voltage is applied between these electrodes and the proof mass, an electrostatic force pulls the proof mass towards the electrode. This force is given by the expression [23]

$$F = \frac{\epsilon_0 A V^2}{2d^2} \quad 6-5$$

where ϵ_0 is the permittivity of free space, d the distance between, A the area of overlap between the electrodes to which voltage V is applied. For the ES chip assuming a distance of 2.5 microns between these electrodes and the proof mass, the overlap area is scaled such that for a ES chip with a 1.5 Hz

resonant frequency, the displacement at the extremities is 5 nm for 1 V. The locations of the electrodes are shown in Figure 6-18.

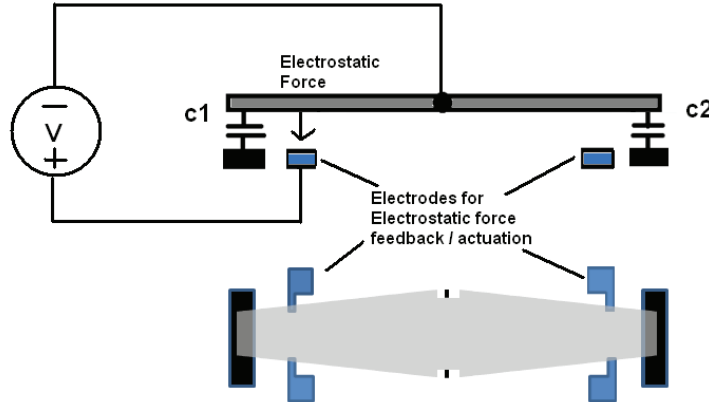


Figure 6-18 Top and side schematic views of the ES showing electrodes for electrostatic actuation

These electrodes will be used for testing the sensor. A known voltage is applied to the sensor, and the resulting change in capacitance can be compared to the expected change in capacitance due to displacement of the proof mass due to the electrostatic force. When a voltage is applied, an optical profiler is used to monitor the displacement of the proof mass in the area adjacent to the actuation electrode. So it can be verified that the change in capacitance corresponds to a physical displacement. Eventually, closed loop operation of the sensor is desirable to measure GGT. In this case, these electrodes can be used to provide the feedback required for closed loop operation. Force feedback is commonly used in accelerometers [55-57]

6.2.4. Displacement measurement design

A capacitive readout has been a standard method to measure displacement of inertial sensors. Typically, an ASIC is custom designed to measure the changing capacitance of an inertial sensor. We don't have access to an ASIC, so we use commercially available capacitance sensors to measure the capacitance change. The table below lists the ICs compared to select the capacitance sensor for which the readout is designed. After an IC is selected for displacement measurement, the capacitive displacement electrodes of the ES chip are then scaled based on the datasheet values for resolution and nominal capacitance that the selected IC can measure.

Capacitance Sense IC	Analog / Digital Output	Peak-to-Peak noise
MS3110[18]	Analog	4 aF/Hz ^½
ZSC31210 [19]	14 bit digital	625 aF (4 Hz update rate)
AD7747 (Analog Devices) [20]	24 bit digital	174 aF (8.1 Hz update rate)
AD7745 (Analog Devices) [21]	24 bit digital	27 aF (9.1 Hz update rate)

Table 6-2 List of COTS components considered for capacitive measurement sensing

Due to the small changes in capacitance to be measured, noise in the measurement electronics should be as low as possible. The capacitance sensor is placed physically as close to the ES chip as possible to keep the length of the connections to the sense electrodes short. A digital readout is preferred since interfacing with and reading the values to a PC is straightforward using Labview. Among the ICs with a digital output, the AD7745 has the lowest peak to peak noise of 27 aF [datasheet], for a rate of 9 capacitance measurements per second.

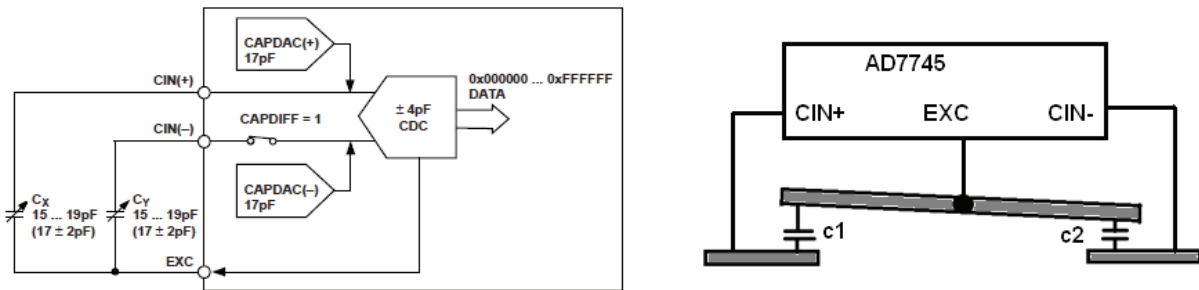


Figure 6-19 Differential Capacitance measurement with AD7745 [21]

As shown in Figure 6-19, the AD7745 generates an excitation signal that is applied to the common terminal of the differential signal to be measured, which is the proof mass of the ES. The sense electrodes are connected to the CIN+ and CIN- terminals of the chip. The AD7745 provides a 24 bit output where 0x000000 corresponds to $\{(CIN+) - (CIN-) = -4 \text{ pF}\}$ and 0xFFFFFFF corresponds to $\{(CIN+) - (CIN-) = 4 \text{ pF}\}$. The AD7745 has an internal programmable negative capacitance of up to 17 pF. This programmable negative capacitance can be used to increase the nominal capacitance being measured until 19 pF as shown in the left of Figure 6-19. The range is more than enough for the ES, which measures a $\{(CIN+) - (CIN-) \sim 2 \text{ fF}\}$ for the maximum expected displacement due to GGT.

Due to the EXC signal being applied, the proof mass is not at ground, when displacement sensing is performed using the AD7745. The EXC signal is 32 / 16 KHz (programmable) square wave from 0 V to Vdd of the AD7746. As discussed in the previous section applying electrostatic force to the sensor assumes that the proof mass of the sensor is at circuit ground. So the AD7747 will also be evaluated for displacement sensing, even though its noise is much worse (126 aF for a rate of 4 capacitance measurement per second). The AD7747 measures capacitance with respect to circuit ground, as shown in Figure 6-21.

The sense electrodes are connected to the CIN+ and CIN- terminals of the chip. The AD7747 provides a 24 bit output where 0x000000 corresponds to $\{(CIN+) - (CIN-) = -8 \text{ pF}\}$ and 0xFFFFFFF corresponds to $\{(CIN+) - (CIN-) = 8 \text{ pF}\}$. The AD7747 also has an internal programmable negative capacitance of up to 17 pF. This programmable negative capacitance can be used to increase the nominal capacitance being measured until 21 pF as shown in the left of Figure 6-20.

Chapter 6: Design of 2nd Generation Earth Sensor

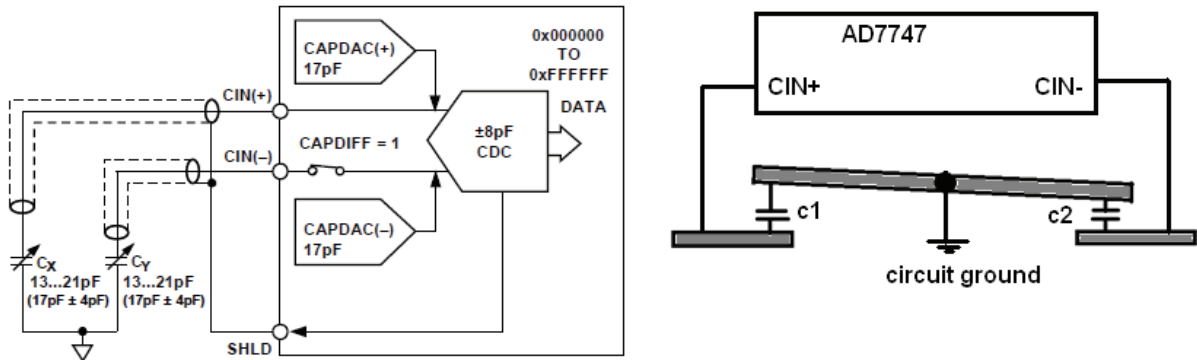


Figure 6-20 Differential Capacitance measurement with AD7747 [20]

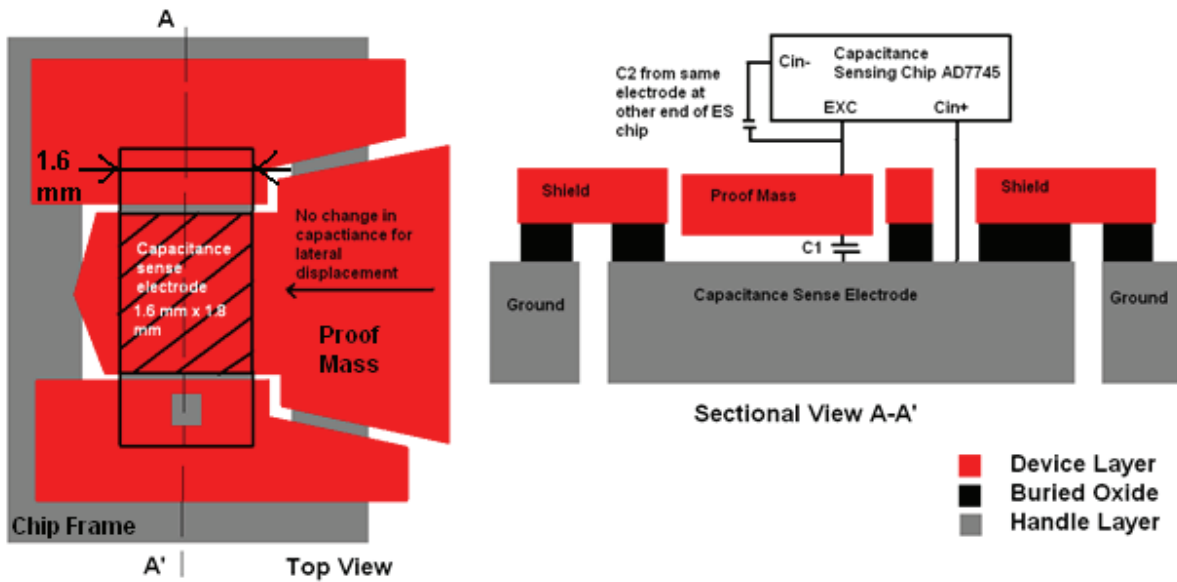


Figure 6-21 Top and side views of capacitance measurement electrode design on ES chip. The striped area indicates the overlap between the proof mass and the capacitance sense electrode that forms the sense capacitance.

Figure 6-21 shows details of the electrode for capacitance measurement. The electrode for the capacitance sensing is defined in the handle layer of the SOI wafer, as shown in gray. The proof mass, which is defined in the device layer, shown in red, overlaps the capacitance sense electrode. The capacitance is given by

$$C = \frac{\epsilon_0 A}{d} \quad 6-6$$

where ϵ_0 is the permittivity of free space, d the gap between, and A the area of overlap between the proof mass and the sense electrode. Due to the rectangular shape of the overlap, a lateral in-plane movement of the proof mass does not result in a change in the area of overlap, so any in-plane

Chapter 6: Design of 2nd Generation Earth Sensor

displacement, such as due to satellite spin, will not register in the capacitance measurement. An out of plane displacement will result in the gap d changing, and the capacitance change is measured.

The left of Figure 6-21 shows how the capacitance sense electrode is held to the chip frame by sections of the device layer and the buried oxide. The device layer sections labelled as “shield” are electrically grounded when the AD7745 is used. While drawing the CAD mask design, the parasitic capacitance between the sense electrode and the shield sections of the device layer should be limited based on the values in the AD7745 / AD7747 datasheet. From the datasheet, even a limited parasitic capacitance can result in an error in the absolute measurement of the capacitance between the proof mass and a single sense electrode. The capacitance between the anchor and the chip frame is limited to 200 pF. This is below the 250 pF limit allowed by the AD7746 / AD7747 [20, 21]. The ES displacement is measured by recording the differential change in capacitance between two sense electrodes and the proof mass. Due to the differential measurement, any absolute error in the measurement of the capacitance of a single electrode can be ignored.

The AD7747 measures the change in capacitance. The AD7747 should measure only the capacitance between the sense electrode and the grounded proof mass. All other capacitances between the sense electrode and grounded sections of the chip are parasitics. For the AD7747 the “shield” device layer sections are connected to the SHLD pin of the chip (Figure 6-20). If connected to ground, for the AD7747 it would introduce a parasitic capacitance many times larger, between the sense electrode and shield section of the device layer. Section 8.7 describes the test procedure to optically verify that the capacitance change occurs only due to displacement of the proof mass, and not due electrical effects.

The sense electrodes and proof mass are connected to the PCB with the AD7745 / AD7747 using wirebonds. Holes are created in the device layer for access to the electrodes defined in the handle layer. Figure 6-21.

For a given displacement due to GGT, a higher capacitance change is better, since it will have a higher electronic signal to noise ratio. For a 1.5 Hz ES chip in an orbit of 700 km, the differential displacement of the proof mass due to a 2 degree angle with the Earth Vector is 0.05 nm. Figure 6-22 shows the change in capacitance due to this displacement for a sense capacitance with different distances between the electrodes. For an angle of 45 degrees with the Earth Vector, the differential displacement of the proof mass is 0.7 nm. Even though the total capacitance is kept at 10 pF, for a given displacement a higher change in capacitance is obtained for a smaller sensing gap.

In microgravity, the gap between the proof mass and sense electrode is determined by the thickness of the buried oxide layer. In 1 g, the sag of the proof mass reduces the gap. In previous sections, the proof mass was designed such that there is a gap of 2.5 microns between the proof mass and the electrode. The 2.5 micron value is obtained using ANSYS. For a total capacitance of 10 pF, with a sensing gap of 2.5 microns, the change in capacitance is 200 aF for the 0.05 nm displacement corresponding to a 2 degree angle with the Earth vector. The peak-to-peak noise at the output of any measurement electronics should be less than 200 aF for the desired accuracy to be achieved.

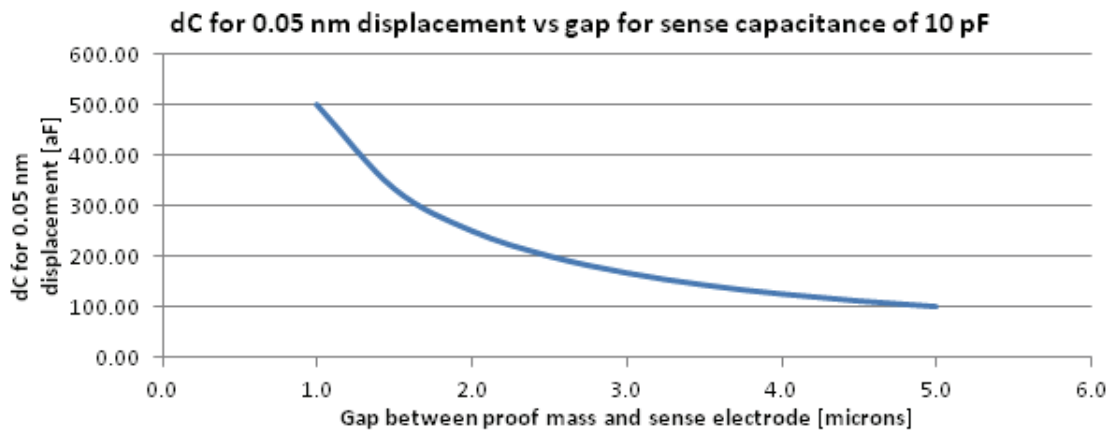


Figure 6-22 Calculated change in the capacitance for a 0.05 nm displacement for different gaps between the proof mass and the sense electrode.

On a fabricated ES chip, this gap can be even lower. For instance the simulation is done with a spring sidewall slope of 1:100. If this slope is higher then the spring will be less stiff, and the proof mass will sag more. The maximum nominal capacitance that can be measured by the AD7745 is 19 pF, even with the internal negative capacitances. The nominal capacitance is fixed keeping a margin, so that even if the gap turns out to be less than 2.5 microns the capacitance measurement does not saturate. The overlap area between the proof mass and sense electrodes is set to 1.8 mm x 1.6 mm. Figure 6-23 shows the increase in capacitance as the gap reduces. At a 2.5 micron gap the nominal capacitance is approximately 10 pF. The margin of 9 pF means that the capacitance displacement sensing will function even the gap reduces to 1.5 microns.

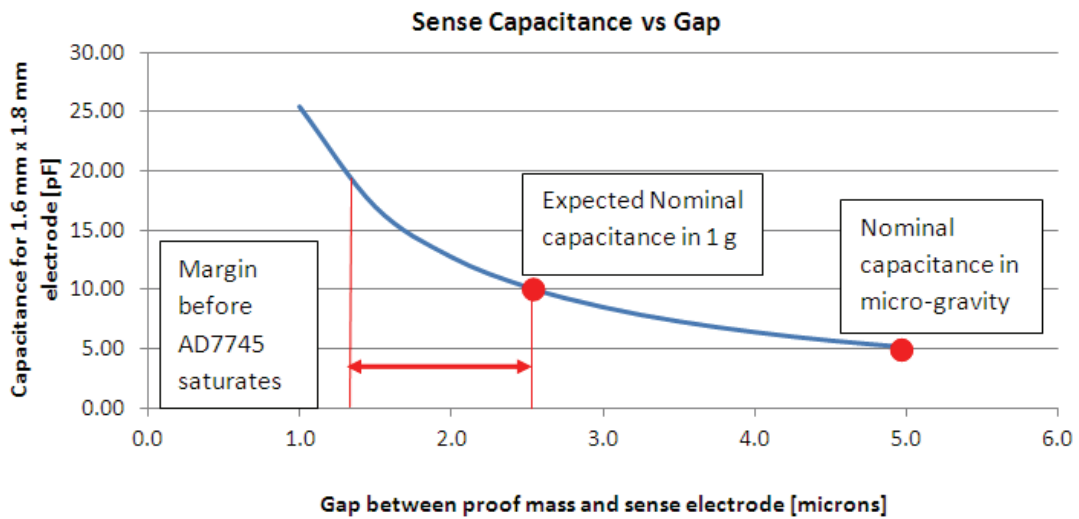


Figure 6-23 The nominal capacitance increases with decreasing gap

6.3.Quality Factor Estimation in Air

In Chapter 2, from the theory of thermal noise in inertial sensors, it can be observed that the Q-factor of

the second order system determines the thermal noise floor of the sensor. For the ES, it is determined that the quality factor of the order of hundreds is necessary for a noise floor low enough to obtain an accuracy of +/- 2° in measuring roll and pitch angles. The quality factor is a measure of the damping in the system. For most MEMS inertial sensors, given the high surface area to volume ratio, fluid damping due to air moving in and out of gaps between the moving proof mass and an underlying substrate is the dominant form of damping [38]. This is referred to as Squeeze Film Damping (SFD), since the air is squeezed in and out of the gap between the proof mass and the substrate [38]. Since the damping determines the transient response of the inertial sensor, and the noise floor, noise theory and squeeze film damping models are commonly used in the design of various inertial sensors [24-28] to try and obtain the desired transient response and noise floor. Various models have been proposed that use different structures to predict gas damping [30-37].

The ES chip is designed for operation in vacuum, so minimizing the damping in air is not a criterion during design. But estimating the damping in air is useful, so that a prediction can be made regarding the increase of Q-factor with decreasing air pressure, in case measuring the Q-factor in vacuum is not possible. Based on the design of the ES chip, it is observed that most of the proof mass surface is in open air, with only the capacitance sense electrodes at the ends of the proof mass having an underlying substrate (Figure 6-24). Hence, the damping in air can be assumed to be dominated by the SFD at the capacitance sense electrodes. The electrodes for electrostatic actuation also underlie the proof mass, but their area is negligible compared to that of the capacitance sense electrodes.

To be able to predict the SFD, the structure of the sense electrode is simplified as shown in Figure 6-25. The proof mass has a series of openings for etching away the oxide between it and the capacitance sense electrodes during fabrication. Since these openings allow air to pass in and out, the proof mass is divided into a series of parallel plates based on the location of these openings to estimate the SFD. The motion of the proof mass is assumed to be perpendicular to the surface of the capacitance sense electrode.

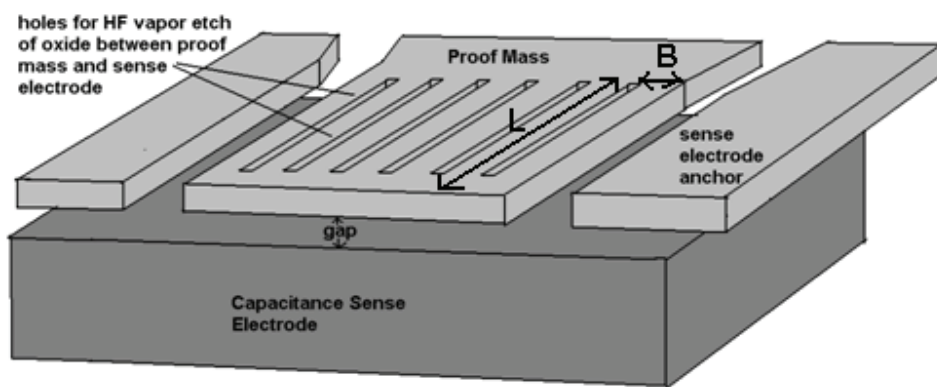


Figure 6-24 Diagram of proof mass extremity with underlying sense electrode. The damping in air is expected to be dominated by squeeze film damping between the proof mass and the capacitance sense electrode

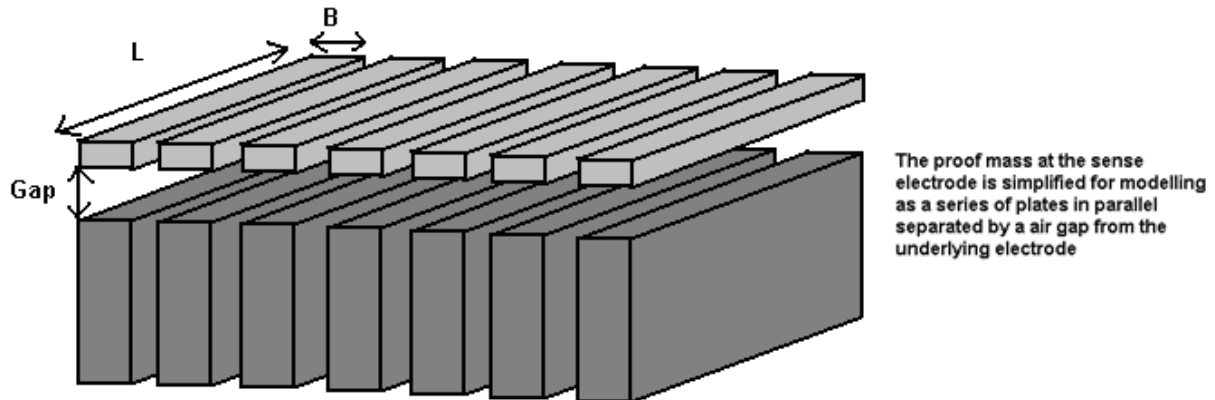


Figure 6-25 Simplification of the proof mass – electrode structure for the purposes of estimating squeeze film damping. The electrode is divided into individual pairs of plates

For a single pair of plates of size L (1900 microns) x B (180 microns) separated by a gap g (2.5 microns) (Figure 6-25) the Andrews model [35] is used to predict the damping factor in air. The Andrews model is chosen since it is a simple model that uses a test device with geometry similar to a single pair of plates in Figure 6-25.

The damping factor calculated by the Andrews model for a single pair of plates is given by [35]

$$C_{Andrews} = 0.42 \frac{L^2 B^2 \mu}{g^3} \quad 6-7$$

Where μ is the dynamic viscosity of air (1.983×10^{-5} kg/m.s at 300 K). Taking into account that the ES proof mass has two capacitance sense electrodes the damping factor for a single pair of plates is multiplied by 14 to obtain the total damping factor for the proof mass. The quality factor can be calculated from the damping factor using the expression

$$Q = \frac{I \omega_n}{c_{Andrews}} \quad 6-8$$

where I is the moment of inertia of the proof mass, and ω_n the natural resonant frequency of the sensor. This calculation is done for the higher out-of-plane plunging mode of the ES chip as well (Table 6-3 right). The same damping factor is assumed to apply for the higher out-of-plane mode as well. As seen from the last row of the table, the fundamental tilting mode is predicted to be heavily overdamped while the plunging mode is predicted to be underdamped.

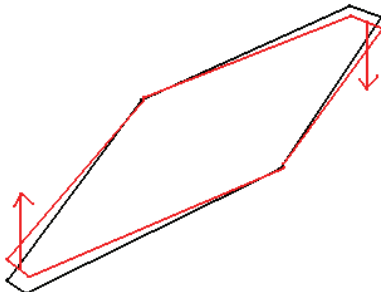
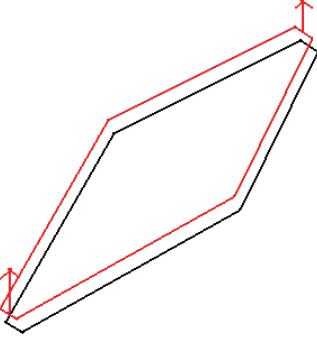
	Fundamental tilt mode	Higher order plunging mode
Mode Shape		
natural frequency ω_n	9.67 (1.53 Hz)	5497 (875 Hz)
Moment of Inertia / mass	1.3×10^{-8} N.m	0.1 g
Damping factor for one pair of plates in air	0.0078	0.0078
Damping factor for complete electrodes (14 pairs of plates)	0.109	0.109
Q_{air}	1.15×10^{-6}	5.04

Table 6-3 Quality factor estimation in air for fundamental tilting mode (left), and higher order plunging mode(right)

6.4.Conclusion

Figure 6-26 shows the complete design of the 2nd generation ES. The 2nd generation sensor is designed with capacitive displacement sensing. Based on the improvements desired from the 1st generation, the sensor is designed so that it is easier to align for test in 1 g. The spring and proof mass are designed so that the sensor can operate on a tumbling satellite. The dimensions are chosen such that the resonant frequency of the sensor is 1.5 Hz, and the sag in 1 g is 2.5 microns.

The spring dimensions are 8 microns x 1000 microns x 108.5 microns. The proof mass outline dimensions are 5 cm x 1 cm, and its thickness is 130 microns. The spring has a trapezoidal cross section. For the purposes of analytical calculation and ANSYS modeling, the sidewalls are assumed to have a 1:100 slope.

For the capacitive displacement sensing, the AD7745 and AD7747 are chosen. The capacitance sensing electrodes are designed so that there is no capacitance change due to in-plane motion. The nominal capacitance is designed to be 10 pF on Earth.

The Q factor of the tilting mode of the sensor is estimated to be 1.15×10^{-6} in air, which indicates the sensor will be extremely overdamped during testing on Earth.

Proof Mass Properties	
Proof Mass Length	5 cm
Proof Mass Breadth at center	1 cm
Proof Mass Breadth at extremities	0.18 cm
Proof Mass Thickness	130 μm
Proof Mass Maximum Moment of Inertia	$1.3 \times 10^{-8} \text{ N.m}^2$
Proof Mass Weight	0.1 g
Spring Properties	
Spring Length	1000 μm
Spring Width	8 μm
Spring Depth (on SOI wafer)	130 μm
Spring depth (compensation for 1:100 sidewall)	108.5 μm
Sensor resonant frequency	1.5 Hz
Capacitive Displacement Detection	
Sense Electrode Area	1.8 mm x 1.6 mm
Sense Electrode Gap from proof mass(from ANSYS)	2.5 μm
Noise of AD774 5 (from datasheet)	27 aF
Noise of AD774 7 (from datasheet)	174 aF
Nominal Capacitance (2.5 μm gap)	10 pF
Force Feedback Electrodes	
Area	200 μm x 235 μm
Distance from springs	19.5 mm
Gap between proof mass and Electrode	2.5 μm
Hard Stops	
Lateral Clearance	10 μm
Vertical clearance	5 – 10 μm
Oxide Overlaps for controlled HF release	
Spring anchors	2000 μm
Electrode Anchors	1200 μm
Structures holding proof mass to chip frame	300 μm
Structures holding chip to wafer	140 μm

Table 6-4 Summary of parameters of 2nd Generation Earth Sensor

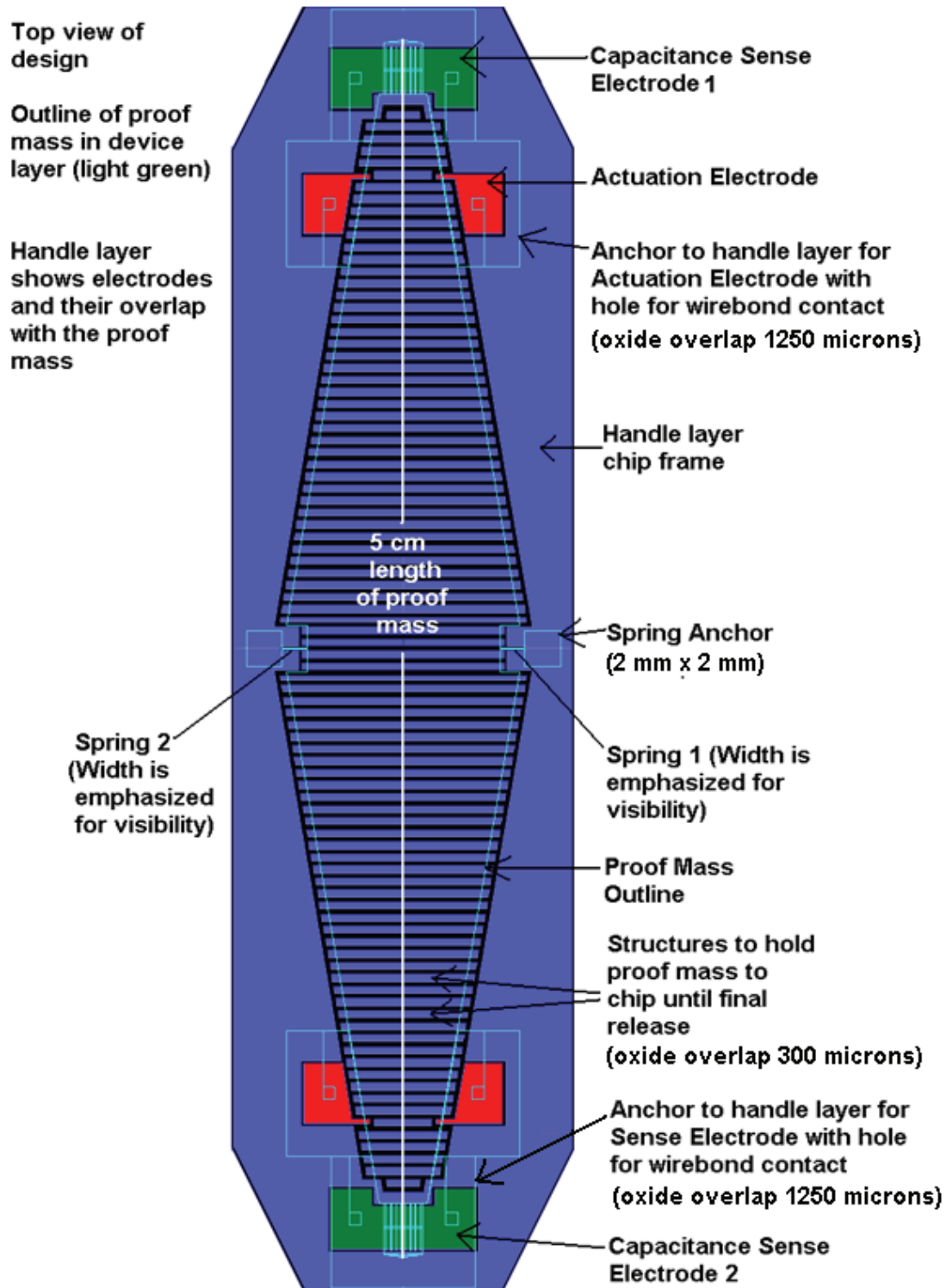


Figure 6-26 Top view of ES chip design; The proof mass outline in the device layer is indicated in light green along with the anchors for the handle layer electrodes; The various electrodes of the handle layer are shown in different colors; Seven such chips can be obtained from a single 100 mm SOI wafer

Chapter 7

Fabrication of 2nd Generation Earth Sensor

This chapter describes the fabrication process for the 2nd Generation MEMS sensor, and the significant issues resolved. The process flow of the 2nd generation sensor is similar to the 1st generation sensor in some part, but several new fabrication steps are needed for the 2nd generation sensor, mainly due to the capacitive readout being used.

7.1. Test Chip

Some test devices are made with the following objectives:

- The capacitance sense electrodes are anchored to the chip using segments of the device layer. These electrodes are connected to the AD7745 / AD7747 using wirebonds. It has to be tested if the anchor can withstand the force of a bonding needle. The test chip has a similar design for the anchor which is used on the ES chips.
- Ohmic contacts are to be made to the silicon electrodes using aluminum deposition and alloying. The contacts are then connected to the AD7745 / AD7747. It is verified that the series resistance of the ohmic contact is within the limits specified by the datasheet of the ICs.
- SOI wafers with 5 micron thick oxide are used to fabricate the ES chip. The test devices are also made from the same kind of wafers in order to debug any process issues that might arise from such a thick oxide being used.

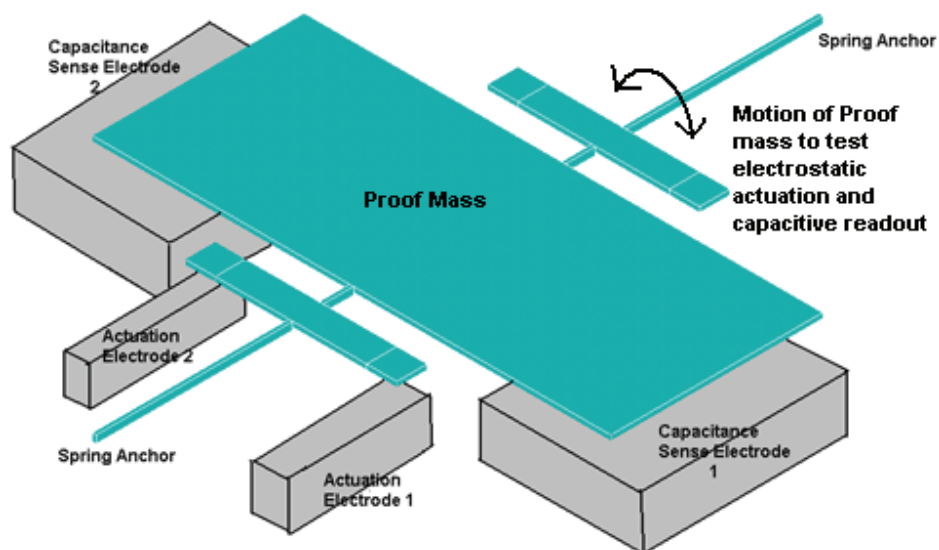


Figure 7-1 Schematic of test MEMS chip that is mechanically similar, but much stiffer compared to ES

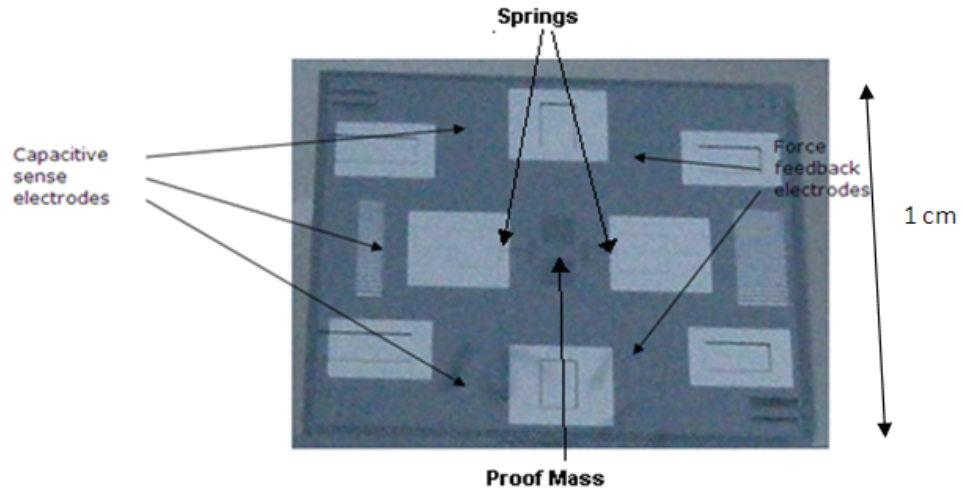


Figure 7-2 Photograph of fabricated test chip, to debug issues with the capacitive displacement sensing

The test chip is mechanically and electrically similar to the ES chip (i.e. proof mass suspended from two springs whose displacement is sensed using a differential capacitance) is made to study the capacitive readout of the Earth Sensor prior to fabrication of the 2nd generation devices. A schematic of the chip is shown in Figure 7-1, and a photograph of the fabricated chip in Figure 7-2.

7.1.1. Results from Test Chip

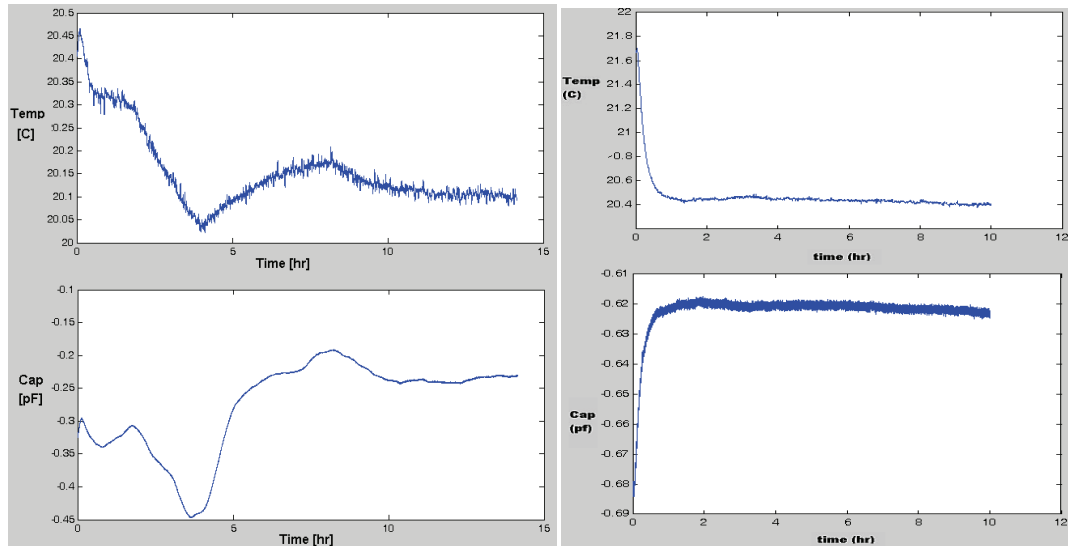


Figure 7-3 Two sets of differential capacitance measurements and temperature data gathered from the test chips. Left: Data gathered using an AD7745. Right: Data gathered using an AD7747. There is a large drift in the measured capacitance (top graphs) which is correlated with the temperature measurements (bottom graphs)

From long-term observations, a considerable drift in the measured capacitance can be observed. The drift is correlated to temperature, and can also be due to charging / discharging effects since the electric potential over all parts of the test chip was not well controlled due to fabrication issues.

7.1.2. Lessons learned

- For the ES, a capacitance measurement on the order of 100 aF – 2000 aF is required. A drift of 200 fF with the temperature is observed for the test chip. The temperature drift is probably due to the mechanical rigidity of the test chip being poor, since it was bonded together by epoxy, due to problems encountered in the final release step of the fabrication process. The ES chip will have a contiguous 500 micron thick silicon layer to ensure mechanical rigidity.
- The likely cause of the charging / discharging effects is that the electric potential over all parts of the test chip was not well controlled due to fabrication issues. Changes were made to the ES chip electrode design so that all parts of the chip will have aluminum ohmic contacts. As seen in Chapter 8, on the ES chip no drift is seen when performing long term noise measurements using the AD7745.
- The DRIE on the wafer with the 5 micron oxide is challenging. Due to the wafer bow the central portion of the chip is raised. Based on feedback from the technician responsible for DRIE (P.A. Clerc), this resulted in poor anisotropy during DRIE since the wafer cannot be maintained at the required temperature. The sidewall angle increases sharply, and is not uniform during the etch. To reduce the wafer bow to below 5 microns, process steps are developed that involve first growing 1.5 micron oxide on both sides of the SOI wafer. Then the thickness of the oxide on the device layer is reduced to the desired value of 500 nm. This changes the curvature of the wafer. Then the oxide on the handle layer side is reduced in steps, and the resulting change in curvature is monitored until it drops below 5 microns (Figure 7-4).
- During wirebonding some anchors are broken by the bonding needle. Better mechanical support by applying more epoxy directly between the electrodes where wirebonding is done, and the underlying PCB on which the test chip is mounted, prevents the anchor from breaking. To minimize the chances of the bonding needed breaking the chip, the size of the holes for the wirebonds is reduced, and the size of the anchor is increased for the ES design.

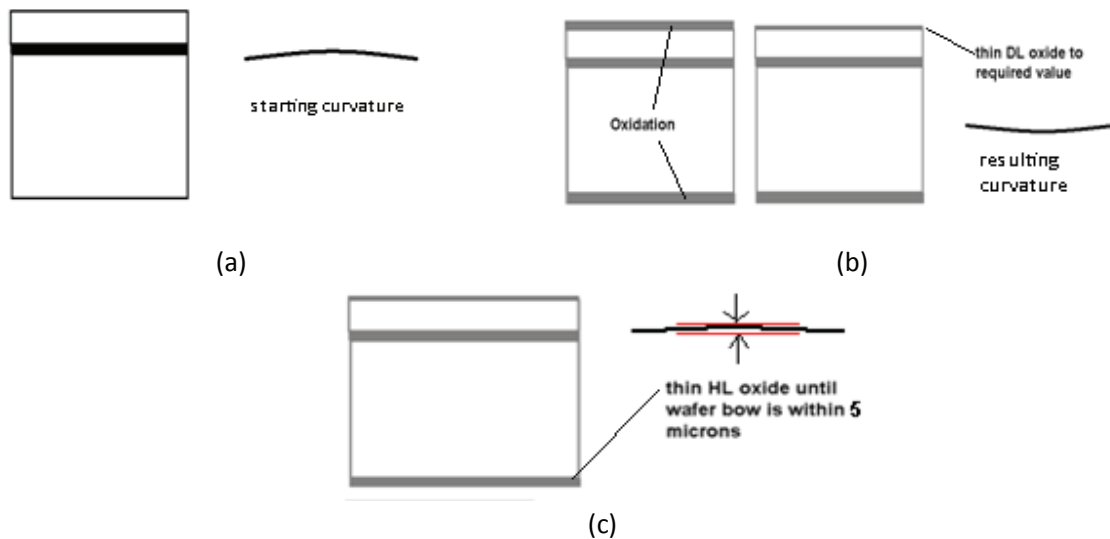


Figure 7-4 Steps for growing and then thinning oxide selectively on both sides of wafer, for stress compensation to obtain a wafer with low curvature. At each step, an example of the resulting change in bow is shown

7.2. Fabrication steps

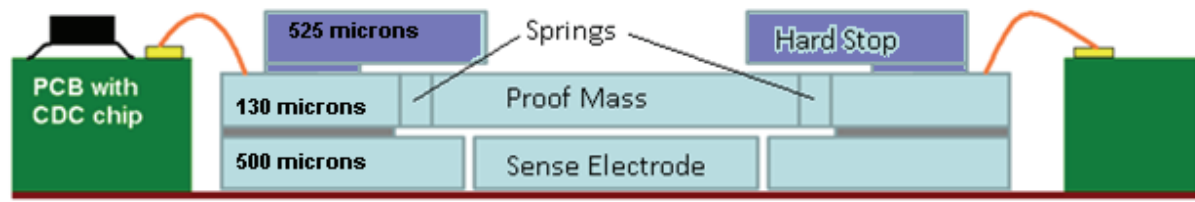


Figure 7-5 Cross sectional schematic of the ES chip mounted on a PCB

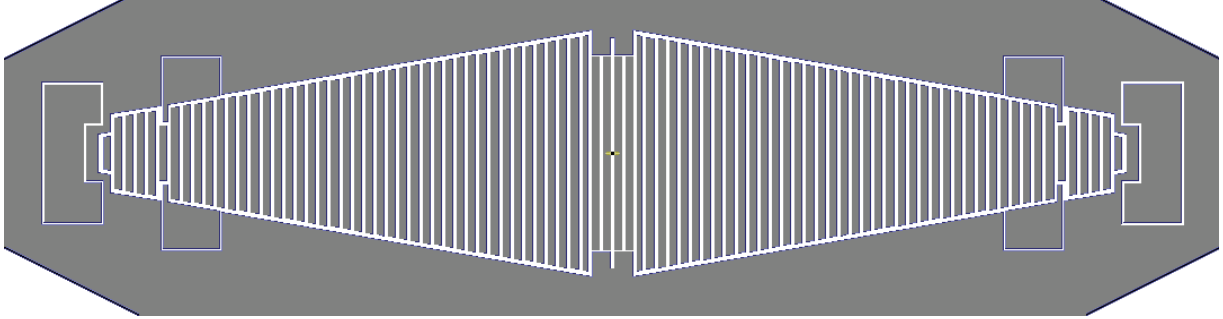
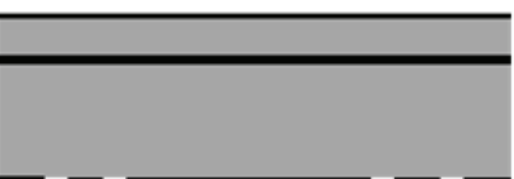
The Earth Sensor chip consists of a stack of two silicon substrates, as shown in Figure 7-5. The top substrate is the hard stops to constrain the ES proof mass. The bottom Silicon on Insulator (SOI) substrate forms the ES proof mass and suspension. The ES chip is mounted on a PCB, with gold wirebonds for connections to the electronics and electrostatic actuation of the ES proof mass.

The top hard stop is constructed from a single layer of silicon, ~525 microns thick. The SOI substrate with the proof mass, consists to two layers of silicon bonded together by 5 microns of oxide. The thinner 130 micron layer is called the device layer, and the thicker 500 micron layer is called the handle layer. The proof mass and springs are etched into the device layer. The capacitance is measured between the proof mass (device layer) and electrodes etched into the handle layer.

The relatively large mass suspended by a very soft spring is susceptible to breakage at loads of just a few g. The motion of the mass must therefore be restricted to just a few microns, so that it can tolerate routine handling. This restriction must be done as part of the fabrication process, prior to the mass being released.

7.2.1. Fabrication of chip with proof mass

Steps in the fabrication of the SOI ES chip	
 130 microns Silicon 5 micron oxide 500 microns Silicon	Start with an SOI wafer with device layer 130 microns thick, handle layer 500 microns thick and oxide thickness 5 microns.

 <p>500 nm oxide</p> <p>oxide thickness to reduce wafer bow to $<5 \mu\text{m}$</p>	<p>Oxide Preparation</p> <ul style="list-style-type: none"> • Standard cleaning • The wafers are oxidized in steam at 1100 degrees Celsius till silicon dioxide of thickness 1.5 microns is formed. The handle layer is covered with photoresist and the device layer oxide is etched in BHF until it is reduced to a thickness of 500 nm. After etching the photoresist is stripped in oxygen plasma. • Now the device layer oxide is covered with photoresist and the handle layer oxide is etched in BHF in steps. At each interval the wafer bow is measured. The etching is stopped when the bow becomes $+/-5$ micron or less. After etching the photoresist is stripped in oxygen plasma.
	<p>Figure 7-6 Schematic of handle layer; the actuation electrodes, capacitance sense electrodes, and release structures that hold the proof mass in place until the hard stops are integrated, are defined in the handle layer</p>
	<p>Handle layer oxide etch: Photolithography is performed on the handle layer to define the electrodes and mechanical support of the ES chip. The exposed oxide is etched in BHF. After etching the photoresist is stripped in oxygen plasma.</p>
	<p>Spring oxide etch (Device layer): Photolithography is performed on the device layer side to etch the oxide from the area of the springs. The oxide is etched in BHF and the photoresist removed by stripping in oxygen plasma.</p>

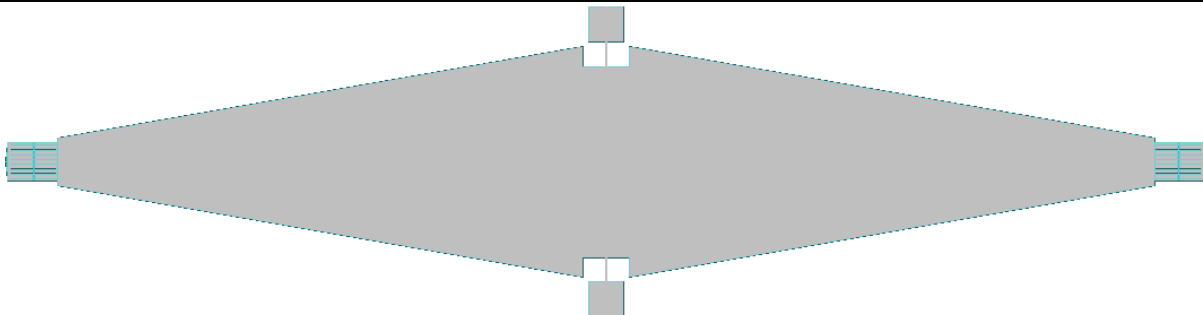
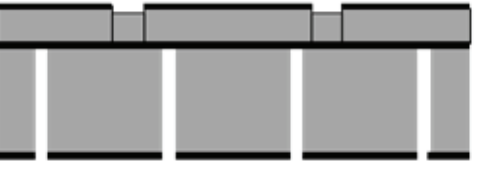
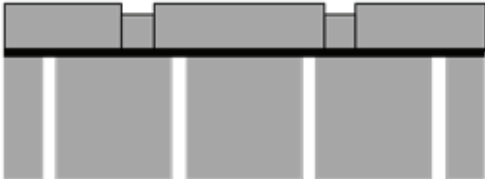
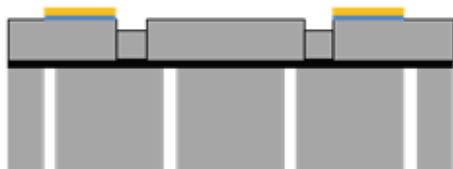
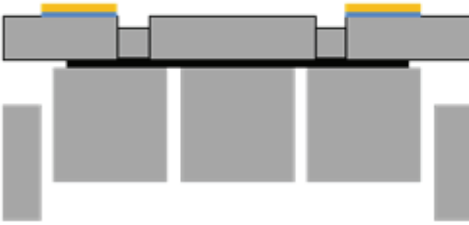


Figure 7-7 Schematic of device layer; the proof mass and springs are defined in the handle layer

	Device Layer DRIE: The device layer structures such as the proof mass and springs are defined in this step. Photolithography is performed using thick photoresist, since a photoresist thickness of at least 7 microns is needed to etch the 130 microns of silicon in the device layer. To avoid swelling of the resist prior to DRIE, it is postbaked overnight at a lower temperature. DRIE is performed and the remaining resist is stripped using oxygen plasma.
	Spring DRIE: Now the oxide forms a mask all over the device layer except for the springs. This oxide mask protects the rest of the device layer while the spring is etched by 22.5 microns so its height becomes 108.5 microns. (This step is not implemented for the final ES chips)
	Handle layer DRIE: The handle layer structures such as the chip outline, proof mass support, sense and feedback electrodes are defined in this step. Photolithography is performed using thick photoresist, since a photoresist thickness of at least 10 microns is needed to etch the 500 microns of silicon in the handle layer. To avoid swelling of the resist prior to DRIE, it is postbaked overnight at a lower temperature. DRIE is performed and the remaining resist is stripped using oxygen plasma.
Standard cleaning	Preparation of the wafers for oxidation
Oxidation	The wafers are oxidized in steam at 1100 degrees Celsius till silicon dioxide of desired thickness is formed on the wafers. This second oxidation ensures that fine particles of silicon that form during DRIE are removed via oxidation. This oxidation step is also used to reduce the width of the springs

	to a desired value, by controlling the depth of oxidation.
	Surface Oxide Removal: The wafers are kept in HF vapor for an hour until the surface oxide on the device and handle layers is removed.
Ohmic contacts 	Aluminum is evaporated through a shadow mask onto the wafers to define the areas where ohmic contacts will be made to the silicon for sensing, feedback and control of electric potential. After Al deposition the wafers are annealed in a nitrogen atmosphere to form the ohmic contacts. A layer of gold is deposited on top of the aluminum to protect the aluminum during the next step, which involves exposure to hydrogen fluoride. Later, wirebonds are made to the gold layer.
HF vapor release of chips 	After the etch is complete, the Earth sensor chip is freed from its wafer by placing it in HF vapor. But the proof mass is still attached to the chip by means of the oxide between handle and device layers.

7.2.2. Fabrication of hard stops

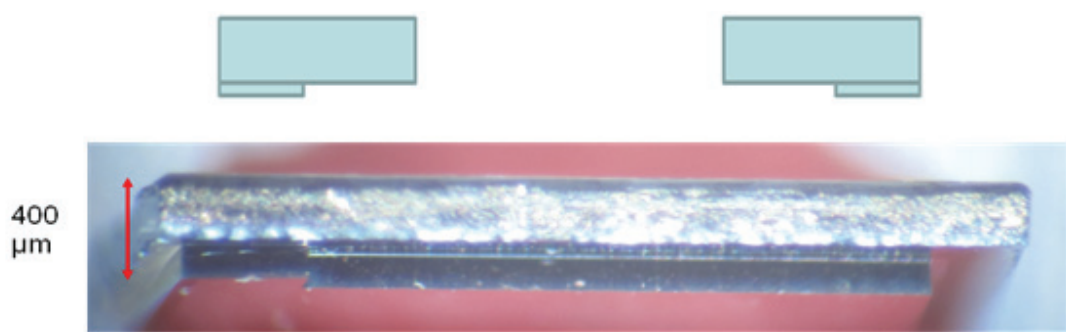
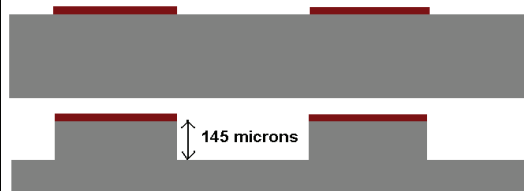
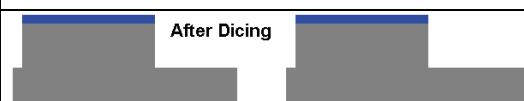
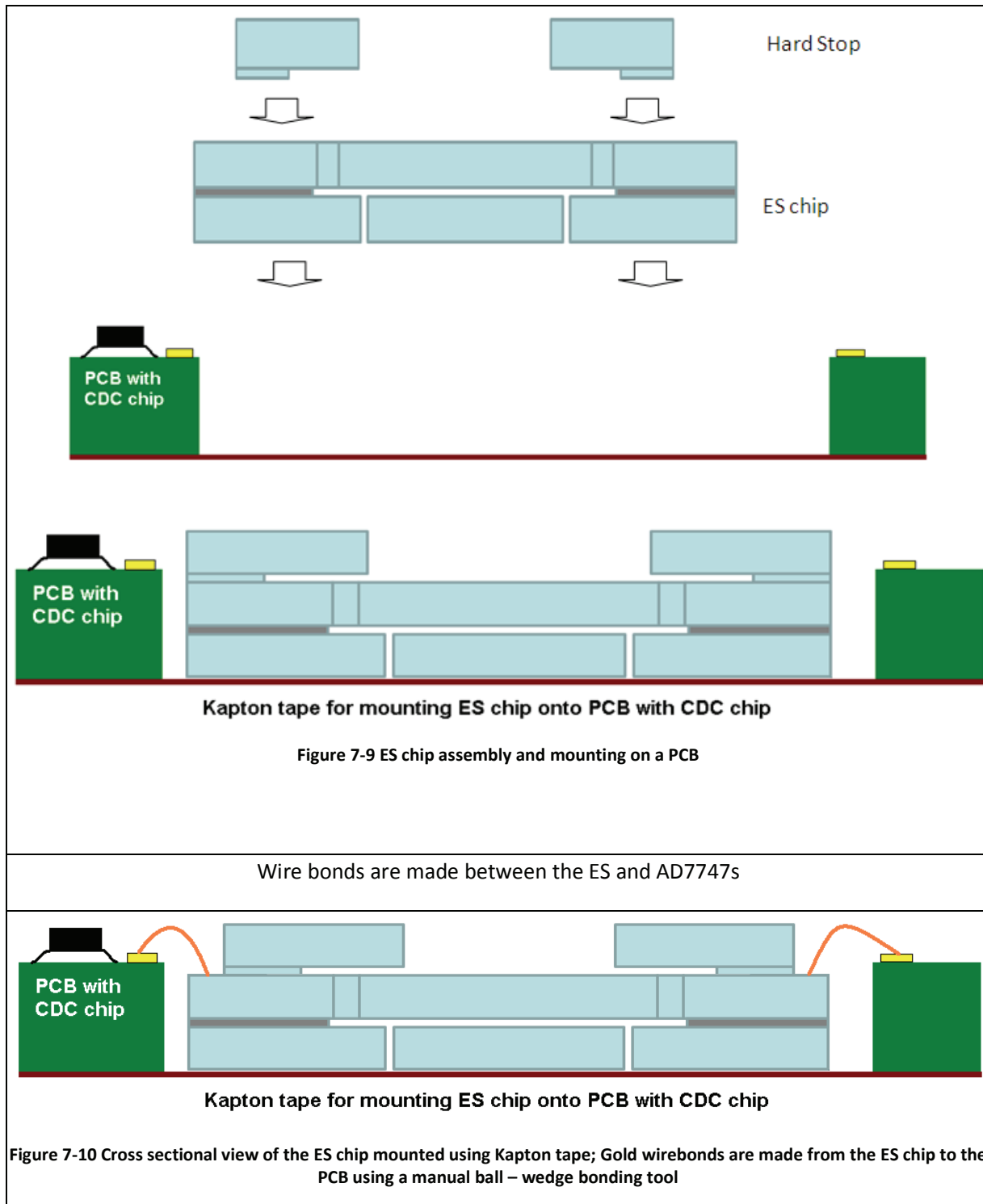


Figure 7-8: Photo showing the fabricated hard stop and the shape that fits into a corresponding slot on the ES chip

Steps to fabricate Si hard stops	
	DRIE is done to define the shape of the hard stop. Photolithography is performed using thick photoresist, needed to etch 145 microns of Silicon. DRIE is performed and the remaining resist is stripped using oxygen plasma.
	Aluminum is evaporated through a shadow mask onto the hard stops. After Al deposition the wafers are annealed in a nitrogen atmosphere. This is required to be able to control the electric potential of the stops.
	The individual hard stops are diced from the silicon wafers

7.2.3. Earth Sensor Assembly

The Hard stops are bonded on the ES chip using conductive epoxy, and the assembly is mounted on a PCB using 6.35 mm wide Kapton tape. Kapton is used since a low stress mounting for the sensor is required (Section 7.4.1)



7.3.Issue with HF release

Based on the experience with the 1st generation sensor, the 2nd generation ES is designed with increased oxide overlap between the device and handle layers, in the region of the anchors that hold the different electrodes to the chip. As compared to the parts that hold the proof mass to the chip, and are etched away to release the proof mass, the oxide overlap at the anchors is 400 percent more. Even with the increased overlap area, the parasitic capacitance between the sense electrode and the anchor, and also the capacitance between the anchor and the chip frame, is limited to 200 pF. This is below the 250 pF limit allowed by the AD7746 / AD7747 [20, 21]. Even with variations in the etch rate, the anchors holding the parts of the chip together are not etched away. The long etch time is seen to damage the aluminum evaporated for the ohmic contacts (Figure 7-11). The resulting surface roughness of the contact also means that wirebonds cannot be made from the PCB to the contact. Attempts to remove the damaged aluminum from the wafer were unsuccessful.

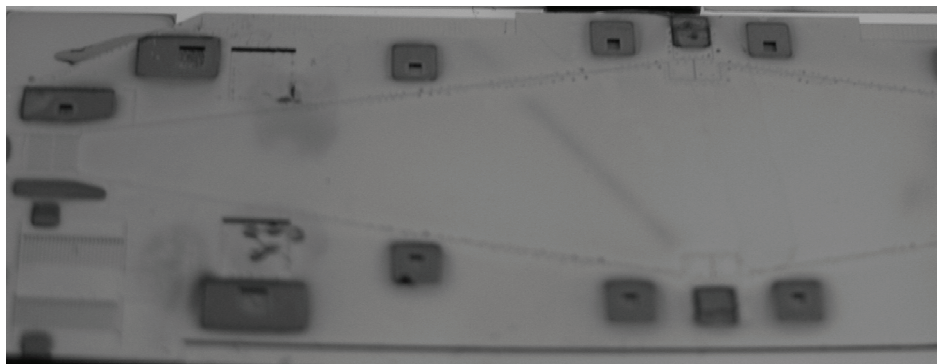


Figure 7-11 Damage to aluminium contacts after exposure to HF vapour

7.3.1. Solution to Uniformity issues

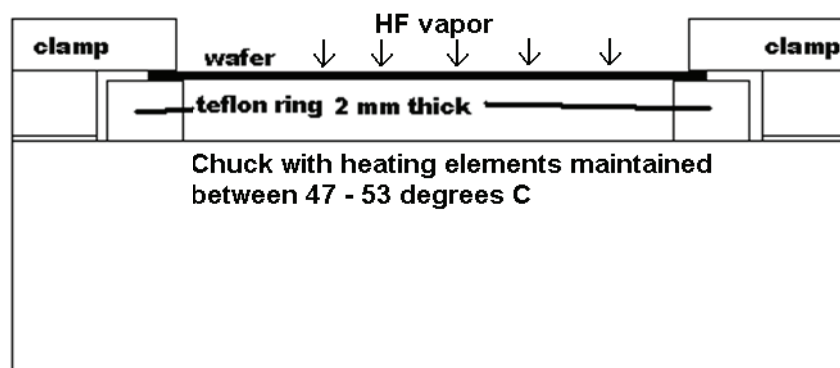


Figure 7-12 Modified HF vapour etch process utilizing a Teflon spacer for convective heating of the wafe

For the next fabrication run, a modified HF vapor etch process is developed. Previously, to control the etch rate, the wafer was heated using conduction from a chuck holding the wafer during exposure to HF release. Due to non-uniform contact between the chuck and the wafer, the etch rate varies by a factor

of two or three across a single chip. To improve the uniformity, a 2 mm thick Teflon ring separates the wafer from the chuck (Figure 7-12). Instead of heating by conduction, the wafer is now heated by convection from the chuck. This results in a more uniform temperature across the wafer. The etch rate is observed to vary by a factor of 1.1 or 1.2 across the wafer. Figure 7-13 shows a series of photos taken using an infra red camera, of different chips on the same wafer after 17 hours of exposure to HF vapor at a temperature of 48°C. The oxide etch rate is seen to be uniform.

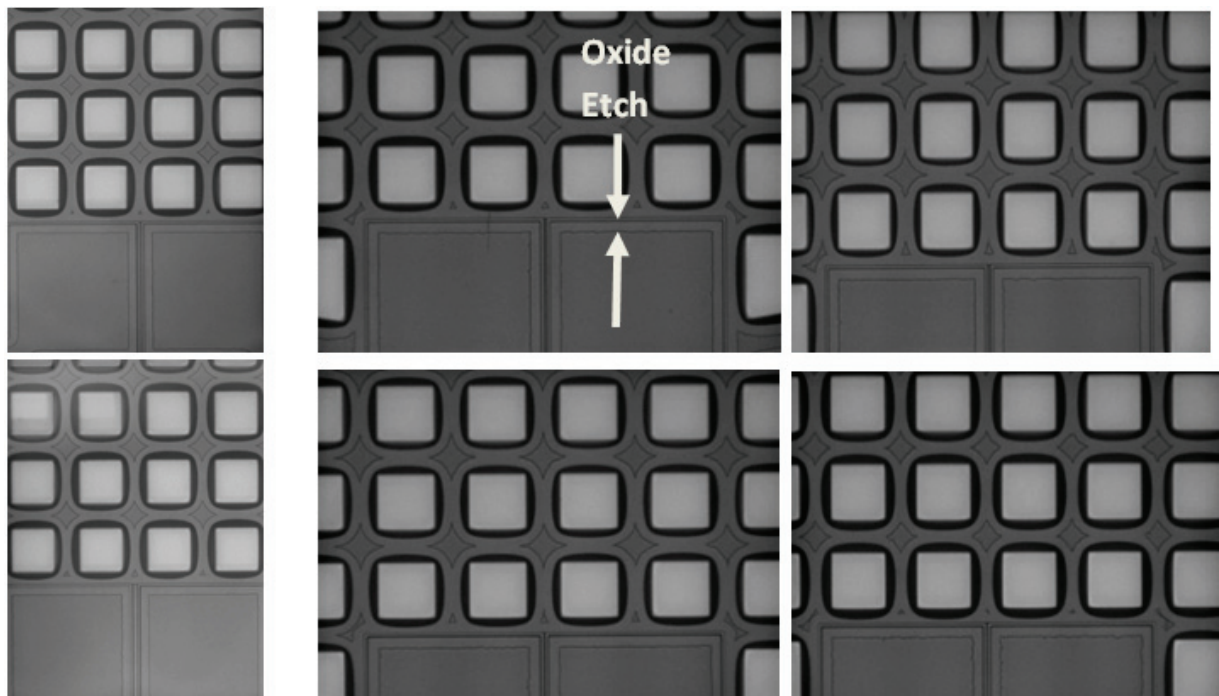


Figure 7-13 Photos of same section of different ES chips on a wafer, showing the uniformity in oxide etch due to convection heating of the wafer

7.3.2. Solution to Aluminum damage

In later fabrication runs, gold of 300 nm thickness is deposited over the aluminum contacts. The gold is not affected by the HF vapor, and prevents the HF vapor from damaging the Aluminum. No damage is observed to the gold over the total 30-36 hour duration of exposure to HF vapor for the release of the proof mass.

The wirebonder used for making the contacts between the chip and the PCB uses gold wire. Ball bonding a gold wire to a gold contact is much more reliable. The PCB contact pads are made from Au-Ni. (Figure 7-14)

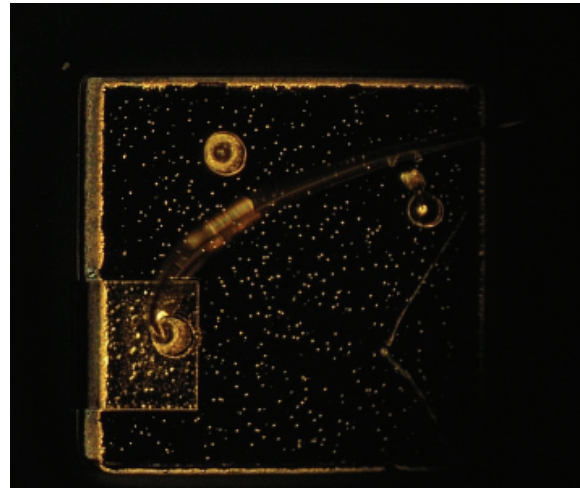
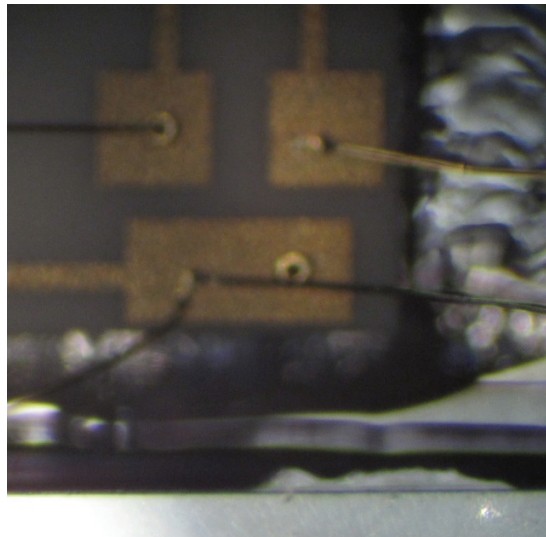


Figure 7-14 Wirebonds on PCB gold pads Wirebond from proof mass chip on gold surface

7.4. ES chip mounting

Though the chips obtained from the initial fabrication runs were not usable for tests due to the aluminum contacts being damaged, they were used to verify further steps such as mounting the ES chip on a PCB.

The test chips fabricated prior to the Earth Sensor were bonded using epoxy to their underlying substrate. The first test chips were bonded using minimal amounts of epoxy, but the resulting mounting was found to be susceptible to damage due to the force of the wire bonding needle while making wirebonds to the capacitance sense electrodes. So each electrode was supported underneath by a epoxy bump and the resulting test chips could survive the force of the bonding needle. The same method was used with the Earth sensor and epoxy was used to bond the proof mass chip to the underlying base chip, with an epoxy bump underneath each electrode.

The surface profile of the proof mass was measured in the region of the capacitance sense electrodes, before and after mounting on the PCB with epoxy using an optical profiler (Wyko DMEMS 1100). Before mounting both ends of the proof mass are seen to be roughly at 2.5 microns below the surrounding chip area (Figure 7-15).

After bonding the proof mass chip to the base chip, the profile measurements at the extremities of the proof mass were redone and the ends of the proof mass of the chip was observed to be above the plane of the chip, instead of below, as seen in the Figure 7-16. The proof mass is observed to be pushed against the vertical hard stops that restrict out of plane motion. One end of the proof mass is 11 microns above the surrounding chip area, and the other is 4.7 microns above.

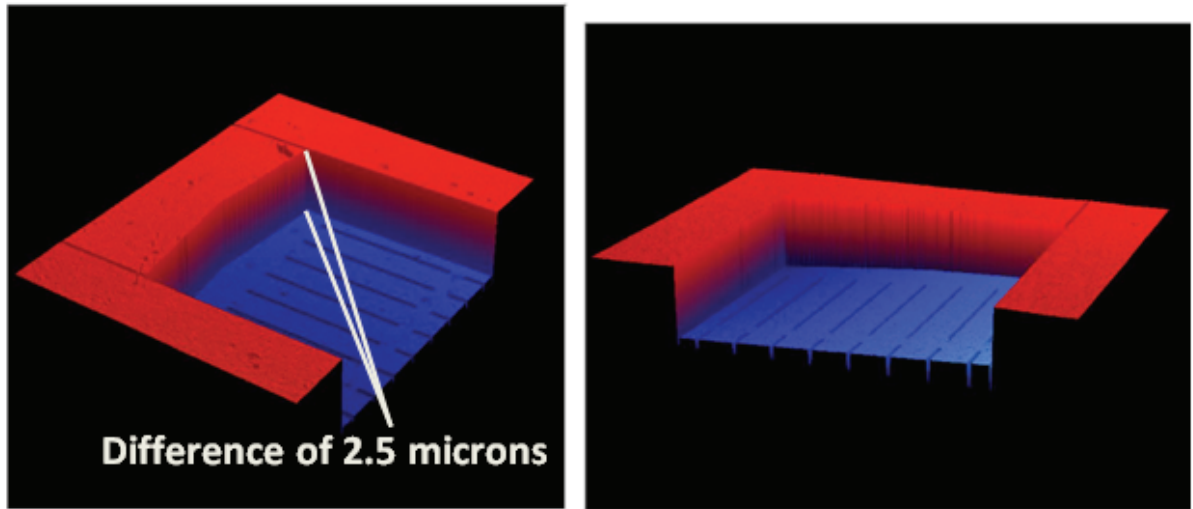


Figure 7-15 Profile measurements of proof mass chip after HF release showing proof mass ends below the plane of the surrounding chip

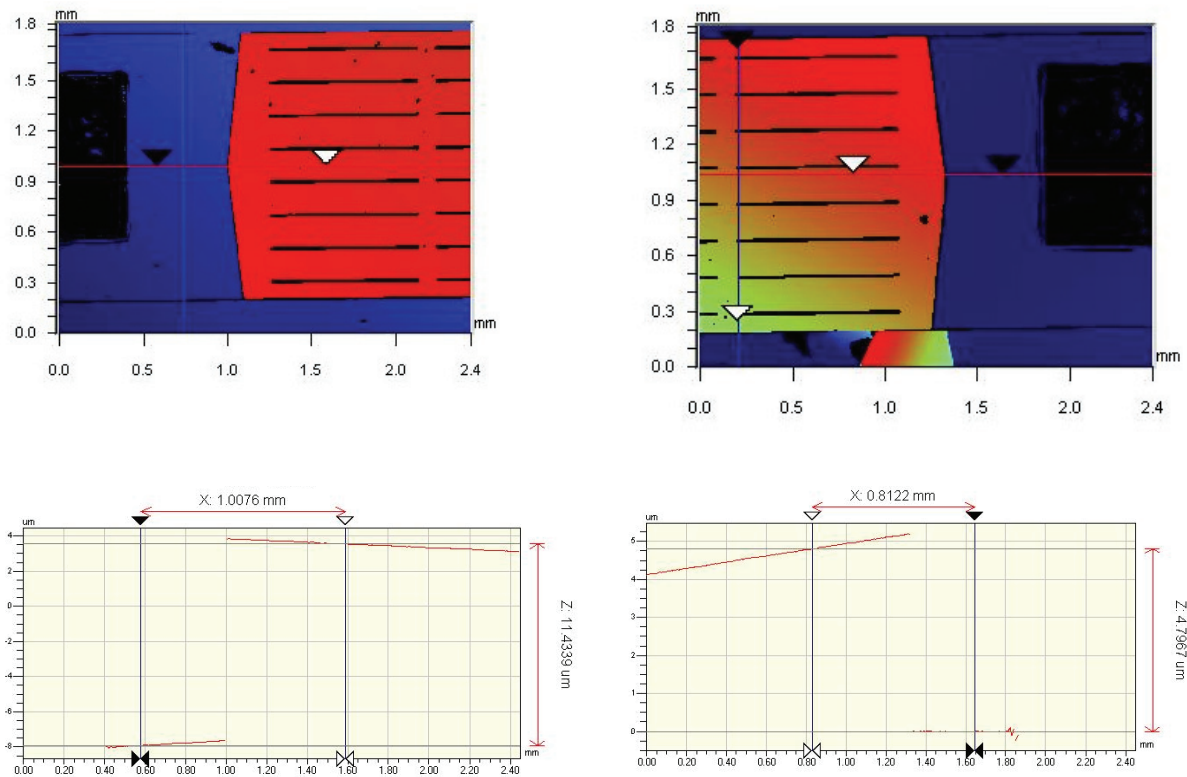


Figure 7-16 Profile measurements of the proof mass, after bonding to base chip, showing the proof mass 11 microns, and 4.7 microns above the plane of the chip, at different ends of the chip

Since this was seen after assembly of the proof mass chip with the PCB, the likely cause of the proof mass being pushed against the hard stops is stress induced on the chip frame due to being glued to the base chip using epoxy, which causes the frame to bend as seen in Figure 7-17 and the proof mass, being released from the chip frame, then comes to rest against the hard stops and cannot move freely.

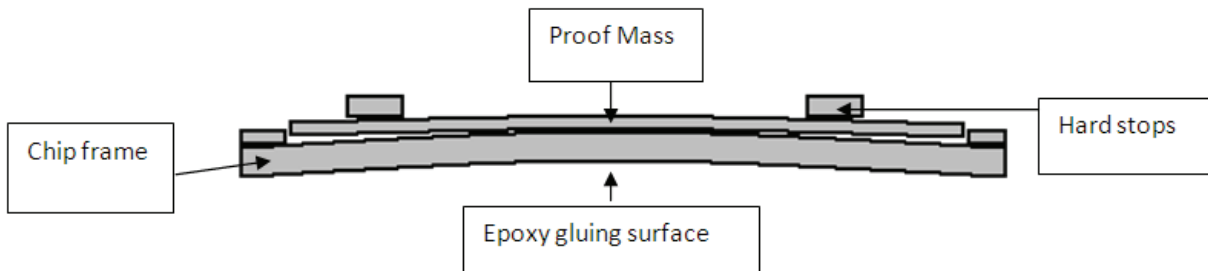


Figure 7-17 bending of the chip frame due to stress coming from epoxy gluing with the base chip

7.4.1. Solution for low stress mounting

The stress is likely to have been introduced due to change in dimension of the epoxy while curing. Also the amount of epoxy at different points around the chip frame will vary by some amount, and this is also likely to stress the frame once the epoxy hardens. To prevent this kind of stress on the proof mass chip, the mounting is done using Kapton tape. Kapton is commonly used in vacuum equipment, and is suitable to use with the Earth Sensor. Since there is no curing involved there should be minimal stress on the chip frame, such as that introduced by the epoxy (Figure 7-18).

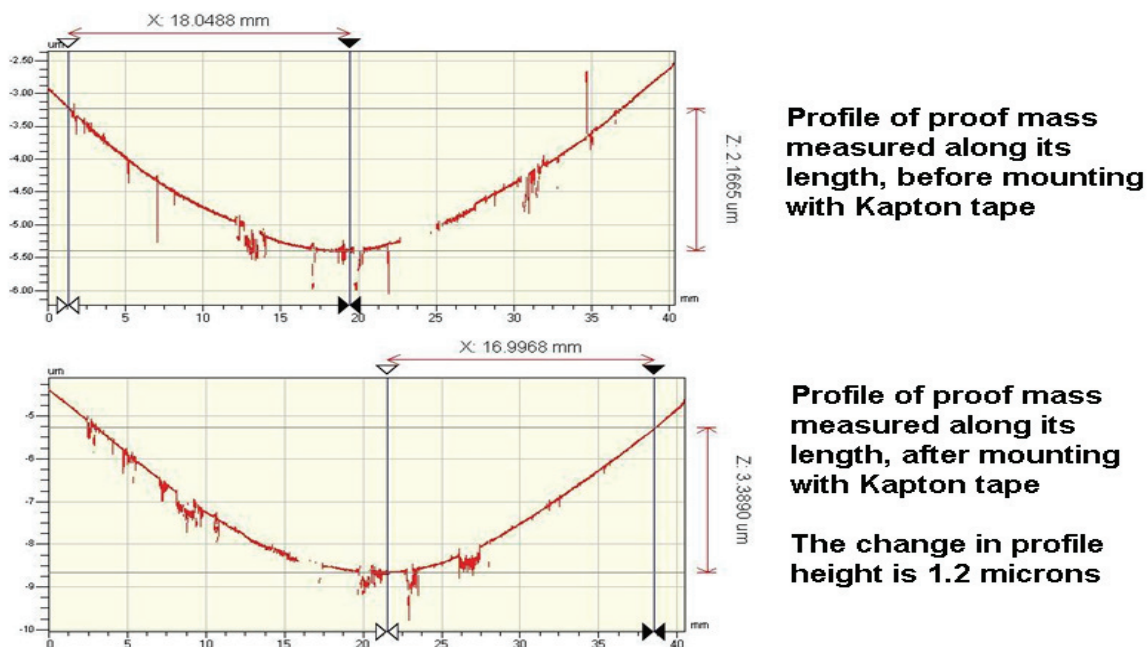


Figure 7-18 Comparison of proof mass surface profile before and after mounting the chip onto a PCB using Kapton tape

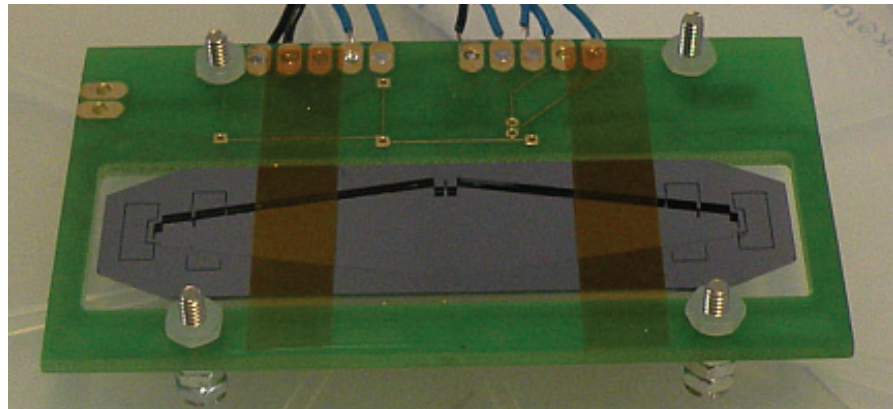


Figure 7-19 2nd Generation MEMS Earth sensor chip mounted with Kapton onto a PCB

7.5.Differential Wafer Bow

The ES chip is made from an SOI wafer, which is comprised of a device layer and handle layer. Earlier in the chapter, during fabrication steps to compensate for the bow of the SOI wafer were described. After fabrication of the chip, the proof mass, which is made from the device layer, is released from the chip frame, which is made from both handle and device layers. The handle layer thickness is 500 microns, and for mechanical rigidity, a continuous piece of the handle layer forms the chip frame.

During the SOI fabrication process, two silicon wafers are bonded together using a layer of oxide. The individual wafers have their own bow. One is polished to form the device layer, the other is polished to form the handle layer. After final release of the proof mass, its shape depends on the bow of the silicon wafer that the device layer is made from, while the chip frame follows the bow of the handle layer wafer.

Figure 7-20 and Figure 7-21 show the surface profile measurement of the handle layer and device layer of the same ES chip, which is placed with the device layer facing the profiler table. Figure 7-20 shows the variation in the profile of the device layer over the length of the chip. The handle layer has negligible bow since the height variation over the 5 cm length of the chip is only 0.3 microns. Figure 7-21 shows the same measurement for the device layer of the chip, measured along the length of the proof mass. A high bow is seen, with the height variation over the 5 cm length of the proof mass being 7.2 microns. This variation is much more than the expected 2.5 micron sag at the extremities of the proof mass due to gravity. This shows the differential bow between the proof mass and the chip frame for the ES chip.

Depending on the differential bow of the two wafers that comprise the SOI wafer the ES chip is produced from, the chip may not be testable. The separation of the proof mass and the different hard stops ranges from 2.5 microns – 10 microns over the 5 cm length of the proof mass. If the differential bow exceeds this amount over the 5 cm length, then the proof mass will end up touching the hard stops. Some examples of the result of differential bow between the chip frame and proof mass are seen in

Chapter 7: Fabrication of 2nd Generation Earth Sensor

Figure 7-22. Even when the chip is testable, the bow can change the characteristics of the capacitance readout. This is examined in more detail in Chapter 8.

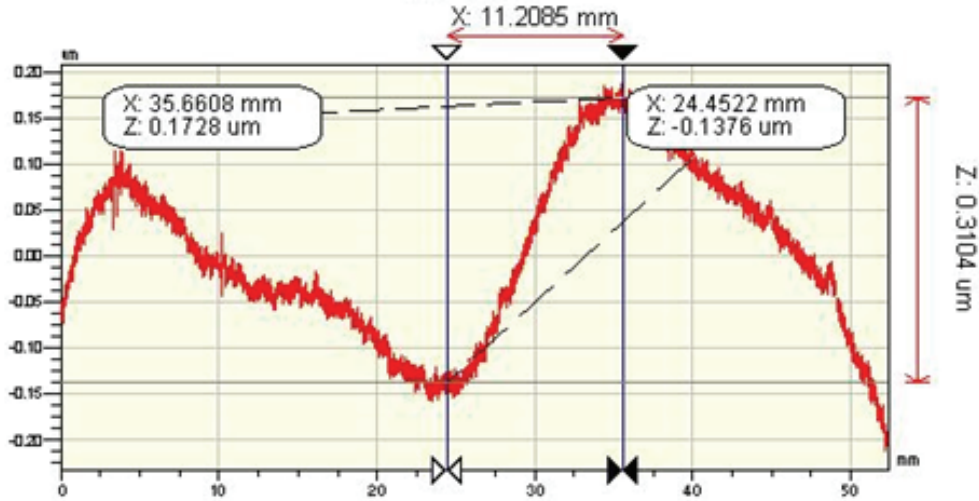


Figure 7-20 Surface profile measurement along length of handle layer of ES chip showing negligible bow

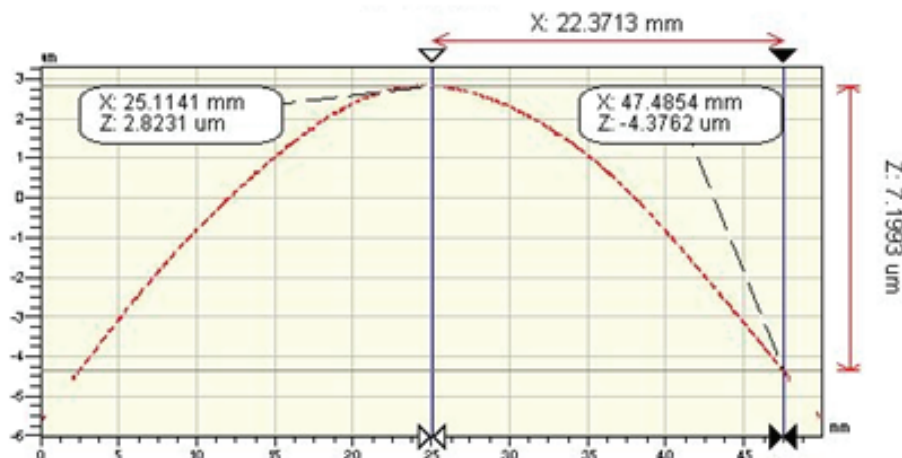


Figure 7-21 Surface profile measurement along length of proof mass (device layer) for same chip as in Figure 7-20, that shows a bow of > 7 microns

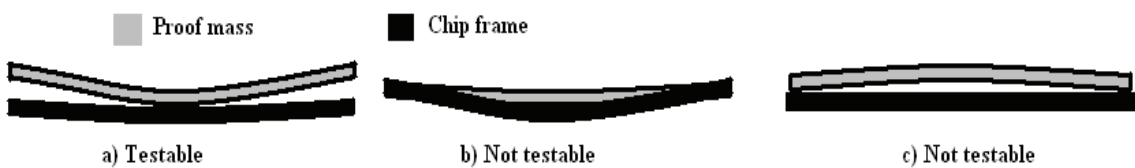


Figure 7-22 Different combinations of the bow of the proof mass and chip frame

7.5.1. Design modification for differential bow

Figure 7-23 shows the initial design of the handle layer. There is a pattern of beams in the area underneath the proof mass to increase the mechanical rigidity of the chip. Figure 7-24 shows the final design in which the beams beneath the proof mass are removed. This does not completely eliminate the bow problem, since the proof mass could still touch the hard stops at the extremities of its length.

Previously, for chips that had a stuck proof mass, it was not possible to determine whether the stiction is due to the proof mass touching the handle layer. Due to the beams, the edge of the proof mass was not visible, and the optical profiler had no reference to measure the gap between the proof mass and the handle layer. The new design removes the beams, and the only sections of the handle layer underneath the proof mass are the sense and actuation electrodes. With this design, the edges of the proof mass are visible, and it is possible to determine if the proof mass is stuck due to bow.

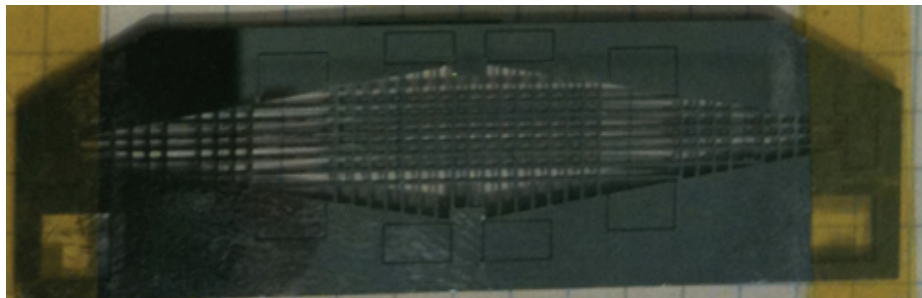


Figure 7-23 Design of handle layer for initial fabrication run. The handle layer has beams underneath the length of the proof mass for greater mechanical rigidity



Figure 7-24 Modified design of handle layer, to mitigate possible stiction at the center of the chip due to bow

7.6. Conclusion

Multiple fabrication runs were necessary for the 2nd generation ES, and issues such as damage of the aluminum contacts by HF, wirebonding problems, and high stress of mounting using epoxy are resolved. The design of the handle layer is changed for the final fabrication run. The fabrication process is improved from that for the 1st generation sensor. Due to resolution of the problems arising from the HF release process step, several chips are obtained for testing. Hard stops fabricated from silicon are integrated in the ES chip. This is done earlier in the fabrication process, and premature release of the proof mass is prevented. Gold wirebonds are made between the electrodes on the ES chip, onto the PCB

Chapter 7: Fabrication of 2nd Generation Earth Sensor

with the CDC chip. Compared to the 1st generation sensor, many more 2nd generation chips were available for testing at the conclusion of fabrication.

	Issues Encountered	Resolution
1 st Fabrication run (2 Wafers)	Large variation in HF etch rates, damage to aluminum contacts	Modified HF vapor etch process for more uniform etch rates, Gold deposition to protect aluminum contacts
2 nd Fabrication run (2 wafers)	Mounting chips with epoxy results in a large stress on the chip frame, resulting in proof mass touching the hard stops, Differential bow between handle layer and device layer results in proof mass touching hard stops	A low stress mounting solution that uses Kapton tape to mount the ES chip on a PCB, Change of chip design for greater tolerance to differential bow, Easier characterization of how the differential bow affects an ES chip
3 rd Fabrication run (3 wafers)	Differential wafer bow still exists, but chips are testable	

Table 7-1 Summary of fabrication iterations for 2nd Generation ES chip

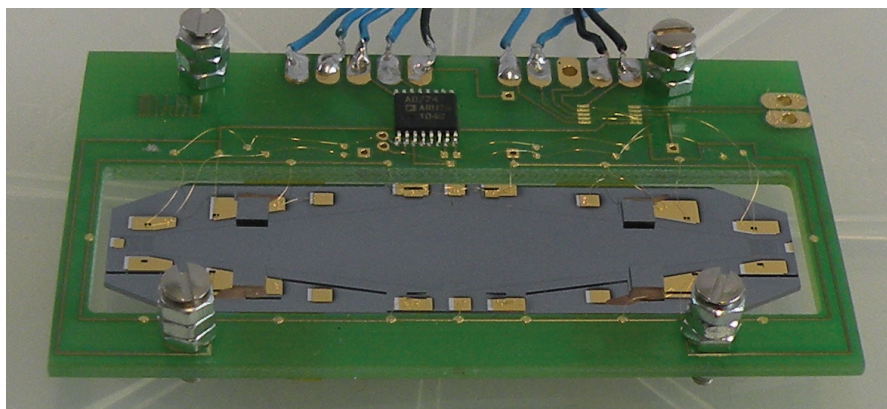


Figure 7-25 Assembled 2nd Generation ES chip with wirebonds to CDC chip for capacitive displacement sensing

Chapter 8

Testing of 2nd Generation Earth Sensor

This chapter describes the tests performed on the 2nd generation Earth Sensor. Due to the improvements in design and fabrication described in Chapters 6 and 7, more chips were available for testing. Due to the changed design, it was easier to setup the chip, such that the proof mass was not touching any of the hard stops, and more tests could be carried out as compared to the 1st generation. Tests were performed on different types of ES chips, fabricated from the same wafer, as listed in Table 8-1. All tests are not performed using all three chips, but the chips are used as required for different kinds of tests.

Chip Designation	Designed Resonant Frequency [Hz]	Readout	Tests Performed
1.5 Hz7745	1.5 Hz	AD7745	Electrical and Mechanical
10Hz7747	10 Hz	AD7747	Electrical and Mechanical
20Hz	20Hz	-	only Mechanical tests

Table 8-1 List of chips used in the tests performed for the testing of the 2nd generation ES

Based on the discussion in Chapter 2 about the required characteristics of a MEMS based sensor to measure GGT, and the detailed design of the 2nd generation ES in Chapter 6, for a fixed orbit height, and fixed moment of inertia of the proof mass, to achieve a sufficiently accurate measurement of the GGT the ES chips should have the following characteristics:

- The resonant frequency of the sensor should be as low as possible, with a minimum limit being imposed by the desired update rate. In Chapter 6 the spring dimensions that should result in a resonant frequency of 1.5 Hz are specified.
- The noise of the capacitive displacement sensing electronics should be low enough to detect the minimum required displacement due to GGT, corresponding to the targeted accuracy of 2° in an orbit of height 700 km. For the sensor design of the ES with the 1.5 Hz resonant frequency, this means sensing a 200 aF change in capacitance for a 0.05 nm displacement. This change in capacitance is computed for a 10 pF sense capacitance at the ends of the proof mass. The sense capacitance depends on the gap between the proof mass and the electrode connected to the AD7745 / AD7747. The ES design takes into account the sag of the proof mass due to gravity, which results in a gap of 2.5 microns.
- The quality factor of the proof mass and spring system in vacuum should be of the order of hundreds.

8.1. Test Goals

To verify how well the fabricated Earth sensors meet the desired characteristics, the following types of tests are performed:

- Estimate the resonant frequency of the ES, by measuring the dimensions of the spring post fabrication
- Measure the noise in the electronics of the capacitive displacement electronics, for both the AD7745 and the AD7747, when no displacement is applied to the proof mass
- Measure the sensitivity of the capacitive displacement sensing by applying a displacement to the proof mass using electrostatic actuation.
- Measure the transient response of the 2nd order spring – proof mass system, and estimate the quality factor from the response
- Test the response of the sensor to electrostatic actuation, so that it can be operated in a closed loop when used on a satellite

8.2. Orientation of ES chips for test

The Earth sensor chips, mounted on a PCB which has the displacement sensing CDC chips on it are oriented with the plane of the proof mass parallel to the ground, as shown in Figure 8-1. The piezo stage shown in Figure 8-1 has some fine adjustment screws on it which allow the tilt of the stage to be adjusted by a few degrees. When the ES chip is placed on the piezo stage, these screws are used to make the stage as flat as possible. Based on ANSYS modeling, the ES chip can tolerate tilts of upto +/- 0.5° in the XZ plane (Figure 8-1) before the proof mass touches the hard stops. The screws on the piezo stage can be used to adjust the tilt of the sensor below +/- 0.5°.

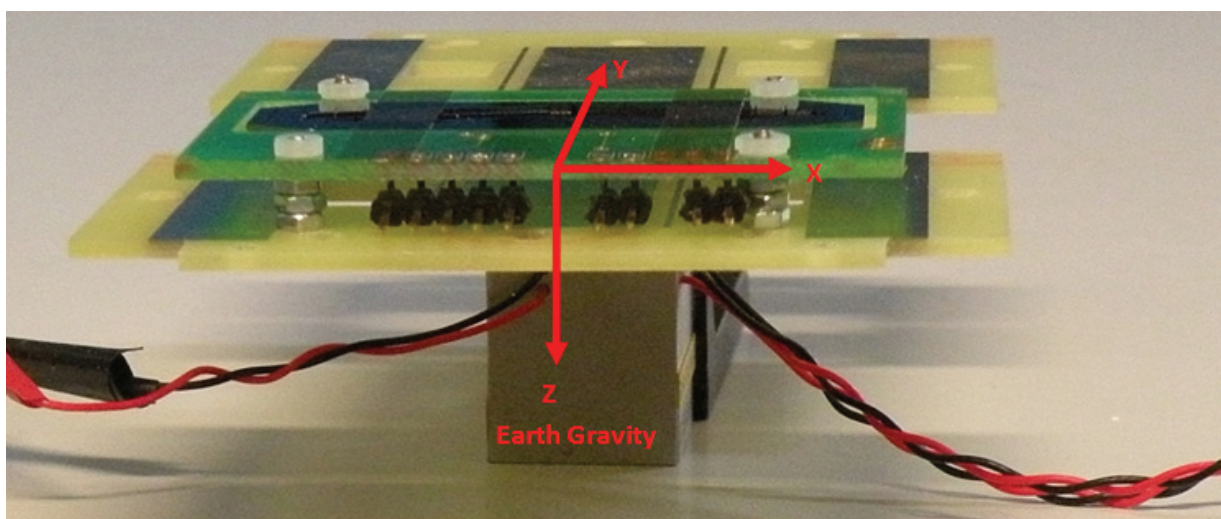


Figure 8-1 Earth sensor placed on piezo tilt stage. For all the tests performed, the Earth sensor chip is placed in this orientation with respect to the Earth's surface.

To ensure that the proof mass is not touching the lateral stops, the extremities of the proof mass are inspected using a microscope. After the tilt of the chip is controlled, the piezos on the stage are used to provide a small rocking motion to the ES chip. If the proof mass is not touching any hard stop, then it will move relative to the chip frame. This motion is recorded by the capacitive displacement sensing and the output of the CDC can be used to verify that the proof mass is freely moving. Then more tests can be performed.

8.3. Estimation of Fundamental Resonant Frequency

In Chapter 6, based on estimates of squeeze film damping in air, the ES is predicted to be overdamped in air for the fundamental mode. This is confirmed by the step response of the sensor measured in Section 8.5. Since no ringing is observed in air, measurements of the fabricated spring are used to estimate the resonant frequency of the sensor.

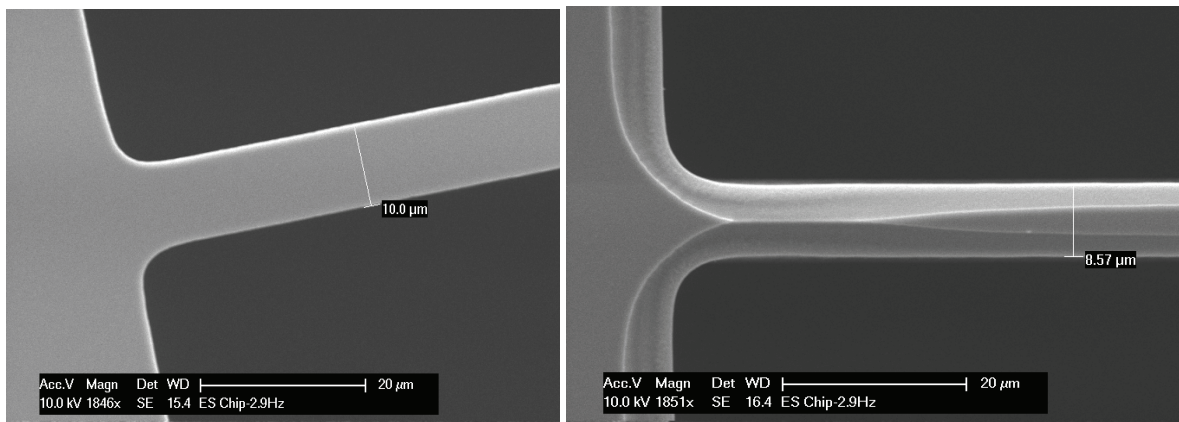


Figure 8-2 SEM photographs of the top (left) and bottom (right) of the spring of an ES chip designed to have a resonant frequency of 1.5 Hz. Some notching is observed on the underside of the spring. The estimated resonant frequency is 2.9 Hz

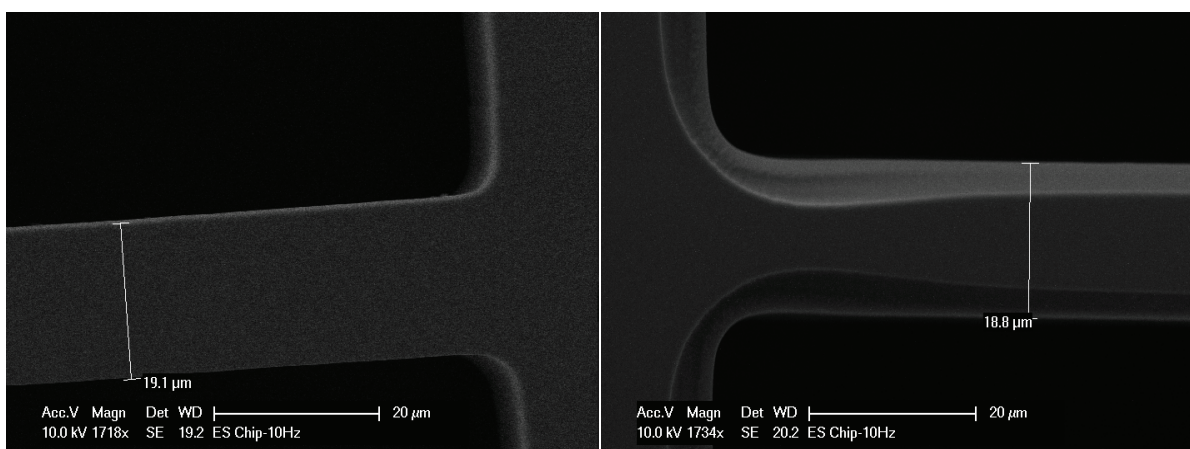


Figure 8-3 SEM photographs of the top (left) and bottom (right) of the spring of an ES chip designed to have a resonant frequency of 9.9 Hz. The estimated resonant frequency is 12.5 Hz

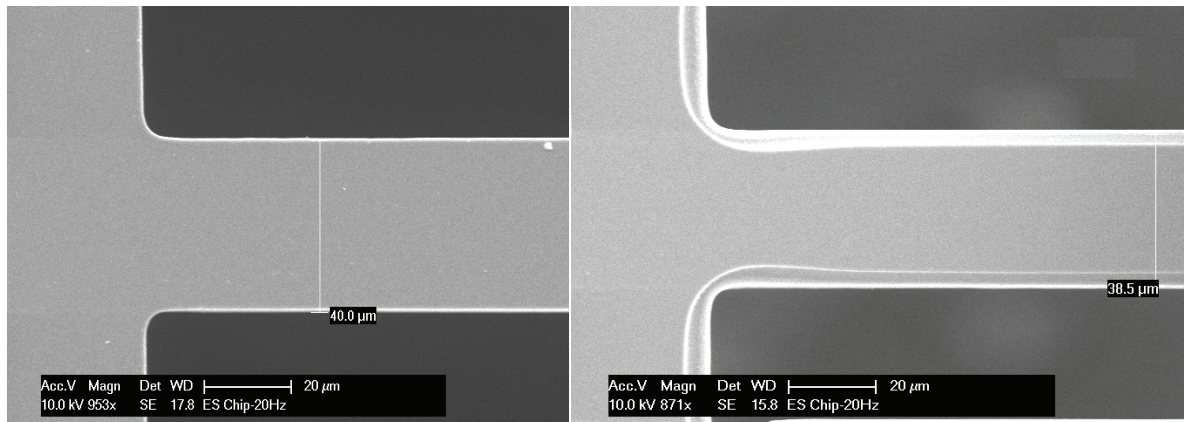


Figure 8-4 SEM photographs of the top (left) and bottom (right) of the spring of an ES chip designed to have a resonant frequency of 20.5 Hz. The estimated resonant frequency is 26 Hz.

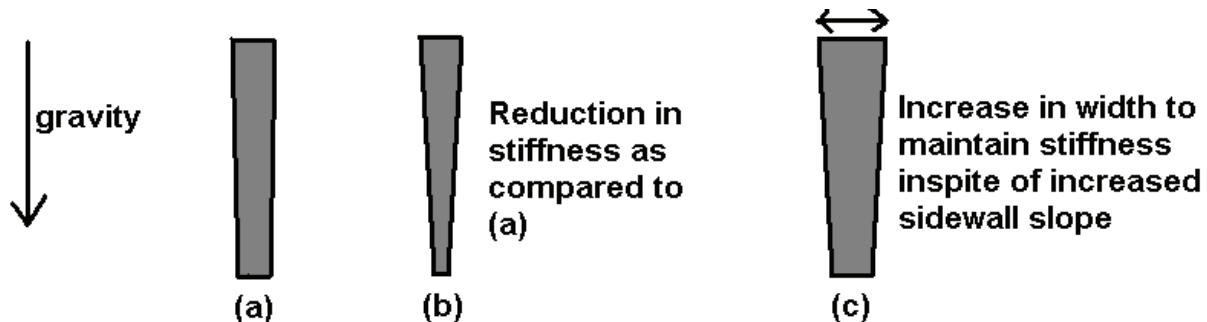


Figure 8-5 a) Spring cross section with low sidewall slope b) spring with reduced stiffness for gravity due to increased sidewall slope c) Increase of width at top to compensate for reduced stiffness due to sidewall angle

Post fabrication, the spring does not have an ideal rectangular cross section. The resonant frequency of the ES depends on the trapezoidal cross section of the spring, which is determined by the sidewall angle during the DRIE etch step. The design for the spring was done assuming a sidewall slope of 100:1. In test fabrication runs done before the ES fabrication, the DRIE sidewall slope was found to be 100:2. Figure 8-5 shows the effect of an increased sidewall slope, due to which the stiffness of the spring in the direction of gravity reduces, which results in a reduction in the gap between the proof mass and the hard stops. The proof mass should not touch any hard stops for tests to be performed. Since obtaining testable chips is important, during fabrication, the width of the spring is kept at 10 microns instead of the 8 microns specified in Chapter 6, to maintain testability of the chips in case the DRIE sidewall slope is higher than anticipated. From SEM photographs of the spring of the ES chip used for testing, the sidewall slope is found to be 100:0.6 (Figure 8-2, Figure 8-4). This results in a spring whose stiffness is greater for GGT than the designed stiffness, but the gap between the proof mass and the hard stops is maintained. In Chapter 6, a reduction in the height of the spring is described, for the purposes of reducing the error in measuring the GGT when the ES is on a spinning satellite. That step is not carried out for the chips fabricated for test, due to time constraints, and to avoid an additional step that might

result in a reduced yield. Using the SEM measurements for analytical calculations and modeling in ANSYS, the increased width and thickness of the fabricated spring result in an overall increase of the resonant frequency of the 1.5Hz7745 chip from the designed 1.5 Hz to 2.9 Hz. For an ES chip in space, this would result in reduced accuracy in measuring the GGT, but having testable chips on Earth is more important at this stage.

	1.5 Hz design (chip 1.5Hz7745)	9.9 Hz design (chip 10Hz7747)	20.5 Hz design (chip 20Hz)
Design spring width at top	8 microns	18 microns	37 microns
Measured spring width at top	10 microns	19.1 microns	40 microns
Expected sidewall slope	100:1	100:1	100:1
Measured sidewall slope	100:0.6	100:0.1	100:0.6
Expected spring width at bottom	5.4 microns	15.4 microns	34.4 microns
Measured spring width at bottom	8.5 microns	18.8 microns	38.5 microns
Resonant Frequency estimated	2.9 Hz	12.5 Hz	26 Hz

Table 8-2 Summary of spring measurements for different ES designs, and estimates of the Q factor

8.4.Characterization of Gap of Capacitance Sense Electrodes

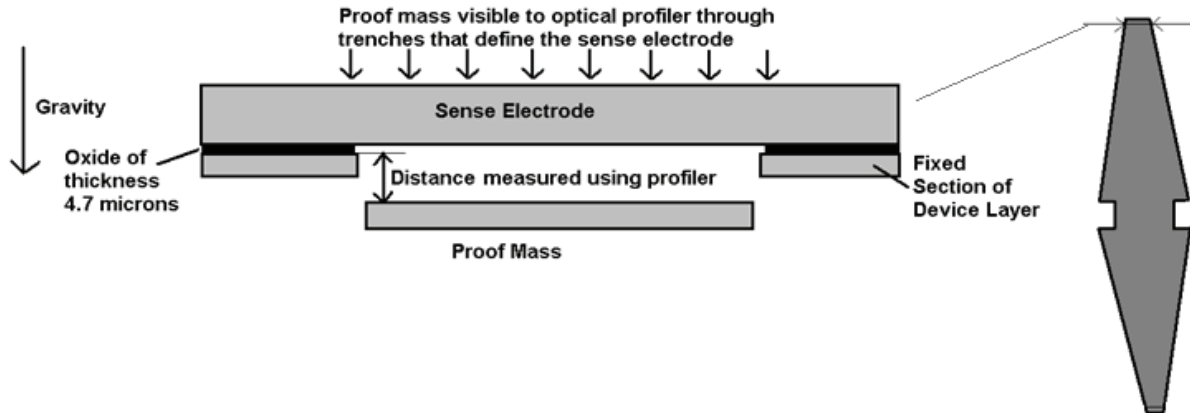


Figure 8-6 Schematic of the cross section of the ES at a when placed upside down for the measurement of the gap between the sense electrode and the proof mass

To determine the nominal capacitance of the sense electrodes, the gap between the proof mass and the electrode is measured using an optical profiler (Wyko DMEMS 1100). In Chapter 7, it was discussed that the nominal capacitance can change due to the differential bow of two layers of silicon that constitute the ES chip. If the differential bow results in the gap between the proof mass and the sense electrode going below 1 micron, then the nominal capacitance of that electrode will be more than what the AD7745 / AD7747 can measure, and the readout will saturate. Before taking measurements on the ES chips, the gap at the sense electrodes is measured as shown in Figure 8-6. To decrease the likelihood that differential bow results in the gap being <1 micron, the chip is placed such that gravity causes the proof mass to sag in the opposite direction from the sense electrode (Figure 8-6) for this

Chapter 8: Testing of 2nd Generation Earth Sensor

characterization. The thickness of the oxide is 4.7 microns measured using a reflectometer during fabrication in the clean room. From the oxide thickness, and the distance measured by the profiler, the actual gap can be calculated.

Figure 8-7 shows the results of the measurement on the chip 1.5Hz7745 using the profiler. At Sense Electrode 1, the proof mass distance is measured to be 6.35 microns, thus giving a total gap of 10.05 microns between the proof mass and Sense Electrode 1. At Sense Electrode 2, the proof mass distance is measured to be -3.85 microns, which then gives a gap of 0.85 microns between the proof mass and Sense Electrode 2. This means that the capacitance measurement from Sense Electrode 2 will result in saturation of the readout. In the first measurements performed with the AD7745 after mounting and wirebonding of the 1.5Hz7745 chip, this is indeed seen to be the case. To work around this, for the tests to characterize the chip, single ended measurements are performed by measuring the capacitance at Sense Electrode 1 only.

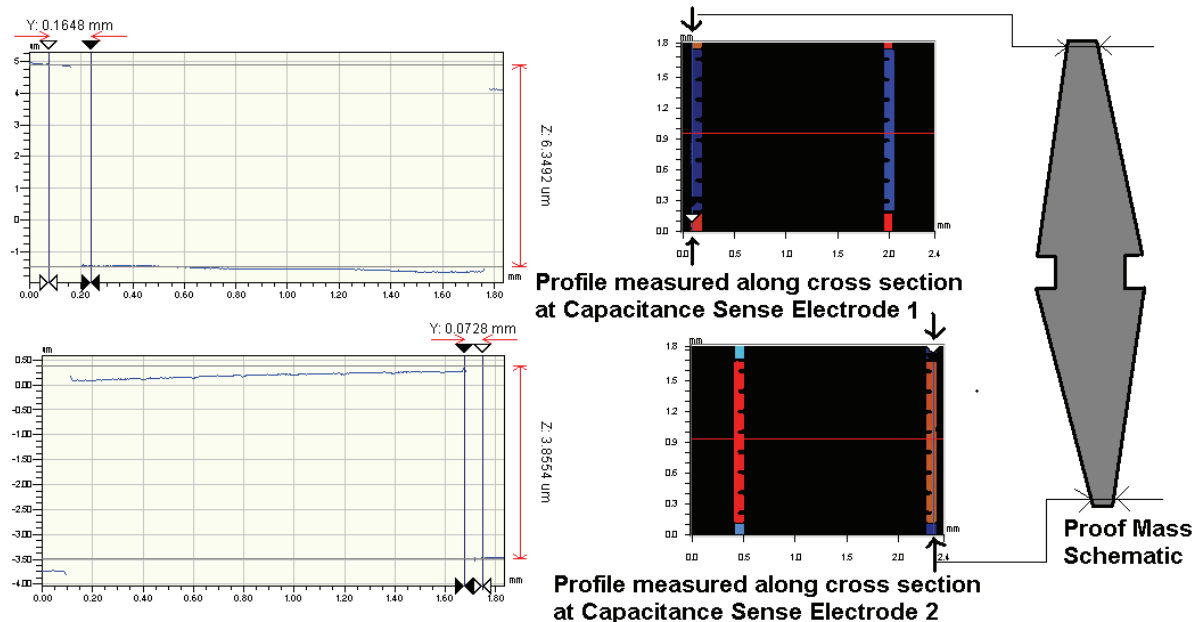


Figure 8-7 Optical profile measurements of the gap at the capacitance sense electrodes of the 1.5Hz7745 chip that has a resonant frequency of 2.9 Hz and uses the AD7745 for measurements

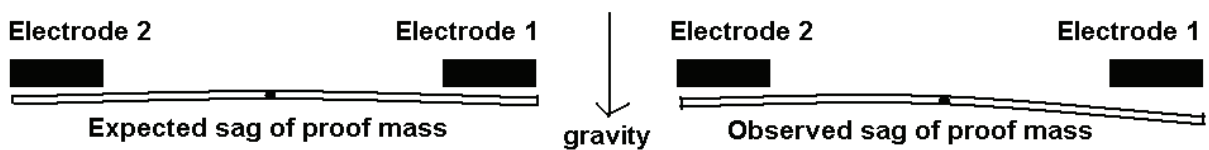


Figure 8-8 Schematics of proof mass for comparison of expected sag and observed profile of proof mass based on measurements in Figure 8-7

Based on the measured gap in Figure 8-7 the sag of the proof mass is asymmetrical. Instead of the expected equal sag at both extremities the proof mass shows a marked out of plane tilting. To

Chapter 8: Testing of 2nd Generation Earth Sensor

investigate this further a profile measurement is performed across the width of the proof mass as shown in Figure 8-9.

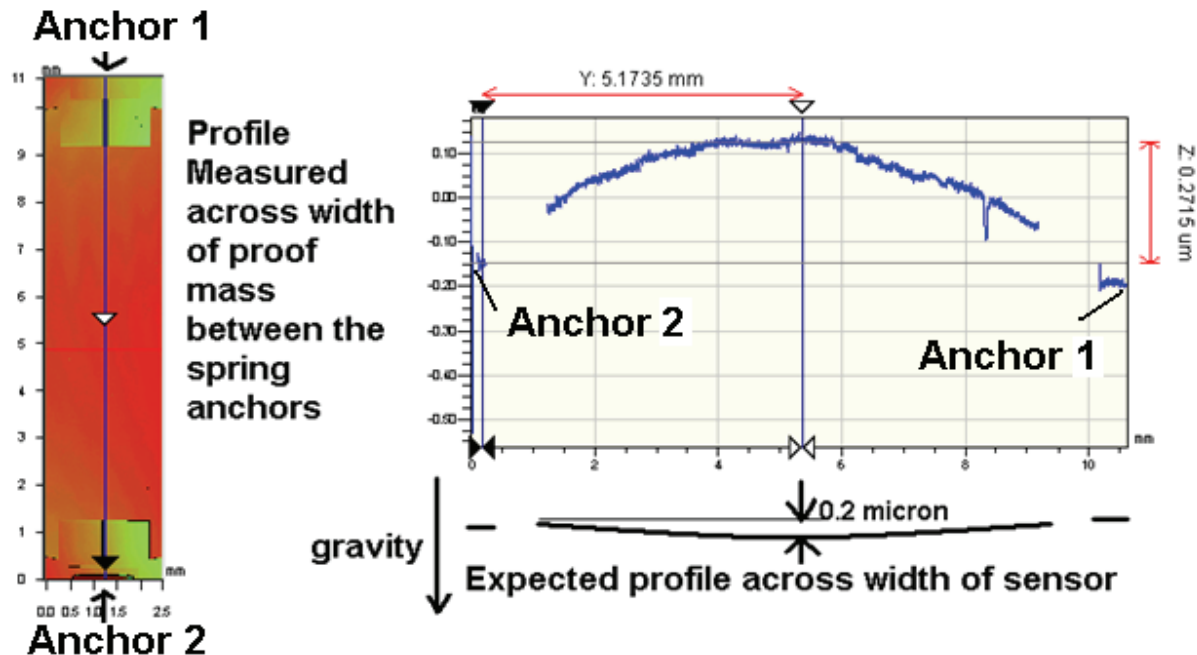


Figure 8-9 Comparison of expected and measured profile of proof mass across the width, between the two anchors of the spring for chip 1.5Hz7745

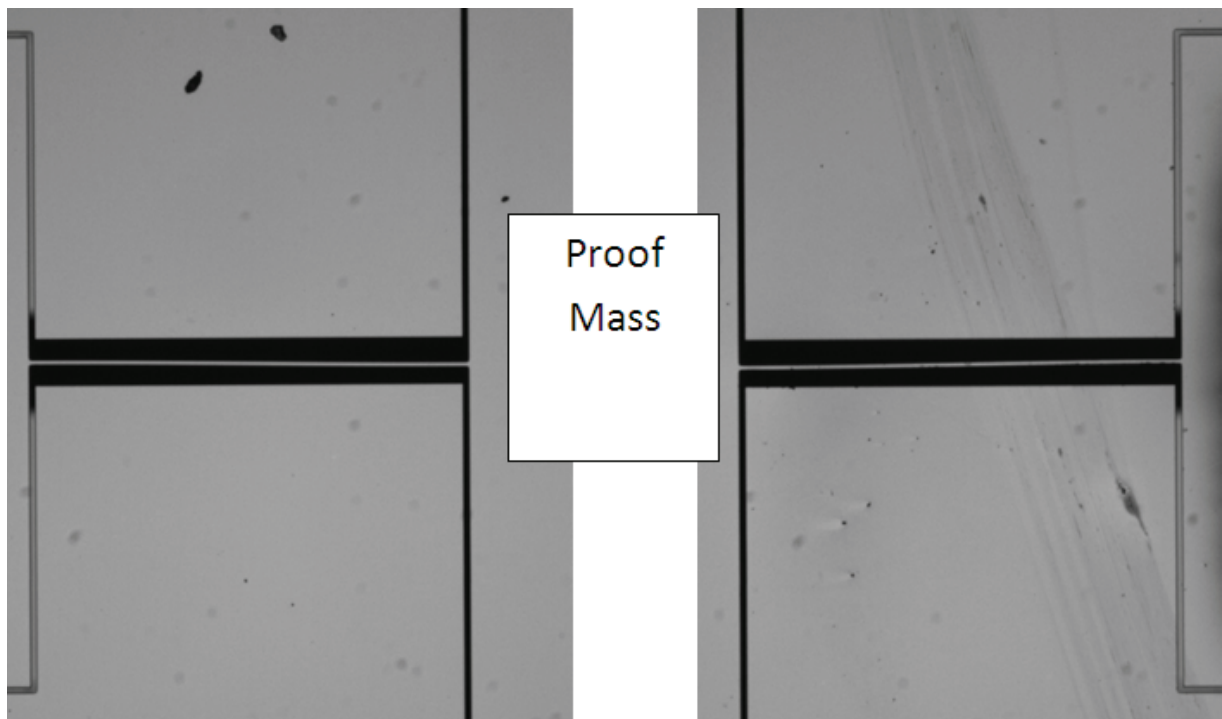


Figure 8-10 Optical micrographs of the two springs of chip 1.5Hz7745. An in-plane buckling of the springs is observed

Chapter 8: Testing of 2nd Generation Earth Sensor

Figure 8-9 shows that the proof mass of the 1.5Hz7745 chip buckles out of plane. The expected sag at the center of the proof mass is -0.2 microns, as predicted by modeling in ANSYS, but the observed sag is actually +0.27 microns.

This buckling of the proof mass and springs could be due to compression caused by the handle layer having a higher bow than the device layer. Under such a compression, the proof mass would tend to get displaced in the most compliant fashion available, which in this case, is the out of plane tilt. Figure 8-10 shows in-plane buckling of the springs as well.

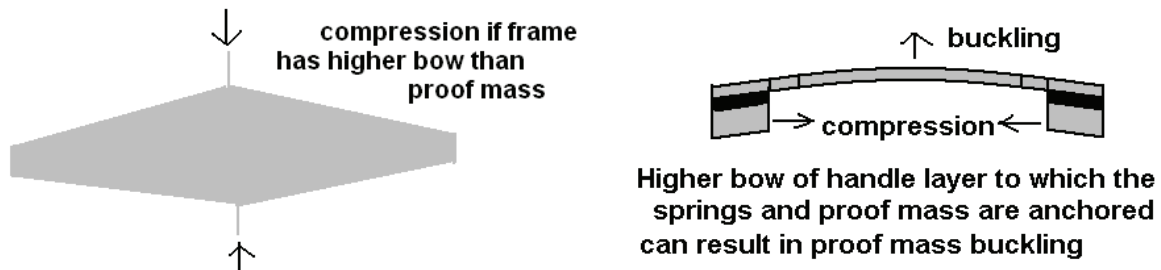


Figure 8-11 Buckling of proof mass due to higher bow of handle layer

For ES chips with a stiffer spring produced from the same wafer, such as the 20Hz chip, this buckling is markedly reduced. Figure 8-12 shows the measured profile of the chip 20Hz. The expected sag at the center of the proof mass -0.072 microns, and the measured sag is -0.035 microns. Figure 8-13 shows the measurement of the gap at the sense electrodes of the chip 20Hz. The gaps (1.5 microns, 1.7 microns) are more uniform as compared to the chip 1.5Hz7745 (10.05 microns, 0.85 microns). The out of plane tilting of the proof mass is much less, since the effect of the compression caused by the handle layer having a higher bow is mitigated by the stiffer spring. However, the 20 Hz chip is too stiff for use as an ES. Solutions to the differential bow issue are discussed in Chapter 9.

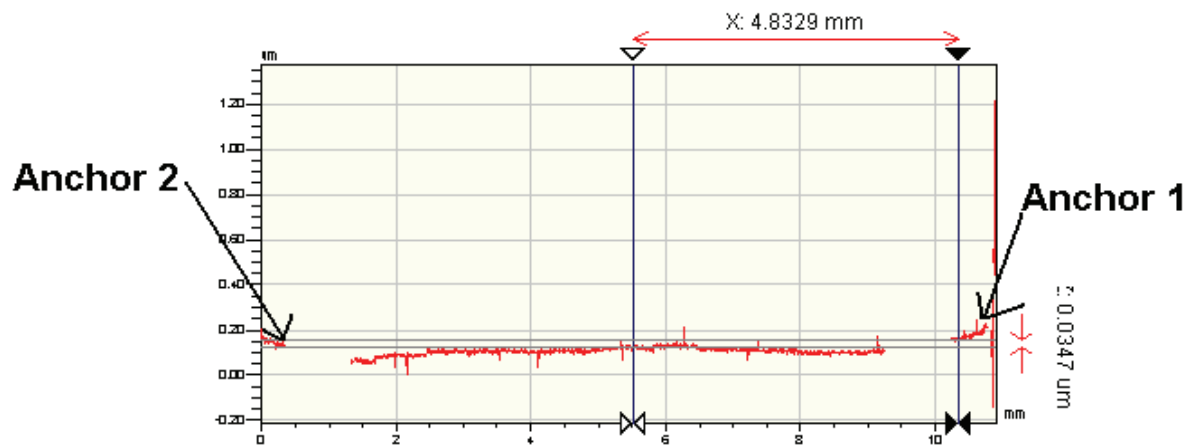


Figure 8-12 Measured profile of proof mass across the width, between the two anchors of the spring for chip 20Hz

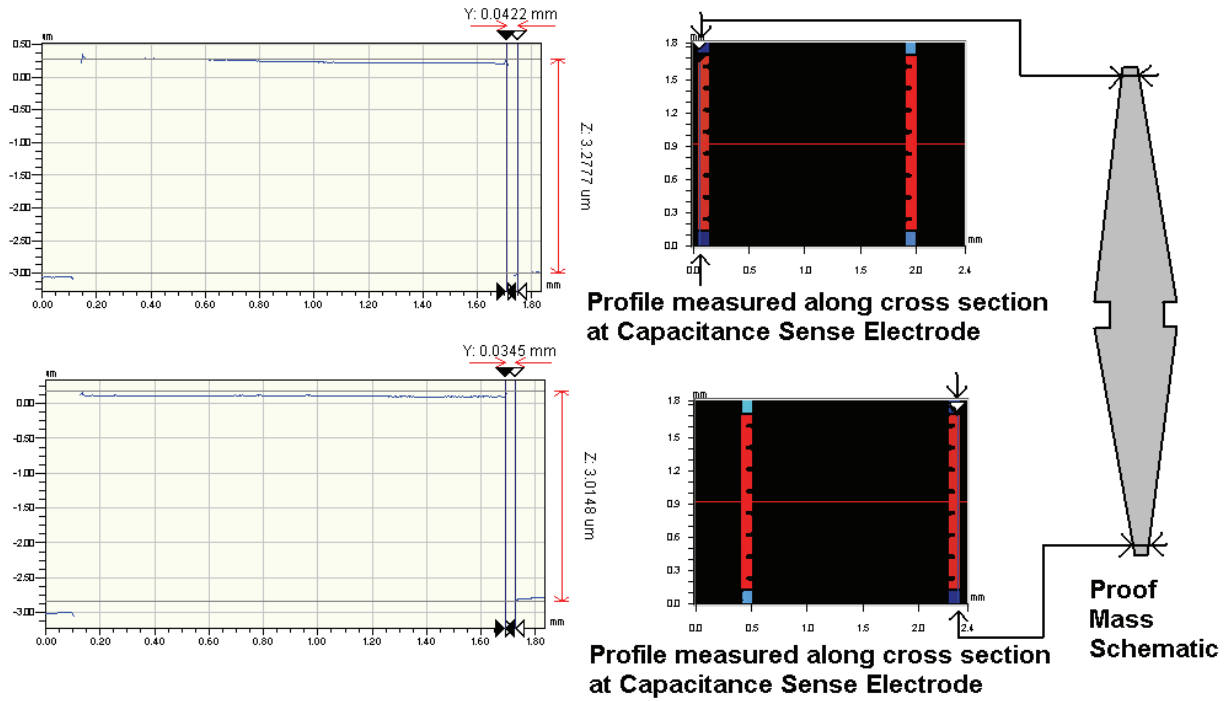


Figure 8-13 Optical profile measurements of the gap at the capacitance sense electrodes of the chip 20Hz

8.5.Noise of Capacitance to Digital Convertor

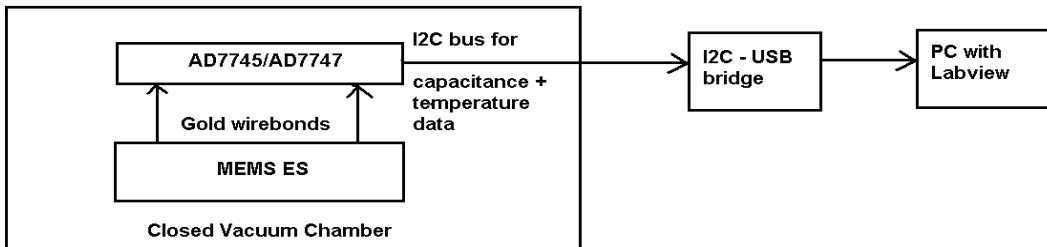


Figure 8-14 Setup for obtaining the capacitance and temperature data from the MEMS chips

In Chapter 2 the limitation of accuracy due to thermal noise of the proof mass and spring system is discussed. If the noise of the displacement readout electronics is higher, it can ultimately determine the accuracy with which the sensor can measure the displacement due to GGT. The noise at the output of the AD7745 and AD7747 is recorded for long durations, without any displacement of the proof mass. For this test, the ES chips, wirebonded to the CDC are placed in a closed vacuum chamber placed on an optical bench

Figure 8-14), to isolate them from the environment. The data is gathered via the I2C bus interface of the chips, and is transferred through a I2C-USB bridge to a PC. Labview is used to program the CDC for

parameters such as the sampling rate, and store the data generated by the CDC. The CDC convertors also have an internal temperature sensor, and the temperature is also recorded along with the capacitance data, to track drift due to changing ambient temperature. Before starting to record the noise, the procedure described in Section 8.2 is followed to verify that the proof mass is freely moving.

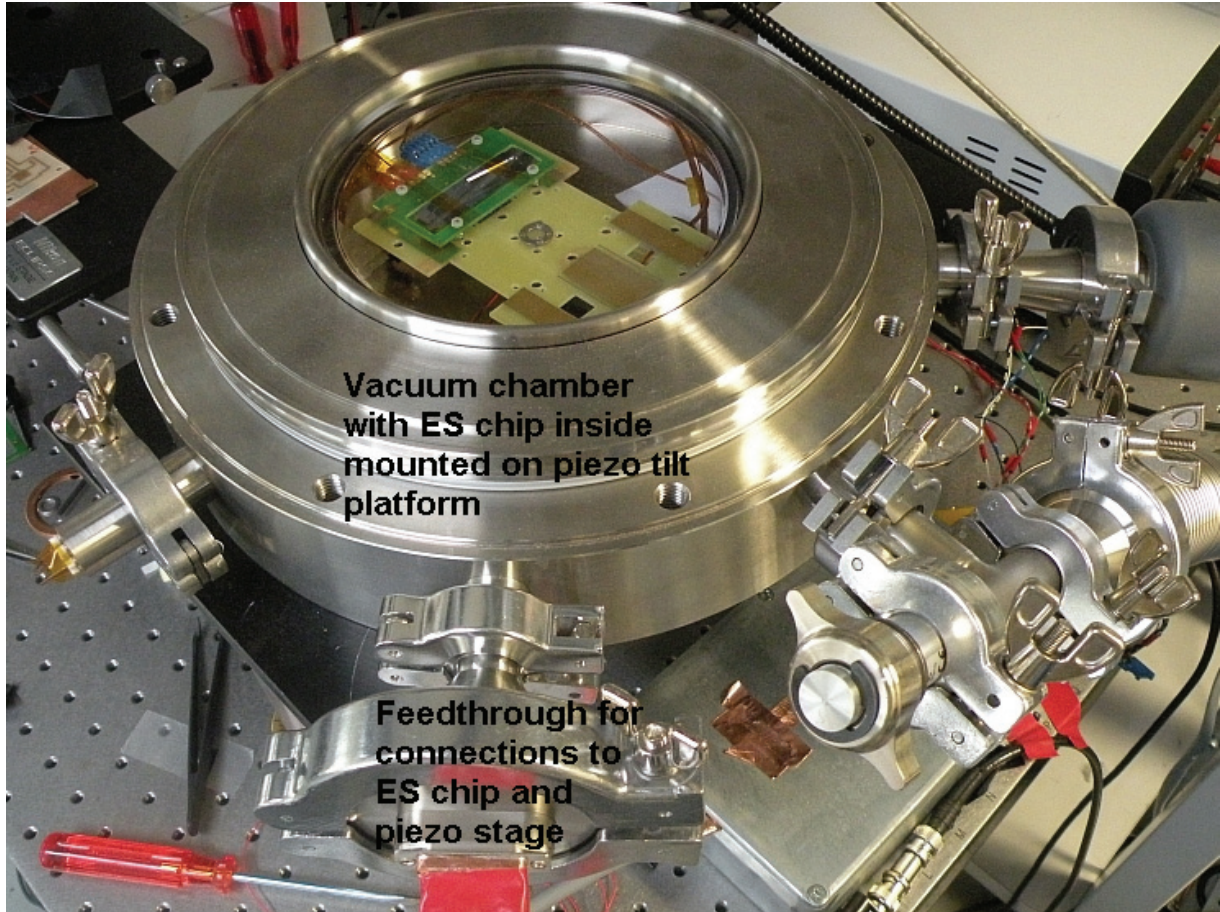


Figure 8-15 Photograph of custom designed vacuum chamber with Earth sensor chip inside. The chip is mounted on a piezo stage. Connections for data and power supply are through a feed through. The chamber is on an optical bench.

8.4.1. AD7745 noise at output

The AD7745 with the 1.5Hz7745 chip is programmed to measure the capacitance at 9.1 Hz, to obtain the highest available sampling time that the AD7745 can provide [21] in order to have the lowest possible noise at the output. A 9 sample moving average is applied to the capacitance data obtained at 9.1 Hz to approximate the noise obtained if a 1 Hz update rate is used for the ES. Figure 8-16 shows the averaged data plotted with respect to time. The peak to peak noise is 500 aF with no noticeable drift. Figure 8-17 shows the temperature data gathered along with the capacitance data from the AD7745. There is a drift within 1°C during the course of the test, due to the MEMS being isolated from the environment. This temperature drift has no noticeable effect on the capacitance measurement.

Chapter 8: Testing of 2nd Generation Earth Sensor

The datasheet of the AD7745 specifies a p-p noise of 27 aF at this update rate. Noise measurements performed by connecting a discrete capacitance to the AD7745 show a p-p noise of 40 aF. For pitch and roll angle measurement with an accuracy of +/- 2° a capacitance change of 200 aF should be sensed. Due to the 500 aF p-p noise of the AD7745 the accuracy of the 2.9 Hz ES chip is degraded to +/- 10°.

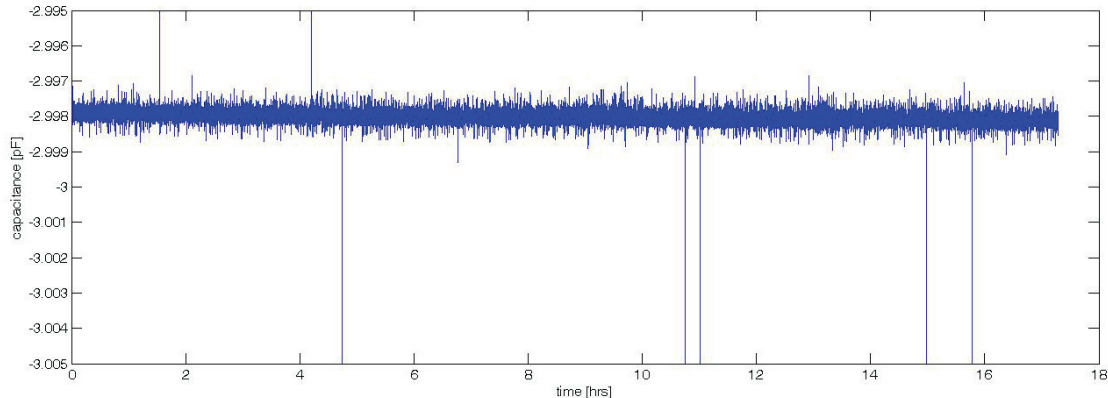


Figure 8-16 Capacitance data gathered from an AD7745 wirebonded to chip 1.5Hz7745, averaged to approximate the noise expected for a 1 Hz update rate. The noise is 0.5 fF p-p

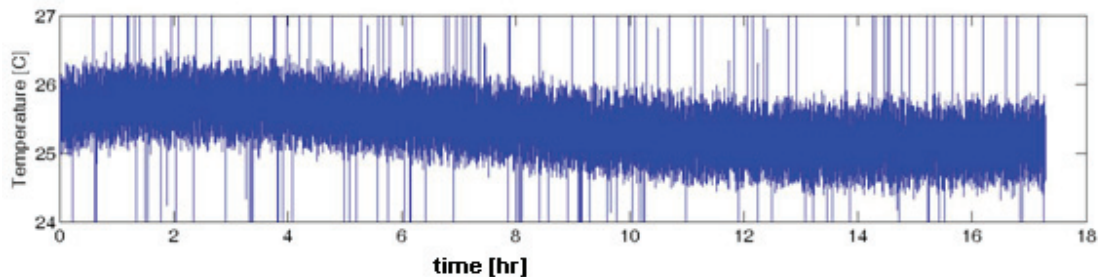


Figure 8-17 Temperature measured along with the capacitance data from the AD7745

8.4.2. AD7747 noise at output

A similar measurement is performed for the chip 10Hz7747. The AD7747 is programmed to measure the capacitance at 4.6 Hz, to obtain the highest available sampling time that the AD7747 can provide [20]. A 4 sample moving average is applied to the capacitance data obtained at 4.6 Hz to approximate the noise obtained if a 1 Hz update rate is used for the ES. Figure 8-18 shows the averaged data plotted with respect to time. The peak to peak noise is 1.5 fF with an observed drift of ~5 fF / hour. Figure 8-19 shows the temperature data gathered along with the capacitance data from the AD7745. There is no significant drift during the course of the test.

The p-p noise indicated in the AD7747 datasheet for this readout rate is 127 aF. The high noise and drift indicate that it cannot be used for the ES readout. However, as seen in Section 8.6, the AD7747 is better suited if closed loop operation with electrostatic force feedback is desired. If readout with the AD7747 is

Chapter 8: Testing of 2nd Generation Earth Sensor

desired, the ES chip has to be designed to give a higher change of capacitance for the same displacement.

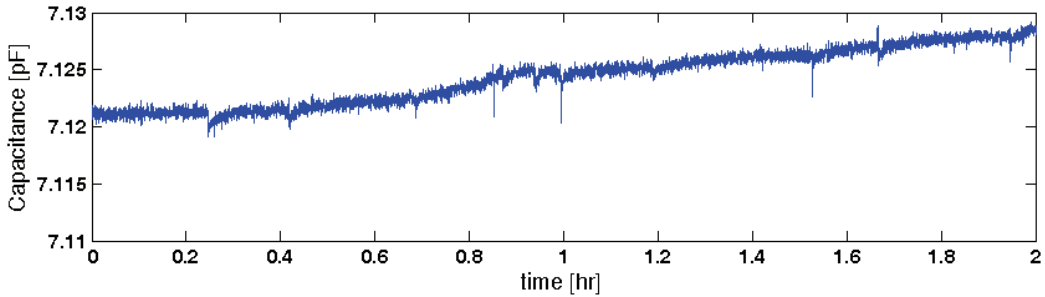


Figure 8-18 Capacitance data gathered from an AD7745 wirebonded to a MEMS ES chip, averaged to approximate the noise expected for a 1 Hz update rate. The p-p noise is 1.5 fF and a drift of 5 fF/hr is observed

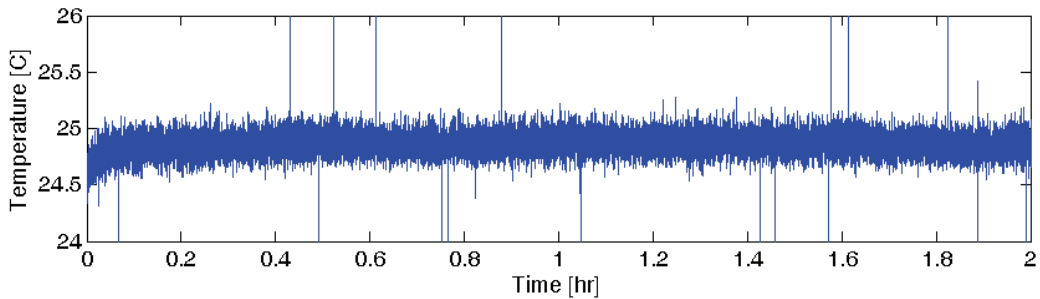
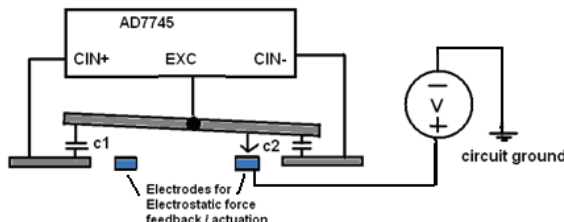
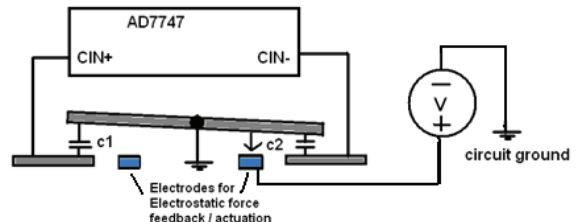


Figure 8-19 Temperature measured along with the capacitance data from the AD7747. The

8.6.Electrostatic Actuation of ES chip proof mass



Electrostatic Actuation circuit for AD7745



Electrostatic Actuation circuit for AD7747

Figure 8-20 Circuits for Electrostatic Actuation of (left) chip 1.5Hz7745, and (right) 10Hz7747

Electrodes are provided on the ES chip to apply electrostatic force on the proof mass. This makes it possible to operate the sensor in a closed loop with electrostatic force feedback, and is useful for testing, since electrostatic force can produce a displacement on the proof mass. Figure 8-20 shows the circuits when electrostatic force is applied to the ES chips using an external voltage referenced to the AD7745/AD7747 ground. With the CDC chip connected to the MEMS, the response of the proof mass to electrostatic actuation is observed to determine if the CDC circuitry causes any interference.

$$F = \frac{\epsilon_0 A V^2}{2d^2} \quad 8-1$$

Equation 8-1 gives the expression for electrostatic force generated by an applied voltage. From the equation, the force is proportional to the square of the voltage. Therefore negative and positive voltages applied to the actuation electrode should result in the same displacement.

The chips are placed one at a time under the optical profiler, and an actuation voltage is applied to the electrodes on the chip. The profiler utilizes interferometry, and the interference fringes are visible on the polished silicon surface of the ES chip. These fringes move when there is an out-of-plane displacement of the proof mass. Using visual observation of the movement of the fringes across the proof mass surface, a rough estimate is made of the effect of positive and negative voltages on the displacement of the proof mass. This is graphically indicated for chip 1.5Hz7745 and chip 10Hz7747 in Figure 8-21. Meanwhile the capacitance change recorded by the respective CDC chip is also monitored. This is done to rule out a purely electronic effect of the applied voltage causing a change in the measured capacitance. It is visually verified that an out-of-plane displacement of the proof mass results in a capacitance change.

With the AD7745, the proof mass is at a floating voltage, determined by the 32 kHz excitation signal supplied by the AD7745 [21]. Instead of having a reference to ground, the electrostatic force between the proof mass and the actuation electrode will depend on the charge supplied to the proof mass by the internal circuitry of the AD7745. For positive actuation voltages applied to chip 1.5Hz7745 little or no movement of the fringes occurs, but for negative voltages appreciable movement of the fringes is observed along with a change in the measured capacitance, along with a large increase in the noise at the output of the AD7745. For the chip 10Hz7747, the proof mass is grounded, and the displacement due to electrostatic actuation is proportional to the square of the voltage. There is no increase in the noise at the output of the AD7747 when actuation voltages are applied to the chip. The AD7747 is suited for operation with electrostatic actuation.

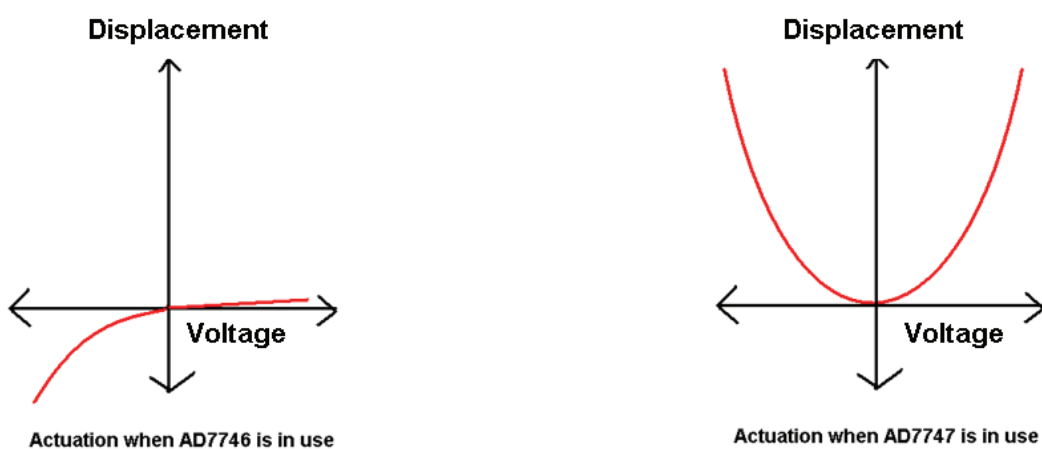


Figure 8-21 An approximated graphical indication based on the visual observation of the proof mass displacement due to electrostatic actuation for chip 1.5Hz7745 (left) and chip 10Hz7747 (right)

8.7.Readout Sensitivity (Change in Capacitance vs displacement)

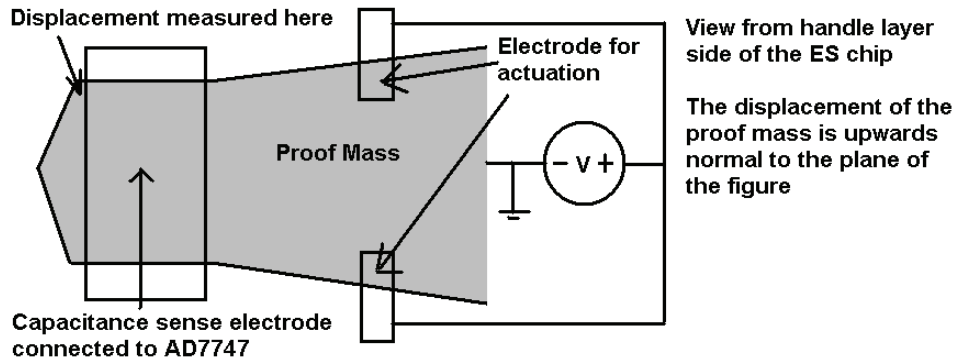


Figure 8-22 Schematic of one end proof mass showing the actuation electrode, the sense electrode and the point where the displacement is measured by the optical profiler

This test is performed by applying a voltage to the actuation electrodes on the chip. Since only the chip 10Hz7747 has the proper response to electrostatic actuation, it is used for this test. The electrostatic force results in a displacement of the proof mass. This displacement is measured by the optical profiler at the area of the capacitance sense electrode. The capacitance change due to the displacement is recorded by the AD7747 chip using a single ended measurement. The procedure is repeated for different voltages applied to the actuation electrode .A set of displacement measurements, and a set of capacitance measurements with respect to the voltages applied (20V, 40V and 60 V) are obtained. A minimum voltage of 20 V is applied to obtain a capacitance change above the AD7747 output noise.

The capacitance change is due to the displacement, which is proportional to the square of the voltage. The displacement measured for different actuation voltages in Figure 8-24 does not show proportionality to the square of the voltage. This is due to noise in the optical profiler. Even in a steady state, a random motion of the interference fringes on the surface of the proof mass is observed. Each profiler measurement of the proof mass surface takes a minimum of a few seconds. During this time, any ambient vibration source in the vicinity of the profiler can result in an error in the displacement measurement. Figure 8-23 shows the change in capacitance measured for the different actuation voltages applied to the chip. The change in capacitance does show an increase that is more proportional to the square of the voltage. Figure 8-25 shows the data based on which the capacitance vs voltage curve is plotted. The data is obtained at 4.6 Hz, and a four sample moving average is applied to approximate the noise expected for a 1 Hz update rate.

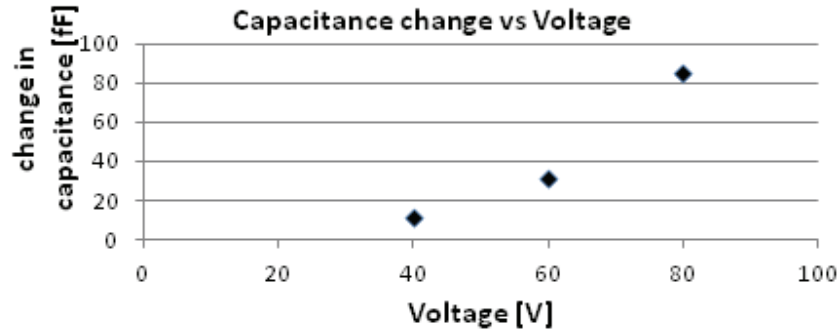


Figure 8-23 For chip 10Hz7747, change in capacitance measured by AD7747 for different actuation voltages

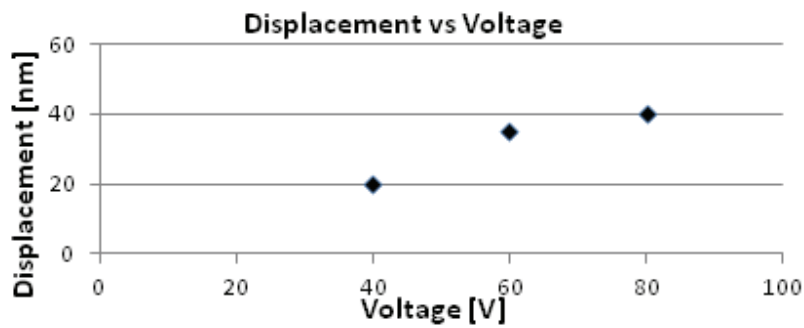


Figure 8-24 For chip 10Hz7747, change in displacement measured by optical profiler for different actuation voltages

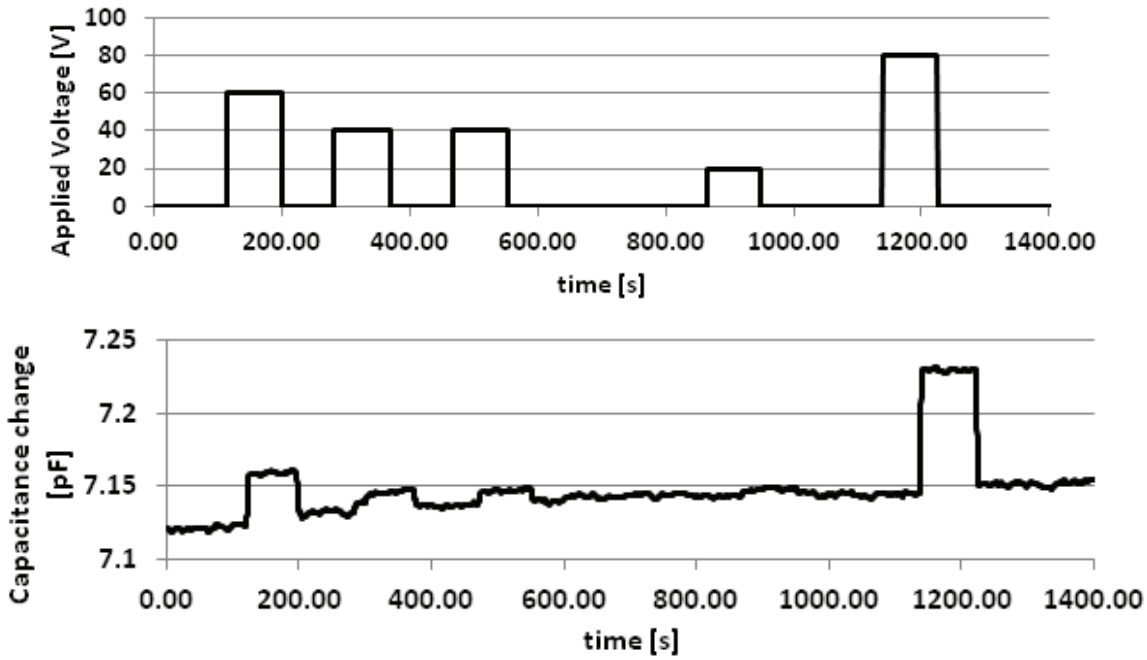


Figure 8-25 Top: Actuation voltage applied to chip 10Hz7747; Bottom: change in capacitance measured by AD7747

Chapter 8: Testing of 2nd Generation Earth Sensor

The information from Figure 8-23 and Figure 8-24 are combined to plot the points in green in Figure 8-26. The measured displacement and capacitance change, for each voltage, are plotted against each other to obtain the change in capacitance for a measured displacement.

The points in red represent the calculated change in capacitance for different displacements on the X axis. The calculation is done based on the measured nominal capacitance of the sense electrode from Figure 8-25 (7.12 pF). The red line has a slope of 2 fF/nm. The green line shows an approximated slope of 1.5 fF/nm based on the measured capacitance points.

For the ES design described in Chapter 6, the sensitivity is 4 fF/nm, for a nominal capacitance of 10 pF at the sense electrode. The reduction in the sense capacitance of chip 10Hz7747 is mainly due to a larger sense gap than what was expected based on ANSYS modeling of the sensor design. This effect of the larger gap is also observed in the reduced nominal capacitance of 7.12 pF. The observed gap of 3.5 microns is due to the differential bow issue described in Section 8.4. An increase in the nominal capacitance of the sense electrode due to the differential bow reduces the sensitivity of the readout, and ultimately the accuracy of the sensor.

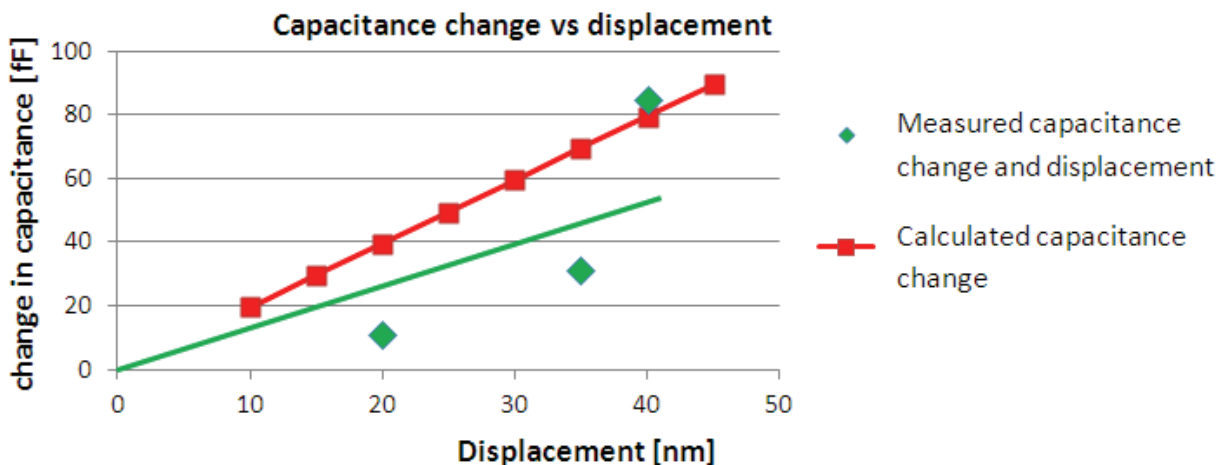


Figure 8-26 Green: AD7747 measured capacitance change for measured displacement; Red: Calculated capacitance change based on nominal capacitance and the displacement

8.7.1. Issue with Electrostatic Actuation

The expected displacement due to the electrostatic force of chip 10Hz7747 is modeled using ANSYS for the different voltages applied to measure the sensitivity of the readout. Table 8-3 shows the comparison of the simulation results to the measured displacement. The measured displacement is more than a hundred times lower than the expected displacement.

Chapter 8: Testing of 2nd Generation Earth Sensor

Applied Voltage[V]	Expected Displacement of proof mass of chip 10Hz7747 [nm]	Measured Displacement [nm]
40	2400	20
60	5400	35
80	9600	40

Table 8-3 Comparison of expected displacement to measured displacement when electrostatic force is applied to chip 10Hz7747

To understand this issue better, all the silicon on the 10Hz7747 is connected to ground, except for the electrostatic actuation electrode on one side of the chip. Voltage is applied to this electrode, and the displacement is observed using the optical profiler at the extreme ends of the proof mass. For an applied voltage of 200 V, a displacement of -270 nm is observed at the end of the proof mass closer to the electrode where the voltage is applied. At the other end of the proof mass, only a displacement of +75 nm is observed. The chip 20Hz is also tested in the same manner and the same behavior is observed, with the end of the proof mass closer to the actuation electrode being displaced ~4x more than the other (Figure 8-27). Further work is required to better understand this issue, which could not be carried out in the time frame of this thesis.

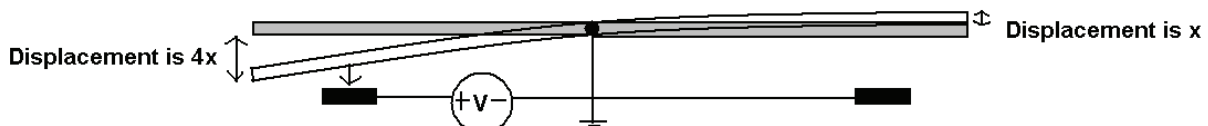


Figure 8-27 Observed displacement at extremities of proof mass when electrostatic force is applied to chip 10Hz7747, and chip 20Hz

8.8. Test for spring stiffness

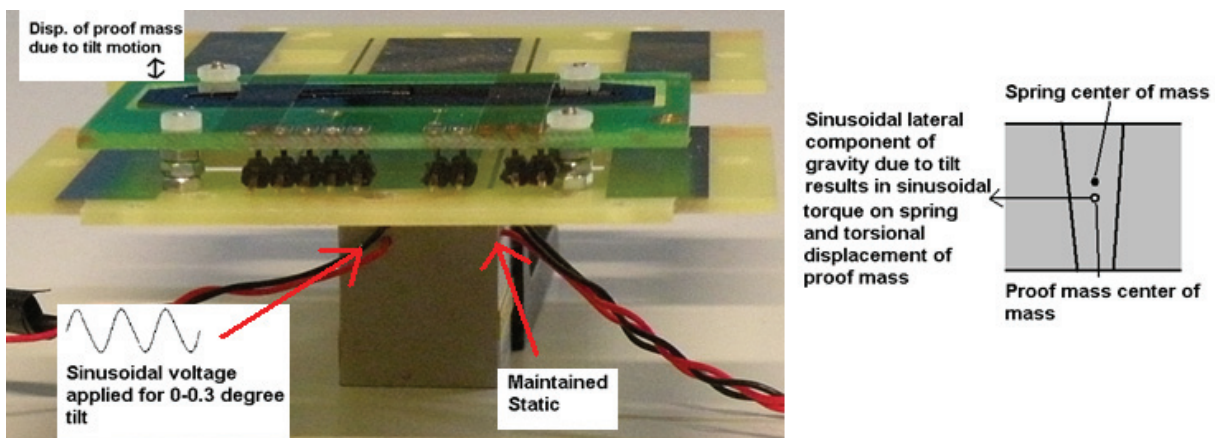


Figure 8-28 Left: Sinusoidal Voltages are applied to one side of the piezo stage to rock the ES chip back and forth; Right: Cross section of spring and proof mass: the resulting sinusoidal changing lateral component of gravity causes a torque around the spring, thus causing a displacement of the proof mass

Chapter 8: Testing of 2nd Generation Earth Sensor

Due to the issue observed with the electrostatic actuation in section 8.7.1, tests are performed on the chips 1.5Hz7745, and 10Hz7747 to determine whether the springs of the ES are much stiffer than designed. A test is setup to displace the proof mass relative to the sense electrodes by mechanical means only. The chip is placed on a piezo stage, and a sinusoidal voltage at 0.2 Hz is applied to tilt the piezo stage and therefore the chip (Figure 8-28 left). The centers of mass of the spring and of the proof mass do not coincide, due to the trapezoidal cross section of the spring. When a tilt is applied to the chip, the lateral component of gravity acting through the center of mass of the proof mass is changed. This results in a torque on the spring, due to which the proof mass is displaced (Figure 8-28 right). The change in capacitance due to this displacement is recorded by the respective CDC chip.

The tilt is monitored by measuring the displacement at each extremity of the chip frame over time using a Laser Doppler Vibrometer (LDV). The phase of the output of the LDV displacement measurement is compared to the phase of the drive signal to the piezo. At one end of the ES chip the displacement of the chip (15 microns) frame is in phase with the drive signal. At the other end the displacement (-11 microns) is 180 degrees out of phase, which shows the chip frame is tilting. From the peak displacement measured at either end the tilt is calculated to be 0-0.032°. This value of the tilt is then used in the ANSYS model of the sensor to predict a displacement. From this predicted displacement the expected capacitance change is calculated. The actuation electrodes are grounded during this test.

The expected capacitance change is compared to the measured capacitance change for the two chips. Figure 8-29 shows the comparison between the measured and expected capacitance variation due to the 0.2 Hz signal applied to the piezo for chip 1.5Hz7745. Figure 8-30 gives the comparison for chip 10Hz7747.

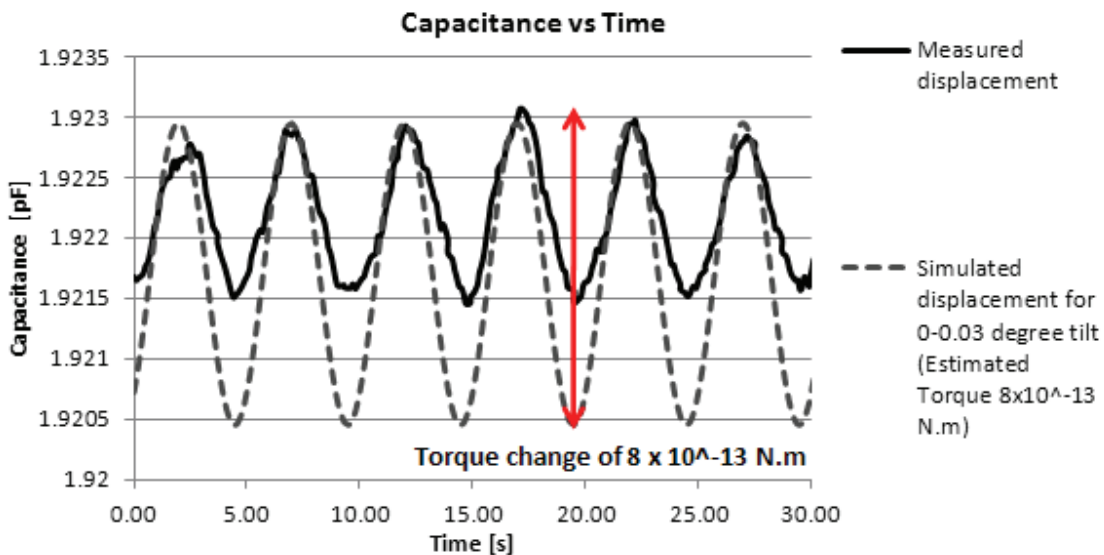


Figure 8-29 Capacitance change recorded from chip 1.5Hz7745, during sinusoidal tilting on piezo stage and compared to expected capacitance change from ANSYS modeling

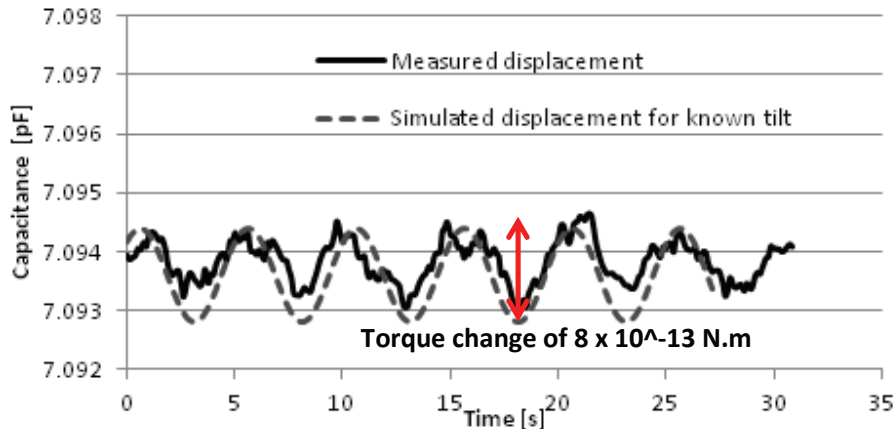


Figure 8-30 Capacitance change recorded from chip 10Hz7747, during tilting on piezo stage and compared to expected capacitance change from ANSYS modeling

From Figure 8-29 and Figure 8-30, it can be observed that the measured and expected displacement due to the lateral component of gravity induced by tilting for both chips is within a factor of two. This applies to the spring stiffness as well. This indicates that increased spring stiffness is not the reason for the observed issue with electrostatic actuation. In Section 8.10 the chip 1.5Hz7745 is very overdamped in air for the fundamental tilting mode. So the observed difference between the measured and predicted capacitance change can be due to damping of the 0.2 Hz oscillation imparted by the piezo stage.

Table 8-4 summarizes the capacitance measurements.

	1.5Hz7745	10Hz7747
Tilt determined by measuring displacement at extremities	0.032 degrees	0.032 degrees
ANSYS prediction of displacement	18.8 nm	1.8 nm
Nominal capacitance	1.922 pF (Figure 8-29)	3.094 pF (Figure 8-30)
Expected change of capacitance, based on nominal capacitance and FEM predicted displacement	2.7 fF	1.2 fF
Estimated peak-to-peak capacitance change from graph	1.5 fF (Figure 8-29)	1 fF (Figure 8-30)

Table 8-4 Summary of test for spring stiffness

8.9.Comparison with expected change of capacitance due to GGT

Figure 8-29 and Figure 8-30 show the capacitance change measured on Earth due to an estimated torque varying from 0 to 8×10^{-13} N.m. The torque is applied by tilting the MEMS ES by 0.03° in gravity (Figure 8-28). The tilt is measured. The weight of the proof mass is estimated from the geometrical model of the proof mass in ANSYS. Based on the measured spring dimensions, ANSYS can estimate the location of the center of mass of the spring, and of the proof mass. From the tilt (0.03°), the weight of

Chapter 8: Testing of 2nd Generation Earth Sensor

the proof mass (0.1 g), and the distance between the center of masses of the spring and proof mass (1.5 μm), the torque is calculated to vary from 0 to 8×10^{-13} N.m.

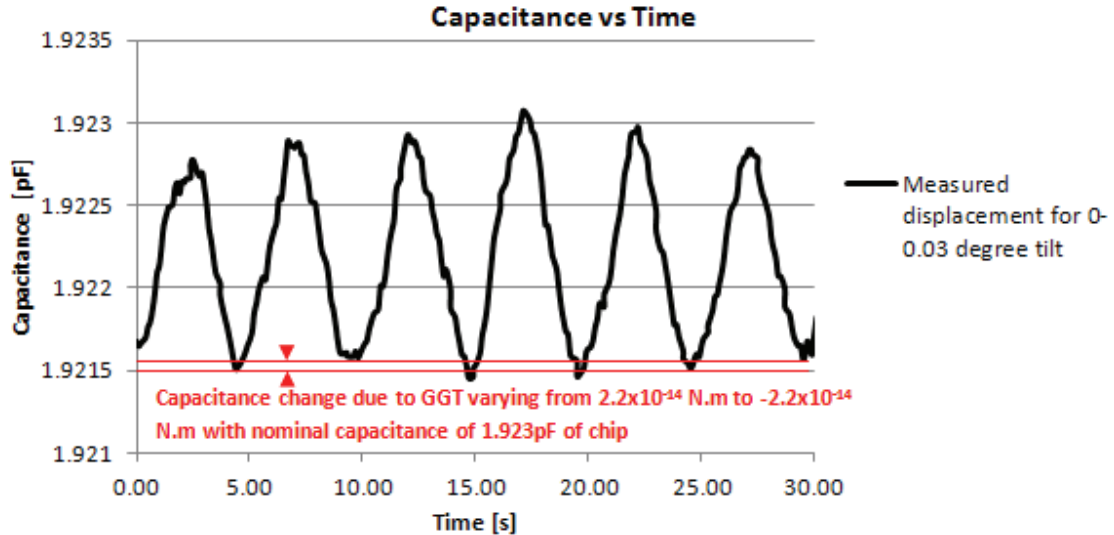


Figure 8-31 Comparison of measured single ended capacitance due to torque varying from 0 to 8×10^{-13} N.m; with predicted capacitance change due to GGT varying from -2.2×10^{-14} to 2.2×10^{-14} on the same MEMS (red) for the nominal chip capacitance of 1.923 pF.

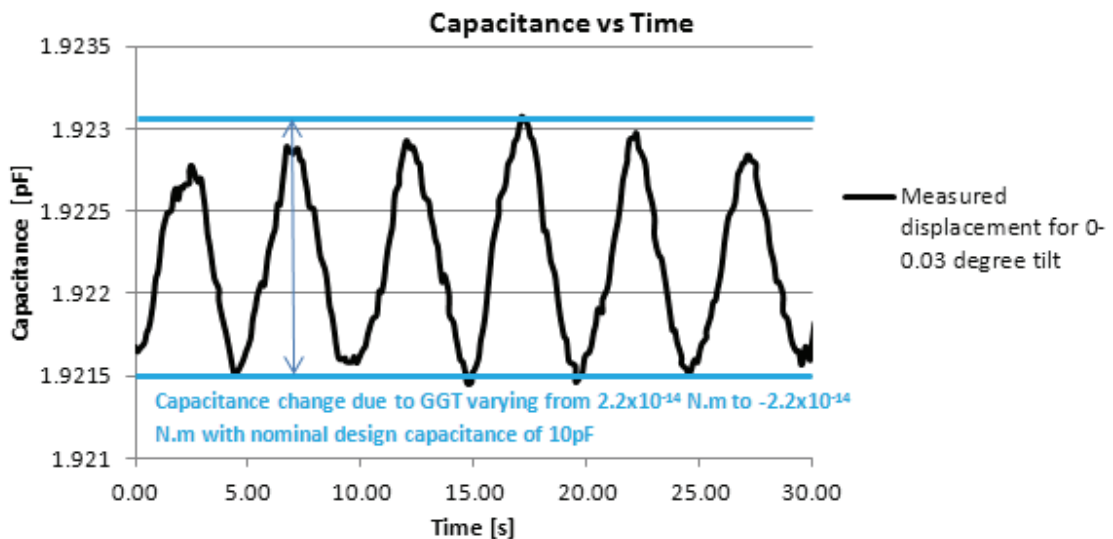


Figure 8-32 Comparison of differential capacitance change due to GGT varying from -2.2×10^{-14} to 2.2×10^{-14} , for a 10 pF nominal capacitance (blue) with measured capacitance due to torque varying from 0 to 8×10^{-13} N.m; to illustrate the effect of reduced nominal capacitance due to wafer bow

For the chip 1.5Hz7745, the GGT at an altitude of 700 km varies from -2.2×10^{-14} N.m for an angle of -45° to the nadir, to 2.2×10^{-14} N.m for an angle of $+45^\circ$ to the nadir. Figure 8-31 compares the change in capacitance due to this change of 4.4×10^{-14} N.m in GGT to the **single ended** measurements performed using chip 1.5Hz7745 with a **nominal capacitance of 1.923 pF**. The total change in capacitance is 50 aF

due to GGT. Due to the wafer bow, the distance between the proof mass and sense electrode changes, and therefore the nominal capacitance is changed from 10 pF (designed) to 1.923 pF. Due to this change in nominal capacitance, the dC due to GGT drops well below the noise of the AD7745.

If the **nominal capacitance were 10pF** as designed, then the total **differential** capacitance change due to a GGT change of 4.4×10^{-14} N.m would be **1600 aF** for a chip with a resonant frequency of 2.9 Hz, which is well above the noise of the AD7745. Figure 8-32 shows a comparison between the change in capacitance measured on Earth due to the estimated torque of 0 to 8×10^{-13} N.m, with the 1600 aF change due to GGT expected with a 10 pF nominal capacitance. The p-p noise of the AD7745 is 500 aF (Figure 8-16). For a MEMS ES with 10 pF nominal capacitance, this corresponds to the change in capacitance obtained if the ES with resonant frequency 2.9 Hz moves from an angle of -10° to the nadir, to an angle of +10°. Therefore the accuracy is +/-10° for a 2.9 Hz sensor with a nominal differential sensing capacitance of 10 pF.

8.10. Step response of Earth sensor

The transient response of the proof mass and spring system is measured to determine the quality factor of the second order system. This is done by applying a step response to the system and measuring the resulting displacement of the proof mass and the change of the displacement over time. The step response is measured for the chip 1.5Hz7745.

8.10.1. Step response measured by capacitance measurements

A PCB with the chip 1.5Hz7745, mounted on the piezo stage, is bolted down on a magnetic shaker. After being bolted down, the piezo is used to verify that the proof mass of the chip can move freely. Then a ramp voltage with a period of 100 s is applied to the shaker as shown in Figure 8-33, to obtain a step input for the ES chip. The transient displacement of the ES proof mass is measured.

From the observed decay in the transient response (Figure 8-34), and the estimated 2.9 Hz resonant frequency of the chip 1.5Hz7745, the quality factor is calculated to be 0.006.

The bandwidth of the capacitance displacement sensing is not sufficient to measure the transient response of the higher order modes. A Laser Doppler Vibrometer (LDV) set at sampling rate of 128 KHz is used to measure the transient response of the proof mass and spring for the higher order out of plane modes. Figure 8-35 shows the measured transient response using the LDV. The response is underdamped. The frequency of the mode is 1.25 KHz and the Q is calculated to be 8.5. Table 8-5 gives a summary of the predicted and measure transient response in air for the chip 1.5Hz7745.

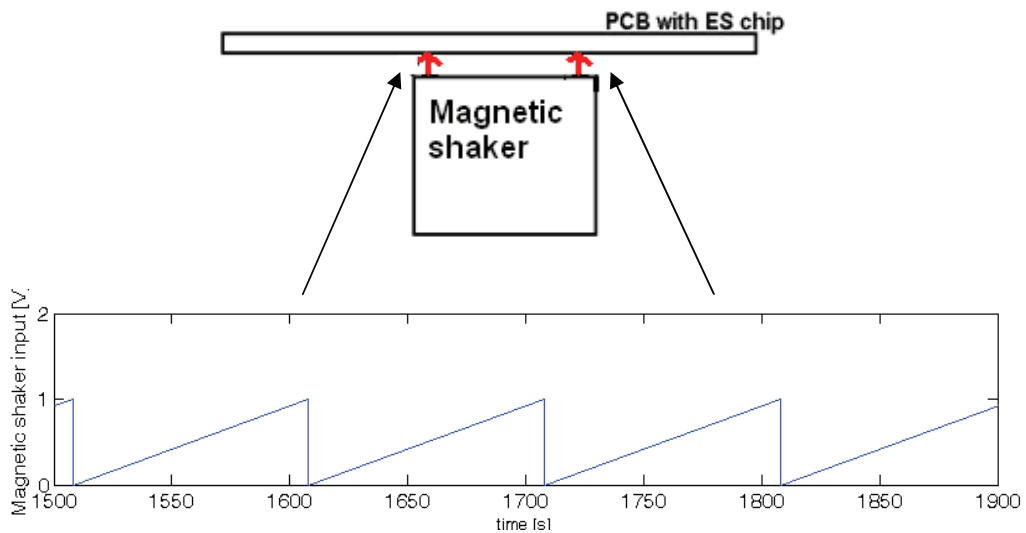


Figure 8-33 Input applied to magnetic shaker for to apply a step input for the ES chip

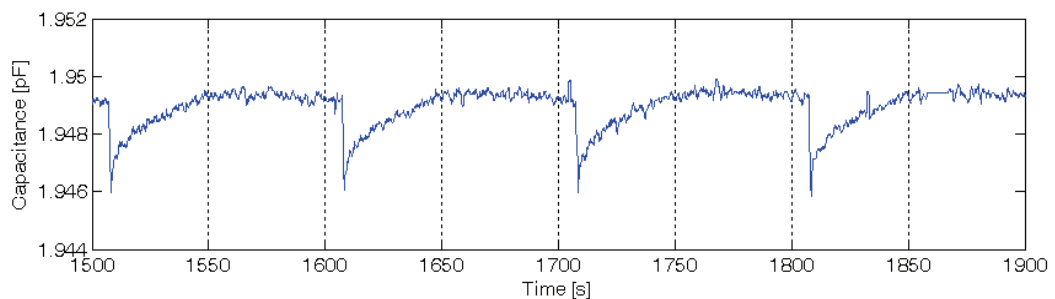


Figure 8-34 Transient response of the 1.5Hz7745 chip. The sensor is much overdamped. The Q factor is calculated to be 0.006

8.10.2. Step response measured by Laser Doppler Vibrometer

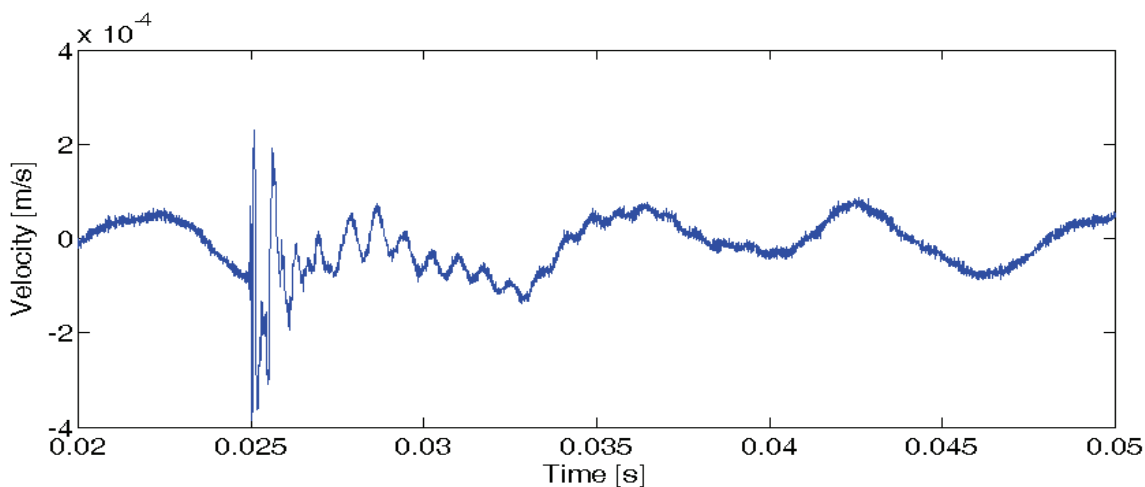


Figure 8-35 Transient response of the chip 1.5Hz7745 for the higher order out of plane mode in air. The long period oscillations are noise in the LDV system. The frequency of the mode is observed to be 1.25 KHz and the q factor is calculated as 8.5 based on the decay envelope

Chapter 8: Testing of 2nd Generation Earth Sensor

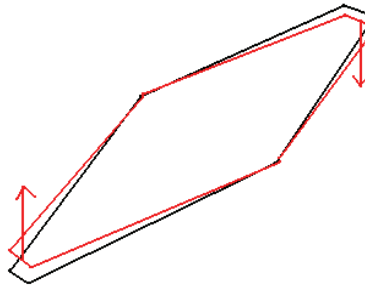
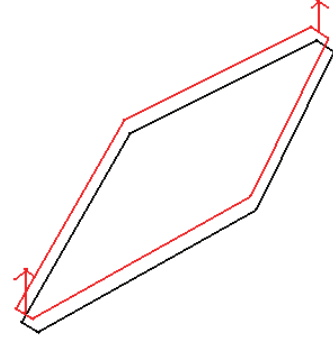
	Fundamental tilt mode	Higher order plunging mode
Mode Shape		
Design natural frequency ω_n	9.67 (1.53 Hz)	5497 (875 Hz)
Moment of Inertia / mass	1.3×10^{-8} N.m	0.1 g
Damping factor in air (predicted from Andrews model)	0.109	0.109
Q factor in air (predicted from Andrews model)	1.15×10^{-6}	5.04
Natural frequency based on spring dimension measurements	2.9 Hz	1.37 KHz
Natural Frequency from transient measurements	-	1.25 KHz
Q factor from transient measurements	0.006	8.5

Table 8-5 Summary of predicted and measured transient response for the chip 1.5Hz7745

In chapter 6, the model used to predict the quality factor for the fundamental mode estimated that the sensor would be overdamped with a Q of 1.15×10^{-6} . Though the measured transient response clearly shows overdamping, the estimated Q is three orders of magnitude higher as compared to the prediction. This can be due to the extremely simplified geometry of the capacitance sense electrode used in chapter 6, to calculate the q due to squeeze film damping at the sense electrodes. In reality the airflow around the sense electrode and proof mass can be very different from that between two parallel plates moving orthogonal to one another.

The Andrews model predicts the Q factor with greater accuracy for the plunging mode. The movement of the proof mass in the plunging mode is orthogonal to the sense electrodes, which has greater similarity to the structure used to validate the Andrews model. The observed ringing at 1.25 KHz is quite close to the analytically calculated value of 1.37 KHz based on the measured spring dimensions. This also indicates that the estimate of 2.9 Hz for the fundamental mode is reasonably accurate.

8.10.3. Q-factor improvement in 1 mbar pressure for higher order out of plane mode

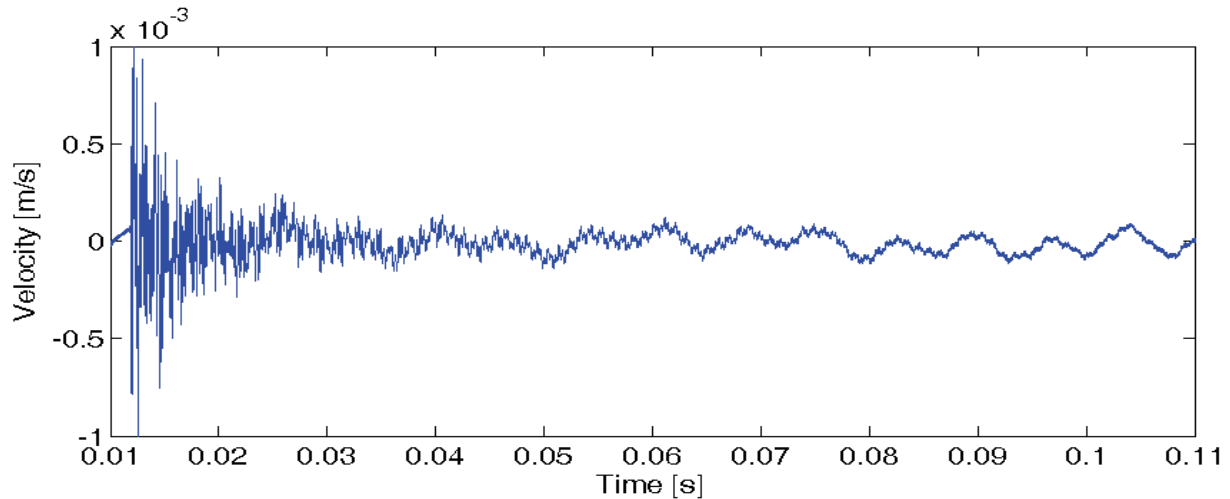


Figure 8-36 Transient response of chip 1.5Hz7745 in 1 mbar for higher order out-of-plane modes. The ringing is observed for a longer time due to less damping.

Figure 8-36 shows the transient response of the chip 1.5Hz7745 measured at 1 mbar pressure. Ringing is observed for much longer than compared to the transient response in air (Figure 8-35). This is due to lower squeeze film damping at lower pressures. A number of higher order modes are excited simultaneously; hence it is not possible to identify ringing of the plunging mode only.

Since the damping for higher order modes is reduced at lower pressures, it can be expected for the fundamental mode as well.

8.10.4. Predicted improvement for Q in vacuum in piston mode

The Andrews model can be extended for calculating the damping at lower pressures. The damping factor calculated by the Andrews model is given by [35]

$$C_{Andrews} = 0.42 \frac{L^2 B^2 \mu}{g^3} \quad 8-2$$

For constant length (L), breadth (B) and gap (g) between the proof mass and the plates, the damping factor is proportional to the dynamic viscosity of air μ . By calculating μ for lower pressures, the damping factor and therefore the quality factor can be calculated for lower pressures.

To calculate the effective viscosity at lower pressures we use a model proposed by Veijola [36]

$$\mu_{eff} = \frac{\mu}{1 + 9.638 K_n^{1.159}} \quad 8-3$$

Where K_n is the Knudsen number. The Knudsen number relates the mean free path length of air molecules at lower pressures to the gap g and is given by [37, 38]

$$K_n = 1.016 \lambda/g$$

8-4

where λ is the mean free path of air molecules at lower pressures.

Based on the datum of Q being 0.006 in air for the tilting mode, equations 8-2, 8-3 and 8-4 are used to calculate the damping factor, and from that the quality factor for the tilting mode at lower pressures.

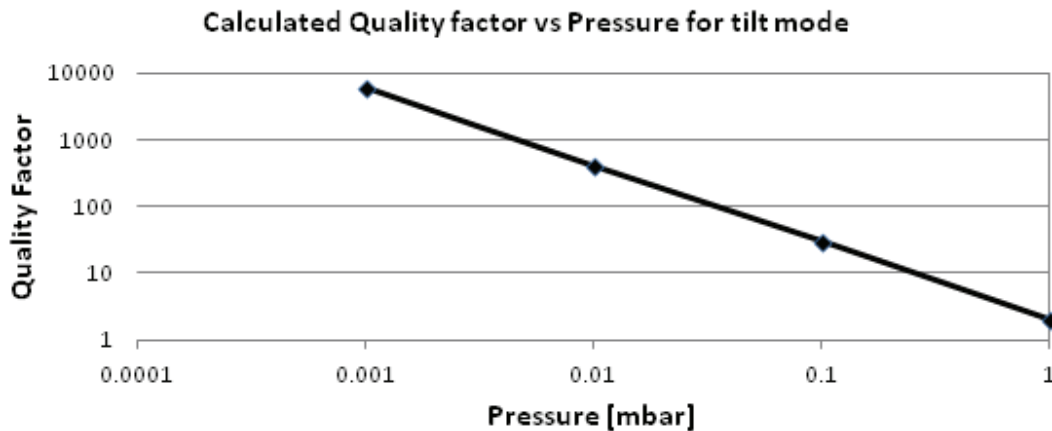


Figure 8-37 Based on Q of 0.006 in air, the quality factor at lower pressures is extrapolated.

Figure 8-37 shows that Q rises into the hundreds for pressures less than 0.01 mbar. The Q will saturate at some point due to damping from sources such as spring anchor losses. This measurement could not be carried out in the time frame of this thesis.

8.11. Vibration Testing of Earth Sensor chip

In Chapter 6 and 7, some design and fabrication steps were discussed to ensure that robust ES chips can be made and tested on Earth. Any instrument for a space application must survive the vibrations encountered during the launch to orbit. Chapter 10 discusses the design of an instrument built around the ES chip to test the sensors on the REXUS (Rocket Experiments for University Students) sounding rocket flight. Some vibration tests are required to determine the survivability of the MEMS chips on REXUS. Therefore, the values specified in the REXUS manual for vibrations tests are adopted.

In Chapter 7, the different fabrication iterations for the 2nd generation ES are described. Some chips with released and moving proof masses were obtained from the initial iterations. These chips could not be used for the above tests, since fabrication problems made wirebonding the chips to the CDC convertor impossible. These chips have the same design of the proof mass and spring as the 1.5Hz7745.

8.11.1. Vibration tests based on REXUS Qualification Tests

For these tests the frequencies specified in the REXUS qualification levels were used, but the tests were started at lower amplitudes of vibration. After each test, the MEMS were visually inspected under a microscope. After the first test at low amplitudes of vibration, damage was observed to the in plane hard stops.

For the test, the MEMS ES PCB is mounted on a magnetic shaker (Brüel and Kjaer System V). The vibration with the conditions described in Table 8-6 and Table 8-7 are set on a control unit for the magnetic shaker. The control unit monitors the shaking amplitude via an accelerometer for feedback. The accelerometer is mounted on the PCB with the MEMS ES. The direction of shaking is perpendicular to the plane of the MEMS.

Frequency	Level	Sweep rate	
50 to 10 Hz and back to 50 Hz	0.003 m/s	4 octave/min	MEMS hard stops damaged (Figure 8-38) Packaging ok
2000 Hz to 50 Hz and back to 2000 Hz	0.1 g	4 octave/min	

Frequency	Level	Sweep rate	
50 to 10 Hz and back to 50 Hz	0.008 m/s	4 octave/min	MEMS hard stops damaged (Figure 8-38) Packaging ok
2000 Hz to 50 Hz and back to 2000 Hz	0.25 g	4 octave/min	

Table 8-6 – Vibration test using frequencies specified for the REXUS qualification test, but with lower amplitudes of vibration

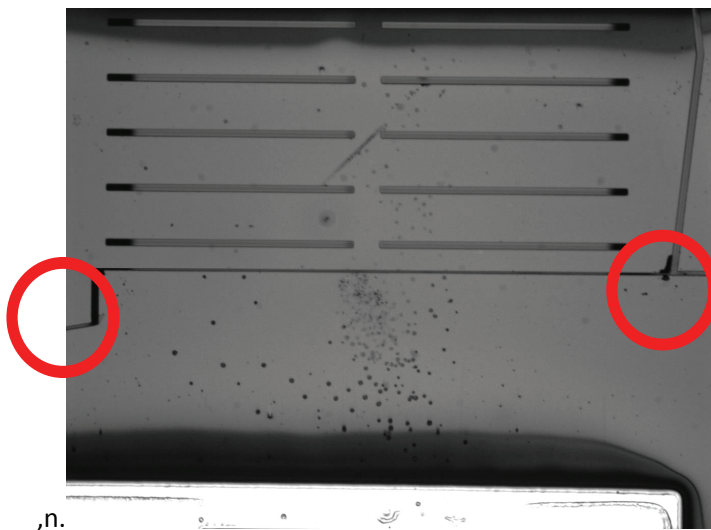


Figure 8-38 Damage to hard stops at extremities of proof mass at lower vibration amplitudes

Chapter 8: Testing of 2nd Generation Earth Sensor

After the 3rd test (Table 8-7), the spring of the MEMS was observed to be broken (Figure 8-39). During the first two tests, the hard stops were damaged. The lateral hard stops were designed such that the distance between the hard stops and the chip frame are less than the distance between the spring and the chip frame. After the hard stops were fractured, the spring would come into contact with the chip frame and break, since the gap provided by the hard stops is no longer available.

Frequency	Level	Sweep rate	
50 to 10 Hz and back to 50 Hz	0.03 m/s	4 octave/min	MEMS spring broken. (Figure 8-39) Packaging ok
2000 Hz to 50 Hz and back to 2000 Hz	1 g	4 octave/min	

Table 8-7 – Vibration test using frequencies specified for the REXUS qualification test, with 1g amplitude



Figure 8-39 broken spring of MEMS. On the right of the image two damaged hard stops can be observed.

8.11.2. Design Modification for spring

In the final fabrication run of the thesis, 2nd generation ES chips that have an increased gap between the chip frame and the spring have been fabricated (Figure 8-40). This should prevent contact of the spring with the chip frame, and should prevent it from fracturing even after the hard stops are eroded.

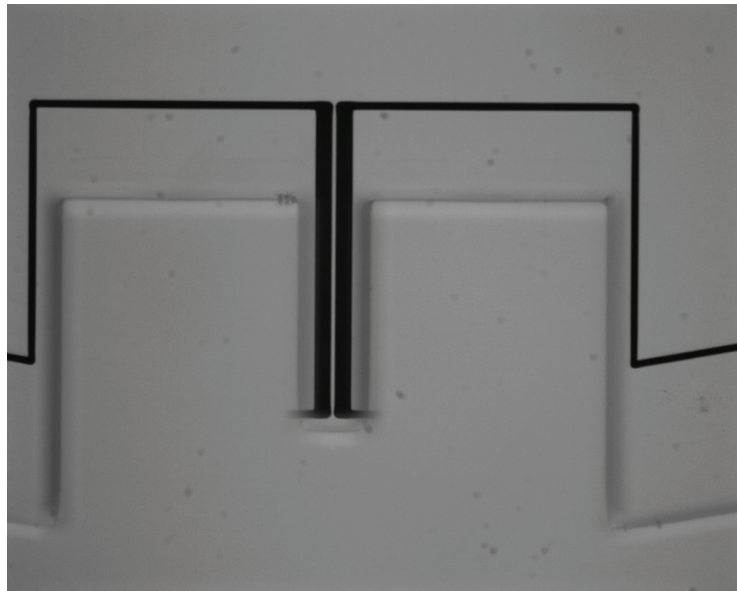


Figure 8-40 design that prevents spring from touching chip frame

8.12. Conclusion

Due to the improved design of the 2nd generation, which made test setup much easier as compared to the 1st generation, more tests were performed on fabricated chips. Three chips of different spring stiffness are used in the tests, 1.5Hz7745, 10Hz7747, and 20Hz. The proof mass shape, and capacitance measurement electrode design is identical for all the chips.

The chip 1.5Hz7745 has the lowest designed spring stiffness and resonant frequency of 1.5 Hz, for measuring GGT in microgravity. Due to choices made to ensure testable chips result from the fabrication process, the spring dimensions are greater than the design, which results in a chip with higher resonant frequency of 2.9 Hz rather than 1.5 Hz. This resonant frequency for the sensor is predicted using ANSYS modeling based on the measured spring dimensions.

Some buckling of the proof mass is observed for the chip 1.5Hz7745. This may be due to the differential bow between the device and handle layers, which can cause compressive stress on the proof mass. For the 20Hz chip, with a stiffer spring much less buckling is observed. This buckling results in out of plane tilting of the proof mass. As a result, the gap at the capacitance sense electrodes changes. If the gap becomes too small, then that particular electrode cannot be used for capacitance measurements any more, since its nominal capacitance value becomes higher than the upper limit measurable by the CDC convertors. Capacitance measurements can be still made using single ended capacitance sensing at only one electrode.

Noise in the CDC chips is recorded for long durations to check the drift and measure the peak to peak noise. The AD7745 has much better noise performance (500 aF peak to peak) as compared to the

Chapter 8: Testing of 2nd Generation Earth Sensor

AD7747 (1.5 fF peak to peak). However, electrical actuation of the proof mass using voltage applied to actuation electrodes can be done properly only when the AD7747 is used to measure the displacement. Electrostatic actuation of the proof mass on a chip, along with using the AD7747 for capacitance measurement, is used to measure the sensitivity of the readout. The readout sensitivity is 1.5 fF/nm for a nominal capacitance of 7.12 pF, which is different from the design nominal capacitance of 10 pF. The nominal capacitance at the capacitance sense electrodes changes from the designed value, due to the bow issue, and this results in the sensitivity changing as well.

The displacement due to electrostatic actuation is about 100 times less than expected. When a voltage is applied, a displacement in the fundamental torsion mode is expected, but the actual displacement probably happens in a higher mode. More tests are needed to better understand this issue.

To rule out increased spring stiffness as the cause of the observed problem with electrostatic actuation, the chips 1.5Hz7745 and 10Hz7747 are mounted on a piezo stage. Mechanical displacement of the proof mass is achieved by small tilts of the piezo stage. Comparison of the recorded capacitance change with the simulated capacitance change shows that the spring stiffness of both chips, are within a factor of two from the expected value.

The step response of the chip 1.5Hz7745 is measured in air using the capacitive displacement sensing, and using a LDV. The capacitance sensing measures the overdamped response, due to squeezed film damping at the capacitance sense electrodes, of the fundamental torsion mode of the sensor, while the LDV measures an underdamped transient oscillation at a frequency corresponding to the higher out of plane plunging mode. Modeling the damping due to squeezed film effects at the capacitance measurement electrodes also predicts an overdamped torsion mode, and underdamped plunging mode. Using the 2.9 Hz resonant frequency, the quality factor of the torsion mode is estimated to be 0.006. Extrapolating the quality factor for lower pressures, using models for estimating the damping factor in the free molecule regime, a Q in the hundreds is obtained for pressures < 0.01 mbar. Further testing is needed to determine the point at which the Q factor saturates due to other factors such as spring anchor losses.

Sinusoidal vibration tests with a frequency sweep based on the qualification specifications of the REXUS rocket are carried out, with lower amplitudes of vibration than specified for REXUS. An ES chip with spring dimensions similar to the chip 1.5Hz7745 is tested at amplitudes of 0.1g, 0.25g until it fails at an amplitude of 1g. The expected cause of failure is the spring impacting the sidewalls, after the hard stops are eroded away. A design modification is made so that the spring does not contact the sidewalls, even if the hard stops are eroded away due to shock or vibration.

Significant improvements are seen in the 2nd generation as compared to the 1st generation due to the design improvements. A MEMS ES chip (1.5Hz7745) with resonant frequency within a factor of two from the design goal is obtained. The proof mass is freely suspended without touching any hard stops, and moves in response to external forces. The sensor can be handled in the lab without special precautions. The capacitance displacement sensing functions as expected and is capable of measuring displacements within a nanometer. The reduction in sensitivity of the readout is due to the differential bow on the chip

Chapter 8: Testing of 2nd Generation Earth Sensor

between the device layer and the handle layer. Possible solutions to the bow issue are discussed in the next chapter.

Chapter 9

Conclusion

The design, fabrication process, and testing of two generations of a novel MEMS inertial sensor to measure the Gravity Gradient Torque (GGT) were presented, a crucial step towards the realization of a novel non-optical Earth sensor Instrument for attitude determination on-board satellites. The target mass and volume for such an instrument is 1 kg and 1 dm³. The sensor is designed for coarse attitude determination, to measure pitch and roll angles with an accuracy of +/- 2° at an update rate of at least 1 Hz, for potential use as a backup and initial attitude acquisition sensor. The MEMS-based Earth sensor uses the Earth's gravity gradient as the reference for attitude determination. The gravity gradient is always in the normal direction towards the Earth's surface, the nadir. The GGT on the proof mass of the MEMS ES depends on the orientation of the proof mass with respect to the nadir. By measuring the displacement due to GGT, the orientation of the proof mass with respect to the nadir can be determined. Such a sensor on-board a satellite can be used to determine the pitch and roll angles for the satellite with respect to the Earth normal.

Four inertial sensors are necessary per ES instrument, to measure the pitch and roll angles required for attitude determination. The four sensors should be obtained from a single wafer, to have well matched characteristics. These requirements, combined with production constraints and the target volume of 1 dm³ limit the proof mass outline dimensions to the order of 1 cm x 6 cm and thickness to 100 microns. The GGT on a proof mass of such dimensions varies from 10⁻¹⁵ N.m to 10⁻¹⁴ N.m depending on the orientation of the proof mass with respect to the nadir. Based on the theory of thermal noise in micromachined inertial sensors, to achieve a noise floor at which the values of GGT corresponding to +/- 2° accuracy can be measured, the spring - proof mass second order system should have a resonant frequency as low as possible, the minimum being set by the desired update rate of 1 Hz, and the quality factor in vacuum should be of the order of hundreds.

A design space is established for the MEMS ES based on the performance targets for a gravity gradient Earth sensor instrument. For the ES chips fabricated and tested on Earth during the course of this thesis, the design is refined based on the fabrication processes available and with a strong emphasis on obtaining chips that can be tested in one gravity on Earth.

9.1.1st Generation MEMS Earth sensor

The sensor for the 1st generation is a pendulum machined from an SOI wafer, with a proof mass of outline dimensions 1 cm x 4 cm and thickness 600 microns, suspended from a single spring of dimensions 15 μm x 1 mm x 100 μm, such that the resonant frequency of the sensor is 1.4 Hz. The proof mass is designed to move in-plane in response to the GGT. Using analytical calculations and ANSYS modeling, the spring and proof mass dimensions are refined to increase the robustness of the sensor so that it can be tested on Earth, and to increase the number of potential ES chips obtained per wafer,

Chapter 9: Conclusion

while keeping the resonant frequency at 1.4 Hz. Due to the ease of integrating optical fibers onto the ES chip, and the known sensitivity of interferometry to measure displacement, an optical fiber based interferometer is chosen to sense the in-plane displacement of the proof mass.

A microfabrication process was developed starting with 100 mm SOI wafer to fabricate the devices, using cleanroom facilities of the CSEM and EPFL. To prevent the proof mass from breaking off during routine handling, the fabrication process integrates hard stops around the proof mass on all axes to limit its displacement to 30 microns due to shock or vibration. The yield of the process was quite low, due to premature breakage of the proof mass before all hard stops are integrated. The primary cause is a high variation in the etch rate of the HF vapor etch process, used to etch away the oxide that holds the proof mass to the chip frame.

In-plane sensing of the proof mass displacement is carried out using a fiber optic interferometer, integrated onto the ES chip. A test setup is created using a piezo stage that can reproduce the expected nm-scale displacement in microgravity, on Earth. After being mounted on the piezo stage, the sensor has to be aligned such that the proof mass does not touch any of the hard stops. Due to the single spring design, this was extremely difficult to do for the 1st generation ES chip, and limited the amount of testing done. The interferometer output is observed to be noisy, and the best accuracy achievable for use in an ES instrument is computed to be +/- 22.5°.

The 1st generation sensor demonstrated that an inertial MEMS sensor to measure GGT, designed with a 1 cm x 4 cm proof mass, with a resonant frequency of the order of 1 Hz could be fabricated and survives routine handling on Earth. A custom test setup using a two axis piezo tilt stage to replicate the small displacements necessary to test the ES chips on Earth is validated.

9.2.2nd Generation MEMS Earth sensor

The 2nd generation sensor improves upon the design in several ways and is significantly modified from the 1st generation. Instead of a proof mass suspended by a single spring, whose displacement is sensed in-plane, the proof mass of the 2nd generation design is suspended from two springs, and the displacement is sensed out-of-plane by differential capacitive sensing. The main advantage of the two spring design is that it is easier to test on Earth. Operation of the sensor on a tumbling satellite is examined in detail, and the design is optimized to minimize the errors arising from centripetal forces on the sensor, and compensate for the errors caused by the fabrication tolerances. The design includes electrodes for closed loop operation using electrostatic force feedback. The outline dimensions of the ES proof mass are 1 cm x 5 cm and the thickness is 130 microns. The proof mass is suspended from two springs, each of which is designed to have dimensions of 1 mm x 8 microns x 108.5 microns.

During the fabrication of the 2nd generation sensor, three fabrication iterations were necessary to develop solutions to the problems encountered during the various process steps, and ultimately a reliable fabrication process is developed. The fabrication process for the 2nd generation ES chip solves

Chapter 9: Conclusion

the problem of the variation in the etch rate of the HF vapor etch. The setup for HF vapor etching is modified, so that the etch rate is controlled by convective heating instead of conductive heating. This reduces the variation in the etch rate to 10-20 %, down from the 300 % variation seen for the 1st generation Earth sensor fabrication. The integration of hard stops is simplified, and overall much fewer chips are lost due to premature breakage of the proof mass. A low stress solution is developed to mount the ES chip on a PCB using Kapton tape. A two layer metallization process using aluminum and gold ensures that the capacitance sense electronics, actuation electrodes and ground electrodes on the ES chip are connected to the readout electronics using gold wirebonds. After fabrication and mounting, the chips are quite robust, and can be handled and stored without special precautions. The ES chip survives 0.25 g sinusoidal vibrations; in a frequency range from 50-2000 Hz. In general, the methods developed in this fabrication process can be extended for MEMS applications that require large cm-scale proof masses suspended from compliant springs, such that the resonant frequency is in the range of Hz.

Tests using an optical profiler and visual check using a microscope show that the 1 x 5 cm² proof mass is free to move without touching any hard stops. Alignment of the proof mass so that it does not touch any hard stops is readily accomplished as compared to the 1st generation ES, using the dedicated test setup of a two axis piezo tilt stage. The piezo is then used to replicate nm-scale motion of the proof mass on Earth, and the capacitive displacement sensing is able to measure the change in capacitance due to this motion. The accuracy is limited by the noise at the output of the IC used to perform the measurement.

The design resonant frequency for the 2nd generation ES is 1.5 Hz. This depends on the dimensions, and therefore stiffness of the spring. Post fabrication, the trapezoidal cross section of the spring diverges from the ideal rectangular cross section. The sidewall slope of the trapezoid is dependent upon process parameters and can vary. Precautions taken during fabrication to obtain testable chips result in a spring wider than the design, and based on SEM measurements, the resonant frequency is estimated to be 2.9 Hz using analytical calculations and ANSYS modeling. Comparing the predictions of ANSYS model of the sensor to the measured motion of the proof mass, due to small tilts produced by the piezo stage, indicate that the spring stiffness is close to the analytical calculation.

The transient response of the sensor, for a step input in air is measured and the sensor is seen to be overdamped. The probable cause is squeeze film damping between the proof mass and the capacitance sense electrodes at the extremities of the proof mass. Squeeze film damping decreases with decreasing pressure, and it is absent in the hard vacuum of space. Based on extrapolation of the squeeze film damping model to lower pressures, a Q factor in the hundreds is possible for pressures less than 0.01 mbar.

Testing of the capacitive displacement sensing is performed using two capacitance to digital converters ICs from Analog Devices, the AD7745 and AD7747. The AD7745 shows lower noise and drift, and is capable of measuring smaller displacements. The AD7747, though showing higher noise and drift is better suited for closed loop operation of the sensor. The use of commercially available ICs which can be directly interfaced to a microcontroller through the I2C bus is an important step towards possible

Chapter 9: Conclusion

further development of the sensor. Though desirable, the development of a dedicated ASIC for the capacitive displacement sensing is unlikely, given the low production volumes for such a sensor. For use in space, extensive analysis of the effects of ionizing radiation on the AD7745 and AD7747 will be necessary.

Due to the use of SOI wafers to fabricate the sensors, differential bow between the device layer (proof mass) and handle layer (chip frame) after the proof mass is released from the chip frame, results in the gap between the proof mass and the capacitance sense electrodes (attached to chip frame) deviating from the design. An increased gap means that the nominal capacitance of the sense electrode is reduced, which drives down the capacitance change obtained due to a given displacement. Due to the differential bow between the proof mass and chip frame, a reduction in sensitivity is observed for the ES chips tested, compared to the designed capacitance change for a given displacement.

The noise of the capacitance displacement sensing is low enough so that the sensor is capable of measuring displacements less than a nanometer, but its sensitivity depends on the nominal capacitance of the sense electrode. By design, the minimum capacitance change that should be measured to achieve an accuracy of +/- 2° is 200 aF. The measured peak-to-peak noise, averaged to 1 Hz for the AD7745, is 500 aF. For the fabricated 2.9 Hz sensor, assuming a nominal capacitance of 10 pF for the sense electrodes, this would result in an accuracy of +/- 10° for the pitch and roll angle measurements.

9.3. Summary

The thesis describes the concept of an Earth sensor instrument that uses the gravity gradient of the Earth as a reference for attitude determination on-board satellites in low Earth orbit. Using the gravity gradient to determine satellite attitude provides a 4π steradian field of view for the instrument. A single unit of mass 1 kg and volume 1 dm³ can replace multiple conventional Earth sensors. This results in mass and power savings for a satellite. A gravity gradient Earth sensor can provide added capabilities as the main Earth sensor or as a backup sensor.

This instrument is based on a novel MEMS inertial sensor that measures the GGT in orbit. Two generations of this novel inertial sensor are designed, fabricated and tested. To be able to measure the GGT with a resolution of 10^{-15} N.m, the 2nd generation ES chip has a proof mass of outline dimensions 1 x 5 cm², suspended by very compliant springs, which results in an estimated resonant frequency of 2.9 Hz for the sensor, which, to the best of our knowledge is the lowest reported resonant frequency for a MEMS inertial sensor. Despite this low spring stiffness, this sensor does not need special handling, and is robust enough to survive low magnitude vibrations

A new microfabrication process, based on SOI wafers, is developed for the ES chips. Integrating hard stops to limit the motion of the proof mass to 10 microns on all axes, along with an improved HF vapor release process, is critical to realizing the high sensitivity, yet robust inertial sensor.

Chapter 9: Conclusion

The sensor design also makes it possible to test for the expected performance in microgravity on Earth. A dedicated test setup to replicate the nm-scale motion of the proof mass is developed, and this is used to test the displacement sensing.

A simple and robust capacitive displacement sensing scheme, developed using commercially available CDC chips from Analog Devices that provide a digital output, allows easy interfacing of the sensor to the additional electronics that would comprise an ES instrument. The noise of the AD7745 is low enough to measure the displacement of the proof mass due to GGT.

This thesis conclusively demonstrates the feasibility of a novel inertial sensor to measure the GGT. We have been able to design, successfully fabricate and test an ES chip on Earth, whose readout is capable of measuring the displacement due to GGT in low Earth orbit. The size and dimensions of the chip are suited to the 1 kg mass and 1 dm³ volume goals of a gravity gradient based Earth sensor.

Developing a full Earth sensor Instrument is a larger task, for which we have been collaborating with RUAG Space (Zurich, Switzerland) for the past 18 months. RUAG Space has developed a conceptual design of the complete instrument, including force-feedback electronics and data processing plan, fitting in the target mass, power and volume budgets. Performance data from future MEMS chips will allow further refining of the design, ultimately leading to a new miniaturized commercially available Earth Sensor Instrument.

9.4.Future Work

Though the feasibility of MEMS ES chips to measure GGT is demonstrated, the performance does not match the design goal of being able to measure pitch and roll angles with an accuracy of +/- 2°. The performance and robustness of the sensor can be increased in the following ways:

- The main problems observed during testing of the 2nd generation sensor arose due to the differential bow of the device and handle layers of the SOI wafers that the ES chip is made from. In the current design, the bow of the chip frame is governed by the bow of the handle layer, while the proof mass bow is governed by the device layer bow. The design can be modified such the chip frame is provided by the device layer as well so that the bow of the chip frame is governed by the device layer, instead of the handle layer. This should allow the chip frame to follow the bow of the proof mass.
- If the device layer is used for the chip frame, then it is advantageous to use a thicker device layer for greater mechanical strength. A thicker device layer also means a thicker proof mass. Though the DRIE etch of the device layer becomes more challenging with, increasing the thickness of the proof mass is desirable, since it provides the following advantages:
 - SOI wafers with 5 micron thick oxide are used for the chips fabricated. The reason for such a thick oxide was to prevent the proof mass from touching any hard stop due to the sag caused by the weight of the proof mass in gravity. A thicker proof mass will sag less, therefore making it possible to reduce the oxide thickness, and therefore the

Chapter 9: Conclusion

capacitance sense gap between the proof mass and the sense electrode will also reduce. This will increase the sensitivity of the displacement measurements.

- A thicker proof mass results in a higher moment of inertia, and therefore a lower thermal noise floor.
- A thicker proof mass will make the DRIE more challenging, but by keeping the DRIE aspect ratio constant, the risk can be reduced.
- A wider trench around the proof mass will result in reduced robustness. External hard stops were fabricated for the 2nd generation ES to limit vertical motion. This concept can be extended to limit lateral motion as well. The DRIE can be then performed with a low aspect ratio. Later, with proper design, hard stops can be integrated close to the proof mass, that limit the lateral motion below the width of the DRIE trench.
- During the vibration tests, erosion of the hard stops is observed. To prevent this, the hard stops could be made using some elastic polymer which can be micro-structured, such as SU-8.

The 2nd generation inertial sensor has been selected by ESA as a payload on the REXUS sounding rocket which is scheduled to fly in March 2012. This provides an excellent opportunity to test the sensor in a microgravity environment, and gain valuable data about the survivability of the MEMS ES on an actual rocket.

Appendix A - Gravity Gradient Earth Sensor Experiment on REXUS 11

REXUS (Rocket EXperiments for University Students) is a European program, organized by ESA in collaboration with the German and Swedish Space agencies, for student experiments on sounding rockets launched from Esrange in Kiruna, northern Sweden.

We submitted a proposal to for an experiment to test the ES sensor developed for this thesis on this sounding rocket flight for a few minutes in microgravity. The proposal was accepted and currently an eight member team of students is working to prepare the experiment payload for the REXUS 11 flight in March 2012. The experiment will carry four 2nd generation ES chips, and the hope is that these chips will be able to measure the gravity gradient while the payload is in freefall.

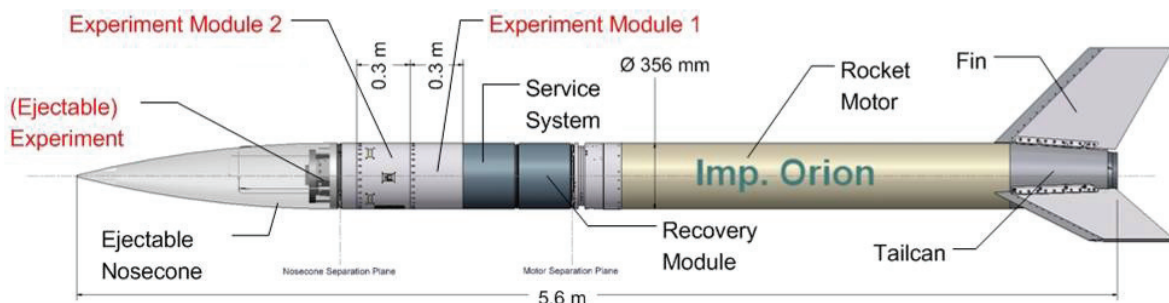


Figure A-0-1 Schematic of REXUS, the rocket provides power supply, telemetry downlink and some control signals for the experiments [58]

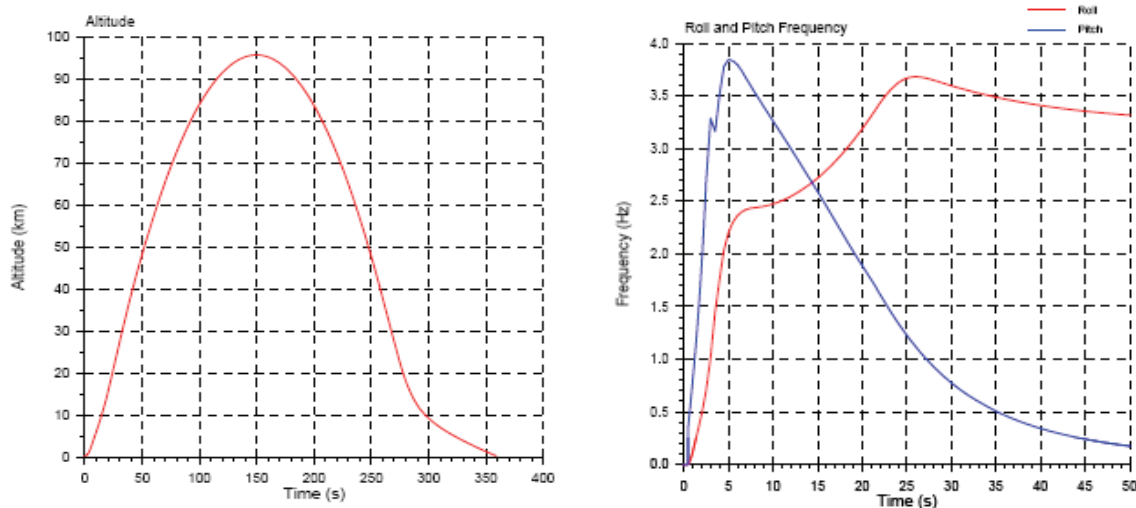


Figure A-0-2 left: REXUS flight profile; right: it is launched spin stabilized, and then despun after the rocket motor burns out [58]

The rocket flight profile and thermal environment pose the majority of requirements on the experiment. For example, apart from gathering data from the MEMS chips, temperature data and information about

Appendix A: GGES Experiment on REXUS

the acceleration and rotation of the payload is gathered throughout the flight. Apart from the science data, one of the objectives of the REXUS program is to provide hands on learning experience for students to design, build and test an experiment for space.

Experiment Objectives:

The experiment objectives are listed in order of priority

- The GGES experiment has passed functional and acceptance tests in order to fly on REXUS 11 during the launch campaign in March 2012
- Record the displacement of a MEMS proof mass due to GGT in free fall.
- Record the external rotational forces acting on the MEMS sensor during the flight.
- Record the external translational forces acting on the MEMS sensor during the flight.
- Post flight, from the displacement data gained, subtract errors estimated from the inertial environment information recorded during the flight and verify that the displacement of the Earth sensor corresponds to the GGT. Estimate the accuracy of the MEMS in measuring the Earth vector.

Figure A-4 shows the functional schematic of the experiment. The experiment is designed with redundancy in mind, and the experiment is split into two sets of identical electronics with two MEMS chips each. One chip in the set of two is oriented to measure roll, and the second MEMS to measure pitch (Figure A-3). With each set of MEMS, an IMU measures the acceleration and rotation, so any errors due to external inertial forces can be subtracted out. Data from the MEMS CDC chips and the IMU is gathered and stored by a microcontroller on a micro SD card. A subset of the data is downlinked via the telemetry service provided by the rocket. The rocket is launched in an ambient temperatures of -30 C, so each MEMS chip has a heater integrated into its package (Figure A-5)

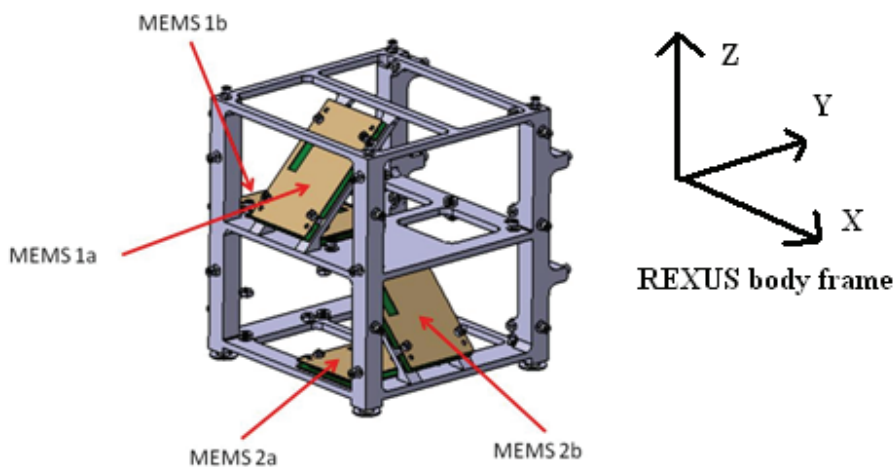


Figure A-0-3 Mechanical frame of the experiment showing the positions of the MEMS chips to measure roll and pitch

Appendix A: GGES Experiment on REXUS

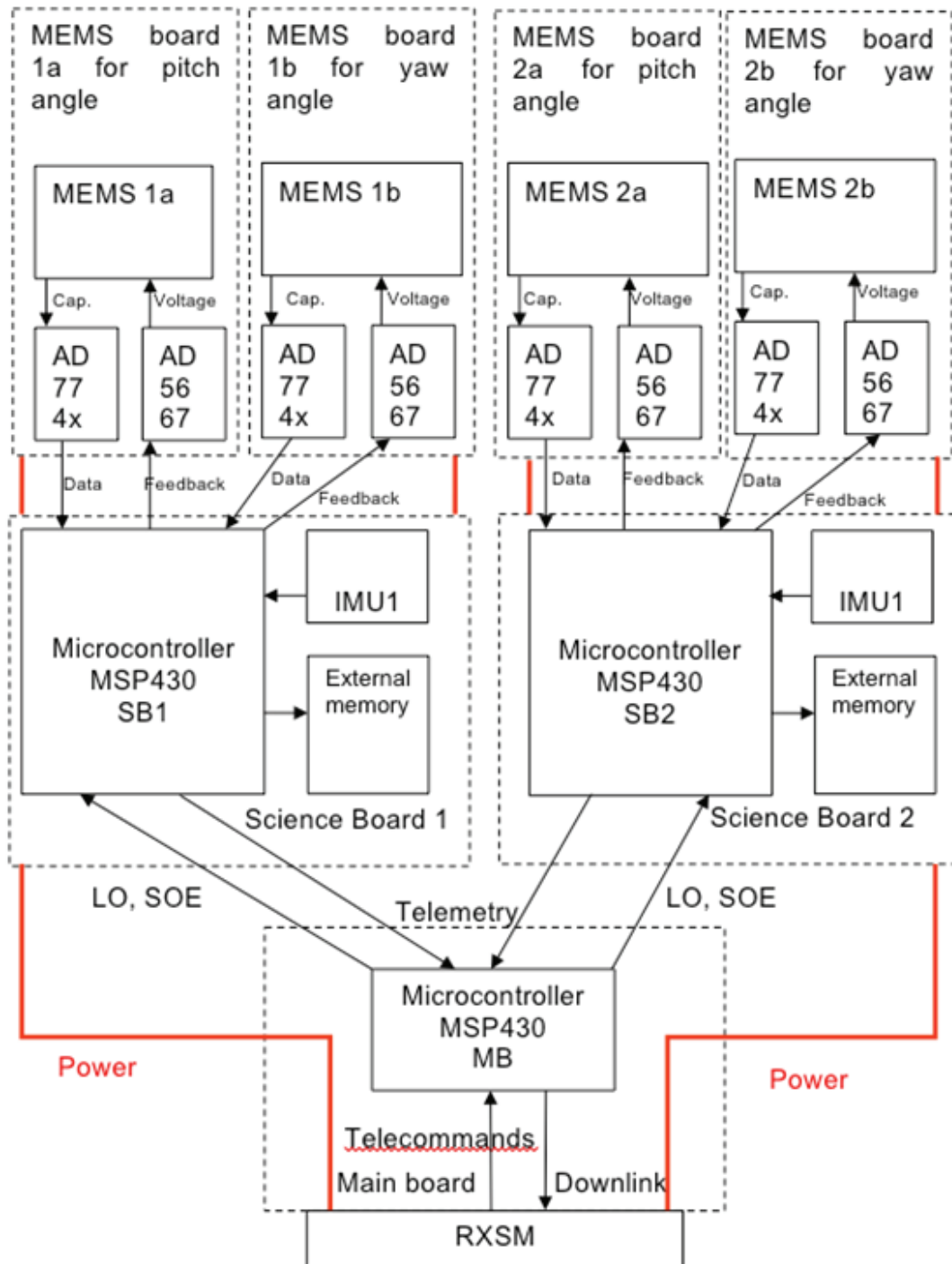


Figure A-0-4 Diagram of GGES experiment setup

Appendix A: GGES Experiment on REXUS

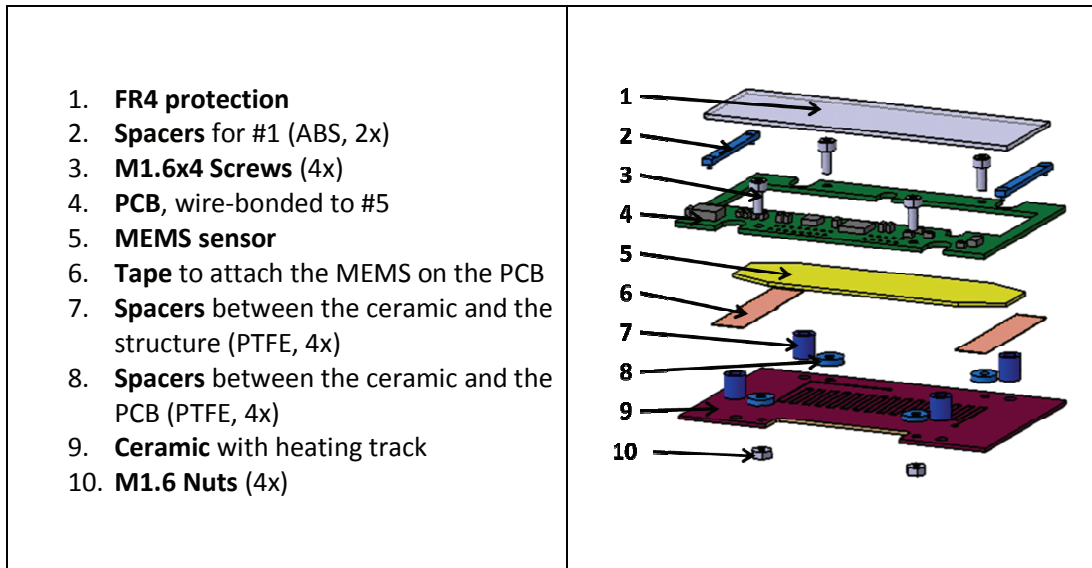


Figure A-0-5 Low stress MEMS Packaging for the flight, with an integrated heater for thermal protection in below zero temperatures

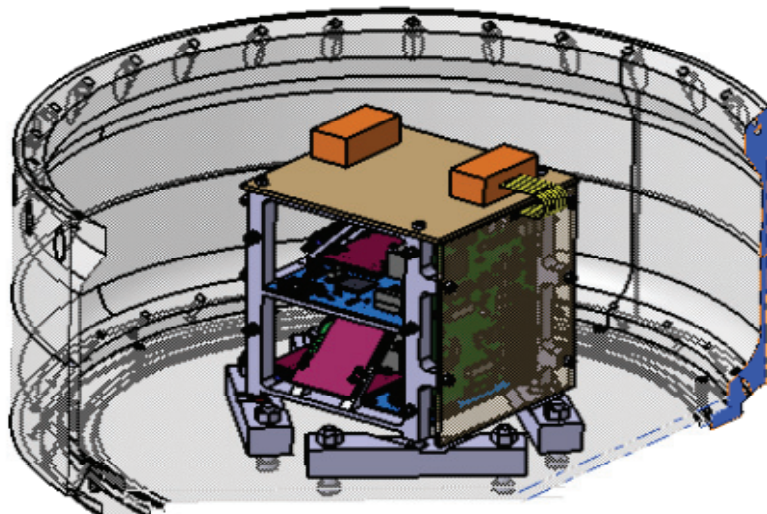


Figure A-0-6 Cutaway drawing of the rocket module showing the experiment mounted on an internal bulkhead

Bibliography

- [1] J.R. Wertz, W.J. Larson, Space Mission Analysis and Design, Kluwer Academic Publishers, Dordrecht, 1999
- [2] Lunde B.K., "A Reliable Earth Sensor For Attitude Sensing", IEEE Transactions on Aerospace and Navigational Electronics, Oct. 1963, Issue: 0 page(s): 3.6.4-1 - 3.6.4-6
- [3] IRES Earth sensor http://www.selex-sas.com/EN/Common/files/SELEX_Galileo/Products/Ires_ne.pdf
- [4] NES Earth sensor ftp://ftp.elet.polimi.it/users/Marco.Lovera/ESAGNC08/S03/01_Boldrini.pdf
- [5] SDT15 Earth sensor http://www.sodern.com/sites/docs_wsw/RUB_52/STD15.pdf
- [6] STD 16 Earth sensor http://www.sodern.com/sites/docs_wsw/RUB_52/STD16.pdf
- [7] Yazdi N., Ayazi F., Najafi K., "Micromachined Inertial Sensors", Proceedings of the IEEE, Aug 1998, Volume: 86, 1640 - 1659
- [8] C. H. Liu and T. W. Kenny, "A high-precision, wide-bandwidth micromachined tunneling accelerometer," J. Microelectromech. Syst., vol. 10, no. 3, pp. 425–433, Sep. 2001
- [9] Hall, N.A.; Okandan, M.; Littrell, R.; Serkland, D.K.; Keeler, G.A.; Peterson, K.; Bicen, B.; Garcia, C.T.; Degertekin, F.L.; , "Micromachined Accelerometers With Optical Interferometric Read-Out and Integrated Electrostatic Actuation," Microelectromechanical Systems, Journal of , vol.17, no.1, pp.37-44, Feb. 2008
- [10]U. Krishnamoorthy, R.H. Olsson, G.R. Bogartb, M.S. Bakera, D.W. Carrb, T.P. Swilera, P.J. Clewsa, "In-plane MEMS-based nano-g accelerometer with sub-wavelength optical resonant sensor", Sensors and Actuators A: Physical Volumes 145-146, July-August 2008, Pages 283-290
- [11]A. Albertella, F. Migliaccio, F. Sanso, "GOCE: The Earth Gravity Field by Space Gradiometry", Celestial Mechanics and Dynamical Astronomy, Vol. 83, 1-4, pp. 1-15, 2002
- [12]Yu N., Kohel J.M., Kellogg J.R., Maleki L., "Development of an atom-interferometer gravity gradiometer for gravity measurement from space", Applied Physics B: Lasers and Optics, 2006-09-01, 647-652, Volume: 84, Issue: 4
- [13]ESA HYPER study http://sci2.esa.int/hyper/docs/HYP-9-04_v10.pdf
- [14]Flokstra, J. and Cupurus, R. and Wiegerink, R.J. and Essen van, M.C., "A MEMS-based gravity gradiometer for future planetary missions". Cryogenics, 49 (11). pp. 665-668
- [15]GEOSAT <http://science.nasa.gov/missions/geosat/>

- [16]TSS-1R <http://www-istp.gsfc.nasa.gov/Education/wtether.html>
- [17]Gabrielson, T.B.; , "Mechanical-thermal noise in micromachined acoustic and vibration sensors," *Electron Devices, IEEE Transactions on* , vol.40, no.5, pp.903-909, May 1993
- [18]MS3110 datasheet <http://www.irvine-sensors.com/pdf/MS3110%20Datasheet%20USE.pdf>
- [19]ZSC 31210 datasheet<http://www.zmdi.com/products/sensor-signal-conditioner/zsc31210/>
- [20]AD7747 datasheet www http://www.analog.com/static/imported-files/data_sheets/AD7747.pdf
- [21]AD7745 datasheet http://www.analog.com/static/imported-files/data_sheets/AD7745_7746.pdf
- [22]W.C. Young, R.G. Budynas, Roark's Formulas for Stress and Strain, McGraw-Hill, New York, 2002
- [23]Seeger, J.I.; Boser, B.E.; , "Charge control of parallel-plate, electrostatic actuators and the tip-in instability," *Microelectromechanical Systems, Journal of* , vol.12, no.5, pp. 656- 671, Oct. 2003
- [24]Starr, J.B.; , "Squeeze-film damping in solid-state accelerometers," *Solid-State Sensor and Actuator Workshop*, 1990. 4th Technical Digest., IEEE , vol., no., pp.44-47, 4-7 Jun 1990
- [25]Yazdi, N.; Najafi, K.; , "An all-silicon single-wafer micro-g accelerometer with a combined surface and bulk micromachining process," *Microelectromechanical Systems, Journal of* , vol.9, no.4, pp.544-550, Dec 2000
- [26]Bernstein, J.; Miller, R.; Kelley, W.; Ward, P.; , "Low-noise MEMS vibration sensor for geophysical applications," *Microelectromechanical Systems, Journal of* , vol.8, no.4, pp.433-438, Dec 1999
- [27]Roszhart, T.V.; Jerman, H.; Drake, J.; de Cotiis, C.; , "An Inertial-Grade, Micromachined Vibrating Beam Accelerometer," *Solid-State Sensors and Actuators, 1995 and Eurosensors IX.. Transducers '95. The 8th International Conference on* , vol.2, no., pp.656-658, 25-29 Jun 1995
- [28]Yazdi, N.; Najafi, K.; , "An all-silicon single-wafer fabrication technology for precision microaccelerometers," *Solid State Sensors and Actuators, 1997. TRANSDUCERS '97 Chicago.*, 1997 International Conference on , vol.2, no., pp.1181-1184 vol.2, 16-19 Jun 1997
- [29]J.D. Zook, D.W. Burns, H. Guckel, J.J. Sniegowski, R.L. Engelstad, Z. Feng, "Characteristics of polysilicon resonant microbeams", *Sensors and Actuators A: Physical*, Volume 35, Issue 1, October 1992, Pages 51-59
- [30]RG Christian, "The theory of oscillating-vane vacuum gauges", *Vacuum*, Volume 16, Issue 4, April 1966, Pages 175-178
- [31]W.E. Newell, Miniaturization of Tuning Forks, *Science* , 161 (3848), 1320-1326, 27 September 1968

- [32]Zsolt Kádár, Wilko Kindt, Andre Bossche, Jeff Mollinger, Quality factor of torsional resonators in the low-pressure region, Sensors and Actuators A: Physical, Volume 53, Issues 1-3, May 1996, Pages 299-303
- [33]Bingqian Li, Haoyang Wu, Changchun Zhu, Junhua Liu, The theoretical analysis on damping characteristics of resonant microbeam in vacuum, Sensors and Actuators A: Physical, Volume 77, Issue 3, 2 November 1999, Pages 191-194
- [34]Minhang Bao, Heng Yang, Hao Yin and Yuancheng Sun, "Energy transfer model for squeeze-film air damping in low vacuum", Journal of Micromechanics and Microengineering, Volume 12, Number 3, 193-197, May 2002
- [35]M. Andrews, I. Harris, G. Turner, A comparison of squeeze-film theory with measurements on a microstructure, Sensors and Actuators A: Physical, Volume 36, Issue 1, March 1993, Pages 79-87
- [36]Timo Veijola, Heikki Kuisma, Juha Lahdenperä, Tapani Ryhänen, Equivalent-circuit model of the squeezed gas film in a silicon accelerometer, Sensors and Actuators A: Physical, Volume 48, Issue 3, 30 May 1995, Pages 239-248
- [37]Timo Veijola, "Compact models for squeezed-film dampers with inertial and rarefied gas effects", Journal of Micromechanics and Microengineering, Volume 14, Number 7, 1109-1118, July 2004
- [38]H. Sumali, "Squeeze-film damping in the free molecular regime: model validation and measurement on a MEMS", J. Micromech. Microeng., Volume 17, Page 2231, 2007
- [39]Hopcroft, M.A.; Nix, W.D.; Kenny, T.W.; , "What is the Young's Modulus of Silicon?," Microelectromechanical Systems, Journal of , vol.19, no.2, pp.229-238, April 2010
- [40]Rugar, D.; Mamin, H. J.; Guethner, P.; , "Improved fiber-optic interferometer for atomic force microscopy," Applied Physics Letters , vol.55, no.25, pp.2588-2590, Dec 1989
- [41]Rugar, D.; Mamin, H. J.; Erlandsson, R.; Stern, J. E.; Terris, B. D.; , "Force microscope using a fiber-optic displacement sensor," Review of Scientific Instruments , vol.59, no.11, pp.2337-2340, Nov 1988
- [42]T.R. Albrecht, P. Grütter, D. Rugar, D.P.E. Smith, Low-temperature force microscope with all-fiber interferometer, Ultramicroscopy, Volumes 42-44, Part 2, July 1992, Pages 1638-1646
- [43]Mamin H.J., Rugar D., Sub-attoneutron force detection at millikelvin temperatures, Applied Physics Letters (2001), 79 (20), pp. 3358-3360
- [44]Analog Devices ADXL150 accelerometer
<http://www.analog.com/library/analogDialogue/archives/30-4/acccel.html>

- [45]ST Microelectronics LIS331DLF accelerometer
http://www.st.com/internet/com/TECHNICAL_RESOURCES/TECHNICAL_LITERATURE/DATASHEET/C_D00213608.pdf
- [46]Huikai Xie; Fedder, G.K.; , "A CMOS z-axis capacitive accelerometer with comb-finger sensing," Micro Electro Mechanical Systems, 2000. MEMS 2000. vol., no., pp.496-501, 23-27 Jan 2000
- [47]Junseok Chae; Kulah, H.; Najafi, K.; , "A monolithic three-axis micro-g micromachined silicon capacitive accelerometer," Microelectromechanical Systems, Journal of , vol.14, no.2, pp. 235- 242, April 2005
- [48]W. H. Juan and S. W. Panga, Controlling sidewall smoothness for micromachined Si mirrors and lenses, Vac. Soc. J. Vacuum Science Technol. B, vol. 14, 1996, pp. 4080–4084
- [49]Colibrys SF3000 <http://www.colibrys.com/e/page/140/>
- [50]MMF Seismic Accelerometers http://www.mmf.de/seismic_accelerometers.htm
- [51]Barbour, N.; Schmidt, G.; , "Inertial sensor technology trends," Sensors Journal, IEEE , vol.1, no.4, pp.332-339, Dec 2001
- [52]Huikai Xie; Fedder, G.K.; , "Fabrication, characterization, and analysis of a DRIE CMOS-MEMS gyroscope," Sensors Journal, IEEE , vol.3, no.5, pp. 622- 631, Oct. 2003
- [53]Alper, S.E.; Akin, T.; , "A Single-Crystal Silicon Symmetrical and Decoupled MEMS Gyroscope on an Insulating Substrate," Microelectromechanical Systems, Journal of , vol.14, no.4, pp. 707- 717, Aug. 2005
- [54]Said Emre Alper, Kivanc Azgin, Tayfun Akin, A high-performance silicon-on-insulator MEMS gyroscope operating at atmospheric pressure, Sensors and Actuators A: Physical, Volume 135, Issue 1, 30 March 2007, Pages 34-42
- [55]Lemkin, M.A.; Boser, B.E.; Auslander, D.; Smith, J.H.; , "A 3-axis force balanced accelerometer using a single proof-mass," Solid State Sensors and Actuators, 1997. TRANSDUCERS '97 Chicago., vol.2, no., pp.1185-1188 vol.2, 16-19 Jun 1997
- [56]Lemkin, M.; Boser, B.E.; , "A three-axis micromachined accelerometer with a CMOS position-sense interface and digital offset-trim electronics," Solid-State Circuits, IEEE Journal of , vol.34, no.4, pp.456-468, Apr 1999
- [57]Hall, N.A.; Okandan, M.; Littrell, R.; Serkland, D.K.; Keeler, G.A.; Peterson, K.; Bicen, B.; Garcia, C.T.; Degertekin, F.L.; , "Micromachined Accelerometers With Optical Interferometric Read-Out and Integrated Electrostatic Actuation," Microelectromechanical Systems, Journal of , vol.17, no.1, pp.37-44, Feb. 2008
- [58]GGES Student Experiment Document RX11_GGES_SEDv3-0_9_August11

- [59]REXUS User Manual v7.3
http://www.rexusbexus.net/images/stories/rexus/rx_ref_usermanual_v7-3_31aug11.pdf
- [60]Fortescue P., Swinerd G., Stark J., *Spacecraft Systems Engineering*, John Wiley and Sons, United Kingdom, 2003
- [61]Yoon S. W., "Vibration isolation and shock protection for MEMS", PhD Dissertation University of Michigan, 2009
- [62]L. B. Wilner, "A high performance, variable capacitance accelerometer," *IEEE Transactions on Instrumentation and Measurement*, vol. 37, pp. 569-571, 1988
- [63]S. Huang et al., "A piezoresistive accelerometer with axially stressed tiny beams for both much increased sensitivity and much broadened frequency bandwidth," *Proceedings of International Conference on Solid-State Sensors, Actuators and Microsystems*, 2003, pp. 91-94
- [64]G. J. O'Brien, J. Hammond, G. Li, D. Koury, and D. J. Monk, "Outrigger: solid outer frame lateral accelerometer design," in the *Proceeding of International Conference on Solid-State Sensors, Actuators and Microsystems (TRANSDUCERS)*, 2005, pp. 176-179
- [65]A. Selvakumar and K. Najafi, "A high-sensitivity z-axis capacitive silicon microaccelerometer with a torsional suspension," *Journal of Microelectromechanical Systems*, vol. 7, pp. 192-200, 1998
- [66]Sang Won Yoon et al., "Analysis and wafer-level design of a high-order silicon vibration isolator for resonating MEMS device", 2011 *J. Micromech. Microeng.* 21 015017
- [67]Sang Won Yoon, Sangwoo Lee, Perkins, N.C., Najafi, K., "Shock-Protection Improvement Using Integrated Novel Shock-Protection Technologies," *Microelectromechanical Systems, Journal of*, vol.20, no.4, pp.1016-1031, Aug. 2011
- [68]Naumann, M., Mehner, J., Lin, D., Miller, T.F., "Design and application of flexible stops for MEMS devices," *Sensors*, 2010 IEEE , vol., no., pp.168-173, 1-4 Nov. 2010
- [69]Junseok Chae, Kulah H., Najafi, K., "An in-plane high-sensitivity, low-noise micro-g silicon accelerometer with CMOS readout circuitry," *Microelectromechanical Systems, Journal of* , vol.13, no.4, pp. 628- 635, Aug. 2004
- [70]Ranjith Amarasinghe, Dzung Viet Dao, Toshiyuki Toriyama, Susumu Sugiyama, "Development of miniaturized 6-axis accelerometer utilizing piezoresistive sensing elements", *Sensors and Actuators A: Physical*, Volume 134, Issue 2, 15 March 2007, Pages 310-320
- [71]Peitao Dong, Xinxin Li, Heng Yang, Haifei Bao, Wei Zhou, Shengyi Li, Songlin Feng, High-performance monolithic triaxial piezoresistive shock accelerometers, *Sensors and Actuators A: Physical*, Volume 141, Issue 2, 15 February 2008, Pages 339-346

Resume of Kaustav Ghose

Education

12/2007 - present	PhD Candidate, EPFL, Switzerland Research Topic – A novel MEMS inertial sensor to measure the gravity gradient torque in orbit
10/2004 – 11/2007	Master of Science, Technical University of Darmstadt, Germany Major – Electrical Engineering with focus on photonics and semiconductors Thesis: Design, simulation, fabrication and characterization of micro-mirror arrays intended to function as multiple independently movable optical tweezers to trap and manipulate laser cooled Rb atoms.
07/1998 – 06/2002	Bachelor of Engineering from the University of Pune, (College - Pune Institute of Computer Technology), India Major - Electronics and Telecommunications Engineering

Professional Experience

12/2007 – present	Microsystems for Space Technologies Laboratory, EPFL, Switzerland Doctoral Assistant at the Microsystems for Space Technologies Laboratory Teaching Assistant for the course "Reliability of Microsystems" System Engineer for the Gravity Gradient Earth Sensor payload on the REXUS 11 sounding rocket
10/2004- 11/2007	Institute for Microwaves and Photonics, TU Darmstadt, Germany Research Assistant with the group of Prof. Dr. Dimitris Pavlidis (III-V devices) – AlN-GaN MISFETs, device modeling and characterization Research Assistant for the group of Prof. Dr. Peter Meissner (Photonics) – MEMS Tunable lasers for telecom and spectroscopy applications
07/2002 - 08/2004	Motorola India Electronics Limited, Bangalore, India Significant projects: <ul style="list-style-type: none">• Operating system services layer for the i275 chipset of Freescale semiconductor• System and Integration test for UMTS and GSM phones
01/2002 – 06/2002	PMC Sierra India Limited – Pune, India Intern: Design and development of a highly reconfigurable multi-protocol packet generator intended for testing chip designs used in high speed optical networks

Publications

"A Micromachined Earth Sensor Based on Measuring the Gravity Gradient Torque", K. Ghose, H.R. Shea, ASME 2009 International Mechanical Engineering Congress & Exposition, November 2009, Lake Buena Vista, Florida, USA

"Using a MEMS pendulum to measure the gravity gradient in orbit: a new concept for a miniaturized Earth sensor", K. Ghose, H.R. Shea, Eurosensors XXIII, September 2009, Lausanne, Switzerland

"Fabrication and Testing of a MEMS Based Earth Sensor", K. Ghose, H.R. Shea, Transducers 2009, June 2009, Denver, Colorado, USA

"AlN/GaN Metal Insulator Semiconductor Field Effect Transistor on Sapphire Substrate", Sanghyun Seo, Kaustav Ghose, Guang Yuan Zhao, and Dimitris Pavlidis, IEICE Trans Electron E91-C: 994-1000

"AlN/GaN MISFET for High Frequency Applications: Physical simulation and Experimental Evaluation", S. Seo, K. Ghose, D. Pavlidis and S. Schmidt European Microwave week 2007

Other Information

Computer skills Proficient with a wide variety of tools and simulators. Significant ones:

- ANSYS
- Cadence from Synopsys
- FlexPDE – a FEM tool suited to electromagnetic fields
- MATLAB
- AutoCAD
- Synopsys Centaurus

Proficient with the C programming language, Advanced in C++

Languages English, Bengali, Marathi, Hindi – Native

German – fluent

French - Beginner

Date of Birth 21-Dec-1980

Citizenship Indian